

UC Santa Barbara

UC Santa Barbara Electronic Theses and Dissertations

Title

Measurement-Induced Phase Transitions in Quantum Circuits

Permalink

<https://escholarship.org/uc/item/9w38s7fp>

Author

Li, Yaodong

Publication Date

2022

Peer reviewed|Thesis/dissertation

University of California
Santa Barbara

Measurement-Induced Phase Transitions in Quantum Circuits

A dissertation submitted in partial satisfaction
of the requirements for the degree

Doctor of Philosophy
in
Physics

by

Yaodong Li

Committee in charge:

Professor Matthew P. A. Fisher, Chair
Professor Sagar Vijay
Professor David M. Weld

September 2022

The Dissertation of Yaodong Li is approved.

Professor Sagar Vijay

Professor David M. Weld

Professor Matthew P. A. Fisher, Committee Chair

July 2022

Measurement-Induced Phase Transitions in Quantum Circuits

Copyright © 2022

by

Yaodong Li

Acknowledgements

I am first and foremost grateful to my advisor, Matthew Fisher, for his warm mentorship over the past five years. Matthew has always been generous with his time in advising me, which as I gather is something quite unusual. He has also been generous in sharing his insights and experiences. In addition, I am thankful for his enthusiasm, open-mindedness, attention to details, and kindness, which have been sources of constant inspiration.

Thanks are due to the QuBrain group, in particular Joshua Straub, Mesopotamia Nowotarski, Manisha Patel, Songi Han, Matt Helgeson, and Jeff Sczechowski, for having me around in the group meetings and answering my questions. I also thank Tobias Fromme, Marshall Deline, Alexej Jerschow, and Stuart Licht, for their most informative talks. I thank Vincent Hou for his initiative in thinking about Posner relaxation, and for many fun discussions.

I am indebted to the larger condensed matter theory group at UCSB. Xiao Chen has been a brotherly figure to me, and I thank him for most enjoyable collaborations and good advice. Andreas Ludwig taught me a tiny fraction of his encyclopedic knowledge of statistical physics and conformal field theory, which I find quite useful. Working with him has been a humbling and rewarding experience. I thank Sagar Vijay for a very fun collaboration and for many useful discussions. I also thank him for agreeing to be on my committee. I thank Tianci Zhou for informative conversations, and for sharing with me many of his notes. I thank Jake Hauser for sharing his enthusiasm and his many ideas, and for his most interesting questions. Thanks are also due to Leon Balents, Cenke Xu, and Chetan Nayak, who encouraged me to come to UCSB and to explore different things. I also thank them for their pedagogy, which I thoroughly enjoyed. I thank David Weld for sharing his notes, and for being on my committee. I have had stimulating discussions with Chao-Ming Jian, Hassan Shapourian, Ali Lavasani, Chaitanya Murthy, Teddy Parker, Dominic Else, Christina Knapp, Xiao-Chuan Wu, Chunxiao Liu, Mark Arildsen, Kasra Hejazi, Alan Tran, Zhitao Chen, Wayne Weng, and Aleksei Khindanov, and it is a pleasure to thank them all.

I had the good fortune of collaborating with many people outside UCSB, and it is a pleasure

to express my gratitude to Tim Hsieh, Shengqi Sang, Sisi Zhou, Zhi-Cheng Yang, Yijian Zou, Paolo Glorioso, Ehud Altman, Romain Vasseur, and Andy Lucas. I am particularly thankful to Tim for his encouragement. I thank Shengqi for being a reliable sounding board, by always making himself available for discussions, and for his most insightful feedback on many things. I thank Yijian for explaining to me many things about MPS, tensor networks, and conformal field theory in a very clear style, and for always available for discussions. I thank Sisi for answering many of my questions about covariant codes, and for useful comments.

It is a pleasure to thank Gang Chen, for introducing me to condensed matter physics and for many good advices. I also thank Guanyu Zhu, Tomas Jochym-O'Connor, and Andrew Cross, for their mentorship at IBM, and for teaching me about quantum error correction.

My past year at Stanford has been a rewarding experience, and I have Vedika Khemani to thank, who made this possible. I thank Matteo Ippoliti, Tibor Rakovszky, Nick O'Dea, Patrick Hayden, Rahul Nandkishore, Nick Hunter-Jones, Chaitanya Murthy, Anirudh Krishna, as well as Vedika, Yijian and Paolo, for insightful and eye-opening discussions. I thank Dominic Williamson for a very warm welcome, and for many interesting suggestions and for encouragement.

I have benefitted from comments and feedback from a long list of colleagues I “met” either at conference or via internet. Special thanks are due to Adam Nahum, Jonathan Ruhman, Nicole Yunger-Halpern, Hans-Peter Büchler, Michael Gullans, David Huse, Mario Motta, Ehud Altman, Soonwon Choi, and Yimu Bao, for extended discussions and/or notes.

My time at UCSB was greatly enriched by my friends, and I am grateful to all who shared the trailer, where I had fond memories. It is a pleasure to thank Joe Costello, Aleksei Khindanov, Joshua Straub, Xiao-Chuan Wu, Zhitao Chen, Seamus O'Hara, Sergio Hernandez Cuenca, Wayne Weng, Sarah Steiger, Noah Swimmer, Aaron Kennon, Will Schulz, Zhiran Zhang, Zeyun Peng, Chunxiao Liu, Simon Meynell, Brent Tan, Tianji Cai, Navin Tsung, Remi Boros, Brad Price, Yubi Chen, Farzan Vafa, and many others, for good times.

I had the chance to meet new friends and reconnect with old ones after moving to the Bay

area, and I thank all of them for enriching my life, in particular Qinqi Li, Yue You, Hao Tan, Mengyu Liu, Wanyu Huang, Siyuan Qiao, Xiaonan Zhang, Yu-ang Liu, Ye Hu, and Lu Liu. I also thank Huitao Shen, Chi Xu, Yiwen Zhu, Ziwei Ji, and Yiqun Wang for being great friends; I haven't met them much over the past years, but I cherish those occasions greatly.

I am grateful to my parents for their upbringing and for always supporting my decisions. I want to also thank my cousins, Yue Ma and Chris Gong, for taking time in visiting me several times at Santa Barbara, and for showing me around. Finally, I am most grateful to Shuyao Bi, for her friendship, love, and moral support. She has made my life much more enjoyable and memorable.

Curriculum Vitæ

Yaodong Li

Education

2022	Ph.D. in Physics (Expected), University of California, Santa Barbara.
2020	M.A. in Physics, University of California, Santa Barbara.
2016	B.Sc. in Computer Science, Fudan University, Shanghai, China.

Publications and Preprints Relevant to this Thesis

1. Y. Li, Y. Zou, P. Glorioso, E. Altman, M.P.A. Fisher. “Linear Cross Entropy Benchmark for Measurement-Induced Phase Transitions”. *In preparation*.
2. Y. Li, R. Vasseur, M.P.A. Fisher, A.W.W. Ludwig. “Statistical Mechanics Model for Clifford Random Tensor Networks and Monitored Quantum Circuits”. [arXiv: 2110.02988 \(2021\)](#).
3. Y. Li, M.P.A. Fisher. “Decodable monitored dynamics with \mathbb{Z}_2 symmetry”. [arXiv: 2108.04274 \(2021\)](#).
4. Z.-C. Yang, Y. Li, M.P.A. Fisher, X. Chen. “Entanglement phase transitions in random stabilizer tensor networks”. *Phys. Rev. B* **105**, 104306 (2022).
5. Y. Li, S. Vijay, M.P.A. Fisher. “Entanglement Domain Walls in Monitored Quantum Circuits and the Directed Polymer in a Random Environment”. [arXiv: 2105.13352 \(2021\)](#).
6. S. Sang, Y. Li, X. Chen, T. Zhou, T.H. Hsieh, M.P.A. Fisher. “Entanglement Negativity at Measurement-Induced Criticality”. *PRX Quantum* **2**, 030313 (2021).
7. Y. Li, M.P.A. Fisher. “Statistical mechanics of quantum error correcting codes”. *Phys. Rev. B* **103**, 104306 (2021).
8. X. Chen, Y. Li, M.P.A. Fisher, A. Lucas. “Emergent conformal symmetry in nonunitary random dynamics of free fermions”. *Phys. Rev. Res.* **2**, 033017 (2020).
9. Y. Li, X. Chen, A.W.W. Ludwig, M.P.A. Fisher. “Conformal invariance and quantum nonlocality in critical hybrid circuits”. *Phys. Rev. B* **104**, 104305 (2021).
10. Y. Li, X. Chen, M.P.A. Fisher. “Measurement-driven entanglement transition in hybrid quantum circuits”. *Phys. Rev. B* **100**, 134306 (2019).
11. Y. Li, X. Chen, M.P.A. Fisher. “Quantum Zeno effect and the many-body entanglement transition”. *Phys. Rev. B* **98**, 205136 (2018).

Abstract

Measurement-Induced Phase Transitions in Quantum Circuits

by

Yaodong Li

This thesis is devoted to the study of quantum dynamics interspersed with quantum measurements. Focusing on a one-dimensional “hybrid” quantum circuit model consisting of random unitary gates and local projective measurements, we provide extensive evidence for a stable “weakly measured phase” that exhibits volume law entanglement entropy, and a novel continuous quantum dynamical phase transition between the weakly measured phase and a strongly measured “quantum Zeno phase” that exhibits area law entanglement entropy. We further study consequences of conformal symmetry at the critical point, as well as properties of the weakly measured phase. In the latter case, we develop an effective domain wall theory which correctly accounts for an unusual subvolume powerlaw correction to the entanglement entropy, and draw close connections between the domain wall theory and an emergent quantum error correcting code. In the last Chapter, we discuss an experimental protocol that can avoid the so-called “postselection problem” and allow scalable experimental observations of such transitions on near term quantum processors.

Contents

Curriculum Vitae	vii
Abstract	viii
1 Introduction	1
1.1 Outlook	5
1.2 Permissions and Attributions	6
2 Hybrid circuit model and the measurement-induced phase transition	8
2.1 The circuit model	12
2.2 The phase diagram	15
2.3 Critical behavior	24
2.4 Circuits with Symmetry	30
2.5 Beyond Clifford	35
2.6 Discussion	42
3 Conformal invariance at the critical point	49
3.1 The hybrid circuit model and the conjecture	54
3.2 Results on rectangular circuits	68
3.3 Periodic boundary condition	92
3.4 Discussion and outlook	96
4 Capillary wave theory of dynamically generated quantum error correcting codes in the volume law phase	104
4.1 Model and setting	107
4.2 Domain wall picture of entanglement entropies	116
4.3 Numerical results	130
4.4 Discussion	134
5 Linear cross entropy benchmark for experimental observation of the phase transition	139
5.1 Linear cross-entropy and an order parameter	141
5.2 Discussions	149

A	Brief review of the stabilizer formalism and gauge fixing	151
A.1	Basics	151
A.2	The clipped gauge	159
A.3	Proof of Theorem 1 in Sec. 4.1.4	168
B	Entanglement dynamics under Clifford unitary-projective evolution	173
B.1	Unitary dynamics	174
B.2	Measurement dynamics	175
B.3	Toy particle traffic-flow model	179
C	Conformal invariance	182
C.1	Review of some elementary results in CFT	182
C.2	Purification dynamics of reference qubits in the Clifford Circuit	184
C.3	The scaling dimension $h_{f f}^{(1)}$ from “localizable entanglement”	189
C.4	Parallel results for the Hartley entropy in Haar circuits from minimal cuts in critical first-passage percolation	190
D	Capillary-wave theory calculations	196
D.1	Domain walls with pinned endpoints	196
D.2	“Waist” domain walls	200
D.3	Point-to-line (pl) domain walls	202
E	Cross entropy as boundary correlation function	203
E.1	Bulk cross entropy	203
E.2	Bulk cross entropy without encoding	207
E.3	Numerical algorithm for cross entropy in Clifford circuits	208
F	Bitstring distribution in the output state	212
	Bibliography	216

Chapter 1

Introduction

There are two fundamental processes in quantum mechanical time evolution, namely unitary ones as governed by the Schrödinger equation, and quantum measurements that break unitarity. On an abstract level, all quantum mechanical evolution in real time can in principle be reduced to a sequence of these two operations. For example, when the measurement results are left unattended or unrecorded, measurements are equivalent to couplings to a dissipative bath, which leads to “decoherence” of the quantum system. Classical behavior of the system invariably follows.

The situation is drastically different when the measurement results are recorded by an observer, so that the time evolution is kept coherent (albeit non-unitary) to the observer. (This is sometimes known as a “quantum trajectory” approach.) One early example is the EPR thought experiment [1], where “quantum entanglement” leads to perfectly correlated measurements on space-like separated particles, an apparent violation of causality. In quantum computing theory, tremendous effort has been devoted to designing such coherent processes of a large number of quantum bits (or “qubits”) – often in the form of quantum circuits – that can solve algorithmic problems beyond the reach of any classical computer. Here, the interplay between unitary time evolution and measurements must be so delicately designed that the measurements return the desired trajectory with a high probability [2].

Due to their inherent quantum mechanical nature and possible technological applications, such “hybrid” processes – particularly in the many-qubit setting – holds interest to both computer scientists and physicists. However, the space of such processes is extremely huge, so even for the purpose of exploration some focus is necessary. In the case of quantum computing, the algorithmic problem itself provides very useful guidance, as well as possible hardware considerations. Here, we are motivated by the theoretical question of possible dynamical “phases” [3, 4, 5, 6, 7, 8, 9, 10, 11] that can arise in such dynamics and their universal properties, as well as their potential of being realized in emerging experimental platforms [12, 13] and near term quantum processors [14], where measurements are native operations and quantum trajectories can be clearly resolved.

This thesis focuses on a particular model of this type, namely one dimensional “hybrid” quantum circuits in discrete time, with random two-qubit unitary gates and single-qubit measurements at random locations occurring with rate p per qubit per each time step [15, 16, 17]; see Fig. 2.1. This model thus describes a system that is constantly “monitored” by an observer. Although a simple idealization, it captures a common ingredient to all such hybrid processes, namely the competing effects between unitaries and measurements on the amount of entanglement, as quantified by the so-called “(von Neumann) entanglement entropy”, between qubits in a subregion A and its complement \bar{A} , defined as

$$S_A := -\ln \text{Tr} \rho_A \ln \rho_A.$$

Here ρ_A is the reduced state on A . While unitaries generically increase the entanglement entropy, measurements collapse the wavefunction and typically tends to reduce it on the trajectories. A main result of the thesis is the phase diagram of this model (Fig. 2.3), which features a stable volume law entangled phase (where $S_A \propto |A|$) for weak measurements and an area law phase (where $S_A = O(1)$) for strong measurements. The two phases are separated by a single second-order phase transition at $p = p_c$.

Notably, the volume law entanglement can coexist with measurements when p is below

a finite threshold. This initially came as a surprise [18], since the number of measurements that can reduce S_A is proportional to L_A , whereas only a constant number of unitaries at the boundary of A can increase S_A . Thus, the aforementioned competition is in an apparent imbalance, and a threshold would seem to be nonexistent. Part of this thesis is motivated by addressing this apparent puzzle, first in Chapter 2 by using various numerical characterizations, and later in Chapter 4 by using the decoupling principle [19] from the theory of quantum error correction; see also Refs. [20, 21, 22, 23, 24]. It is not an exaggeration to say that quantum error correction and the phenomenon of quantum information scrambling form the “conceptual pillar” [25] for such dynamics.

To put these results into context, it is useful to compare the hybrid dynamics with *purely* unitary quantum dynamics. With strong measurements, the steady state is area law entangled, and resembles ground states of gapped Hamiltonians rather than finite temperature Gibbs states. In this sense, measurements provides a mechanism to avoid thermalization.¹ We discuss this perspectives in more details at the beginning of Chapter 2; see also a recent review by Potter and Vasseur [26].

There is however an important aspect that is unique to this hybrid model. The phases are defined by entanglement entropies on individual quantum trajectories, which are themselves labelled by the measurement record. In general such trajectories can only be obtained by postselecting on the record. However, the number of trajectories is exponential in the number of measurements, for the history “branches” every time a measurement is made. Thus, it is not immediately clear what ramifications the phase transition would have on observable quantities, even if we can build the circuit perfectly in the lab. Related to the distinction between “recorded” and “unrecorded” measurements that we emphasized at the beginning of this Chapter, the transition must be probed by using the measurement outcomes explicitly, in one way or another. The most straightforward option is to experimentally postselect on the

¹As we show in Chapter 4, even in the volume law phase the steady state is also typically nonthermal, as evidenced by a subvolume powerlaw correction to the entanglement entropy. The correction is subtle, but crucial to the stability of the volume law phase.

measurements, but as we have argued this is not scalable. Alternatively, we may try to look at the probability distribution over measurement outcomes, which contains a lot of information. This is a first step towards our protocol in Chapter 5.

Yet another option is to relate the phase transition as one in the computational hardness of simulating either the hybrid dynamics in 1d [16] or unitary dynamics in 2d [27] on a classical computer. The phase transition is thus measured by the growth of classical resources with increasing circuit size.

The rest of this thesis is organized as follows. In Chapter 2, we define the model and our numerical method in detail, and provide extensive numerical characterizations of the phase diagram. We reveal that the phase transition exists is generic to hybrid circuits, and is largely independent of the microscopic details. We make heavy use of the stabilizer formalism in our numerical simulations, which allows us to confirm critical scaling behavior and unveil a subvolume powerlaw correction to the entanglement entropy in the volume law phase. In Chapter 3, we focus on the critical point, and provide extensive evidence to an emergent conformal symmetry. In turn, we use the conformal symmetry to obtain accurate estimates of several critical exponents. These results places the transition in a different universality classes than critical percolation, the latter describing the phase transition in certain simplifying limits. We also find EPR-like nonlocality as a necessary consequence of conformal invariance. In Chapter 4, we develop a capillary wave theory for the volume law phase based on analytical mappings of the circuit to statistical mechanical models [28, 29, 30, 31]. We relate certain properties of the statistical mechanical model to properties of a dynamically generated quantum error correcting code. In Chapter 5, we propose a protocol for experimentally probing the phase transition. This protocol tries to estimate the so-called “linear cross entropy” between bulk measurement outcomes, and has several advantages over existing ones.

We also bring the reader’s attention to a few more references that improves upon the results in this thesis, but not included here. Refs. [32, 33, 34] contains more recent results on the family of critical points discussed in Chapter 3. Ref. [32] also proposed a measure of multipartite

entanglement for a broader class of measurement induced phase transitions, which may be of independent interest. Ref. [35] improves the capillary wave theory in Chapter 4 by taking into account of quenched disorder, and the new theory – that the entanglement domain walls behave like directed polymer in random media – is in *quantitative* agreement with numerics.

1.1 Outlook

There are various models besides the random circuit model considered here that exhibit measurement-induced phases and phase transitions. We sample a few from these, and discuss future theoretical directions that could be made possible by these developments.

An important class is “measurement-only circuits” [36, 37, 38, 39, 40, 41, 42, 43]. These circuits do not have any built-in unitary gates, and the nontrivial dynamics is generated instead by competing local measurements drawn from a finite set. In many such models, one finds “measurement-protected phases” [39] with area law entanglement entropies favored by different types of measurements, and transitions between these area law phases can also be transitions in the channel capacity from finite to zero. Because the measurements are prevalent, the measurement-only circuits closely resemble the conventional “decoding” dynamics of a stabilizer code [44, 45, 46, 47] – with competing check operator measurements and interspersing errors – rather than an encoding circuit. This connection was noticed in Refs. [42] and explored in Refs. [42, 48], where the repetition code and the toric code are considered. Whether such connections can be further bolstered is a question worth further exploring. In particular, it would be extremely appealing to understand if certain refined notions, such as soundness [49] and single-shot properties [50], can be understood in universal terms.

Another interesting class of dynamics are those with continuous $U(1)$ symmetry, first defined in Refs. [51, 52, 53]. Due to symmetry constraints, the circuit dynamics is inevitably less scrambling, and as a consequence an observer is more effective in gaining information about the system (than in circuits without continuous symmetry) by making local charge measurements. This leads to a new type of phase transition, termed “charge sharpening transition”, where when

$p < p_{\#}$ (“charge fuzzy phase”) it takes polynomial time for the observer to read out the total charge in the system (which is conserved under time evolution), whereas when $p > p_{\#}$ (“charge sharp phase”) it takes only constant time to do so. This is in sharp contrast to the volume law phase of circuits without continuous symmetry, where this time scale is exponential in the system size, as would be the case whenever a domain wall picture with finite surface tension is at work. A description of the two phases would presumably not be in terms of domain walls, and is most intriguing. It would also be interesting if results from covariant quantum error correction [54, 55, 56] can be informative in understanding these phases.

Most recently, there have been works that try to find analogs of such hybrid quantum dynamics in classical systems [57, 58]. It would indeed be meaningful to perform such a comparison. For systems of basic degrees of freedom that are point-like, the dynamics considered are very similar to so-called probabilistic cellular automata, which strictly obey causality. On the other hand, if the point-like degrees of freedom are connected by strings, dynamics under local update rules of these points can induce certain nonlocal moves on the strings. It would be interesting to know to what extent classical dynamics can mimic quantum hybrid dynamics.

1.2 Permissions and Attributions

1. The content of Chapter 2 and Appendices A, B is the result of collaborations with Xiao Chen and Matthew P. A. Fisher [17, 59], and has previously appeared in *Physical Review B*.
2. The content of Chapter 3 and Appendix C is the result of collaborations with Xiao Chen, Andreas W. W. Ludwig, and Matthew P. A. Fisher [60], and has previously appeared in *Physical Review B*.
3. The content of Chapter 4 and Appendix D is the result of collaborations with Matthew P. A. Fisher [61], and has previously appeared in *Physical Review B*.
4. The content of Chapter 5 and Appendices E, F is the result of ongoing collaborations

with Yijian Zou, Paolo Glorioso, Ehud Altman, and Matthew P. A. Fisher [62].

Chapter 2

Hybrid circuit model and the measurement-induced phase transition

Quantum many-body systems under unitary dynamics will generally thermalize [3, 4, 5, 6, 7, 8, 9]. But is thermalization inevitable? Are there systems in which the thermalization of entanglement entropy is avoidable? One example is many-body localization [10, 11], in which entanglement growth is suppressed by strong quenched disorder. Repeated local measurements provide an alternative approach for taming the growth of entanglement. While unitary dynamics tends to increase entanglement, local measurements tend to disentangle. When measurements are made continually, the steady-state wavefunction should exhibit non-maximal, and non-thermal, entanglement entropy [63]. If measurements are made as frequently as possible, the wavefunction will become localized in the Hilbert space near a trivial product state – a quantum Zeno effect [64]. What happens in the intermediate regime when measurements are made at a small but finite rate? Can the volume law scaling of entanglement entropy survive in the presence of a non-zero rate of measurement? These questions are pertinent to our basic understanding of quantum information dynamics.

In Refs. [18, 16, 17], a prototypical (1+1)d circuit model with both unitary dynamics and projective measurements was introduced and explored. Local unitary gates acted on all neighboring qubits, while single (or two-) qubit measurement gates were sprinkled throughout the circuit, with each space-time point occupied with probability p , representing the strength of the measurements. In Ref. [18] it was argued that the volume law entangled phase is destroyed by arbitrary rare measurements, for all $p > 0$, while the authors in Refs. [16, 17] presented arguments and numerical evidence for a stable volume law entangled phase, separated from an area law entangled phase at a critical value of measurements, $p_c > 0$. Due to different approaches taken in these papers, a direct comparison was not immediate.

In this Chapter, we continue to investigate these hybrid circuit models with unitary-measurement dynamics. Our goal is to explore and characterize both the nature of the entanglement transition and the properties of the volume law entangled phase in the presence of weak measurements. A central focus is on generic circuits with randomness in both the unitary gates and in the locations of the measurement gates. The least constrained model we consider is a “random Haar circuit”, with 2-qubit unitaries taken from the Haar measure [65, 66] and single qubit measurements randomly scattered across the circuit [18, 16]. However, the high entanglement in the volume law phase poses formidable numerical challenges even in one dimension. We thus will largely study “random Clifford circuits” with the Haar unitaries replaced by random two-qubit Clifford unitaries, and the single qubit measurements restricted to the Pauli group [44, 67, 68]. Such Clifford circuits can be efficiently simulated on a classical computer, enabling us to perform extensive large scale numerical studies. We draw several conclusions from our data in the random Clifford circuit:

- At long times, measurements reduce the entanglement entropy from maximal, and the steady-state entanglement fluctuates weakly over time and over circuit realizations, independent of the initial conditions. These “typical” steady states are non-thermal, qualitatively distinct from thermal states.
- The volume law phase persists when measurements are infrequent, consistent with results

from Refs. [16, 17]. The algebraic structure of the Clifford dynamics provides a convenient framework for characterizing the entanglement structure of these wavefunctions, revealing an unusual scaling form of the entanglement entropy, namely $S_A = \alpha \ln |A| + s|A|$ for a contiguous subsystem A .¹ The sub-leading correction is exposed by analyzing the length distributions of the “stabilizers” – mutually commuting Pauli string (eigen)operators of the Clifford wavefunctions with unit eigenvalue. The stabilizer distribution is “bimodal”, consisting of a power law distribution of “short” stabilizers that contribute to the logarithm, and “long stabilizers” with length $\ell \approx L/2$ giving the volume law piece (L being the system size). This sublinear correction is conjectured to be a generic feature of volume law steady states in the presence of measurements.

- The “entanglement transition”, from volume law to area law states [16, 17], occurs when the weight under the “long stabilizer” peak at $\ell \approx L/2$ vanishes continuously upon approaching p_c from below. Remarkably, the power law tail of “short” stabilizers remains, implying a purely logarithmic form for the entanglement entropy right at the critical point, $p = p_c$. The entanglement transition exhibits conformal symmetry of the mutual information at criticality, and we extract several critical exponents. In particular, we find that in all the models we study, the mutual information between two small regions separated by a large distance, r , scales as $1/r^4$. Off criticality the mutual information decays exponentially.
- We explore the fluctuations of certain spin-spin correlation functions across the transition, and find that they are enhanced at the critical point, mimicking the mutual information.

We establish the generality of these results by exploring models with imposed spatial symmetry constraints – specifically Clifford circuits with the unitaries periodic in space and time (Floquet) and/or the measurement locations periodic in space and time. All models are found to exhibit a measurement-driven entanglement transition, with similar exponents and similar

¹ It was later realized, after the publication of Ref. [59], that the subleading correction should be $|A|^\beta$ with $\beta \approx 1/3$, after a careful comparison with directed polymer in random media [35]. This comment similarly applies to Fig. 2.3 and Eq. (2.19).

behavior of the stabilizer length distribution as in the random Clifford circuit. Apparently the randomness in the unitaries and measurement locations are inessential, with the remaining stochasticity in the measurement outcomes sufficient to account for the presence and universality of the entanglement transition.

Going beyond Clifford, we implement a full quantum simulation of more general circuit models for systems with size up to $L = 20$ qubits. Both random Haar circuits and (non-Clifford) Floquet circuits exhibit behavior consistent with their Clifford counterparts. We also explore models with (non-projective) “generalized measurements”, with each and every qubit being measured at each time step, and find evidence for an entanglement transition, with accessible exponents being consistent with the Clifford circuits. Of particular interest is a space-time translationally symmetric Floquet model with generalized measurements, which exhibits an entanglement transition where the only stochasticity is in the results of the quantum measurements.

Motivated by the remarkable consistency between all of our different models, we conjecture that generic hybrid circuits have a volume law phase with logarithmic correction for weak enough measurements, and exhibit an entanglement transition in a single universality class.

This Chapter is organized as follows. In Sec. 2.1 we define the circuit models of interest. Extensive numerical results for Clifford circuits are reported in Sec. 2.2 and 2.3. In particular, Sec. 2.2 contains evidence for the phase transition in entanglement entropy, and allows characterization of the volume-law phase in terms of stabilizers. Sec. 2.3 is devoted to a detailed analysis of the critical behavior of the entanglement transition. In Sec. 2.4, we systematically explore Clifford circuit models with space and time symmetries imposed, either in the unitaries or the measurement locations – or both. In Sec. 2.5, we consider more generic non-Clifford circuits, establishing complementary results via a full quantum simulation for smaller systems. We close with discussions in Section 2.6.

Finally, in Appendix A we review Clifford circuits and define the stabilizer length distribution, and detail measurement and unitary Clifford *dynamics* – beyond the steady state – in

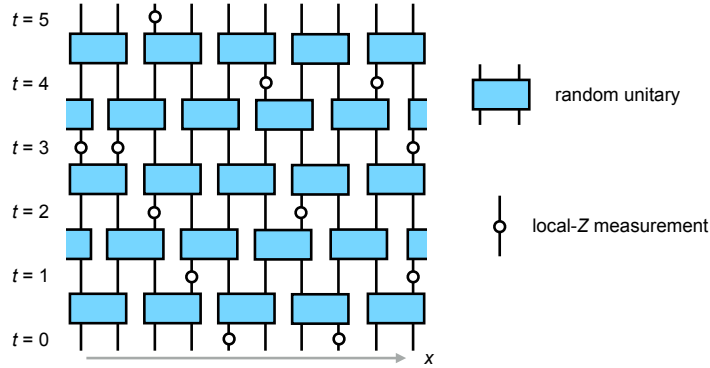


Figure 2.1: The random circuit model with random measurements. In this circuit, the unitaries are arranged in a brick-layer fashion, while the single qubit Z -measurements are positioned randomly in space and time. We depict the Poissonian arrangement in this figure, for which the measurements take place at each available space-time site independently with probability p . For a circuit with L qubits and with depth D , there are LD such available sites.

Appendix B.

2.1 The circuit model

Consider first the prototypical quantum circuit model, shown in Fig. 2.1, with L qubits arranged on a one-dimensional chain. The circuit dynamics is composed of two parts, as depicted in Fig. 2.1 and detailed below (in order), namely (i) the background unitary evolution, and (ii) measurements made on selected qubits scattered throughout the system.

- (i) The background unitary time evolution of the L -qubit wavefunction is determined by applications of local unitary gates which are arranged in a bricklayer pattern, such that the geometry of the circuit is periodic in both space and time. The local unitaries act on neighboring pairs of qubits. Each discrete time cycle of the circuit consists of two layers, and each layer has $L/2$ two-qubit unitary gates, acting on all the odd links in the first layer, and all the even links in the second. We primarily consider circuits with periodic spatial boundary conditions, except in Appendix B where circuits with open boundary condition are more convenient.

We define the depth of a circuit to be the number of unitary layers, and denote it by D .

Therefore, a circuit with depth D has $T = D/2$ time cycles. The circuit as a whole can be regarded as a unitary transformation in the Hilbert space of many-body wavefunctions on L qubits,

$$U_T = \prod_{t=0}^{T-1} U(t), \quad (2.1)$$

where $U(t)$ is the time evolution operator for the t -th time cycle,

$$U(t) = \left(\prod_{x \text{ odd}} U_{(x,x+1),2t+1} \right) \left(\prod_{x \text{ even}} U_{(x,x+1),2t} \right), \quad (2.2)$$

where $U_{(x,x+1),d}$ is the gate on link $(x, x + 1)$ at depth d . Under the action of a unitary gate, the wavefunction transforms as,

$$|\psi\rangle \rightarrow U_{(x,x+1),d} |\psi\rangle, \quad (2.3)$$

so that the wavefunction at arbitrary time T is $|\psi(T)\rangle = U_T |\psi(0)\rangle$.

- (ii) The full dynamics of the model is *non-unitary*, wherein the space-time sheet of the unitary circuit is punctuated with measurements – for simplicity chosen as single-qubit measurements. In a circuit with depth $D = 2T$, there are $L \times D$ available space-time locations between unitary layers available for such measurements. Measurements are made on a fraction p of all these sites, chosen either randomly or deterministically. The parameter p is thus the rate of measurement. In Sections 2.1–2.3 of this Chapter we will choose these sites randomly (Poisson distribution) as depicted in Fig. 2.1, a model first proposed in Refs. [18, 16]. The unitary background is obtained by setting $p = 0$.

Under the action of a measurement the wavefunction transforms as,

$$|\psi\rangle \rightarrow \frac{M_\alpha |\psi\rangle}{\|M_\alpha |\psi\rangle\|}, \quad (2.4)$$

where $\{M_\alpha\}$ are a set of linear “generalized measurement” operators satisfying $\sum_\alpha M_\alpha^\dagger M_\alpha = 1$ [69]. Under such a measurement, the process described by Eq. (2.4) is probabilistic, with outcome α happening with probability $p_\alpha = \langle \psi | M_\alpha^\dagger M_\alpha | \psi \rangle$. Throughout much of the Chapter, and unless specified to the contrary, we will choose these “generalized measurement” operators to be mutually orthogonal projectors, that is $M_\alpha \rightarrow P_\alpha$, with $P_\pm = (1 \pm Z)/2$ measuring the Z -component of the spin of individual qubits. Such projectors satisfy $P_\alpha P_\beta = \delta_{\alpha\beta} P_\alpha$ and $\sum_\alpha P_\alpha = 1$.

For a convenient initial wavefunction (unentangled, for example), once the realizations of each unitary and measurement gate are specified as well as the measurement outcomes, the many body wavefunction at any time step is determined, by following the transformations defined in Eqs. (2.3, 2.4). This pure state time evolution is known as a *quantum trajectory* [70]. As emphasized in Refs. [16, 17] the entanglement physics of interest to us will not be contained in the time evolution of the mixed state density matrix (appropriate when/if the measurement results are summed over, rather than tallied), which appears in more familiar treatments of open quantum systems [71].

While unitary gates generically increase entanglement, local measurements tend to reduce the entanglement entropy on average. This competition is subtle since the effect of the unitary gates on the entanglement is strictly local and incremental [72], while the measurement operators are expected to have some non-local effects on entanglement. Moreover, this competition could lead to interesting entanglement dynamics at early times. For example, in Ref. [16] the entanglement dynamics can be mapped to the first passage percolation [73, 74, 75, 76] in certain limits, while in Ref. [17], sublinear power-law growth of entanglement was observed at a critical measurement rate, in contrast to the linear growth in purely unitary circuits. Non-monotonic growth of entanglement can also occur in this type of circuit [18, 77]. However, in this Chapter we will primarily focus on the entanglement entropy of the late-time steady state, rather than its early-time dynamics. We leave a detailed study of the latter to the future.

The primary quantity we use to characterize the steady state wavefunctions is the Rényi

entropy, defined as,

$$S_A^n = \frac{1}{1-n} \log_2 \text{Tr}(\rho_A)^n, \quad \rho_A = \text{Tr}_{\bar{A}} |\psi\rangle \langle \psi|, \quad (2.5)$$

where (A, \bar{A}) is a bipartition of the L -qubit system with A being a contiguous subregion, and $|\psi\rangle$ is the pure state wavefunction we obtain by following the quantum trajectory. A closely related quantity is the mutual information between two subregions,

$$I_{A,B}^n = S_A^n + S_B^n - S_{A \cup B}^n. \quad (2.6)$$

The mutual information is guaranteed to be non-negative when $n \leq 1$.

For a large part of the Chapter, we will consider Clifford circuits. In this case, all Rényi entropies are equal to each other due to the flat entanglement spectrum [78, 79], and we will drop the Rényi index (the superscript n).

The generic circuit has three types of randomness: (i) a random ensemble of unitary gates, (ii) the random locations of the measurements, and (iii) the intrinsic random outcome of each quantum measurement. We will mostly consider the mean values of the entanglement entropies, averaged over the various forms of randomness present in the circuit. As we shall see in Sec. 2.2, the distributions of the entanglement entropies in the steady state are narrow, so well represented by their averages.

2.2 The phase diagram

In this section we discuss the phase diagram of a generic circuit with random Clifford unitaries and random measurement placements. Specifically, we consider circuits of the structure exactly as in Fig. 2.1, wherein the unitary gates are sampled from the uniform distribution on the two-qubit Clifford group (see Appendix A), and the measurements are taken to be single-qubit Pauli- Z measurements, namely $P_{\pm} = (1 \pm Z)/2$, at random positions chosen independently with probability p (the Poissonian fashion). We shall refer to this specific model as

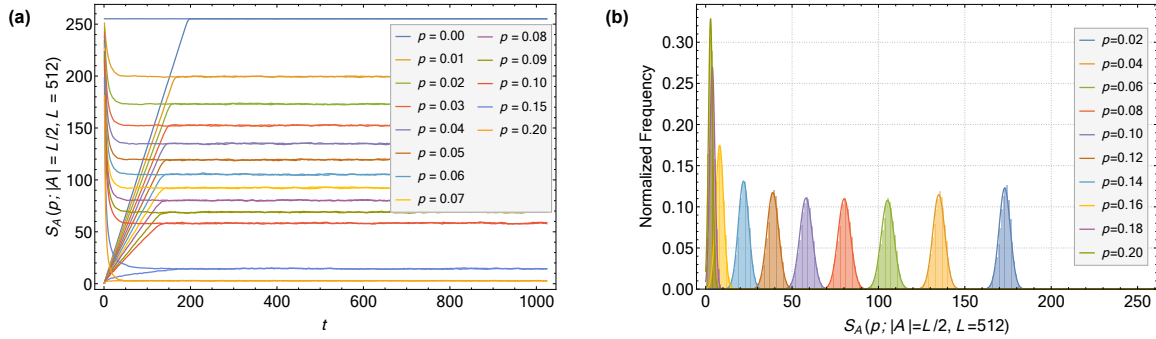


Figure 2.2: (a) Time dependence of the entanglement entropy S_A with $|A| = L/2$ and $L = 512$, in the random Clifford circuit averaged over circuit realizations, starting from either a maximally entangled state or a trivial product state. (b) Distribution function of S_A for different circuit realizations and over time well after saturation. The solid lines are fits to a normal distribution.

the “random Clifford circuit”, in short.

The primary motivation for studying the random Clifford circuits, rather than the more generic circuits with non-Clifford gates (e.g. random Haar unitaries), is numerical tractability. On the single gate level, the random Clifford unitaries approximate the random Haar unitaries quite well, being known as a unitary 2-design [80]. Our expectation for the equivalence in terms of the entanglement physics is partially justified in Sec. 2.5, where comparisons are made between the two circuits for small system sizes – and consistency is found.

The simulability of Clifford circuits is a result known as the Gottesman-Knill theorem [44, 67, 69, 68]. As reviewed in Appendix A, the methodology involves following the dynamics of “stabilizers” – mutually commuting and independent Pauli string operators – that uniquely specify the wavefunction, and readily allow for calculation of the entanglement entropy [81, 82, 83, 72]. Clifford circuits have proven useful in the study of entanglement and operator dynamics in various contexts [72, 28, 84].

2.2.1 The steady state

Given a circuit of a finite length L of qubits, we are primarily interested in the late time behavior when $T \rightarrow \infty$. In this infinite time (circuit depth) limit we expect the system to evolve into a steady state, characterized by a typical value of entanglement entropy that depends on

the measurement rate p , but not the dynamics at finite times. To check that this limit is well-defined, we compute the time dependence of the entanglement entropies starting from two types of initial states, namely,

- The trivial product state, $\prod_x |0\rangle_x$, which is a stabilizer state, i.e. the simultaneous eigenvector with eigenvalue 1 of its stabilizers $\mathcal{G} = \{Z_1, Z_2, \dots, Z_L\}$.
- The maximally entangled state, obtained by evolving the random Clifford circuit without measurements well after saturation.

The results, averaged over circuit realizations, are plotted in Fig. 2.2(a). For all values of p and for both choices of the initial state, the entanglement entropy saturates to a value that is determined solely by p . We believe that this holds for an *arbitrary* choice of the initial state. Therefore, we can talk about the “steady state” for a given rate of measurement without referring to the initial state. The steady state is thus a *bulk property* of the circuit.

After saturation there are only minimal fluctuation in the entropies over time. Moreover, the fluctuations are also small over different circuit realizations. In Fig. 2.2(b), we plot the distribution of the entanglement entropy taken from an ensemble of circuits, and over many time steps well after saturation. Notice that the functions are sharply peaked for each p , and fit well to the Gaussian distribution.²

We define $S_A(p; |A|, L)$ to be the late-time entanglement entropy of a subsystem with size $|A|$, when averaged over different circuit realizations, for a circuit with length L and measurement rate p . Given the (average) spatial translational symmetry this quantity only depends on the size (but not the location) of the subregion A . In the following we will usually refer to this quantity as *the entanglement entropy*, unless otherwise specified.

²Similarly to footnote 1, this statement is updated in Ref. [35]. The distribution is not Gaussian, but rather the (scaled) GSE Tracy-Widom distribution with a width growing as $L^{1/3}$. The two distributions have apparently similar density functions, and subtle but important differences in their tails.

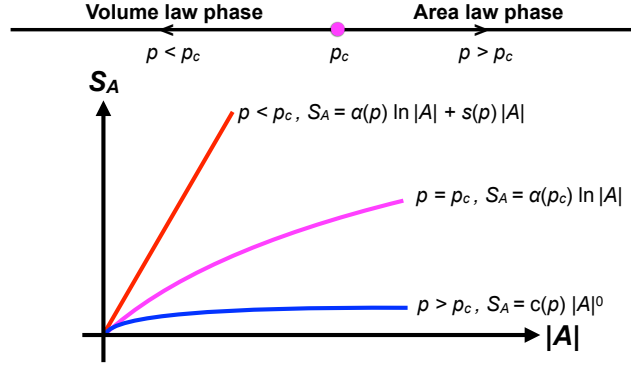


Figure 2.3: The phase diagram and scaling behavior of the entanglement entropy in both phases and at criticality. Note that the asymptotic scaling of S_A in the volume law phase, as presented in this figure, is incorrect. We refer the reader to footnote 1 for a discussion of this issue.

2.2.2 The two phases

Attempts have been made to map out the phase diagram [18, 16, 17]. The limiting cases are easy to understand. When $p \rightarrow 1$, the steady state is close to a trivial product state, and has area law entanglement entropy. The other limit, $p \rightarrow 0$, corresponds to the random unitary circuit, where the steady state is characterized by maximal volume law entanglement entropy [72]. The putative phase diagram is shown schematically in Fig. 2.3, which shows a volume law phase and an area law phase separated by some critical rate of measurement, p_c . Whether p_c is 0 or finite was not agreed upon in earlier work.

Here our numerics for the random Clifford circuit supports a finite p_c , consistent with [16, 17]. In Fig. 2.4(a), we plot the entanglement entropy $S_A(p; |A| = aL, L)$ for different values of p as functions of L , with a fixed $a = 1/2$. We find qualitatively distinct behavior of S_A below and above $p_c \approx 0.16$. For $p < p_c$, the curves asymptote to straight lines of slope 1 on a log-log scale, suggesting volume law scaling of the entanglement entropy, $S_A(p; |A| = aL, L) = s(p)L$. For $p > p_c$, the curves are saturating to zero slope, suggesting an area law scaling, $S_A(p; |A| = aL, L) = c(p)L^0$.

In Fig. 2.4(b), we plot $S_A(p; |A|, L)$ as a function of $|A|$ while fixing $L = 512$. Similar scaling behavior is observed.

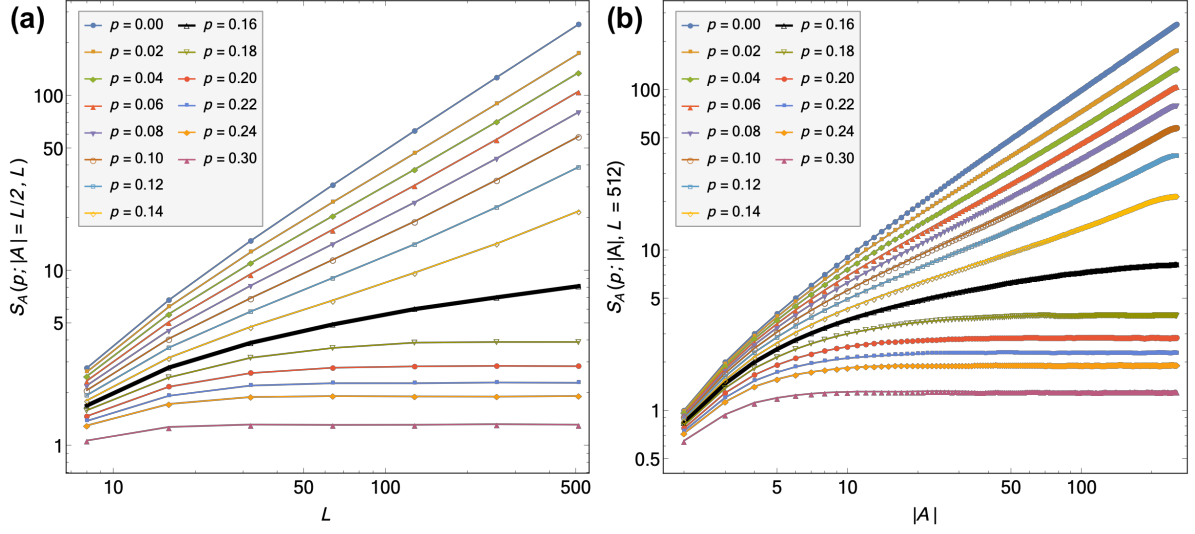


Figure 2.4: (a) Entanglement entropy $S_A(p; |A|, L)$ with fixed $|A|/L = 1/2$, as functions of L , for different values of p . (b) $S_A(p; |A|, L)$ with fixed $L = 512$, as functions of $|A|$, for different values of p . Both plots are on a log-log scale. Notice that curves in (a) and (b) corresponding to the same value of $p < p_c$ has the same slope, $s(p)$ (see main text).

2.2.3 Entanglement entropy from stabilizer distribution

For Clifford circuits further information about the nature of the two phases can be revealed by examining the stabilizer distributions, as we now discuss. We start by listing several results regarding the stabilizer formalism [44, 67, 69, 68, 72]. These results are also reviewed in Appendix A.

1. A wavefunction $|\psi\rangle$ in the Clifford circuit of L qubits is uniquely characterized by L mutually commuting and independent Pauli string operators $\mathcal{G} = \{g_1, \dots, g_L\}$ such that each one “stabilizes” the wavefunction, $g_i |\psi\rangle = |\psi\rangle$.

Elements of \mathcal{G} are called *stabilizers*. Such a wavefunction is called a *stabilizer state* or *codeword*. Only stabilizer states appear in the Clifford circuit.

Being Pauli string operators, the stabilizers have endpoints where they terminate. Specif-

ically, we define the *left* and *right endpoints* of a stabilizer to be

$$\mathbf{l}(g) = \min\{x : g \text{ acts non-trivially on site } x\}, \quad (2.7)$$

$$\mathbf{r}(g) = \max\{x : g \text{ acts non-trivially on site } x\}, \quad (2.8)$$

where x is the coordinate of the site, which takes values in $\{1, 2, \dots, L\}$. For systems with periodic spatial boundary conditions, there is an arbitrariness in choosing the origin of the coordinate system, and there is no absolute distinction between left and right. However, we note that the functions $\mathbf{l}(g)$ and $\mathbf{r}(g)$ are well-defined once the origin is chosen and fixed, which we will always assume to be the case in the rest of the Chapter.

2. The choice of \mathcal{G} is not unique. For any stabilizer state, one can choose \mathcal{G} such that there are exactly two stabilizer endpoints on each site,

$$\rho_{\mathbf{l}}(x) + \rho_{\mathbf{r}}(x) = 2, \text{ for all sites } x. \quad (2.9)$$

We say \mathcal{G} is in the *clipped gauge* [72].

Notice that \mathcal{G} is *not* uniquely fixed by this gauge condition.

3. Within the clipped gauge, the entanglement entropy of a *contiguous* subregion A is given by half the number of stabilizers that cross either its left or right boundary,

$$S_A = \frac{1}{2} \#\{g \in \mathcal{G} : (\mathbf{l}(g) \in A \text{ and } \mathbf{r}(g) \in \overline{A}) \text{ or } (\mathbf{l}(g) \in \overline{A} \text{ and } \mathbf{r}(g) \in A)\}. \quad (2.10)$$

With periodic spatial boundary conditions, the subregion A can be either sites $\{x, x + 1, \dots, x + |A| - 1\}$ when $x + |A| \leq L + 1$, or $x, x + 1, \dots, L, 1, 2, \dots, x + |A| - (L + 1)$ when $x + |A| > L + 1$. In the clipped gauge, the entanglement entropy is given solely by the end positions of the stabilizers, and does not depend on their “internal” contents.

Consider the bigrams of stabilizer endpoints which encode the “span” of each stabilizer,

$$\mathcal{B}(\mathcal{G}) \equiv \{(1(g_1), \mathbf{r}(g_1)), \dots, (1(g_L), \mathbf{r}(g_L))\}. \quad (2.11)$$

As shown in Appendix A, for a given wavefunction this object is unique, provided $\mathcal{G} = \{g_1, \dots, g_L\}$ is in the clipped gauge. Generally there may be many different choices of \mathcal{G} that satisfy the (clipped) gauge condition, which all share the same bigram. Nevertheless, the bigram fully characterizes the entanglement entropy of the wavefunction(s) through the relation in Eq. (2.10), being insensitive to the gauge redundancy.

It is convenient to define the normalized stabilizer (spatial) distribution function,

$$D_{\mathcal{G}}(x, y) = \frac{1}{L} \overline{\sum_{i=1}^L \delta_{1(g_i), x} \delta_{\mathbf{r}(g_i), y}}, \quad (2.12)$$

where the overline represents an ensemble average of the bigrams taken over different circuits and times. We can also define the normalized stabilizer length distribution function,

$$\mathfrak{D}_{\mathcal{G}}(\ell) = \frac{1}{L} \overline{\sum_{i=1}^L \delta_{1\text{en}(g_i), \ell}}, \quad (2.13)$$

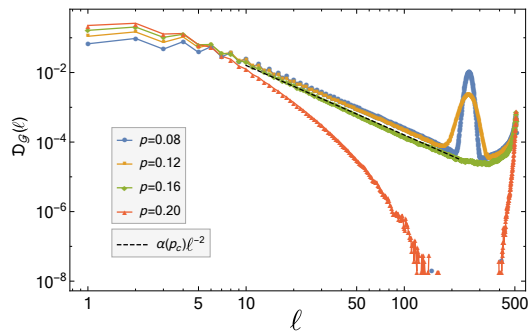


Figure 2.5: The normalized stabilizer length distribution $\mathfrak{D}_{\mathcal{G}}(\ell)$ plotted on a log-log scale for a system with size $L = 512$. Here we take $\alpha(p_c) = 1.6$.

where $\text{len}(g_i) = \mathbf{r}(g_i) - \mathbf{l}(g_i)$. The latter is the integral of the former,

$$\mathfrak{D}_{\mathcal{G}}(\ell) = \sum_{x,y} \delta_{\ell, y-x} D_{\mathcal{G}}(x, y). \quad (2.14)$$

For circuits with periodic spatial boundary conditions, our numerics reveal (data not shown) that the spatial distribution of the stabilizers for a particular length ℓ is uniform, true at each value of ℓ and p . That is,

$$D_{\mathcal{G}}(x, y) = D_{\mathcal{G}}(x', y') \text{ if } y - x = y' - x'. \quad (2.15)$$

Thus, taking into account the geometric constraint that a stabilizer with length ℓ can only have its left endpoint in the range $(0, L - \ell)$, we have

$$D_{\mathcal{G}}(x, y) = \frac{\mathfrak{D}_{\mathcal{G}}(y - x)}{L - (y - x)} \approx \frac{\mathfrak{D}_{\mathcal{G}}(y - x)}{L}, \quad (2.16)$$

where the last approximation applies when $y - x \lesssim L/2$. These two distribution functions depend on each other through a simple relation, and one can be inferred from the other.

In Fig. 2.5, we plot the distribution function $\mathfrak{D}_{\mathcal{G}}(\ell) \approx D_{\mathcal{G}}(x, y) \times L$, where $\ell = y - x$, at different values of p , for fixed $L = 512$. The distribution function is quite remarkable.

- In the volume law phase $p < p_c$, the distribution is “bimodal”, namely a tail of “short stabilizers”, which is checked to be independent of L (data not shown), and a peak of “long stabilizers” at $\ell \approx L/2$ ³. On a log-log plot, the short stabilizer distribution for $p < p_c$ looks like a straight line with slope -2 , corresponding to a power-law distribution $\mathfrak{D}_{\mathcal{G}}(\ell) \sim \ell^{-2}$. The peak at $\ell \approx L/2$ has nonzero weight in the volume law phase, and the weight vanishes continuously as one approaches the critical point from $p < p_c$.

- In the area law phase, $p > p_c$, the power-law distribution of “shorter” stabilizers becomes

³We also notice a small hump at $\ell \approx L$. This part of the distribution is a boundary effect due to the periodic boundary condition, and the height of the hump decays as $1/L$ as we go to the thermodynamic limit. Moreover, from Eq. (2.10), these long stabilizers of length $\sim L$ barely contribute to the entanglement entropy. Thus we ignore this unimportant hump.

truly short-ranged.

The results in Fig. 2.5 can be schematically summarized as,

$$\mathfrak{D}_{\mathcal{G}}(\ell) \sim \begin{cases} \alpha(p) \frac{1}{\ell^2} + s(p) \delta(\ell - L/2), & p < p_c \\ \alpha(p) \frac{1}{\ell^2}, & p = p_c \\ \alpha(p) \frac{e^{-\ell/\xi}}{\ell^2}, & p > p_c \end{cases} \quad (2.17)$$

where $\alpha(p)$ is the weight of the power law, which has weak dependence on p or L , $s(p)$ is the weight of the peak, and ξ is some finite length scale that cuts off the length of the stabilizers in the area law phase.

From the formula for entanglement entropy Eq. (2.10), we see that for a region A with $1 \ll |A| \ll L$,

$$\begin{aligned} S_A &= \frac{1}{2} \int_{x \in A} \int_{y \in \bar{A}} [\theta(y-x) D_{\mathcal{G}}(x, y) \times L + (x \leftrightarrow y)] \\ &= \frac{1}{2} \int_{x \in A} \int_{y \in \bar{A}} [\theta(y-x) \mathfrak{D}_{\mathcal{G}}(y-x) + (x \leftrightarrow y)]. \end{aligned} \quad (2.18)$$

Combined with Eq. (2.16) and (2.17), we have

$$S_A \sim \begin{cases} \alpha(p) \ln |A| + s(p) |A|, & p < p_c \\ \alpha(p) \ln |A|, & p = p_c \\ \alpha(p) \ln \xi. & p > p_c \end{cases} \quad (2.19)$$

This scaling behavior is consistent with our findings in Fig. 2.4. When $p < p_c$, the two parts of the distribution contribute to the two terms separately: the volume law entanglement comes from the peak at $\ell \approx L/2$, while the logarithmic correction comes from the power law distribution of the “shorter” stabilizers, which gets exposed at the critical point.⁴

⁴The comment in footnote 1, that sublinear correction should be $|A|^\beta$ rather than $\ln |A|$, similarly applies here. Fitting the stabilizer length distribution to a powerlaw can be tricky, for the clipping algorithm requires cutting the periodic b.c. system somewhere, thereby explicitly breaking the translational symmetry. The stabilizers

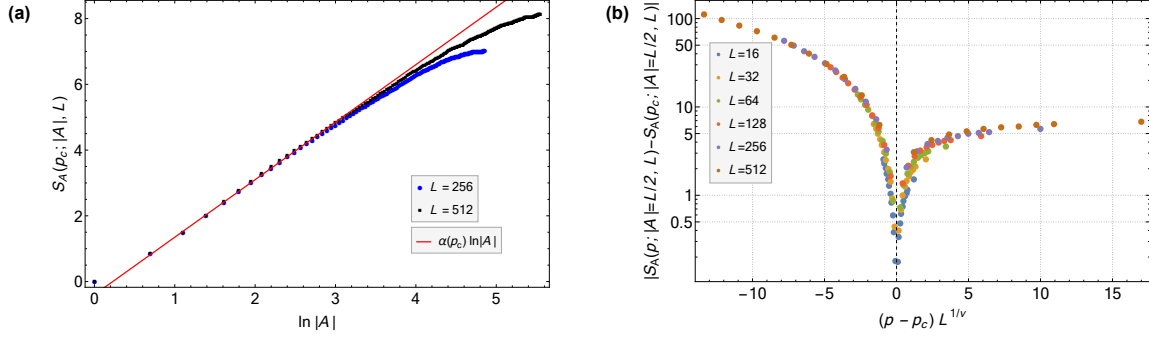


Figure 2.6: (a) Entanglement entropy at the critical point fits well to a purely logarithmic function, $S_A(p_c; |A|, L) \approx \alpha(p_c) \ln |A|$, where $\alpha(p_c) = 1.6$, plotted for $|A| < L/4$. (b) Collapsing the $S_A(p; |A| = L/2, L)$ data to the scaling form in Eq. (2.22), where we find $p_c = 0.16$ and $\nu = 1.3$.

From the stabilizer length distribution, the existence of a phase transition is rather obvious. The transition is accompanied by the vanishing of $s(p)$ as we approach p_c from below, and by the divergence of ξ as we approach p_c from above.

2.3 Critical behavior

2.3.1 Finite size scaling of entanglement entropy

As seen from Eq. (2.19), the inverse-square power law form of the stabilizer length distribution at $p = p_c$ implies that the entanglement entropy right at the critical point should vary logarithmically with sub-system size. In Fig. 2.6(a) we plot $S_A(p; |A|, L)$ with fixed values of L at p_c , and see that it indeed has the desired scaling form. The coefficient of the logarithmic function matches well to that of the inverse square power law, $\alpha(p_c)$, as expected.

To further probe the entanglement transition, we consider a finite size scaling form for $S_A(p; |A| = aL, L)$,

$$S_A(p; |A| = aL, L) = \alpha(p_c) \ln L + F\left((p - p_c)L^{1/\nu}\right). \quad (2.20)$$

are then subject to the geometrical constraint that they cannot span the cut. [In particular, a longer stabilizer will have fewer places to be, therefore a larger “effective” density. Roughly this effect contributes to a larger subleading term.] This issue should disappear in the thermodynamic limit, but the system sizes accessed here do not seem enough. We refer the reader to Ref. [35] for numerical results that reveals the powerlaw correction.

In order to match on to Eq. (2.19) in the thermodynamic limit, the function F must be proportional to L when $p < p_c$, and cancel the $\ln L$ term when $p > p_c$. Therefore $F(x)$ has the following asymptotics,

$$F(x) \approx \begin{cases} |x|^\nu, & x \rightarrow -\infty \\ \text{const}, & x = 0 \\ -\alpha(p_c)\nu \ln |x|, & x \rightarrow +\infty \end{cases} \quad (2.21)$$

Therefore, from Eq. (2.19) we identify $s(p)$ with $(p_c - p)^\nu$ for $p < p_c$, and ξ with $|p - p_c|^{-\nu}$ having the meaning of the correlation length.

This scaling form appeared in Refs. [16, 85]. In Ref. [85] this formula follows if/when the entanglement entropy can be mapped to the change of the free energy caused by the insertion of two boundary condition changing operators in a 2d classical spin model. These two operators are inserted at the boundaries of the subsystem A and the free energy cost for them can be represented as the logarithm of the two point correlation function. Deep within the two phases, the volume law and area law scalings of the entropy are consistent with the free energy of a domain wall connecting the two boundaries of A in the ordered and disordered phases of the classical spin model, with finite and zero surface tensions, respectively. The logarithmic correction in the volume phase would be accounted for by the contributions to the free energy due to capillary wave fluctuations of the interface in the ordered phase of the spin model [86, 87]. Right at the critical point the two point correlation function of the boundary condition changing operator decays as a power law. Thus, upon taking logarithms, the coefficient $\alpha(p_c)$ in the entanglement entropy has the meaning of twice the scaling dimension of the boundary condition changing operator.

In order to put Eq. (2.20) into a conventional finite size scaling form, we will subtract out the critical entropy to cancel out the $\ln L$ term, and fit our entanglement entropy data to the

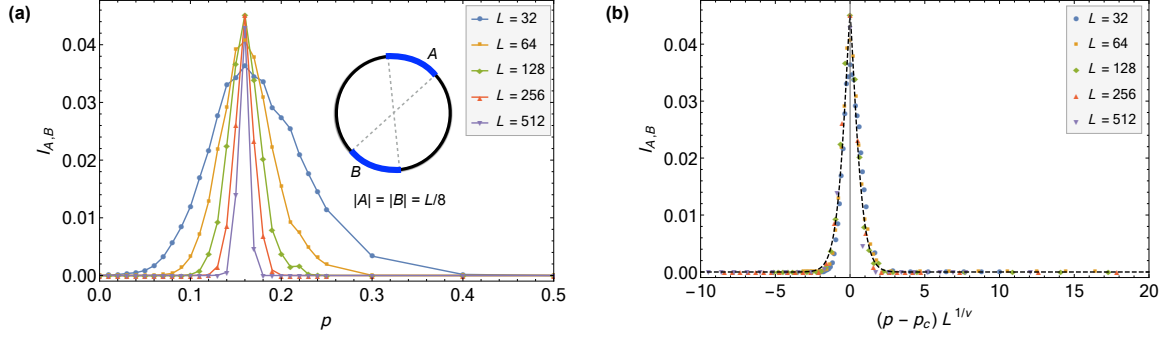


Figure 2.7: (a) The mutual information, $I_{A,B}$, with region sizes $|A| = |B| = L/8$ and separation $r_{A,B} = L/2$, as shown in the inset. (b) Data collapse of the curves in (a), where we have taken $\nu = 1.3$. Dashed lines show the function $f(x) = e^{-c|x|^\nu}$ where $c \approx 1.7$.

scaling form,

$$|S_A(p; |A| = aL, L) - S_A(p_c; |A| = aL, L)| = \tilde{F} \left((p - p_c)L^{1/\nu} \right). \quad (2.22)$$

In Fig. 2.6(b) we plot the left hand side of Eq. (2.22) (with $a = 1/2$) versus $(p - p_c)L^{1/\nu}$ for values of p both below and above p_c , choosing the exponent $\nu = 1.3$ to give the best scaling collapse. The quality of the data collapse supports the existence of a diverging correlation length $\xi \sim |p - p_c|^{-\nu}$ and the validity of the scaling hypothesis near criticality.

Notice that in Ref. [17] a different scaling form was used for data collapse, and a different ν was found.

2.3.2 Mutual information and correlations near criticality

The bipartite mutual information $I_{A,B}$ is one convenient measure of correlations between two disjoint regions A and B . Loosely speaking, it is the entanglement shared only between A and B , but not with any third party. We will first focus on the mutual information when the two regions A and B , of size $|A| = |B| = L/8$, are antipodal in the system with periodic boundary conditions, their centers separated by $r_{A,B} = L/2$. In both phases, away from criticality, we expect the mutual information to fall off exponentially with the system size, varying as $I_{A,B} \sim \exp(-L/\xi)$, much like the behavior of correlation functions in conventional

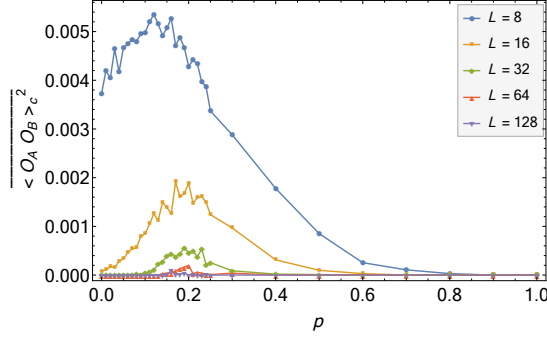


Figure 2.8: The squared correlation function for two regions A and B , as shown in Fig. 2.7.

finite temperature transitions away from the critical point. Right at criticality we expect $I_{A,B}$ to be enhanced due to the longer range correlation [16].

In Fig. 2.7(a), we plot the mutual information $I_{A,B}(p; |A| = |B| = L/8, r_{A,B} = L/2, L)$ as a function of p for different system sizes. The mutual information has a peak at $p = p_c$, which gets sharper with increasing system sizes, as we expect. Moreover, the height of the peak saturates to a constant that is independent of L , which is consistent with the conformal symmetry discussed in the next subsection.

In Fig. 2.7(b), we attempt a data collapse with the following finite size scaling form,

$$I_{A,B}(p; |A| = |B| = L/8, r_{A,B} = L/2, L) = f\left((p - p_c)L^{1/\nu}\right), \quad (2.23)$$

where $f(x) \propto e^{-c|x|^\nu}$, and c is a non-universal constant. The collapse is with high quality, and the data fits well to the predicted functional form of $f(x)$.

The von Neumann mutual information serves as an upper bound on the fluctuation of connected correlation functions between two disjoint regions A, B [88],

$$I_{A,B} \geq \frac{1}{2} \frac{|\langle \mathcal{O}_A \mathcal{O}_B \rangle_c|^2}{\|\mathcal{O}_A\|^2 \|\mathcal{O}_B\|^2}, \quad (2.24)$$

where $\langle \dots \rangle_c$ denotes the connected correlation function, \mathcal{O}_A and \mathcal{O}_B are operators on A and B , respectively, and $\|\dots\|$ is the operator norm. For the purpose of illustration, we take A and B

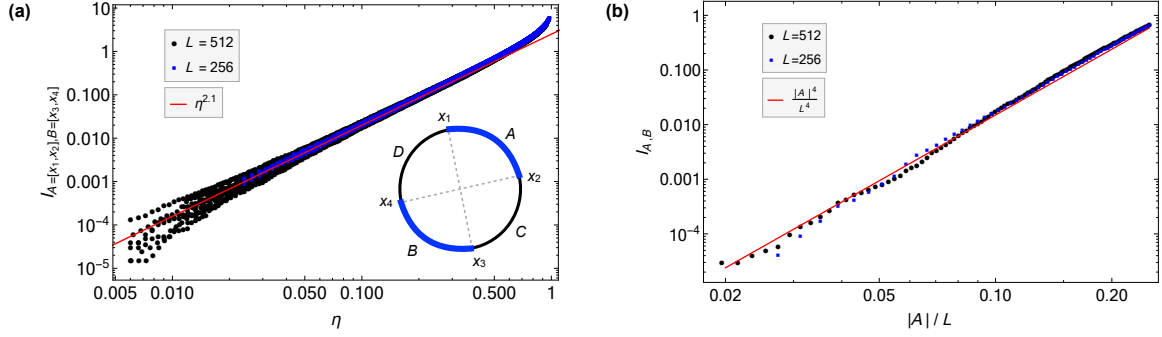


Figure 2.9: (a) Data collapse for the mutual information, $I_{A,B}$, at p_c as a function of the cross ratio η , on a log-log scale. The red line corresponds to $\eta^{2.1}$. (b) Fitting $I_{A,B}$ at p_c to Eq. (2.29), where we vary $|A| = |B|$ but keep $r_{A,B} = L/2$ fixed. The red line shows the function $(|A|/L)^4$.

to be the same antipodal subregions as above with $|A| = |B| = L/8$, and the operators to be

$$\mathcal{O}_A = \sum_{x \in A} Z_x, \quad \mathcal{O}_B = \sum_{x \in B} Z_x. \quad (2.25)$$

In Fig. 2.8 we plot the averaged value of $|\langle \mathcal{O}_A \mathcal{O}_B \rangle_c|^2$ as a function of p . Notably, the curves all show a peak at p_c , which gets sharper as L is increased.

We emphasize that the average squared correlation function is only obtained by examining the quantum trajectories one by one, and cannot be written as the expectation value of any operator,

$$\overline{\langle \mathcal{O}_A \mathcal{O}_B \rangle_c^2} \neq \text{Tr}(\rho \mathcal{O}_{A \cup B}). \quad (2.26)$$

Indeed, since ρ is the infinite temperature density matrix for arbitrary $p > 0$, it does not contain any information about the entanglement phase transition [16, 17].

2.3.3 Emergent conformal symmetry at criticality

In 1d equilibrium quantum critical systems, the entanglement entropy and mutual information of the ground state show universal scaling behaviors, as predicted by conformal field theories (CFT) [89]. The logarithmic scaling of the entanglement entropy and the diverging

correlation length suggest that our non-unitary entanglement transition might likewise be described by some appropriate conformal field theory [85, 16].

To check for such possible underlying conformal symmetry, we compute the mutual information between two disjoint intervals, whose size and locations can be varied. Let $A = [x_1, x_2]$, $B = [x_3, x_4]$, $C = [x_2, x_3]$, $D = [x_4, x_1]$ be a partition of the system. In a conventional conformal field theory the mutual information between A and B is related to a 4-point correlation function of boundary condition changing operators, $I_{A,B} = F(\langle\langle\phi(x_1)\phi(x_2)\phi(x_3)\phi(x_4)\rangle\rangle)$. As a direct consequence of the conformal symmetry, it is a function only of the cross ratio [90], i.e.,

$$I_{A,B} = f(\eta), \text{ where } \eta \equiv \frac{x_{12}x_{34}}{x_{13}x_{24}}, \quad (2.27)$$

where x_{ij} is taken as the chord distance, $x_{ij} = \frac{L}{\pi} \sin\left(\frac{\pi}{L}|x_i - x_j|\right)$ because of the periodic boundary condition.

We numerically compute the mutual information for a sequence of choices for the partition such that the cross ratio takes value across several orders of magnitude. In Fig. 2.9(a), we plot the mutual information versus the cross ratio at the critical point. We find that the data points lie on a single curve, confirming the prediction of CFT. In the limit $\eta \ll 1$, we find $I_{A,B} \propto \eta^\Delta$, where $\Delta \approx 2$.

One interesting regime is when A and B are distant sites, $|A| = |B| = 1 \ll r_{A,B} \ll L$. Here $\eta \propto r_{A,B}^{-2}$, so that,

$$I_{A,B} \propto r_{A,B}^{-2\Delta}. \quad (2.28)$$

Since the left and right boundaries of A (or B) are close, one can apply the operator product expansion (OPE) to simplify the 4-point correlation function, and the mutual information can now be viewed as the sum of 2-point correlation functions between operators that appear in the OPE. The dominant term comes from the operator with lowest scaling dimension, which can now be identified with Δ in the putative underlying CFT.

We can also consider another regime where $\eta \ll 1$. Let $|A| = |B| = aL$, with $a \ll 1$ and $r_{A,B} = L/2$, so that $\eta \propto a^2$. We thus have,

$$I_{A,B} \propto \eta^\Delta \propto a^{2\Delta} = \left(\frac{|A|}{L}\right)^{2\Delta}, \quad (2.29)$$

as verified in Fig. 2.9(b) with $\Delta = 2$, and confirming the result in Fig. 2.7 where the height of the peak saturates to a constant with increasing L . This setup will prove useful in extracting Δ in other models.

To summarize, the numerical results strongly support an emergent conformal symmetry at the critical point, and open up the possibility of an underlying CFT description.

2.4 Circuits with Symmetry

In previous sections we have been focusing on stochastic circuit models which have three types of randomness present: (i) spatial and temporal randomness in the unitary gates, (ii) spatial and temporal randomness in the positions of the measurements, and (iii) stochasticity in the measurement outcomes. Due to (i) and (ii) these models are quite generic, with no imposed symmetries or constraints (excepting the Clifford constraints). In this section we consider simple Clifford circuit models which have additional constraints imposed, involving space or time translational symmetry. In all examples considered we find the existence of a phase transition sharing similar critical exponents with the random Clifford circuit. Remarkably, this is true even for our most constrained model which has both space and time translational symmetry in the unitary gates and the measurement locations (spatially uniform Floquet) – the only remaining stochasticity being the measurement outcomes. This indicates the ubiquitous and universal character of the entanglement transition in hybrid unitary-measurement systems.

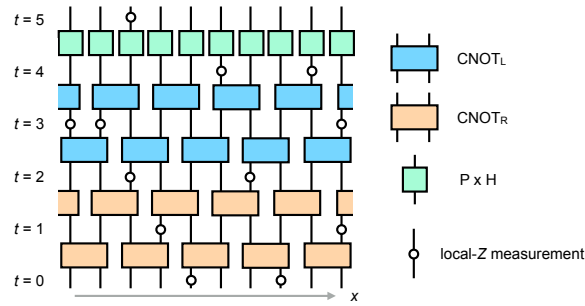


Figure 2.10: The Floquet Clifford circuit model within one time period. Measurements are made at random locations between each adjacent unitary layer. The $\text{CNOT}_{L/R}$ gate is the controlled-NOT gate with the left/right qubit as the control, and P and H are the phase gate and the Hadamard gate, respectively (see Appendix A).

2.4.1 Floquet circuits with randomly located measurements

Unitary circuit models without measurements are naturally adapted for mimicking systems with periodic drive [8, 91, 92, 93, 94]. In such circuits, the unitary gates are periodic in time, but could be either random or regular in space. As for unitary Hamiltonian dynamics, there is a notion of chaos in such Floquet circuits, as diagnosed by the entanglement growth [95, 96], the operator growth (and butterfly effect in out-of-time-order correlator) [97], the level spacing statistics and the spectral form factor [98, 91, 94, 92], etc; familiar examples include the kicked Ising model, which will be discussed in the next section. The temporal randomness is not essential for the development of chaos.

Here we first examine the measurement-driven entanglement transition in Floquet Clifford circuits where the unitary background has both spatial and temporal translation symmetries, but the measurements are still made at random positions, as shown in Fig. 2.10. We choose the Floquet Clifford unitaries to be “chaotic”, having a recurrence time that is exponential in the system size and maximal entanglement at shorter times. For the Clifford gates shown in Fig. 2.10 we check that this holds by examining small system sizes (data not shown).

For the circuit in Fig. 2.10 the results for our numerical simulation are shown in Fig. 2.11. The stabilizer length distribution shown in Fig. 2.11(a) has a behavior very similar to that of the random Clifford circuit, clearly indicating the existence of both a phase transition and

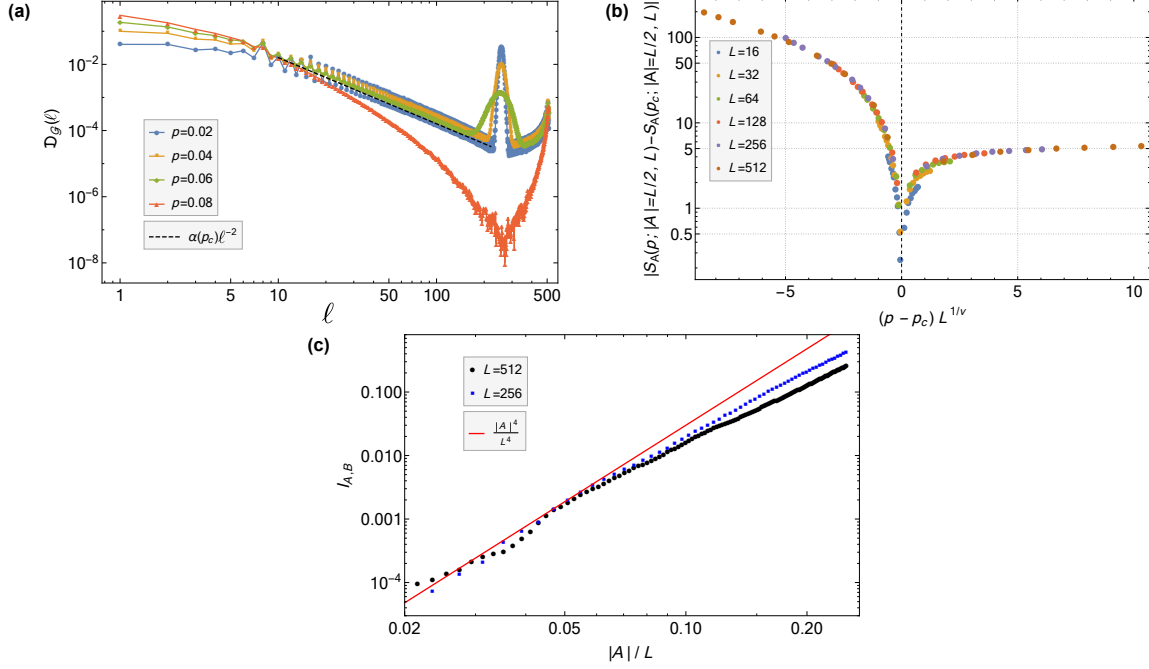


Figure 2.11: Numerical data for the circuit in Fig. 2.10. (a) The normalized stabilizer length distribution for $L = 512$, where $\alpha(p_c) = 1.6$. (b) Collapsing the $S_A(p; |A| = L/2, L)$ data to the scaling form in Eq. (2.22), where we set $p_c = 0.075$ and $\nu = 1.3$. (c) Mutual information at p_c for the geometry as in Fig. 2.9(b). We can similarly extract the exponent $\Delta \approx 2$ from the data with $|A|/L \ll 1$.

of $S_A = \alpha \ln |A| + s|A|$ scaling of the entanglement entropy in the volume law phase. The coefficient of the critical logarithmic entropy, $\alpha(p_c) \approx 1.6$, as extracted from the stabilizer length distribution, is close in value to that of the random Clifford circuit. Moreover, we can fit the entanglement entropy data near the transition with the finite-size scaling form in Eq. (2.22) using the same critical exponent $\nu \approx 1.3$, and find a reasonable collapse (see Fig. 2.11(b)). Finally, from the mutual information at criticality for the geometry as in Fig. 2.9(b), we can extract the exponent $\Delta \approx 2$ (see Fig. 2.11(c)), consistent with the random Clifford circuit results.

2.4.2 Random unitary circuit with periodic measurements

We next consider a circuit in which the measurements are arranged (quasi-)periodically, while the background unitary circuit is still composed of random Clifford unitaries, as illus-

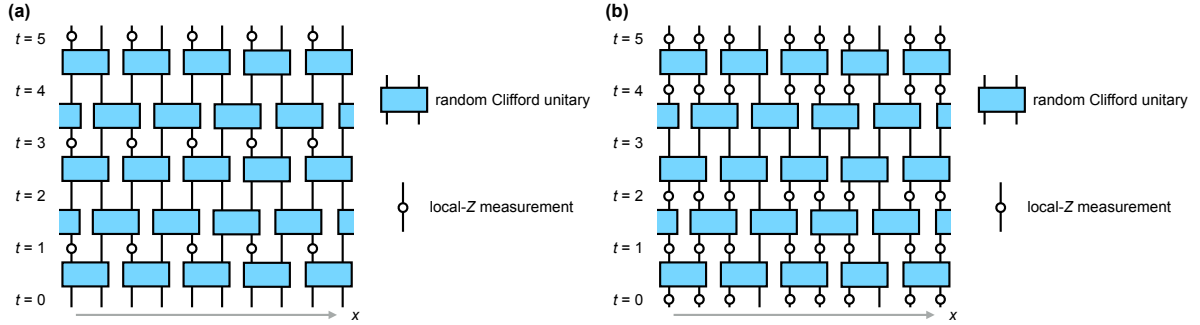


Figure 2.12: Two examples of circuits with random Clifford unitaries but quasi-periodic measurements, for (a) $p < 0.5$, and (b) $p > 0.5$.

trated in Fig. 2.12. Specifically, at a fixed measurement rate p , for each spacetime site (x, d) a measurement is made if and only if

$$\lfloor x\sqrt{p} \rfloor < \lfloor (x+1)\sqrt{p} \rfloor, \text{ and } \lfloor d\sqrt{p} \rfloor < \lfloor (d+1)\sqrt{p} \rfloor, \quad (2.30)$$

where $\lfloor r \rfloor$ is the largest integer that is not greater than r .

In Fig. 2.13, we plot the numerical results for this circuit, and observe behavior that is essentially the same as in the earlier models – both the random and Floquet Clifford circuit models with randomly located measurements. Evidently, eliminating the randomness in the locations of the measurements does not change the existence – or universality class – of the entanglement transition.

2.4.3 Circuits with space-time translational symmetry

Lastly, we consider a circuit with translational symmetry in space and time for both the unitaries and measurement positions. The only remaining stochasticity is in the randomness in the outcome of a measurement, which is intrinsic to quantum mechanics.

In our circuit we superpose the Floquet unitary background in Fig. 2.10 with the quasi-periodic measurement pattern in Fig. 2.12. Numerical results are shown in Fig. 2.14. As compared to our earlier models, we once again find essentially the same stabilizer length distribution indicative of two phases and an entanglement transition. Moreover, the critical ex-

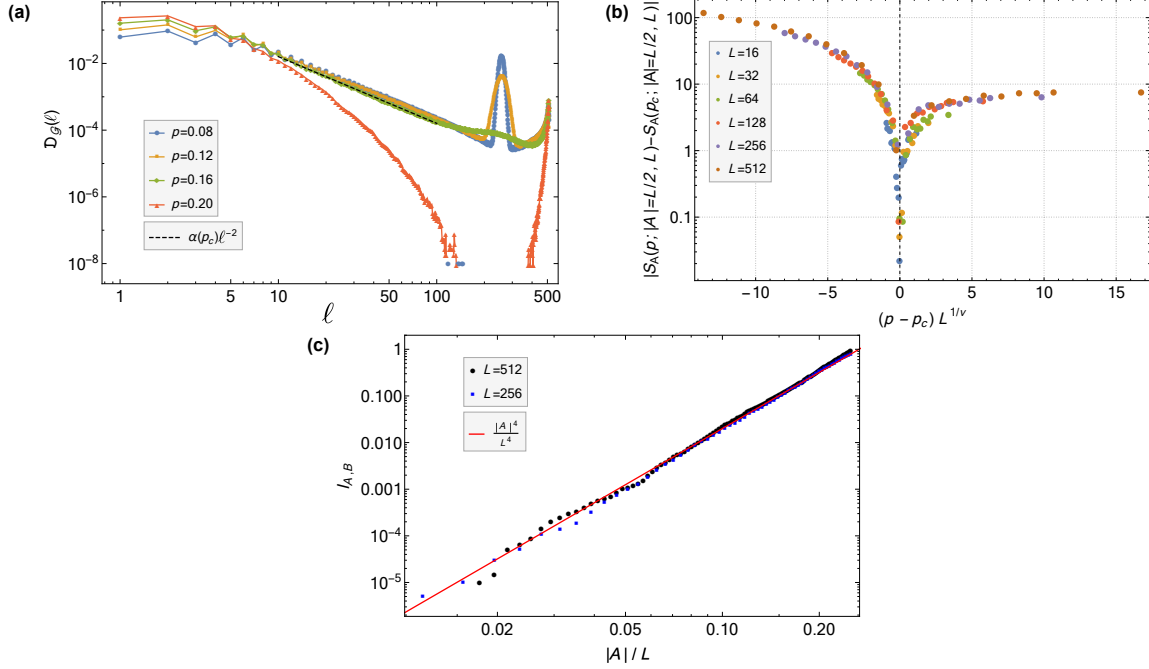


Figure 2.13: Numerical data for the circuit in Fig. 2.12 with periodically located measurement gates. (a) The normalized stabilizer length distribution for $L = 512$, where $\alpha(p_c) = 1.6$. (b) Collapsing the $S_A(p; |A| = L/2, L)$ data to the scaling form in Eq. (2.22), where $p_c = 0.162$ and $\nu = 1.3$. (c) Mutual information at p_c for the same geometry as in Fig. 2.9(b), where we identify $\Delta \approx 2$.

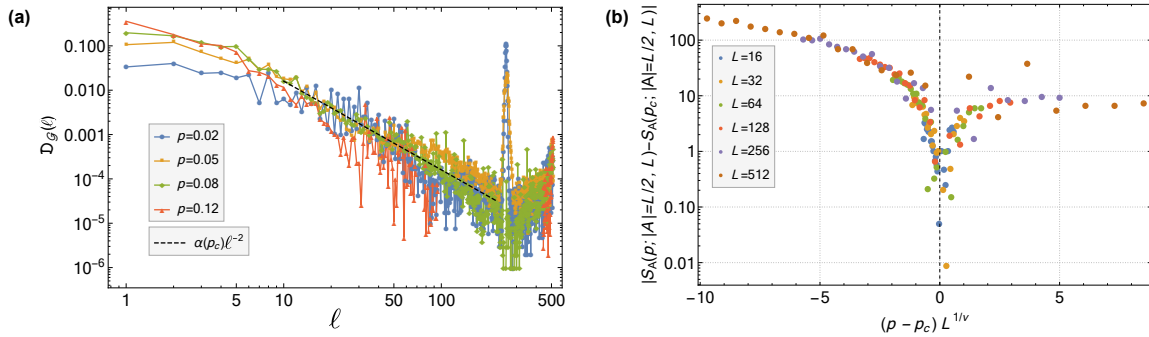


Figure 2.14: Data for a Clifford circuit with space-time translational symmetry, as defined in subsection 2.4.3. (a) The normalized stabilizer length distribution for $L = 512$, where $\alpha(p_c) = 1.6$. (b) Collapsing the $S_A(p; |A| = L/2, L)$ data to the scaling form in Eq. (2.20), where $p_c = 0.08$ and $\nu = 1.3$.

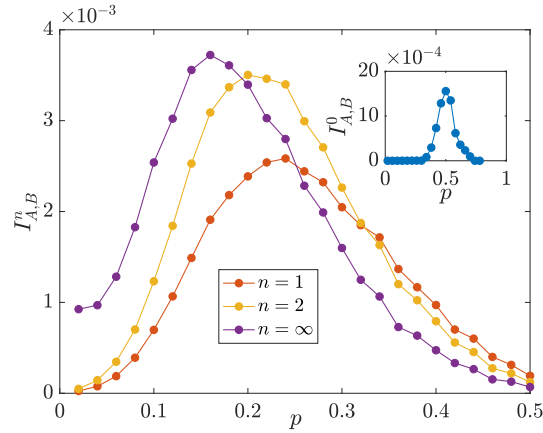


Figure 2.15: The mutual information for the random Haar circuit with projective measurements. In the numerical simulation the two regions A and B have size $|A| = |B| = 1$ and are antipodal in a system with periodic boundary conditions of size $L = 20$. Here the regions A and B are single sites.

ponents $\nu = 1.3$ and $\alpha(p_c) = 1.6$ at the entanglement transition are the same as in the other models.

The significant fluctuations in Fig. 2.14 are due to the lack of averaging – since we have only a single circuit in this case there is no ensemble averaging. Moreover, for Clifford circuits with Pauli measurements, the measurement outcomes are represented by the signs of the stabilizers, and do not affect the entanglement structure or the mutual information. Thus, the randomness in the measurement outcomes has no effect on the quantum information quantities here, and we have an almost deterministic Clifford circuit. The only type of averaging available is as a function of time.

2.5 Beyond Clifford

In this section we explore the transition in qubit systems beyond the stabilizer formalism.

2.5.1 Random Haar circuit

Consider the random Haar circuit with the structure shown in Fig. 2.1, where each rectangle now represents a two qubit gate which is a 4×4 matrix chosen randomly and independently

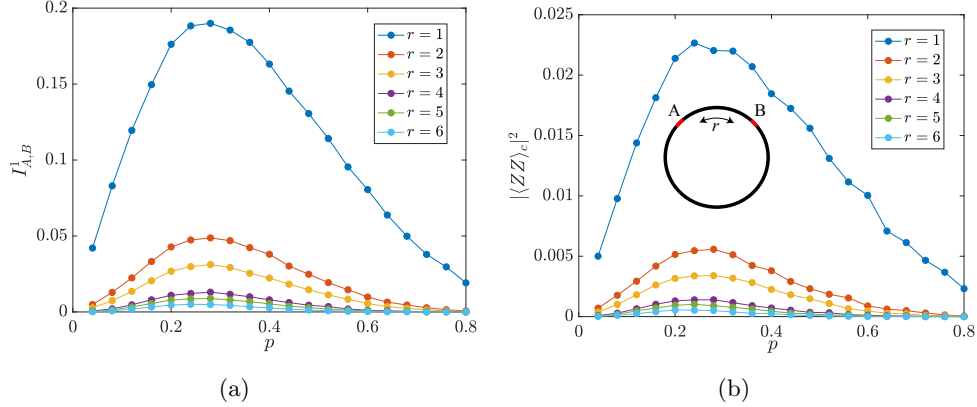


Figure 2.16: Comparison between (a) the mutual information and (b) the squared correlation function, in the random Haar circuit with projective measurements. In the numerical calculation A and B are separated by distance r with $|A| = |B| = 1$ (see the inset).

from the Haar measure of the unitary group [65, 66, 99]. Without measurements, this is a minimal model to study operator dynamics and chaos propagation in systems with small onsite Hilbert space and local interaction [28, 100]. With measurements, it is the most generic model in which the unitary-measurement dynamics can be addressed.

Random Haar circuit with projective measurements

We first consider the random Haar circuit with projective measurements. As in Fig. 2.1, the single site projective measurements, taken to be $P_{\pm} = (1 \pm Z)/2$, are introduced on each site independently with probability p . This model is closest in spirit to the random Clifford circuit studied in Sec. 2.2 and 2.3, with which comparisons should be made.

As for the Clifford circuits, we use mutual information between two antipodal regions (in a system with periodic boundary conditions) to diagnose the putative phase transition. This approach is particularly useful for small systems with $L = 20$, where it is hard to distinguish between volume law and area law scaling behavior by directly looking at the entanglement entropy. The numerical results, where the two regions are taken to be single sites, are shown in Fig. 2.15.

We notice that the mutual information for all Rényi indices show a peak, signifying the

existence of a transition. Within the Haar circuit, Rényi entropies and the mutual information can depend on the Rényi index n , and we discuss them separately. For $I_{A,B}^0$, the peak is located at $p_c = 0.5$, as predicted by the percolation mapping [16] (see the inset of Fig. 2.15). This situation is different for $I_{A,B}^n$ with $n \geq 1$, whose peaks are located at p much smaller than 0.5, and there is no obvious mapping to percolation⁵. While these peaks are rather broad due to finite size effects, they sit close to one another, suggesting that p_c is independent of n for $n \geq 1$ – i.e. there is a single transition (instead of a different transition for each n).

As discussed in Sec. 2.3, the fluctuation in the connected correlation function is upper bounded by the mutual information. We consider the following quantity in this model,

$$|\overline{\langle \mathcal{O}_A \mathcal{O}_B \rangle_c}|^2, \text{ where } \mathcal{O}_A = Z_1 \text{ and } \mathcal{O}_B = Z_{r+1}, \quad (2.31)$$

and the distance r is varied. In our numerical calculations shown in Fig. 2.16, we find that it takes a similar form as $I_{A,B}^1$ and has a peak at the corresponding p_c .

Random Haar circuit with generalized measurements

Projective measurements can be generalized to measurements that model imperfect measuring devices, known as “generalized measurements” or “weak measurements” [69]. Here, the coupling between the system and the measuring device is weak, and less information (\leq one bit) is extracted from the system by one such measurement. We consider a model in which the single site measurement gates in Fig. 2.1 are taken to be generalized measurements with operators,

$$M_{\pm} = \frac{1 \pm \lambda Z}{\sqrt{2(1 + \lambda^2)}}. \quad (2.32)$$

These measurement operators satisfy the required completeness relation, $M_+^\dagger M_+ + M_-^\dagger M_- = 1$.

The parameter λ represents the measurement strength: in the limit $\lambda \rightarrow 0$, the system and the

⁵Notice that for Rényi indices greater than 1, there is no subadditivity of entanglement, and the mutual information is not necessarily non-negative, although in our data the mean values are never negative.

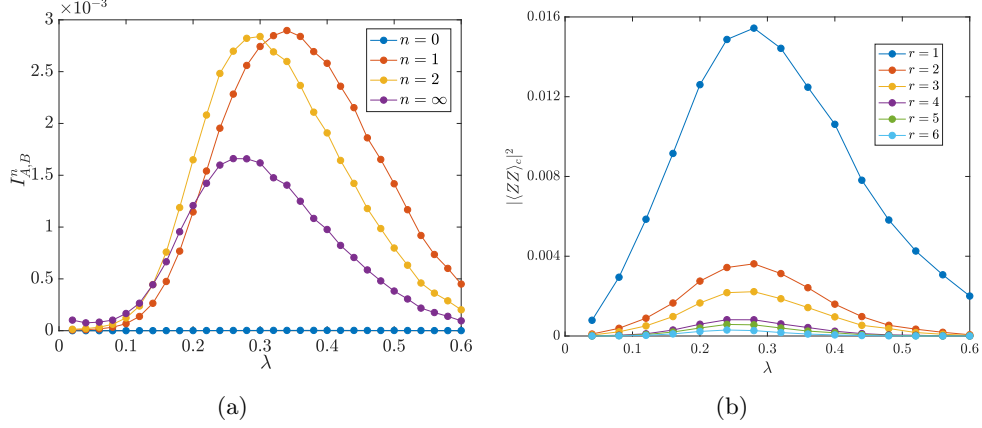


Figure 2.17: Data for the Haar unitary circuit with generalized measurements. (a) The mutual information, $I_{A,B}^1$, where A and B are antipodal in the system with periodic boundary conditions. (b) The squared correlation function as a function of λ . Here the two intervals A and B are separated by distance r (see the inset of Fig. 2.16(b)). In both (a) and (b), we take $L = 20$ and $|A| = |B| = 1$.

measuring device are totally decoupled and M_{\pm} acts trivially on the wavefunction, while in the limit $\lambda \rightarrow 1$, it becomes a projective measurement. For simplicity, we take the measurement rate $p = 1$ so that the generalized measurements are uniformly applied to each and every qubit in the circuit. Notice that these generalized measurements do not have a Clifford counterpart.

In Fig 2.17(a), we present results for $I_{A,B}^n$, where we find a peak for $n \geq 1$. The closeness of the peaks again suggests a single phase transition, as in the Haar circuit with projective measurements. Compared to the projective measurement case we note that here there is no phase transition in S_A^0 – as long as $\lambda < 1$, S_A^0 obeys a volume law. Moreover, we compute the squared correlation function and find a peak close to λ_c (see Fig. 2.17(b)).

Despite the uniformly imposed generalized measurements, the wavefunctions are not completely disentangled as long as $\lambda < 1$. Moreover, the volume law phase is stable for $\lambda < \lambda_c$.

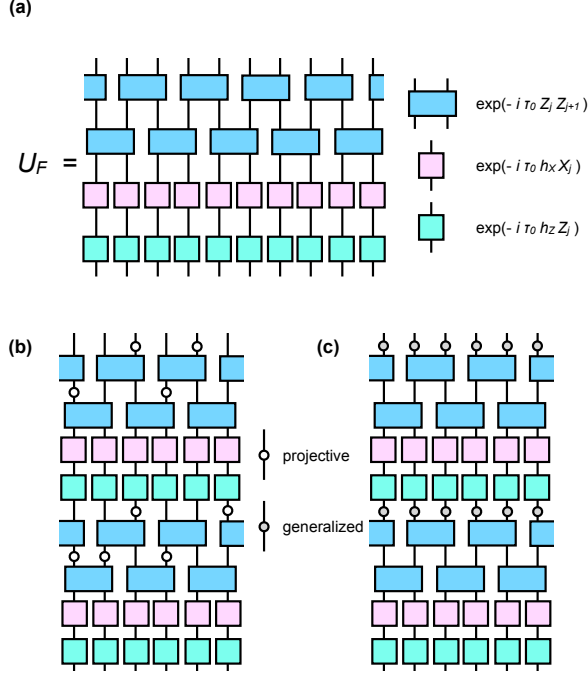


Figure 2.18: (a) The Floquet operator is specified by a quantum circuit. (b) The projective measurements are introduced in the circuit after each two-qubit gate layer with probability p . (c) The generalized (weak) measurements are applied uniformly with $p = 1$ in the circuit after each Floquet operator, U_F .

2.5.2 Floquet Ising circuits

As a generalization of the Floquet Clifford circuits from Sec. 2.4, we consider a Floquet Ising spin chain model with the following Floquet operator,

$$U_F = \exp[-i\tau_0 H_Z] \exp[-i\tau_0 H_X], \quad (2.33)$$

where

$$\begin{aligned}
 H_X &= h_X \sum_{j=1}^L X_j, \\
 H_Z &= \sum_{j=1}^{L-1} Z_j Z_{j+1} + h_Z \sum_{j=1}^L Z_j.
 \end{aligned} \quad (2.34)$$

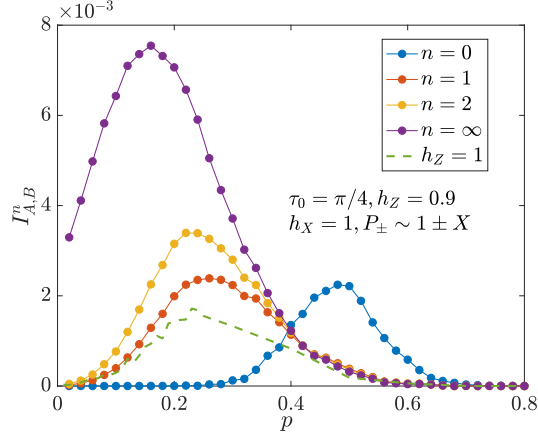


Figure 2.19: Mutual information $I_{A,B}^n$ for the Floquet spin chain model with projective measurements. A and B are antipodal in the periodic boundary condition. We take $L = 20$ and $|A| = |B| = 1$.

The Floquet operator defines a one-dimensional periodically driven system with period $T = 2\tau_0$. This Floquet model is integrable when $h_Z = 0$. We will focus on the generic non-integrable case with $h_Z \neq 0$. The circuit in Fig. 2.18(a) represents a particular discretization of the Floquet operator that we adopt. For the special parameter set, $(\tau_0, h_X, h_Z) = (\pi/4, 1, 1)$, the discretized Floquet operator falls within the Clifford group. Without measurements, the Floquet circuit has both temporal and spatial translational symmetries, and no randomness is present.

Floquet Ising circuit with projective measurements

We introduce projective measurements in the Floquet circuit (see Fig. 2.18(b)), taking the measurement gates to be $P_{\pm} = \frac{1}{2}(1 \pm X)$. The single site projective measurements are applied randomly in the same fashion as in Fig. 2.10.

In Fig. 2.19 we show data for the mutual information as a function of p . Here we have taken the parameter $h_Z = 0.9$, with the rest of the parameters the same as the Clifford parameters. There is a peak in $I_{A,B}^n$, with the location of the peak depending weakly on the Rényi index, which we identify as p_c . Again, the data supports the existence of the entanglement transition.

The dashed line in Fig. 2.19 shows the data for $h_Z = 1.0$, i.e. the Clifford limit in which there is no n dependence. The Clifford curve is close to the $n = 1$ curve for the non-Clifford

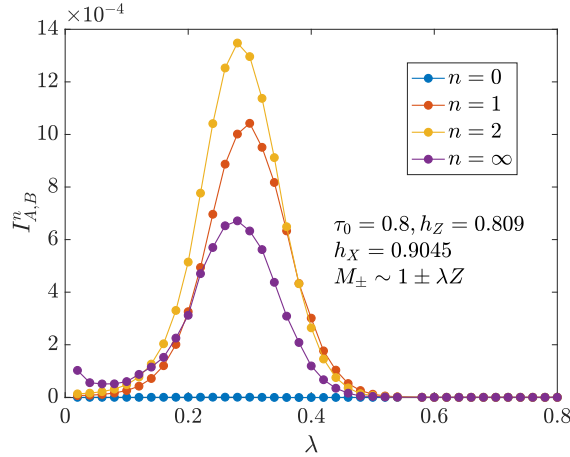


Figure 2.20: Mutual information $I_{A,B}^n$ for the Floquet spin chain model with generalized measurements. A and B are antipodal in a system of size $L = 20$ with periodic boundary conditions, while $|A| = |B| = 1$. The Floquet parameters are chosen as $(\tau_0, h_X, h_Z) = (0.8, 0.9045, 0.809)$ [8].

circuit and gives a consistent estimation of p_c . This comparison further justifies using the Clifford circuits as a convenient stand-in for more generic (non-Clifford) quantum circuits.

Floquet Ising circuit with generalized measurements

We next introduce generalized measurements in the Floquet spin chain model, again taking the measurement rate $p = 1$, so that the generalized measurements are uniformly applied at each and every site after U_F (see Fig. 2.18(c)). The result for the mutual information is presented in Fig. 2.20. Once again, the presence of the peak is indicative of an entanglement transition. As in the random Haar circuit with generalized measurements, there is no phase transition in S_A^0 .

2.5.3 Various properties at criticality

The location of p_c

The previous numerical results for random Haar circuit and Floquet Ising model suggest that p_c is independent of the Rényi index n when $n > 1$. This result can be further supported

by the following inequality for Rényi entropies,

$$S_A^\infty \leq S_A^n \leq \frac{n}{n-1} S_A^\infty, \quad (2.35)$$

where the second inequality holds when $n > 1$. Since S_A^n is bounded on both sides by S_A^∞ , in the thermodynamic limit, the scaling behavior of S_A^n ($n > 1$) must be the same at any p . This indicates that the transition for S_A^n with $n > 1$ occurs at the same p_c and the critical exponent ν should also be the same. However, the coefficient α in $S_A^n(p_c; |A|, L) = \alpha(p_c) \ln |A|$ at the critical point could depend on n .

Scaling of mutual information

As shown in Sec. 2.3.3, for the Clifford circuits we were able to extract the operator scaling dimension of a (putative) underlying CFT from the scaling of mutual information at criticality. Here, we attempt the same for the four non-Clifford models considered in this Section. To this end, we compute $I_{A,B}$ with fixed $|A| = |B| = 1$, varying the distance $r_{A,B}$ between the two sites. In this case the cross ratio varies as $\eta \propto r_{A,B}^{-2} \ll 1$.

In Fig. 2.21 we plot the mutual information as a function of the cross ratio η , which is defined in Eq. (2.27) for a system with periodic boundary conditions. At small values of η , the mutual information for all four models varies as a power law, $I_{A,B}^1 \propto \eta^\Delta$ with $\Delta \approx 2$, consistent with the Clifford circuit results (see Figs. 2.9(b), 2.11(c), and 2.13(c)).

2.6 Discussion

2.6.1 Summary

In this Chapter we have investigated a broad class of hybrid quantum circuit models constructed by interleaving unitary and measurement gates, the latter breaking the circuits unitarity. Under the circuit dynamics we have followed quantum trajectories of the qubits, focussing on the entanglement properties of the evolving pure state wavefunction at late times (in the

steady state). Entanglement generated by the unitary gates competes with the disentanglement from the measurements. As established numerically, upon varying the frequency of measurements, p , the phase diagram has two stable phases – a volume law entangled phase when measurements are rare/weak ($p < p_c$), and an area law entangled phase when measurements are frequent/strong ($p > p_c$). These two phases are separated by a critical point at $p = p_c$, with associated universal scaling properties.

The entanglement entropy in the volume law phase has a remarkable sub-leading correction that is logarithmic in the sub-system size, $S_A = \alpha(p) \ln |A| + s(p)|A|$, as we established by analyzing the length distribution of stabilizers used to simulate our Clifford circuits. The coefficient of the logarithm is non-universal throughout the volume law phase, but vanishes in the absence of measurements, $\alpha(0) = 0$. The coefficient of the linear piece in the entanglement entropy, $s(p)$, smoothly vanishes as one approaches the phase transition from the volume law phase, scaling as $s(p) \sim \xi^{-1} \sim (p_c - p)^\nu$ with a universal correlation length exponent $\nu \approx 1.3$. At the critical point, the logarithmic scaling of the entanglement entropy survives, with a universal coefficient given by $\alpha(p_c) \approx 1.6$. Moreover, the mutual information between two sites was found to decay as a power law of the distance at the critical point, $r^{-2\Delta}$ with exponent $\Delta \approx 2$, while the bipartite mutual information for more general geometries depends only on the cross ratio, as expected for a conformal field theory (CFT). Together with the logarithmic entanglement at p_c , this suggests the possible existence of an underlying CFT description.

It should be emphasized that these results were established by considering a large class of quantum circuits, both with and without Clifford gates. In addition to generic random models with no symmetries, we also explored circuits with space-time translational symmetries of the unitary dynamics and/or the measurement gate locations. In all cases we found stable volume law phases with a logarithmic correction, and similar critical exponents as in models without those symmetries.

2.6.2 Volume law phase and powerlaw correction

We now discuss a general framework incorporating measurements and unitaries that can be used to help better understand and bolster our numerical results. As above, we emphasize that the steady state entanglement properties of purely unitary circuits are qualitatively different from those circuits with measurements. In the absence of measurements, the steady state is maximally entangled, i.e. each subset A has an entanglement entropy of $S_A = |A|$. Measurements on a portion p of all qubits immediately reduces S_A from $|A|$ to $(1 - p)|A|$. This result is a direct consequence of the subadditivity of entanglement. Thus the maximally entangled state is very susceptible to measurements. Indeed, if we assume that this pS_A reduction in S_A is true for any volume law entangled state, we would reach the conclusion that no volume law phase should exist [18].

However, this intuition does not carry over to the case for the generic volume law entangled states present with measurements, which, firstly, have a linear slope s smaller than $1 - p$, so that the subadditivity bound on entanglement is no longer tight. With less entanglement, local measurements would have a weaker effect. Indeed, taking the limit of a trivial product state, a local measurement has only a local effect because of the lack of entanglement.

To illustrate this argument, we consider the following “surface growth” picture, as considered in Ref. [16] and shown in Fig. 2.22. Taking open spatial boundary conditions, we define a “height” function, $h(x)$, to be the entanglement entropy of the subsystem containing the first x qubits,

$$h(x) = S_{A=\{1,2,\dots,x\}}. \quad (2.36)$$

It is convenient to define the average height function,

$$\bar{h} := \frac{1}{L} \sum_x h(x). \quad (2.37)$$

In the volume law phase, $\bar{h} \propto L^1$, while in the area law phase $\bar{h} \propto L^0$, similar to the scaling of

the entanglement entropy with subsystem size. Consider now the effect of the circuit dynamics. At all times, \bar{h} grows under unitary time evolution. After a unitary layer in the circuit, it is expected that,

$$\Delta_U \bar{h} \propto L^0. \quad (2.38)$$

Recall that each measurement layer has pL measurement gates distributed homogeneously across the L qubits, after which the reduction in \bar{h} is,

$$\begin{aligned} \Delta_M \bar{h} &= \frac{1}{L} \sum_{i=1}^{pL} \sum_{x=1}^L \left(h^{(i)}(x) - h^{(i-1)}(x) \right) \\ &= \sum_{i=1}^{pL} \delta_M \bar{h}^{(i)}, \end{aligned} \quad (2.39)$$

where $h^{(i)}$ is the height function after the first i measurements are made, and $\delta_M \bar{h}^{(i)} := \frac{1}{L} \sum_{x=1}^L (h^{(i)}(x) - h^{(i-1)}(x))$ is the reduction of \bar{h} by the i -th measurement. Each of the $\delta_M \bar{h}^{(i)}$ has a non-positive expectation value.

At this point, we ignore the correlations and causal relations among measurements within the circuit, and treat $\delta_M \bar{h}^{(i)}$ for all measurements deep within the circuit as an independent samplings of a single random variable, $\delta_M \bar{h}$. This simplification is based on the assumption that in a generic circuit with little structure, the disentanglement of a single measurement should depend only on the entanglement structure of the pre-measurement wavefunction, which fluctuates weakly over time after saturation.

Therefore, Eq. (2.39) can be simplified as

$$\Delta_M \bar{h} = (pL) \langle \delta_M \bar{h} \rangle, \quad (2.40)$$

where $\langle \dots \rangle$ denotes the expectation value, taken within the ensemble of all measurements after saturation. Here, $\delta_M \bar{h}$ quantifies the disentangling ability of a single local measurement.

By definition, within the steady state, the entangling and disentangling effects must balance out, i.e. $\Delta_U \bar{h} + \Delta_M \bar{h} = 0$, therefore $\langle \Delta_M \bar{h} \rangle \propto L^0$, or

$$\langle \delta_M \bar{h} \rangle = O\left(\frac{1}{L}\right). \quad (2.41)$$

This is a relation that must hold for all $p > 0$, regardless of the steady state entanglement entropy. In particular, it must hold in any volume law entangled state in the presence of measurements, despite the fact that $\langle \delta_M \bar{h} \rangle = O(L^0)$ in a maximally entangled state and in a Bell pair state as discussed in Ref. [18].

Direct numerical evidence for the validity of Eq. (2.41) for all $p > 0$ can be established in our Clifford circuits, as we now discuss. As detailed in Appendix B, we compute the normalized distribution function of $\delta_M \bar{h}$ for the random Clifford circuit. Specifically, the distribution function of the “disentanglement length” $R \equiv -L \times \delta_M \bar{h}$, which we denote as $\mathcal{P}(R)$, takes the following schematic form within the volume law and area law phases,

$$\mathcal{P}(R) \sim \begin{cases} R^{-\gamma(p)}, p < p_c, \\ e^{-R/R_0} R^{-\gamma(p)}, p > p_c, \end{cases} \quad (2.42)$$

where R_0 is proportional to the correlation length in the area law phase. Here the power $\gamma(p)$, which varies with p throughout the volume law phase, grows as we increase p , consistent with our intuition that less entanglement implies less disentanglement. For p very small $\gamma(p)$ appears to approach 2, and is close to 3 when $p = p_c$, $\gamma(p_c) \approx 3$. Throughout the volume law phase $\gamma(p)$ is always larger than 2. Thus, despite the power law distribution of the disentangling scale, R , in the volume law phase, the *average disentangling length*, $\langle R \rangle = \int^{L/2} dR R \mathcal{P}(R)$ is finite for all $p > 0$. We then conclude that $\langle \delta_M \bar{h} \rangle = -\langle R \rangle / L = O(1/L)$, validating Eq. (2.41).

When restricted to Clifford circuits, the difference between the maximally entangled state and a general volume law entangled state in the presence of measurements is well illustrated by the stabilizer length distribution. As we show in Appendix B, within the clipped gauge,

a local measurement (say Z_x) replaces one of the L stabilizers with Z_x , while rearranging the others in a way that more or less preserve their lengths. When $p = 0$, the stabilizer distribution function is a delta function at $\ell \approx L/2$. In other words, there are only long stabilizers but no short ones. In this case, a local measurement will inevitably replace a long stabilizer with Z_x , causing a non-local change in the entanglement structure, as seen from Eq. (2.10). On the other hand, when $p > 0$, the power law distribution of “shorter” stabilizers protects the long stabilizers in the $\ell \approx L/2$ peak from always being replaced by a unit length one (Z_x), so that the replacement and rearrangement only happens within the “shorter” stabilizers, thereby preserving the volume law entropy. In the (rare) case when a long stabilizer does get replaced by Z_x , the power law distribution of “short” stabilizers can shift to the right under unitary evolution and compensate this reduction, rendering the distribution steady. In all models that we have studied, the inverse-square power law distribution of the “shorter” stabilizers is present, giving the sub-leading logarithmic correction to the entanglement entropy. We might thus say that the logarithmic correction is necessary for the stability of the volume law phase.

It seems plausible that the power law distribution in the measurement induced “disentanglement length”, $\mathcal{P}(R)$, and the power law distribution of the “shorter” stabilizers are related to one another, but the exact relation remains unknown to us. Although the distribution $\mathcal{P}(R)$ was computed for the random Clifford circuit it is defined with complete generality, and we believe that both the stability criterion $\gamma > 2$ as well as the logarithmic correction are universal for volume law phases stable against measurements in generic hybrid circuits.

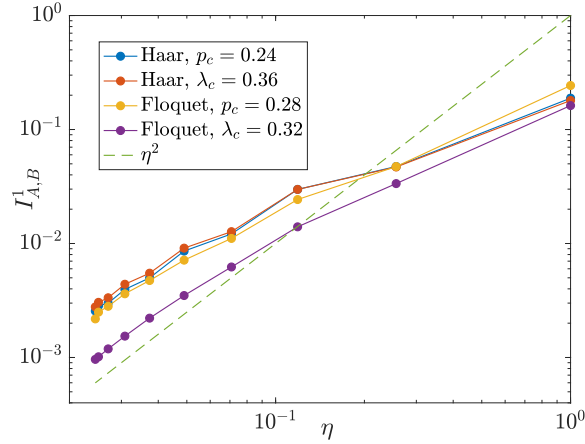


Figure 2.21: The mutual information $I_{A,B}^1$ for the four non-Clifford models studied in Section VI, each at their respective critical points, plotted versus the cross ratio, η , on a log-log scale. Here, the critical values, p_c and λ_c were determined by the peak location of $I_{A,B}^1$ when $r_{A,B} = L/2 = 10$.

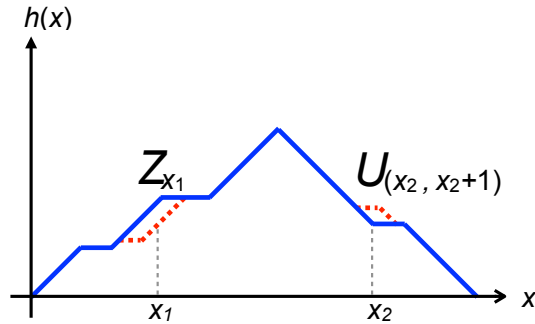


Figure 2.22: The entanglement entropy growth problem can be transformed into a surface growth model. While the unitary entanglement growth is local, the disentanglement of a local measurement (Z_{x_1}) can be non-local.

Chapter 3

Conformal invariance at the critical point

Entanglement is a central concept in quantum physics. It violates classical laws of physics in dramatic ways, and makes quantum communication and quantum computation fundamentally more powerful than their classical counterparts [69]. In recent years, the entropy of entanglement has proven useful in condensed matter physics, providing new insights and tools for understanding quantum states of matter, either in or out of equilibrium, at zero or finite temperature [3, 4, 101, 89, 102, 103, 104, 10, 11].

One of the most bizarre aspects of entanglement, namely quantum non-locality, has always involved wavefunctions subject to measurements. The measurements, albeit local, have non-local influences on the states and their entanglement structure. In the famous EPR thought experiment [1, 105], one destroys entanglement between a pair of distant qubits by making local measurements in exchange for perfectly correlated measurement outcomes. Conversely, one can entangle a pair of distant qubits with local measurements via a mechanism similar to quantum teleportation [106, 107], without the two ever needing to talk to one another – a phenomenon known as “entanglement swapping” that has found wide applications in quantum information science [106, 108, 109, 110] (see Fig. 3.1(a) for an illustration). These are examples

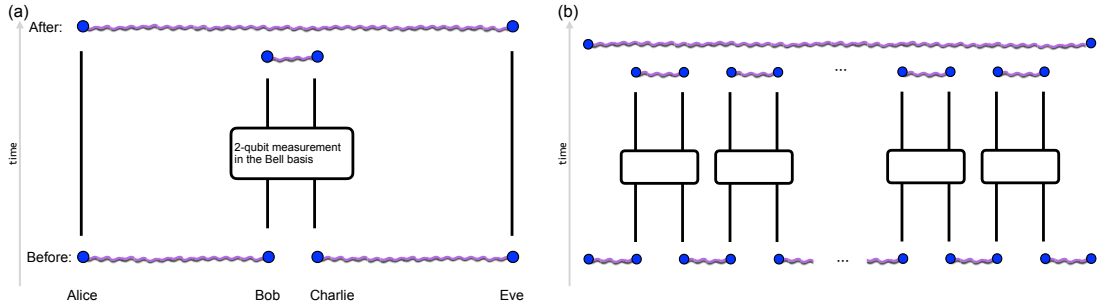


Figure 3.1: Illustration of the entanglement swapping protocol. (a) An example with four parties. The initial state consists of two Bell pairs, (Alice, Bob) and (Charlie, Eve), with Alice and Bob far apart, as well as Charlie and Eve. Suppose Bob and Charlie are spatially proximate and they make a collective 2-qubit measurement in the Bell basis ($\{\frac{1}{\sqrt{2}}(|00\rangle \pm |11\rangle), \frac{1}{\sqrt{2}}(|01\rangle \pm |10\rangle)\}$) [69]. The measurement “swaps” the entangled pairs, and now we have entangled pairs (Alice, Eve) and (Bob, Charlie). Notice that Alice and Eve never directly talked to one another, but nevertheless become entangled due to the measurement: for each one of the four possible measurement outcomes, Alice and Eve share a different state in the Bell basis. Since the distance between Alice and Eve is arbitrary, the speed of entanglement is arbitrarily large. However, no information is transmitted: in order for Alice and Eve to know what their wavefunction is, classical information about the measurement outcome must be obtained from Bob and Charlie via classical communication. (b) A many-qubit example of entanglement swapping. In this circuit with nearest neighbor gates, only a finite circuit depth is required to generate a long-range entangled Bell pair, given that the initial state is properly set-up and each two-qubit Bell measurement is perfect. This fine-tuned example merely serves the purpose of illustrating the possibility of infinite entangling speed in many-body systems. Notice the similarity with the actual circuit in Fig. 3.2.

of “measurement-induced quantum non-locality” in systems of a few qubits, and the experiments usually require carefully following specific protocols (that is, making the right unitary gates and right measurements at the right place and right time). One is therefore led to the following question: can quantum non-locality show up in many-body quantum dynamics under measurements *without* fine tuning? Notice that this is never possible in unitary systems, since information as well as quantum entanglement must evolve in a strictly local fashion, as required by the Lieb-Robinson bound [111, 112].

The numerical accessibility of the hybrid circuit model defined in Chapter 2 (see Fig. 2.1) alone makes it a convenient theoretical platform for investigating non-unitary quantum dynamics. For example, one can ask if the aforementioned measurement-induced quantum non-locality shows up in such circuits. In Ref. [59], it was suggested that the disentangling capabilities of local measurements are indeed non-local, as evidenced by the powerlaw distribution

of the “disentanglement length” throughout the volume-law phase and at the critical point. However, this was an indirect probe lacking an explicit information-theoretic meaning.

On a seemingly separate note, it was found that the steady state wavefunction right at the critical point exhibits long-range correlations and conformal invariance [16, 59, 30]. While in random unitary circuits the time-evolution is well understood [72, 28, 100], exactly how the long-time critical entanglement structures of the hybrid quantum circuits emerge under the real-time evolution, has not been explicitly described (see relevant discussions in Refs. [16, 30]).

In the present work, we establish the emergence of conformal symmetry in the spacetime circuit right at the critical point – by illustrating its role in describing the critical entanglement dynamics – and discuss the physical mechanism underpinning its emergence, namely the aforementioned non-locality induced by quantum measurements. Our starting point is a simple postulate that at the critical point, the spacetime manifold of the hybrid circuit hosts a Euclidean field theory, with the real-time direction of the circuit playing the role of imaginary/Euclidean time of the field theory (this naturally accounts for the absence of a Lieb-Robinson bound, as we briefly explain below). This idea was already implicit in the mappings to effective spin models [31, 30] relating quantum entanglement entropy to the *boundary free energy* of a classical statistical mechanics model [85]. Once time is interpreted as another spatial dimension, and entanglement entropies as boundary free energies, it is immediate that the conformal invariance – therefore also “criticality” and long-range correlations – makes already detailed predictions for entanglement dynamics at the very early times. Long-range correlations at arbitrarily early times imply an infinite entangling speed (as detailed in Eqs. (3.75, 3.76)), giving a positive answer to the question raised above – that there is indeed a many-body version of entanglement swapping induced by measurements in the circuit, despite the fact that the circuit is composed of completely random unitaries and measurements (as opposed to carefully designed protocols as in Fig. 3.1).¹ This suggests that “measurement-induced quantum non-locality” is

¹There are important subtleties in this statement, which we clarify immediately below.

- Entanglement itself does not contain information, and absence of lightcone in entanglement dynamics does not imply the ability to send information faster than light. As emphasized in the caption of Fig. 3.1, to verify the entanglement that has been generated by entanglement swapping, classical communication of

a consequence of broken unitarity, rather than of specific protocols/algorithms.

We establish the main results by studying the random Clifford circuit model for a 1d chain of Qubits, introduced in Ref. [59], taking a trivial product initial state and open spatial boundary conditions, tuned to the transition. The space-time region of the circuit is thus a rectangle. The Gottesman-Knill theorem [44, 67, 68] enables efficient simulation of Clifford circuits of up to thousands of qubits on a laptop, allowing us to perform detailed scaling analyses. We numerically compute the entanglement entropies and mutual information for various subregions at all time steps of the evolution, and verify that their dynamics are completely characterized by boundary 3- and 4-point correlation functions, respectively, of a CFT in the finite rectangular geometry. From the data we also extract several critical exponents characterizing the underlying Clifford CFT.

We further explore several different sets of boundary conditions of the Clifford circuit, by “inserting” physical qubits initialized in a trivial product state at the spatial and/or temporal boundaries of the finite circuit. Remarkably, the boundary qubits become critically entangled through the bulk as an intermediary, despite the fact that they never talked directly to each other – another manifestation of entanglement swapping. Numerical computations of entanglement entropies and mutual information further confirm the presence of conformal symmetry, and give consistent estimates of corresponding boundary operator scaling dimensions appearing in various *different* observables.

Among various different setups, of particular interest is the one in which the initial state consists of L Bell pairs (i.e. of L maximally entangled pairs of qubits). By taking one qubit

the measurement outcomes is necessary (for specifying the pure state wavefunction after the measurement, much like in a quantum teleportation experiment). This type of communication between “people” that perform and monitor the experiment is of course not included in the simple circuit model.

- The entanglement dynamics is only accessible in the pure state quantum trajectories, and is not accessible in the mixed state density matrix. In fact, in the density matrix everything remains local, since we are only applying local operations. To experimentally access the nonlocal entanglement one needs to prepare several copies of the same wavefunction, which requires heavy post-selection on the measurement outcomes. The need of introducing an “experimenter” doing all the work of recording measurement outcomes and post-selecting them, is in some sense similar to the aforementioned need of classical communication between “parties” in order to verify entanglement swapping.

from each pair, we form a length- L qubit chain which is subsequently subject to the hybrid circuit dynamics (the “system qubits”); the remaining qubit chain (the “environment qubits”) is left unevolved. The two qubit chains appear to be on the same footing and have identical entanglement structures at all times. In particular, while the system qubits experience the entanglement transition, the environment qubits also know about the transition. After tracing out the environment qubits, this setup is equivalent to the one in Ref. [21], where a mixed-state density matrix was time-evolved. The entanglement entropy between the system qubits and the environment qubits is correspondingly interpreted as the “purity of the system”, and the entanglement transition is now a “purification transition”, between a “mixed phase” and a “pure phase” characterized by, among other things, slow and fast purification dynamics, respectively. In our CFT language, this setup maps to the same bulk theory but with a different boundary condition, so the purification transition is indeed the same bulk transition as the transition in entanglement entropy with a pure initial state. We show that the $(T/L)^{-1}$ decay (T is the circuit depth) of the entanglement entropy between “system” and “environment” at early times, observed in the numerics of Ref. [21], follows directly from conformal symmetry, which in turn identifies the amplitude of that decay as a universal (boundary) scaling dimension of the CFT (up to a factor of π). We also show that the universal exponential decay of the same quantity at late times is a consequence of crossover to a quasi-one-dimensional system, the rate of decay being given by yet another universal (boundary) scaling dimension of the CFT, which we identify here. These results are consequences solely of the conformal invariance; they hold in all CFTs, and thus hold, in particular equally in other critical hybrid quantum circuits described by CFTs, presumably including those with Haar unitaries.

We apply the same reasoning to the analysis of the problem of the 0th Rényi (Hartley) entropy in random Haar circuits, which is believed [16] to be described by two-dimensional critical first-passage percolation. Comparison between the critical properties of the von Neumann entropy in Clifford CFT and those of the so-obtained zeroth Rényi (Hartley) entropy in the Haar circuits is made, and their relationship is discussed.

The rest of this Chapter is organized as follows. In Sec. 3.1, we introduce the random hybrid circuit model in rectangular geometry with several sets of boundary conditions. We then give a statement of the conjecture regarding the presence of conformal symmetry, as well as a concrete prescription for computing the entanglement entropy of an arbitrary segment at an arbitrary time step. In Sec. 3.2, we present the main results of this Chapter, namely the numerical data on entanglement entropy and mutual information dynamics in the rectangular circuit, and compare them with CFT calculations. In Sec. 3.3, we present results for circuits with periodic boundary condition, that are used for fixing tuning parameters of our fitting scheme. In Sec. 3.4, we discuss the universality of our results, relations to other works, and possible future directions. In Appendix C.1, we provide, for reference, a list of elementary facts from conformal field theory used in this Chapter. In Appendix C.2, we discuss purification dynamics of “reference qubits” recently introduced in Ref. [113], which reveals a boundary operator scaling dimension taking different values in the Clifford CFT and in critical percolation. This result is further confirmed by a separate calculation in Appendix C.3. In Appendix C.4, we present parallel numerics and analysis of two-dimensional critical first-passage percolation.

3.1 The hybrid circuit model and the conjecture

3.1.1 The hybrid circuit models with different boundary conditions

Amongst various versions of the hybrid quantum circuit model [16, 17, 59, 20, 21, 31, 30], we take the one with random Clifford unitaries on pairs of qubits (with local Hilbert space dimension $q = 2$) and projective measurements of single-site Pauli operators made in a Poissonian fashion with probability p , which was introduced in Ref. [59] and referred to as “the random Clifford circuit”. We focus on the critical point of the entanglement transition, taking $p = p_c \approx 0.1600$ in this particular model [59, 21] (see Sec. 3.3 for the location of the transition).

The circuit model is always defined together with its boundary conditions (b.c.), which we take, for the most part of this Chapter, to be open spatial boundary conditions. In Fig. 3.2, we

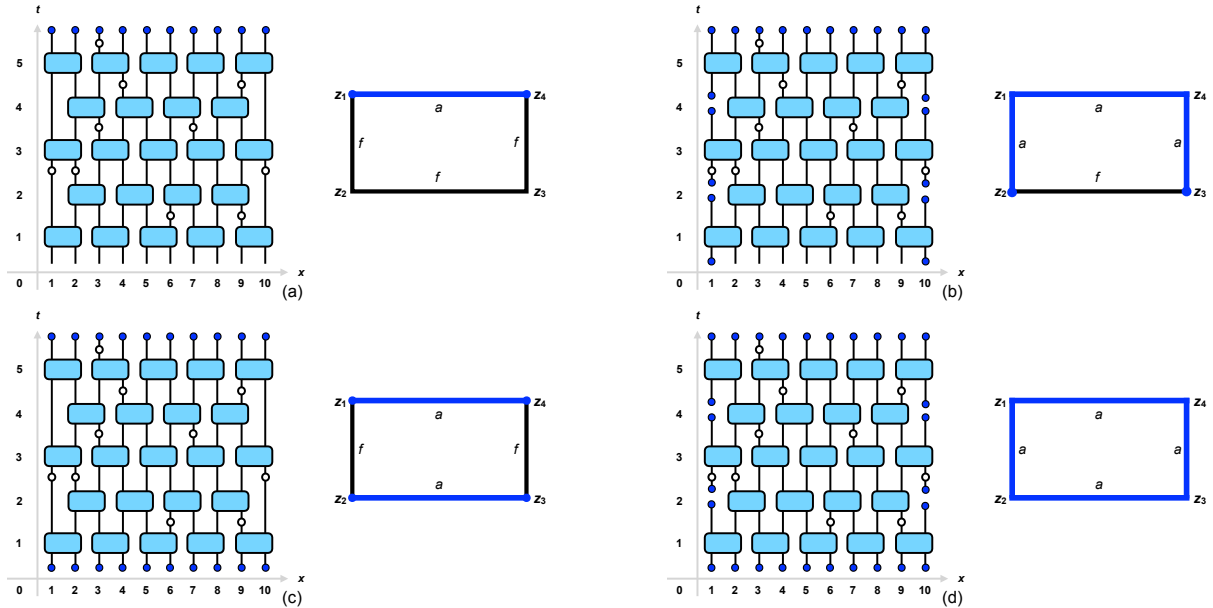


Figure 3.2: Random hybrid Clifford circuit model with different boundary conditions. The rectangles in cyan represent random Clifford unitary gates, arranged in a brickwork fashion. Between the unitary layers are projective measurements of single-site Pauli operators made at random sites at probability $p = p_c$, represented by hollowed circles. The blue solid circles at the upper boundary represent physical qubits after evolution of circuit depth T . Notice that time runs “upwards”. In (a), we illustrate the simplest b.c. of all, with a trivial product state and open spatial b.c. These two are assumed to correspond to the same “free b.c.”, denoted f and represented with black color. The blue edge represents a “physical qubit b.c.”, denoted a . The two boundary conditions are separated by boundary condition changing (bcc) operators at the corners, denoted z_1 and z_4 . In (b), we “insert” initially unentangled physical qubits at the left and right edges of the circuit at every time period, so that we have the a b.c. on three edges of the rectangle, with the other one still in f . In (c), we take the initial state of L Bell pairs, and take one qubit from each pair to form a qubit chain (the system) which undergoes the circuit dynamics, leaving the other qubit chain untouched (the environment). We put the environment and the system on the $t = 0$ and $t = T$ boundaries, respectively, and both in the a b.c. In (d) we combine the initial state in (c) and the “temporal insertion” setup, to obtain a circuit with a on all four sides. We shall refer to the four sets of boundary conditions as (a) $fffa$, (b) $afaa$, (c) $fafa$, and (d) $aaaa$, respectively.

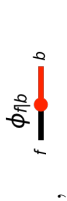
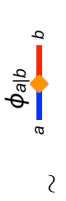
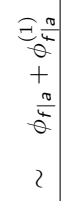
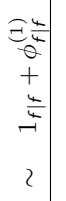
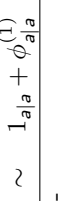
bcc operator	Definition	Scaling dimension	Reference
$\phi_{f a}, \phi_{f b}$		$h_{f a} = h_{f b}$ is unknown	Eqs. (3.2, 3.4, 3.5, 3.33).
$\phi_{a b}$		$h_{a b} = 0.76 \ln(2) = 0.53$	Eqs. (3.4, 3.23, 3.47); Figs. (3.5, 3.6, 3.8, 3.9, 3.11, C.1)
$\phi_{f a}^{(1)}$		$h_{f a}^{(1)} = h_{f a} + 0.9$	Eq. (3.33); Figs. (3.5, 3.6).
$\phi_{f f}^{(1)}$		$h_{f f}^{(1)} = 0.41$	Eq. (3.58); Figs. (3.8, C.1, C.2, C.3).
$\phi_{a a}^{(1)}$		$h_{a a}^{(1)} = 2.0$	Eq. (3.36, 3.48); Fig. (3.9)
-	-	$x_{p.b.c} = 0.125$	Eq. (3.84); Fig. (3.11).

Table 3.1: A summary of boundary conditions (b.c.), boundary condition changing (bcc) operators, and their operator product expansions (OPE) that will appear later in this Chapter. There are three types of b.c., namely (1) f , corresponding to product initial state and open spatial b.c. of the circuit; (2) a , corresponding to physical qubits; and (3) b , corresponding to qubits for which the entanglement entropy is computed. Exchange symmetry between a and b is assumed. The fundamental bcc operator is the one separating f and a , which we denote as $\phi_{f|a}$ (or its symmetric counterpart $\phi_{a|b}$). The OPE between $\phi_{a|f}$ and $\phi_{f|b}$ gives rise to a bcc operator separating a and b , and we define $\phi_{a|b}$ to be the leading term with smallest scaling dimension. These two operators $\phi_{f|a}$ and $\phi_{a|b}$ are assumed to transform as primary fields under conformal transformations [114]. We further define operators $\phi_{f|a}^{(1)}$ and $\phi_{a|a}^{(1)}$ as the *subleading* operators in the corresponding OPE channels. In these OPEs we have suppressed prefactors and only kept the operator content; the full form will be provided when they are encountered (see also Appendix C.1). We summarize scaling dimensions extracted for these operators and their appearance in this Chapter, which we refer to for more detailed explanations. Notice that we are unable to extract the scaling dimension for $\phi_{f|a}$ since it does not explicitly appear in the entanglement entropy calculation. $x_{p.b.c}$, appearing at the bottom is not associated to scaling dimensions of bcc operators; rather, it is a universal scaling exponent of the bulk CFT (see Sec. 3.3).

illustrate the circuit model with the corresponding space-time geometry of a finite rectangle, with length L (measured in terms of the number of qubits) and depth T (measured in terms of the number of unitary layers), where we define 4 sets of different b.c. on its edges. In order to introduce the circuit models, we have to make several postulates in assigning the boundary conditions; in this section we neither explain the physical meanings of these boundary conditions, nor provide justifications of our assumptions. We postpone these issues to later sections: Sec. 3.1.2, Sec. 3.2 and Appendix C.4. We proceed by listing the four sets of boundary conditions that we consider:

- (a) The simplest of all is the one with a product initial state and open spatial b.c. at the right and left boundaries of the rectangle (Fig. 3.2(a) – time goes “upwards”). We posit that these two map to the same b.c. (in the sense described in Sec. 3.1.2), which we refer to as the “free b.c.”, denoted f . We further posit that the physical qubits at the boundary representing the quantum state at final time $t = T$ map to a different b.c., which we refer to as the “physical qubit” b.c., denoted a .

Since the b.c. change from f to a at the corners denoted by z_1 and z_4 in Fig. 3.2(a), we say that there are (analogous to Ref. [85, 30]) boundary condition changing (bcc) operators $\phi_{f|a}(z_1)$ and $\phi_{a|f}(z_4)$ located at these corners. The meaning of the bcc operators will be specified in Sec. 3.1.2.

As a result, we have a circuit with boundaries labeled by the sequence of boundary conditions $fffa$ in counter-clockwise order (starting from the left boundary of the rectangle).

- (b) In the 2nd case, we introduce physical qubits at the left and right edges of the rectangle in the following manner (see Fig. 3.2(b)). We retain $L - 2$ qubits sitting at positions $x = 2, \dots, L - 1$ of the chain, and at each time step, we introduce two “fresh” qubits, each initially in a disentangled 1-qubit pure state (the specific state is unimportant), and “inject” them into the system as the 1st and the L -th qubit of the circuit. The L -qubit chain is then evolved under the circuit dynamics for one time period (notice that one time step corresponds to two consecutive unitary layers). After that period, we take out the 1st

and the L -th qubit, keep them somewhere else without further actions on them, and fill their positions in the chain with two new fresh qubits in the next time period. For a circuit of depth T (with T even), by the end of its evolution, the left and right edges will each have $T/2$ qubits, namely those “fresh” qubits that have been “injected” on the right and left edges, in addition to the $L - 2$ qubits at the final time $t = T$ (the upper edge of the rectangle), taking the same position as qubits in the previous setup (a). We posit that they map to the same b.c. a , as that discussed in the previous setup (a). As compared with Fig. 3.2(a), we now have eliminated the bcc operators at the corners denoted by z_1 and z_4 , at the cost of introducing new bcc operators $\phi_{f|a}(z_2)$ and $\phi_{a|f}(z_3)$ at the corners denoted by z_2 and z_3 . By the same convention as above, we refer to this b.c. as *afaa*.

- (c) In the 3rd case, we take an initial state composed of L pairs of maximally entangled qubits (i.e. Bell pairs), where different pairs are unentangled with each other (as required by monogamy of entanglement). Taking one qubit from each pair, we form an L -qubit chain (which we call the “system”), and the rest form another L -qubit chain (which we call the “environment”). We let the “system chain” undergo the circuit dynamics of depth T , while the “environment chain” is left unevolved. By the end of the evolution, we naturally have the “system” at the upper edge of the rectangle, and we assume that the “environment” “lives” on the lower edge (in a sense to be specified in Sec. 3.1.2). We further posit that the upper and lower edges are described again by the same b.c. a , discussed in the previous two setups (a) and (b), as shown in Fig. 3.2(c).

In this setup, there are bcc operators at all 4 corners to start with: $\phi_{f|a}(z_1)$, $\phi_{a|f}(z_2)$, $\phi_{f|a}(z_3)$, $\phi_{a|f}(z_4)$. We refer to this b.c. as *fafa*.

- (d) In the 4th case, we combine the b.c. in (b) and (c) so that we have physical qubits on all four edges. Specifically, we take the initial state as described in (c), and while evolving the “system”, we inject physical qubits at each time step as in (b). The physical qubits on all four edges are assumed to correspond to the same b.c., a , as shown in Fig. 3.2(d).

In this setup, we do not have any bcc operators at any of the corners (since the b.c. do not change). We refer to this b.c. as *aaaa*.

As clarified above, at this point issues like the “labelling” of the boundary conditions (with *f* or *a*) and “where the physical qubits sit on the rectangle” are meaningless until certain observables are assigned to them. As we will see next in Sec. 3.1.2, the boundary conditions are important in defining boundary free energies within the putative conformal field theory.

3.1.2 Statement of the conjecture and example calculations of entanglement entropy

Previous works on the measurement-induced entanglement transition are quite suggestive of the presence of full conformal invariance in spacetime, though the models considered differ from one another in details. Among these are Ref. [16], where the critical percolation description of the 0th (Hartley) Rényi entropy in circuits with random Haar gates was already manifestly conformally invariant; Refs. [17, 21], where a dynamic exponent of $z = 1$ was found; and Ref. [59], where the presence of conformal invariance in the steady state was numerically confirmed, all for Clifford circuits. More recently in Refs. [31, 30], concrete critical spin models which admit conformal field theory (CFT) descriptions at their critical points were proposed to describe the n th Rényi entropies with $n \geq 1$ in hybrid quantum circuits with Haar random unitaries in the limit of infinite local Hilbert space dimension.

Motivated by these considerations, we propose the following conjecture(s) at entanglement transitions in generic hybrid quantum circuits:

1. There is an emergent CFT living on the two-dimensional finite spacetime manifold of the circuit (with certain spatial and temporal b.c.), where the real-time direction of the circuit becomes the “imaginary time” of the CFT.
2. Physical qubits live on boundaries of the finite circuit, and the von Neumann entanglement entropy² of a contiguous segment A of qubits is given by the change in (boundary) free

²Throughout the Chapter we consider Clifford circuits, for which all Renyi entropies are equal to the von

energy of the CFT in the finite geometry due to change of the b.c. inside A (recall that free energies of a CFT depend crucially on the specific b.c.³.)

Specifically, for a contiguous segment A of the boundary of the rectangle with endpoints located at z_1 and z_2 , which we denote by $A = [z_1, z_2]$, we posit that

$$S([z_1, z_2]) \equiv -\ln \frac{Z_{\text{circuit}}[\phi(z_1)\phi(z_2)]}{Z_{\text{circuit}}}, \quad (3.1)$$

where Z_{circuit} is a suitably defined background “circuit partition function” of the rectangle specified by boundary conditions of the circuit, and $Z_{\text{circuit}}[\phi(z_1)\phi(z_2)]$ is the partition function with the same boundary conditions as Z_{circuit} , except that in the boundary segment $A = [z_1, z_2]$ the boundary condition has changed as compared to Z_{circuit} , which in a CFT can be accounted for by the insertion of boundary condition changing (bcc) operators ϕ at the endpoints z_1 and z_2 of A . An expression similar to Eq. (3.1) first appeared in the extreme volume-law phase of Random Tensor Networks aimed at describing gravitational Ryu-Takayanagi behavior [116], then in Random Tensor Network Models for entanglement transitions [85] which are [30] very close cousins of the entanglement transitions in hybrid circuits discussed here, and shortly after in the present context of measurement-driven entanglement transitions [59, 31, 30].

We remark on an apparent conceptual leap on which we briefly elaborate at the end of this paragraph: While previously in Fig. 3.2 the bcc operators $\phi_{f|a}$ are merely placeholders to signify the change of boundary condition, in a CFT they become scaling fields that define the partition function; we further assume that these fields are what is called *primary* [114]. These boundary scaling fields are the central objects of this Chapter, and govern the entanglement structure of the circuit through Eq. (3.1).

The expression Eq. (3.1) can be obtained directly by repeating the steps presented in Ref. [30], but now for the reduced density matrix for the random *Clifford* circuit with measurements, upon making the only assumption that an effective statistical mechanical model

Neumann entropy.

³See, e.g., Ref. [115] for a review.

emerges after averaging, which exhibits a conformally invariant transition in the bulk of the circuit.⁴ We provide in this paper extensive evidence for the validity of this assumption for Clifford circuits. All the remaining assumptions made in this Chapter about the appearance of boundary condition changing operators follow from general properties of CFT. In particular, any microscopic boundary condition (satisfying certain locality conditions) on a CFT will at long distance scales in general always turn into a “conformal boundary condition” described by a (boundary) fixed point of the Renormalization Group. Moreover, at a point on the boundary where two different such “conformal boundary conditions” meet, a boundary condition changing conformal boundary operator will appear. For the convenience of subsequent discussions in this Chapter, we summarize in Table 3.1 all relevant boundary conditions, bcc operators, and their operator product expansion (OPE), that will appear in later sections.

We illustrate the prescription in Eq. (3.1) with the *ffa* circuit in Fig. 3.2(a), which we choose, in the present case, to represent the “background” configuration of boundaries. Because of the two bcc operators at the corners $\phi_{f|a}(z_1)$ and $\phi_{a|f}(z_4)$ (as defined in Table 3.1), the circuit partition function is given as (see Fig. 3.3(a))

$$Z_{\text{circuit}} = \langle \phi_{f|a}(z_1) \phi_{a|f}(z_4) \rangle Z_0, \quad (3.2)$$

where $\langle \dots \rangle$ denotes the “expectation value” taken in an underlying $(2+0)$ -dimensional CFT in the bulk of the rectangle, which can be thought of as some suitable classical statistical mechanics system representing the CFT; and Z_0 is the partition function of this CFT living in a rectangle with free boundary condition f on all four sides.

Next, let us consider the entanglement entropy of a contiguous segment A of physical qubits within $[z_1, z_4]$. According to the conjecture, $S(A)$ is the change in free energy due to change of b.c. in A from a to yet another one, denoted by b , which is assumed to be of the same type as

⁴Hybrid circuits with periodic, non-random (Floquet) unitaries and/or (quasi-)periodically located measurements in space and time also appear to exhibit an entanglement transition in numerics [59]. Provided these are also conformal transitions, with which the numerical evidences appear to be consistent, general assumptions of this Chapter also apply, although a statistical mechanical model cannot be readily obtained along the lines outlined in Ref. [30].

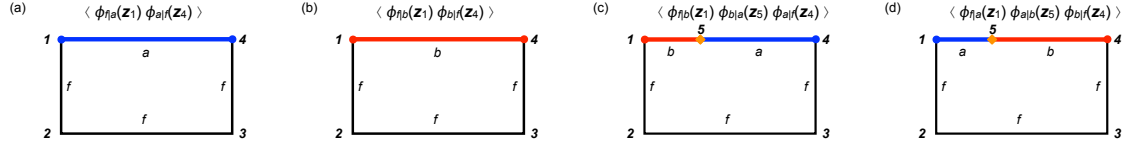


Figure 3.3: Pictorial representations of the partition functions with bcc operators inserted at the corner and on the edge, for computations of bipartite entanglement entropies in the $fffa$ circuit shown in Fig. 3.2(a). (a) The “background” partition function, given by correlation function of bcc operators at z_1 and z_4 separating f and a . (b) The partition function corresponding to computation of entanglement entropy of the whole qubit chain. Since the entire system is in a pure state, the entanglement entropy should be 0, as realized by the exchange symmetry between a and b (see Eq. (3.5)). (c, d) The partition functions corresponding to the calculation of $S(A = [z_1, z_5]) = S(\bar{A} = [z_5, z_4])$ (see Eq. (3.4)).

a , but different (we will be more specific below). Such effects are accounted for by inserting bcc operators at the endpoints of A , separating boundary conditions a (outside A) and b (inside A). We denote such an operator $\phi_{a|b}$ (see Table 3.1 for its definition).

In the simple case when $A = [z_1, z_5]$ as depicted in Fig. 3.3(c), i.e. having one of its endpoint at the corner z_1 (therefore specifying a single bipartition of the top boundary of the rectangle at z_5), the boundaries of the rectangle is labelled by three distinct boundary conditions: a in $\bar{A} = [z_5, z_4]$, b in $A = [z_1, z_5]$, and f elsewhere, in counter-clockwise order. The corresponding partition function should therefore be given by the correlation function of three bcc operators located at z_1, z_5 and z_4 . Explicitly, following Eq. (3.1), the bipartite entanglement entropy $S(A)$

can be written as ⁵

$$\begin{aligned}
 & S(A = [z_1, z_5]) \\
 &= -\ln \frac{Z_{\text{circuit}}[\phi_{a|b}(z_1)\phi_{b|a}(z_5)]}{Z_{\text{circuit}}} \\
 &= -\ln \frac{\langle \phi_{f|b}(z_1)\phi_{b|a}(z_5)\phi_{a|f}(z_4) \rangle}{\langle \phi_{f|a}(z_1)\phi_{a|f}(z_4) \rangle}. \tag{3.3}
 \end{aligned}$$

For a pure wave function, the entanglement entropies satisfy $S(A) = S(\bar{A})$, where \bar{A} is the complement of the segment A on the upper boundary of the rectangle. This requires that the partition function is invariant under exchanging a and b ; indeed, using Eq. (3.3), we have (see Fig. 3.3(c, d))

$$\begin{aligned}
 & S(A = [z_1, z_5]) \\
 &= -\ln \frac{\langle \phi_{f|b}(z_1)\phi_{b|a}(z_5)\phi_{a|f}(z_4) \rangle}{\langle \phi_{f|a}(z_1)\phi_{a|f}(z_4) \rangle} \\
 &= -\ln \frac{\langle \phi_{f|a}(z_1)\phi_{a|b}(z_5)\phi_{b|f}(z_4) \rangle}{\langle \phi_{f|a}(z_1)\phi_{a|f}(z_4) \rangle} \\
 &= S(\bar{A} = [z_5, z_4]). \tag{3.4}
 \end{aligned}$$

⁵In fact, literally following Eq. (3.1), this entropy is related to the correlation function involving the inserted two bcc operators at z_1 and z_5 , in addition to the existing ones at the corners z_1 and z_4 . Thus we have a four-point correlation function:

$$\begin{aligned}
 & S(A = [z_1, z_5]) \\
 &= -\ln \frac{Z_{\text{circuit}}[\phi_{a|b}(z_1)\phi_{b|a}(z_5)]}{Z_{\text{circuit}}} \\
 &= -\ln \frac{\langle \phi_{f|a}(z_1)\phi_{a|b}(z_1)\phi_{b|a}(z_5)\phi_{a|f}(z_4) \rangle}{\langle \phi_{f|a}(z_1)\phi_{a|f}(z_4) \rangle}.
 \end{aligned}$$

In going from this to Eq. (3.3), we have implicitly invoked the following OPE (to leading order; see Table 3.1),

$$\phi_{f|a}(z_1)\phi_{a|b}(z_1 + \epsilon) \sim \epsilon^{-h_{a|b}}\phi_{f|b}(z_1) + \dots$$

to account for the coincidence of the left endpoint of A with the corner of the rectangle, therefore effectively reducing the four-point function to a three-point function, as expected. Despite its apparent complexity, the physical picture is intuitive: after $\phi_{f|a}(z_1)$ and $\phi_{a|b}(z_1 + \epsilon)$ have fused into $\phi_{f|b}(z_1)$, there are only three ‘‘colored segments’’ on the boundary, and therefore the partition function is given by a simple three point function.

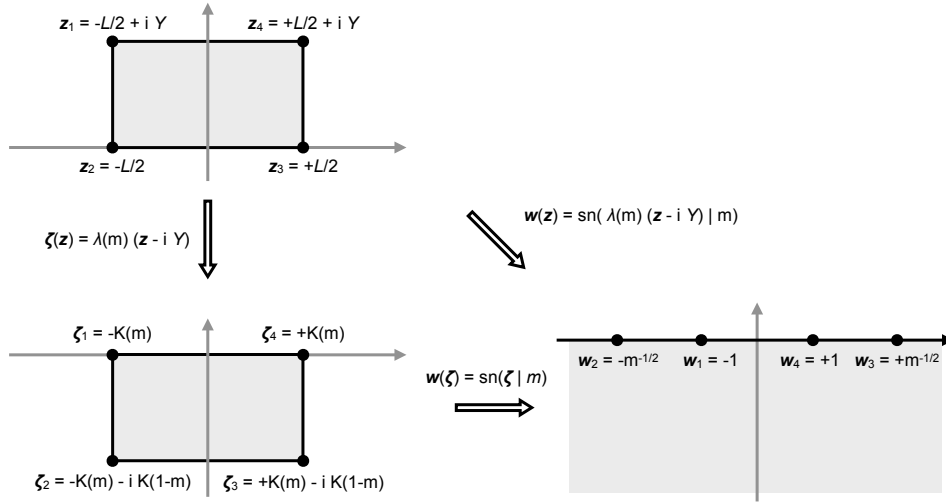


Figure 3.4: The conformal mapping, from the finite rectangle to the LHP. The parameter m is chosen such that the aspect ratio match. The boundary of the rectangle, highlighted, is mapped to the real axis of the LHP, where the 4 vertices of the rectangle map to $w_1 = -1$, $w_2 = -m^{-1/2}$, $w_3 = +m^{-1/2}$, and $w_4 = +1$, respectively.

In the limit when A includes all the physical qubits (– i.e. when $z_5 = z_4$, see Fig. 3.3(b)),

$$S([z_1, z_4]) = -\ln \frac{\langle \phi_{f|b}(z_1) \phi_{b|f}(z_4) \rangle}{\langle \phi_{f|a}(z_1) \phi_{a|f}(z_4) \rangle} = 0, \quad (3.5)$$

as expected for a pure state. Again, we have used the exchange symmetry between a and b . These considerations illustrate more specifically the sense in which “the boundary condition b is of the same type as a , but different”, as mentioned above.

Although for simplicity, we have only considered the *ffa* circuit and have only taken segment A to start from either z_1 or z_4 in this calculation, straightforward generalizations can be made to other cases, as we will see in Sec. 3.2.

Our approach here is “experimental”, though reasonably motivated by general principles. For example, we notice that the exchange symmetry between a and b comes about naturally from the general requirement of purity of the wavefunction. In Sec. 3.2, we will provide numerical evidences for CFT calculations like Eq. (3.4), supporting our conjectures, together with the prescription for computing entanglement entropies and the assignments of boundary conditions.

3.1.3 Finite rectangular geometry and the Schwarz-Christoffel mapping

In most of this Chapter we will focus on systems as in Fig. 3.2, where the circuit manifold has the geometry of a finite rectangle (open boundary conditions); the case of cylindrical geometry (periodic boundary conditions) is treated in Sec. 3.3. The former case is convenient because the rectangle is simply connected, and can thus be mapped to the lower half plane (LHP) via a conformal mapping (due to Schwarz-Christoffel)⁶, allowing simple calculations of correlation functions in the rectangle (such as those in Fig. 3.3), due to their conformal covariance in the putative CFT (see Appendix C.1). Since all rectangles are conformally equivalent to the LHP, one can relate dynamics at different time scales via the conformal mapping, using the LHP as an intermediary. Similar ideas have been applied to crossing probabilities in two-dimensional critical percolation [118].

We first address an important subtlety in mapping the circuit to a CFT in a finite rectangle. In the circuit model, the physical qubits undergo real-time evolution, and there is no obvious space-time rotational symmetry; therefore, space and time are on separate footing, and in particular, a circuit with $L = T$ does not necessarily correspond to a square system when viewed as a CFT. We must therefore introduce a suitable “lattice spacing” for both the space and time directions, λ_x and λ_t , with λ_x measured in the number of qubits, and λ_t in the number of layers. The “correct” aspect ratio of the rectangular circuit when viewed as a CFT is therefore given by

$$\tau := \frac{T/\lambda_t}{L/\lambda_x} \equiv \frac{Y}{L}, \quad (3.6)$$

where $Y = \left(\frac{\lambda_x}{\lambda_t}\right) T$ is the “rescaled (imaginary) time” or “depth”. For the random Clifford circuit, we fix the ratio $Y/T \approx 0.61$; the determination of this ratio is detailed in Sec. 3.3. We emphasize that Y/T is a bulk property and is independent of the boundary conditions. The value $Y/T \approx 0.61$ is thus fixed for all boundary conditions of the random Clifford circuit

⁶See, e.g. Ref. [117] for an introduction.

considered in this Chapter. However, Y/T is non-universal and can vary from circuit to circuit; in particular, for the percolation problem that describes the zeroth Rényi entropy in Haar random circuits, there is explicit rotational symmetry therefore $Y/T = 1$ (see Appendix C.4).

In the rest of this subsection, we detail the particular conformal mapping we use to relate the finite rectangle and the LHP, as summarized in Fig. 3.4. Points in the original rectangle are labeled by a complex coordinate,

$$z = x + iy, \tag{3.7}$$

where we take the convention $x \in [-L/2, L/2]$ for the position of the qubit, and $y = \frac{Y}{T}t \in [0, Y]$ the rescaled time coordinate. As a first step, we perform a translation by $-iY$, followed by an overall scaling, to transform the $L \times Y$ rectangle (living in the complex z -plane) to the $2K(m) \times K(1 - m)$ “canonical” rectangle (living in the complex ζ -plane), where the overall scaling factor is

$$\lambda(m) := 2K(m)/L \stackrel{!}{=} K(1 - m)/Y. \tag{3.8}$$

Here $K(m)$ is the complete elliptic integral of the 1st kind with parameter $m \in [0, 1]$, and m is chosen such that aspect ratios match,

$$\tau(m) := K(1 - m)/2K(m) \stackrel{!}{=} Y/L. \tag{3.9}$$

It is only through this parameter m that the aspect ratio (hence time) comes into the correlation

functions. We will take the convention that the four corners of the rectangle sit at [117]

$$\zeta_1 = -K(m), \tag{3.10}$$

$$\zeta_2 = -K(m) - iK(1 - m), \tag{3.11}$$

$$\zeta_3 = +K(m) - iK(1 - m), \tag{3.12}$$

$$\zeta_4 = +K(m). \tag{3.13}$$

In the second step, we map the canonical rectangle to the LHP via a Jacobi sn function [117],

$$w(\zeta) = \text{sn}(\zeta|m), \tag{3.14}$$

and we have

$$w_1 = w(\zeta_1) = -1, \tag{3.15}$$

$$w_2 = w(\zeta_2) = -m^{-1/2}, \tag{3.16}$$

$$w_3 = w(\zeta_3) = +m^{-1/2}, \tag{3.17}$$

$$w_4 = w(\zeta_4) = +1. \tag{3.18}$$

Thus, the composition of these two maps, $z \rightarrow \zeta \rightarrow w$, reads

$$w(z|\tau(m) = Y/L) = \text{sn}(\lambda(m)(z - iY)|m). \tag{3.19}$$

It is useful to recall [117] the asymptotic forms of $\tau(m)$,

$$\tau(m) \sim \begin{cases} \frac{\pi}{2} \left(\ln \frac{16}{1-m} \right)^{-1}, & \text{as } m \rightarrow 1 \ (\tau \rightarrow 0), \\ \frac{1}{2\pi} \ln \frac{16}{m}, & \text{as } m \rightarrow 0 \ (\tau \rightarrow \infty), \end{cases} \tag{3.20}$$

and also the asymptotic forms of the the cross ratio,

$$\eta = \frac{w_{12}w_{34}}{w_{13}w_{24}} \sim \begin{cases} 16 \exp(-\pi/\tau), & \tau \rightarrow 0 \\ 1 - 16 \exp(-\pi\tau), & \tau \rightarrow \infty \end{cases}$$

where $w_{ij} := w_i - w_j$ ($i, j = 1, \dots, 4$).

3.2 Results on rectangular circuits

In this section we present results of numerical simulation of the Clifford circuits defined in Sec. 3.1. Unless otherwise noted, we will take the circuit with length $L = 512$ (measured in the number of qubits), and varying the depth up to $T = 1024$, (measured in the number of unitary layers). The simulation uses the stabilizer formalism [67], and follows the standard algorithm in Ref. [68]. The computation of entanglement entropies [81, 82, 83, 78, 79] is done in the “clipped gauge”, which is a particular choice of stabilizers where entanglement entropies can be efficiently computed [72, 59]. It is always implicit that the entanglement entropies and mutual information are computed for various subregions at each time step, individually for each pure-state quantum trajectory, and then averaged over ensembles of trajectories. Only a subset of data points for selected time windows are presented to avoid crowding; we have verified that other data points also collapse well onto the same curves. The included time windows range from early times $\tau \ll 1$ to late times $\tau \gtrsim 1$. Due to limited numerical precision of floating point numbers on a standard computer, we exclude from the plots data at extremely early time $\tau(m) \lesssim 0.03$, where $|1 - m(\tau)| \leq 10^{-16}$. We do not think this is an important issue, but merely a technical nuisance we have yet to fully resolve.

We will always take $p_c = 0.1600$ and $Y/T = 0.61$ for all b.c., where Y is the rescaled time (see Sec. 3.1.3). The determination of these values are discussed in Sec. 3.3.

Some of the analytic calculations make use of standard results of simple correlation functions and Operator Product Expansions (OPEs) in CFT, which are listed in Appendix C.1.

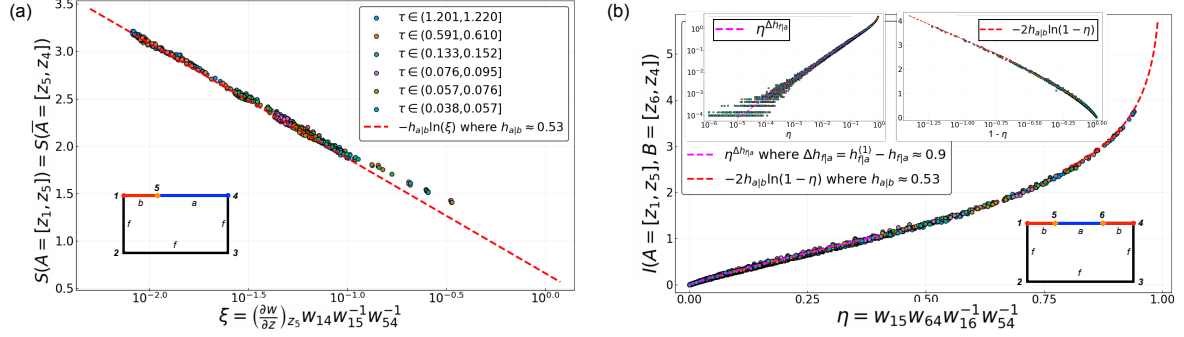


Figure 3.5: (a) Entanglement entropies for the *fffa* circuit, where the data collapse follows Eq. (3.23). The apparent deviation of the data from the predicted form at larger values of ξ is due to non-universal corrections when z_1 and z_5 are close on the lattice. (b) Mutual information for two subregions sitting next to the corners, where the data collapse follows Eq. (3.32). The limiting behaviors for $\eta \rightarrow 0$ and $\eta \rightarrow 1$ follow Eqs. (3.35) and (3.40), respectively, and are shown in the insets.

Throughout the paper we compute the entanglement entropy by taking the natural logarithm on the reduced density matrix, following a convention adopted in Refs. [30, 31, 101],

$$S(A) := -\text{Tr} \rho_A \ln \rho_A. \quad (3.21)$$

We notice that this convention differs from that in Refs. [16, 17, 59, 20, 21, 113], where the base-2 logarithm is used.

3.2.1 Circuit with boundary conditions *fffa* - Fig. 3.2(a)

Bipartite entanglement entropies as 3-point functions

Bipartite entanglement entropies within the *fffa* circuit (with a product initial state and open spatial b.c.; see Fig. 3.2(a)) were already discussed as an example in Sec. 3.1. This setup, as shown in Fig. 3.3(c), has three bcc operators. The simplicity of 3-point functions in CFT

allows us to carry out the computation in Eq. (3.4) explicitly⁷

$$\begin{aligned}
 & \exp[-S([z_1, z_5])] && \text{(Fig. 3.5(a))} \\
 = & \frac{\langle \phi_{f|b}(z_1) \phi_{b|a}(z_5) \phi_{a|f}(z_4) \rangle}{\langle \phi_{f|a}(z_1) \phi_{a|f}(z_4) \rangle} \\
 = & \left(\frac{\partial w}{\partial z} \right)_{z_5}^{h_{a|b}} \frac{\langle \phi_{f|b}(w_1) \phi_{b|a}(w_5) \phi_{a|f}(w_4) \rangle}{\langle \phi_{f|a}(w_1) \phi_{a|f}(w_4) \rangle} \\
 \propto & \left(\frac{(\frac{\partial w}{\partial z})_{z_5} w_{14}}{w_{15} w_{54}} \right)^{h_{a|b}} . && (3.22)
 \end{aligned}$$

Thus,

$$S([z_1, z_5]) = -h_{a|b} \ln \left(\frac{(\frac{\partial w}{\partial z})_{z_5} w_{14}}{w_{15} w_{54}} \right) + \text{const.} \quad (3.23)$$

The data collapse for $S([z_1, z_5])$ where $z_5 = x_5 + iY$ with varying x_5 and Y (that is, bipartite entanglement entropies for varying positions of the bipartition at different circuit depths) against $\xi = \frac{(\frac{\partial w}{\partial z})_{z_5} w_{14}}{w_{15} w_{54}}$ is shown in Fig. 3.5(a). Consistency with Eq. (3.23) is found, and we fit for $h_{a|b} \approx 0.53$.⁸

Entanglement dynamics

The quality of the data collapse in Fig. 3.5(a) (together with Fig. 3.5(b); see below) lends strong support to our conjecture regarding the conformal invariance of the circuit, together with our assumptions about the boundary conditions and the algorithm for computing the entanglement entropy. Assuming these are indeed correct assumptions, the 3-point functions, in turn, provide a complete description of the entanglement entropy dynamics and mutual

⁷A boundary operator $\phi_{f|b}(z)$, if initially located at a position z on a straight edge (say, top or side edge) *away from* the corner, is known to acquire, as it approaches the corner z_1 , a powerlaw singularity in the distance $(z_1 - z)$, because the scaling dimension of the operator is twice as large when placed at the 90-degree corner, as compared to at a straight edge. This singularity is a consequence of the conformal mapping. The same powerlaw singularity occurs in the denominator of the ratio appearing in the equation below and cancels out. The same type of cancelation occurs in all other ratios of correlation functions involving boundary operators located directly at a corner that we consider in this Chapter.

⁸We note that $h_{a|b} \approx 0.76 \ln 2$, where the value 0.76 is consistent with Refs. [59, 21].

information dynamics, as we show in this subsection and the next. For example, as we will now show, Eq. (3.23) leads to the logarithmic temporal growth of entanglement entropies at early times [16, 17], as well as the logarithmic scaling with spatial size in the steady state [16, 17, 59]. To see this explicitly, we focus on the two simplifying regimes when $\tau = Y/L \ll 1$ and when $\tau = Y/L \gg 1$, where we recall that $Y \propto T$ is the rescaled imaginary time (proportional to the circuit depth).

1. $\tau \ll 1$. In this limit, the conformal mapping for $z = x + iY$ reduces to

$$\lim_{\tau \rightarrow 0} w(z) = \lim_{m \rightarrow 1} \operatorname{sn}(\lambda(m)x|m) = \tanh \left[\frac{\pi}{2Y} x \right], \quad (3.24)$$

so that Eq. (3.23) takes the following simple form

$$\begin{aligned} S([z_1, z_5]) &= -h_{a|b} \ln \frac{\pi}{Y} + \text{const.} \\ &= h_{a|b} \ln Y + \text{const.} \end{aligned} \quad (3.25)$$

This is independent of z_5 since when $L \gg Y$ the corners of the rectangle are infinitely far away.

2. $\tau \gg 1$. In this limit, the conformal mapping for $z = x + iY$ reduces to

$$\lim_{\tau \rightarrow \infty} w(z) = \lim_{m \rightarrow 0} \operatorname{sn}(\lambda(m)x|m) = \sin \left[\frac{\pi}{L} x \right], \quad (3.26)$$

and Eq. (3.23) becomes

$$\begin{aligned} S([z_1, z_5]) &= h_{a|b} \ln \left(\frac{L}{\pi} \sin \left[\frac{\pi x_{15}}{L} \right] \right) + \text{const.}, \end{aligned} \quad (3.27)$$

where $x_{15} = x_1 - x_5$, reminiscent of the Cardy-Calabrese formula [101], and when $x_{15} \ll L$,

reduces to $S([z_1, z_5]) = h_{a|b} \ln x_{15}$.

Mutual information as 4-point functions

We take a segment away from the corners, $A = [z_5, z_6]$, where $z_j = x_j + iY$ and $-L/2 = x_1 < x_5 < x_6 < x_4 = L/2$, and compute $S([z_5, z_6])$. (According to our prescription, this is the entanglement entropy of the segment $A = [z_5, z_6]$ at time $y = Y$.) Since the segment A is away from the corners, this geometry involves four boundary changing operators at positions z_1, z_5, z_6, z_4 along the upper boundary of the rectangle; see the inset of Fig. 3.5(b). Following Eq. (3.1), this is given by

$$\begin{aligned}
 & \exp[-S([z_5, z_6])] && \text{(Fig. 3.5(b))} \\
 = & \frac{\langle \phi_{f|a}(z_1) \phi_{a|b}(z_5) \phi_{b|a}(z_6) \phi_{a|f}(z_4) \rangle}{\langle \phi_{f|a}(z_1) \phi_{a|f}(z_4) \rangle} \\
 = & \frac{\langle \phi_{f|b}(z_1) \phi_{b|a}(z_5) \phi_{a|b}(z_6) \phi_{b|f}(z_4) \rangle}{\langle \phi_{f|b}(z_1) \phi_{b|f}(z_4) \rangle} \\
 = & \left(\frac{\partial w}{\partial z} \right)_{z_5}^{h_{a|b}} \left(\frac{\partial w}{\partial z} \right)_{z_6}^{h_{a|b}} \\
 & \times \frac{\langle \phi_{f|b}(w_1) \phi_{b|a}(w_5) \phi_{a|b}(w_6) \phi_{b|f}(w_4) \rangle}{\langle \phi_{f|b}(w_1) \phi_{b|f}(w_4) \rangle} \\
 \propto & \left[\frac{\left(\frac{\partial w}{\partial z} \right)_{z_5} \left(\frac{\partial w}{\partial z} \right)_{z_6}}{(w_{56})^2} \right]^{h_{a|b}} F_{fbab}(\eta), && (3.28)
 \end{aligned}$$

where

$$\eta = \frac{w_{15}w_{64}}{w_{16}w_{54}} \quad (3.29)$$

is the cross ratio, and we have defined $F_{fbab}(\eta)$ with the following convention,

$$\begin{aligned}
 & F_{fbab}(\eta) \\
 = & \frac{\langle \phi_{f|b}(w_1) \phi_{b|a}(w_5) \phi_{a|b}(w_6) \phi_{b|f}(w_4) \rangle}{\langle \phi_{f|b}(w_1) \phi_{b|f}(w_4) \rangle \langle \phi_{b|a}(w_5) \phi_{a|b}(w_6) \rangle}. && (3.30)
 \end{aligned}$$

Given $S([z_5, z_6])$, we are now ready to compute another quantity of physical interest, namely the mutual information between two subregions sitting next to the corners, $A = [z_1, z_5]$ and $B = [z_6, z_4]$ (illustrated in the inset of Fig. 3.5(b)). We have

$$\begin{aligned}
 & I([z_1, z_5], [z_6, z_4]) \\
 &= S([z_1, z_5]) + S([z_6, z_4]) - S([z_1, z_5] \cup [z_6, z_4]) \\
 &= S([z_1, z_5]) + S([z_6, z_4]) - S([z_5, z_6])
 \end{aligned} \tag{3.31}$$

for a pure state, so that

$$\begin{aligned}
 & \exp[-I([z_1, z_5], [z_6, z_4])] \\
 & \propto \frac{1}{F_{fbab}(\eta)} \left(\frac{\eta}{1-\eta} \frac{1}{1-\eta} \right)^{-h_{a|b}},
 \end{aligned} \tag{3.32}$$

where we have used Eq. (3.23), (3.28), and the exchange symmetry between a and b . Thus, the mutual information is a function only of the cross ratio η , and this is supported by the data collapse shown in Fig. 3.5(b), where the numerical data is again obtained at different times with various values of z_5 and z_6 .

We note in passing that the scaling form of the entropy $S[z_5, z_6]$ (illustrated in the inset of Fig. 3.5(b)) is fully determined by that of the mutual information in Eq. (3.32), as well as those of $S([z_1, z_5])$ and $S([z_6, z_4])$, as already discussed in subsection 3.2.1.

Limits of the 4-point function from Operator Product Expansion (OPE)

Let us examine the limit in which $z_5 \rightarrow z_1$, or $z_6 \rightarrow z_4$, so that the crossratio $\eta \rightarrow 0$. In this limit, $\phi_{f|b}(z_1)$ and $\phi_{b|a}(z_5)$, as well as $\phi_{a|b}(z_6)$ and $\phi_{b|f}(z_4)$, are close to one another, and it is the following OPE that is needed in Eq. (3.30) (see Table 3.1),

$$\begin{aligned}
 & \phi_{f|b}(w_1)\phi_{b|a}(w_5) && \text{(Fig. 3.5(b))} \\
 \sim & w_{15}^{-h_{a|b}} \left(\phi_{f|a}(w_1) + C_{f|b|a}^{(1)} w_{15}^{h_{f|a}^{(1)} - h_{f|a}} \phi_{f|a}^{(1)}(w_1) + \dots \right), && (3.33)
 \end{aligned}$$

where we have denoted by $\phi_{f|a}^{(1)}(w_1)$ the subleading bcc operator in the $f|a$ -channel with a larger scaling dimension $h_{f|a}^{(1)} > h_{f|a} = h_{f|b}$. With this, $F_{fbab}(\eta)$ in Eq. (3.30) reads

$$\begin{aligned}
 & F_{fbab}(\eta) \\
 \propto & \left(\frac{\eta}{1-\eta} \right)^{-h_{a|b}} \left(1 + \# \eta^{h_{f|a}^{(1)} - h_{f|a}} \right), \eta \rightarrow 0. && (3.34)
 \end{aligned}$$

Inserting this equation into Eq. (3.32), we obtain the mutual information as a powerlaw function of η ,⁹

$$\begin{aligned}
 & I([z_1, z_5], [z_6, z_4]) = I(\eta) \\
 \approx & \# \eta^{h_{f|a}^{(1)} - h_{f|a}} + h_{a|b} \times \eta, \quad \eta \rightarrow 0. && (3.35)
 \end{aligned}$$

When $h_{f|a}^{(1)} - h_{f|a} < 1$, the first term is more dominant than the analytic term of order $O(\eta)$. From the fit in Fig. 3.5(b) (see inset), we find the powerlaw exponent $h_{f|a}^{(1)} - h_{f|a} \approx 0.9$.

Referring again to Fig. 3.5(b), another limit of interest is $z_5 \rightarrow z_6$, where $\eta \rightarrow 1$. The following OPE appearing in Eq. (3.30) is now relevant (see Table 3.1),

$$\begin{aligned}
 & \phi_{b|a}(w_5)\phi_{a|b}(w_6) && \text{(Fig. 3.5(b))} \\
 \sim & w_{56}^{-2h_{a|b}} \left(\mathbf{1}_{b|b} + C_{b|a|b}^{(1)} w_{56}^{h_{b|b}^{(1)}} \phi_{b|b}^{(1)}(w_6) + \dots \right) && (3.36)
 \end{aligned}$$

⁹Here (and in all following equations), we use the symbol $\#$ to denote an order one, nonuniversal number.

After the two operators on the left hand side fuse, the b.c. is b on both sides of the new operator, therefore the leading behavior is captured by the identity operator, in addition to which we also include the subleading operator $\phi_{b|b}^{(1)}$, which denotes the most relevant operator with positive scaling dimension in the spectrum¹⁰ of all possible boundary operators at boundary condition b , with the scaling dimension being $h_{b|b}^{(1)} = h_{a|a}^{(1)}$. At the same time, the following OPE-channel of the remaining two operators in the 4-point function appearing in Eq. (3.30) is relevant in the limit $\eta \rightarrow 1$ (compare Fig. 3.5(b)),

$$\begin{aligned} & \phi_{b|f}(w_4)\phi_{f|b}(w_1) && \text{(Fig. 3.5(b))} \\ \sim & w_{41}^{-2h_{f|b}} \left(\mathbf{1}_{b|b} + C_{b|f|b}^{(1)} w_{41}^{h_{b|b}^{(1)}} \phi_{b|b}^{(1)}(w_1) + \dots \right) \end{aligned} \quad (3.37)$$

From these two OPEs, and that $h_{b|b}^{(1)} = h_{a|a}^{(1)}$, we obtain the following behavior of the 4-point function (defined in Eq. (3.30))

$$F_{fbab}(\eta) \propto 1 + \# (1 - \eta)^{h_{a|a}^{(1)}}, \eta \rightarrow 1. \quad (3.38)$$

Using this result and Eq. (3.32) to compute the mutual information, we find

$$\begin{aligned} & \exp[-I([z_1, z_5], [z_6, z_4])] \\ \propto & \frac{1}{1 + \# (1 - \eta)^{h_{a|a}^{(1)}}} \left(\frac{\eta}{1 - \eta} \frac{1}{1 - \eta} \right)^{-h_{a|b}} \\ \approx & \frac{(1 - \eta)^{2h_{a|b}}}{1 + \# (1 - \eta)^{h_{a|a}^{(1)}}}, \end{aligned} \quad (3.39)$$

so that

$$\begin{aligned} & I([z_1, z_5], [z_6, z_4]) \\ = & -2h_{a|b} \ln(1 - \eta) + \# (1 - \eta)^{h_{a|a}^{(1)}}, \quad \eta \rightarrow 1. \end{aligned} \quad (3.40)$$

¹⁰This spectrum of operators is of course not analytically known to us in the present theory.

The leading term fits well to the data in Fig. 3.5(b); however, we cannot reliably extract $h_{a|a}^{(1)}$ from these data since here the leading term diverges in this limit while the subleading term goes to zero. Here we mention that a different way to determine the same exponent for different b.c.'s of the background circuit will yield in Eqs. (3.68),(3.69) of Sec. 3.2.4 the estimate¹¹ $h_{a|a}^{(1)} = 2.0$.

Note that in the limit where $z_5 \rightarrow z_6$, and thus $\eta \rightarrow 1$, the regions (intervals) $A = [z_1, z_5]$ and $B = [z_6, z_4]$ sit close to each other, so that $S(A \cup B) \rightarrow 0$, and the mutual information becomes twice the entanglement entropy of A (or B , which has equal entanglement entropy). Therefore, Eq. (3.40) must recover the result in Eq. (3.23). Indeed,

$$\begin{aligned}
 & \lim_{z_6 \rightarrow z_5} I([z_1, z_5], [z_6, z_4]) \\
 & \approx -2h_{a|b} \lim_{z_6 \rightarrow z_5} \ln(1 - \eta) \\
 & = -2h_{a|b} \lim_{z_6 \rightarrow z_5} \ln \frac{w_{56}w_{14}}{w_{16}w_{54}} \\
 & \approx -2h_{a|b} \ln \frac{\left(\frac{\partial w}{\partial z}\right)_{z_5} w_{14}}{w_{15}w_{54}} \\
 & \approx -2h_{a|b} \ln \xi \\
 & = 2S(A).
 \end{aligned} \tag{3.41}$$

3.2.2 Circuit with boundary conditions *afaa* - Fig. 3.2(b)

We briefly discuss the *afaa* circuit defined in Fig. 3.2(b). In this setup, we still evolve from the product state, but with physical qubits injected at the left and right sides of the circuit. The situation here is entirely similar to the circuit with boundary conditions *fffa*, discussed in the previous subsection 3.2.1, except that we have moved the corner bcc operators from z_1 and z_4 “down” to z_2 and z_3 (compare the insets of Fig. 3.6 with those of the previous Fig. 3.5).

¹¹ For the reader interested in details, we remark here on a subtlety: Our CFT could be what is called a “logarithmic CFT”[log-CFT] in which, roughly speaking, certain powerlaws are not the pure powerlaws which we display in the equations of this Chapter, but some of the same powerlaws would be in fact multiplied by a logarithm of the argument of the powerlaw. However, the presence or absence of such multiplicative logarithms is unlikely to be convincingly identifiable in numerics. For this reason we will not elaborate in this Chapter on the presence of possible logarithms, such as e.g. those described in Ref. [119]. In particular, the appearance of the scaling dimension $h_{a|a}^{(1)} = 2.0$ may be related to the situation discussed in this Reference. We plan on coming back these questions in future work.

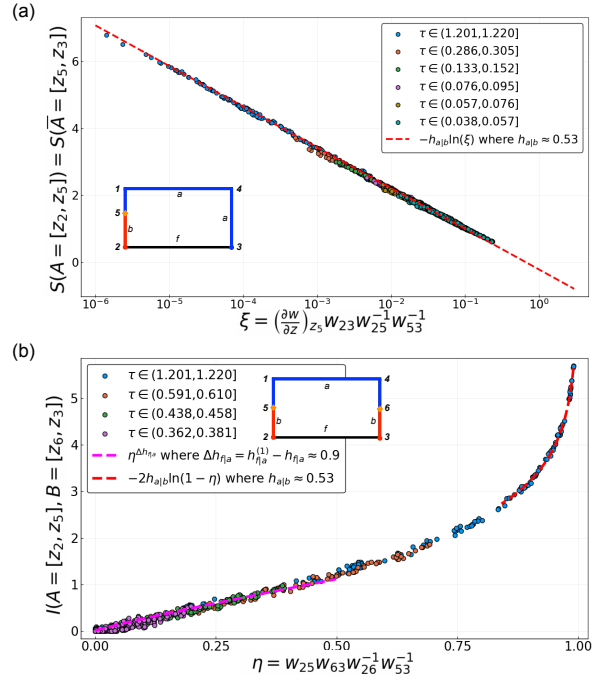


Figure 3.6: Numerical results for the *afa*a circuit. (a) Entanglement entropies, where z_5 takes different locations on either the left ($[z_2, z_1]$) or the right ($[z_4, z_3]$) side of the rectangle. The data collapse follows Eq. (3.23). (b) Mutual information for two subregions sitting next to the corners, with $z_5 \in [z_2, z_1]$ and $z_6 \in [z_4, z_3]$. The data collapse confirms Eq. (3.32). The limiting behaviors for $\eta \rightarrow 0$ and $\eta \rightarrow 1$ follow Eqs. (3.35) and (3.40), respectively.

Accordingly, we compute the entanglement entropies and mutual information for regions that begin at the lower corners of the rectangle at z_2 and/or z_3 . This amounts to modifying Eq. (3.23) to

$$S([z_2, z_5]) = -h_{a|b} \ln \left(\frac{\left(\frac{\partial w}{\partial z}\right)_{z_5} w_{23}}{w_{25} w_{53}} \right) + \text{const.}, \quad (3.42)$$

and to a different choice for the cross ratio,

$$\eta = \frac{w_{25} w_{63}}{w_{26} w_{53}}, \quad (3.43)$$

where the forms of the mutual information in Eq. (3.32), as well as its limits in Eq. (3.35) and (3.40), remain unchanged, since they are given by the same 4-point correlation functions.

The numerical results are given in Fig. 3.6, which has similar interpretations as Fig. 3.5; in

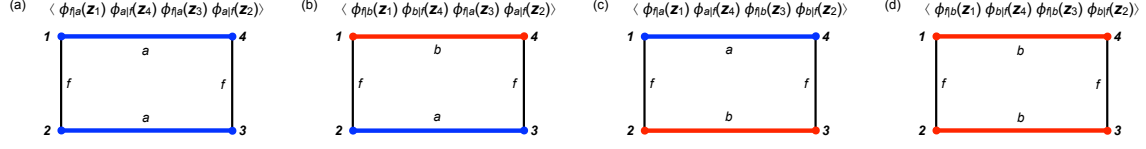


Figure 3.7: Pictorial representations of the partition functions for the *fafa* circuit, with the L -Bell pair initial state. (a) represents the background circuit, while (b) and (c) represents the partition functions relevant to computations of the entanglement entropy of $[z_1, z_4]$ and $[z_2, z_3]$, respectively. (d) corresponds to the partition function for the computation of the entanglement entropy of $[z_1, z_4] \cup [z_2, z_3]$, i.e. all the physical qubits. We notice the similarity between this figure and an illustration in Ref. [31].

particular, it gives consistent estimations of the scaling dimensions. The data for *afaa* provide further evidence for the presence of conformal invariance, and justifies our assumption about the b.c. corresponding to physical qubits at the left and right sides of the rectangle.

We also studied yet another similar circuit with b.c. *ffaa* with physical qubits only on the left side, which is again consistent with *fffa* and *afaa* (data not displayed).

3.2.3 Circuit with boundary conditions *fafa* - Fig. 3.2(c)

We consider the *fafa* circuit (see Sec. 3.1 and Fig. 3.2(c)), where the initial state consists of L Bell pairs, so that we have, as discussed above, two maximally entangled chains of qubits of length L each, and only one chain is evolved under the circuit dynamics with open boundary condition (the “system”); the other chain is left unevolved (the “environment”). We are interested in the entanglement entropy between the “system” (living on the upper boundary of the rectangle) and the “environment” (living on the lower boundary of the rectangle). We have $S([z_1, z_4]) = S([z_2, z_3])$ which arises physically from the maximal entanglement of the original Bell pairs (compare Eqs. (3.45),(3.46) below). We illustrate the boundary conditions for these computations in Fig. 3.7, following our general prescription in Sec. 3.1.

The partition function for the *fafa* circuit reads (see Fig. 3.7(a))

$$Z_{\text{circuit}} = \langle \phi_{f|a}(z_1) \phi_{a|f}(z_4) \phi_{f|a}(z_3) \phi_{a|f}(z_2) \rangle, \quad (3.44)$$

having the form of a 4-point correlation function of bcc operators at all four corners. For

Fig. 3.7(b,c), we have

$$\begin{aligned}
& \exp[-S([z_1, z_4])] \\
&= \frac{\langle \phi_{f|b}(z_1) \phi_{b|f}(z_4) \phi_{f|a}(z_3) \phi_{a|f}(z_2) \rangle}{\langle \phi_{f|a}(z_1) \phi_{a|f}(z_4) \phi_{f|a}(z_3) \phi_{a|f}(z_2) \rangle} \\
&= \frac{\langle \phi_{f|a}(z_1) \phi_{a|f}(z_4) \phi_{f|b}(z_3) \phi_{b|f}(z_2) \rangle}{\langle \phi_{f|a}(z_1) \phi_{a|f}(z_4) \phi_{f|a}(z_3) \phi_{a|f}(z_2) \rangle} \\
&= \exp[-S([z_2, z_3])], \tag{3.45}
\end{aligned}$$

where we used the exchange symmetry between a and b , as expected for a pure state, while for Fig. 3.7(d),

$$\begin{aligned}
& \exp[-S([z_1, z_4] \cup [z_2, z_3])] \\
&= \frac{\langle \phi_{f|b}(z_1) \phi_{b|f}(z_4) \phi_{f|b}(z_3) \phi_{b|f}(z_2) \rangle}{\langle \phi_{f|a}(z_1) \phi_{a|f}(z_4) \phi_{f|a}(z_3) \phi_{a|f}(z_2) \rangle} \\
&= \frac{\langle \phi_{f|a}(z_1) \phi_{a|f}(z_4) \phi_{f|a}(z_3) \phi_{a|f}(z_2) \rangle}{\langle \phi_{f|a}(z_1) \phi_{a|f}(z_4) \phi_{f|a}(z_3) \phi_{a|f}(z_2) \rangle} \\
&= 1, \tag{3.46}
\end{aligned}$$

again consistent with a pure state.

The computation in Eq. (3.45) involves a 4-point function whose explicit form we do not know. We can nevertheless examine the two limits of small and large (relative) circuit depth, $\tau \rightarrow 0$ and $\tau \rightarrow \infty$, as we discuss in the next two sections. (τ is the aspect ratio of the rectangle defined in Eq. (3.6).)

Before diving into the calculations, we notice an important point, namely the symmetry between the “system”, the upper edge $[z_1, z_4]$, and the “environment”, the lower edge $[z_2, z_3]$ of the rectangle. Viewed geometrically, the symmetry is merely a reflection. Viewed as collections of qubits, the two edges are drastically different: the “system” qubits actually experience the circuit dynamics, while the “environment” qubits are merely sitting there. The symmetry between the two edges implies that they have identical average entanglement structures. This means that if we take an arbitrary subset of qubits A of the upper edge $[z_1, z_4]$ and its counterpart B ,

i.e. the subset of the lower edge $[z_2, z_3]$ which contains precisely the qubits that are initially Bell-entangled with those in A , their entanglement entropies will have the same expectation value at all times, despite that they might be described by multi-point functions in the CFT which we do not know how to compute explicitly. In particular, this implies that at long times, when the upper and the lower edges have disentangled with each other, they will both appear “critical”. This is possible since the qubits in lower edge $[z_2, z_3]$, initially unentangled with one another, can nevertheless have nontrivial entanglement structure due to the a “entanglement swapping” mechanism induced by local measurements performed in upper edge $[z_1, z_4]$.¹² This symmetry has been checked numerically (data not displayed) and can be justified in the case of the Hartley entropy in random Haar circuits with measurements, using heuristic arguments based on its description by a “minimal cut” optimization problem in percolation [16] (see also Appendix C.4 for detailed discussions).

Bell-pair entanglement entropy at early times

The regime of a shallow depth circuit, $\tau \rightarrow 0$, is illustrated in Fig. 3.8(a). We observe that the $\tau \rightarrow 0$ limit corresponds to the $m \rightarrow 1$ limit, where m is the parameter for the conformal mapping (see Eq. (3.20) of Sec. 3.1.3). The bcc operator at corner z_1 is now very close to that at corner z_2 (and the same is the case for the bcc operators at corners z_3 and z_4), so that they can be described by the OPE of these operators, describing their “fusion”, as illustrated in Fig. 3.8(a). After mapping to the lower half complex plane (LHP), the distance between these point is precisely $w_{12} = w_{34} = m^{-1/2} - 1$, and vanishes in the limit $m \rightarrow 1$.

¹²For example, a possible such event “swaps” two inter-chain pairs for two intra-chain pairs (see Fig. 3.1).

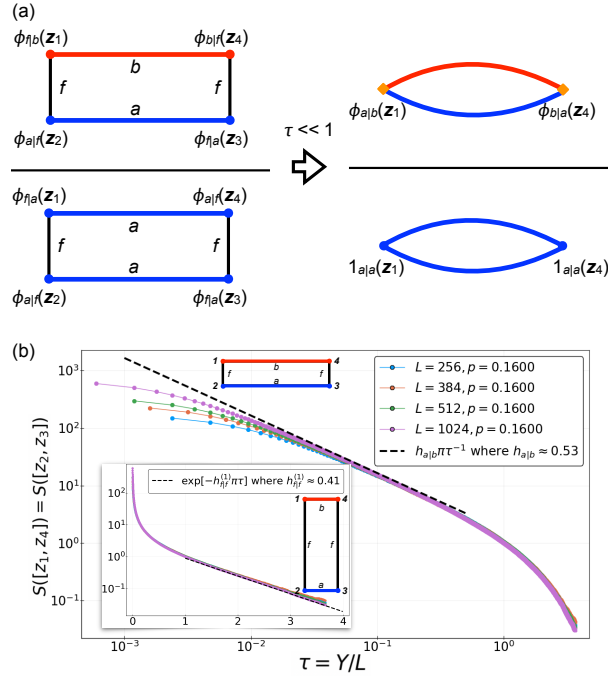


Figure 3.8: (a) Pictorial representations of the partition functions with bcc operators inserted at the corners, with the Bell-pair initial state, in the limit $\tau \rightarrow 0$. The relevant OPEs are Eq. (3.48), (3.47). (b) Numerical data for $S([z_1, z_4]) = S([z_2, z_3])$, in the limits $\tau \rightarrow 0$ (main) and $\tau \rightarrow \infty$ (inset). The data agrees well with calculations in Eq. (3.50), (3.63). We see from the data that $S([z_1, z_4])$ is smaller than the predicted value when $\tau \lesssim 10^{-2}$. We attribute this deviation to finite size effects. The entanglement entropy of the system $[z_1, z_4]$ is always bounded from above by $L \ln 2$. Thus, the formula must break down when $h_{a|b} \pi \tau^{-1} > L$, or $\tau < \tau_0(L) := h_{a|b} \pi L^{-1}$. This temporal cutoff $\tau_0(L)$ vanishes in the thermodynamic limit; this trend is confirmed in Fig. 3.8(b).

We assume the following forms of the OPE to leading order (see Table 3.1),

$$\begin{aligned} & \phi_{a|f}(w_2) \phi_{f|b}(w_1) \\ & \sim w_{12}^{-2h_{f|a} + h_{a|b}} \phi_{a|b}(w_1) + \dots \end{aligned} \quad (3.47)$$

$$\begin{aligned} & \phi_{a|f}(w_1) \phi_{f|a}(w_2) \\ & \sim w_{12}^{-2h_{f|a}} \left(\mathbf{1}_{a|a} + w_{12}^{h_{a|a}^{(1)}} C_{a|f|a}^{(1)} \phi_{a|a}^{(1)}(w_2) + \dots \right), \end{aligned} \quad (3.48)$$

Using these, we obtain Eq. (3.45) in the limit $z_1 \rightarrow z_2$, $z_3 \rightarrow z_4$ (compare Fig. 3.8(a))

$$\begin{aligned}
 & \exp[-S([z_1, z_4])] && \text{(Fig. 3.8(a))} \\
 = & \frac{\langle \phi_{a|f}(z_2) \phi_{f|b}(z_1) \phi_{b|f}(z_4) \phi_{f|a}(z_3) \rangle}{\langle \phi_{a|f}(z_2) \phi_{f|a}(z_1) \phi_{a|f}(z_4) \phi_{f|a}(z_3) \rangle} \\
 \propto & \frac{w_{12}^{-2h_{f|a}+h_{a|b}} w_{34}^{-2h_{f|a}+h_{a|b}} \langle \phi_{a|b}(w_1) \phi_{b|a}(w_4) \rangle}{w_{12}^{-2h_{f|a}} w_{34}^{-2h_{f|a}}} \\
 \propto & w_{12}^{h_{a|b}} w_{34}^{h_{a|b}} \langle \phi_{a|b}(w_1) \phi_{b|a}(w_4) \rangle \\
 \propto & (w_{12} w_{34})^{h_{a|b}} \\
 \propto & (m^{-1/2} - 1)^{2h_{a|b}}, && (3.49)
 \end{aligned}$$

where we used the fact that $w_{14} \rightarrow 2$ (a constant) in that limit. Using the asymptotic form of τ in Eq. (3.20), we obtain the asymptotic behavior $m \sim 1 - 16 \exp(-\frac{\pi}{2\tau})$ where the second term is small as $\tau \rightarrow 0$. Using this in the previous equation yields the following asymptotic behavior of the entropy in the limit $\tau \rightarrow 0$ of a shallow-depth circuit

$$\begin{aligned}
 & \exp[-S([z_1, z_4])] \\
 \propto & (m^{-1/2} - 1)^{2h_{a|b}} \\
 \propto & \exp\left[-\frac{\pi}{2\tau}\right]^{2h_{a|b}} \\
 \propto & \exp\left[-\frac{h_{a|b}\pi}{\tau}\right], && (3.50)
 \end{aligned}$$

implying

$$S([z_1, z_4]) = S([z_2, z_3]) = h_{a|b}\pi\tau^{-1}, \quad (\tau \rightarrow 0), \quad (3.51)$$

a form first obtained numerically in Ref. [21]. The fit in Fig. 3.8(b) gives $h_{a|b} \approx 0.53$, consistent with estimation of $h_{a|b}$ in the previous section.

Alternatively, the asymptotic τ^{-1} behavior of the entropy as $\tau \rightarrow 0$ can be understood in terms of the transfer matrix formalism. Here we take the *spatial* direction to be the “direction of

propagation” of the transfer matrix, and denote the generator of translations in this direction by H_{ab} . Specifically, H_{ab} denotes the Hamiltonian of the CFT in question, defined on an interval of length Y (compare Eq. (3.6)), with boundary conditions a and b at the two ends of the interval. The (finite size) spectrum of energies E_{ab} of the Hamiltonian H_{ab} is known [120] in any CFT to take on the form

$$E_{ab} = E_0 + \frac{\pi(h_{a|b}^{(j)} + n)}{Y}. \quad (3.52)$$

Here $n \geq 0$ is an integer, and $h_{a|b}^{(j)}$, where $j = 0, 1, 2, \dots$, denotes the spectrum¹³ of scaling dimensions (in increasing order) of all possible primary bcc operators that occur when the boundary condition changes from a to b . The smallest such scaling dimension corresponding the $j = 0$, we denoted previously by $h_{a|b}$, i.e. $h_{a|b} = h_{a|b}^{(j=0)}$. (The quantity E_0 cancels out in the observables of interest to us, and is not needed in the sequel.)

A special case of the above situation is the case where the two boundary conditions are the same, $a = b$. In this case the (finite size) spectrum takes the form

$$E_{a|a} = E_0 + \frac{\pi(h_{a|a}^{(j)} + n)}{Y}. \quad (3.53)$$

As before, $n \geq 0$ is an integer, and $h_{a|a}^{(j)}$, with $j = 0, 1, 2, \dots$ denotes the spectrum of scaling dimensions of all possible primary bcc operators that occur at a *given* boundary condition a . The smallest such scaling dimension corresponding the $j = 0$, is the identity operator, i.e. $\phi_{a|a}^{(j=0)} = 1$ corresponding to $h_{a|a}^{(j=0)} = 0$.

The partition function of the rectangle is written in the usual manner in terms of the transfer matrix $\exp(-H_{ab} \times L)$ and a state $|f\rangle$ representing the vertical boundary of the rectangle (compare Fig. 3.8(a)) with free boundary condition f , as the amplitude

$$Z_{ab} = \langle f | \exp(-H_{ab} \times L) | f \rangle. \quad (3.54)$$

¹³Here we choose for simplicity a notation suitable for a discrete spectrum.

Upon inserting a complete set of eigenstates, one sees that in the limit $L \gg Y$, both Z_{ab} and Z_{aa} are dominated by their respective lowest energy eigenvalues $h_{a|b}^{(j=0)} = h_{a|b}$ and $n = 0$, as well as $h_{a|a}^{(j=0)} = 0$ and $n = 0$, yielding the following asymptotic form of the ratio

$$\frac{Z_{ab}}{Z_{aa}} \sim \exp(-h_{a|b}\pi L/Y). \quad (3.55)$$

The resulting entanglement entropy thus behaves asymptotically as (recall from Eq. (3.6) that $\tau = Y/L$)

$$S([z_1, z_4]) = -\ln \frac{Z_{ab}}{Z_{aa}} \sim h_{a|b}\pi\tau^{-1}, \quad (\tau \rightarrow 0). \quad (3.56)$$

Bell-pair entanglement entropy at late times

For a very deep circuit where $\tau \rightarrow \infty$, corresponding to $w_{14} \rightarrow 0$ and $w_{23} \rightarrow 0$, we now have the cross ratio

$$\eta = \frac{w_{12}w_{34}}{w_{24}w_{13}} \rightarrow 1. \quad (3.57)$$

In this limit, to compute 4-point correlation functions defined in Eq. (3.45), we need the the vacuum channel OPE in Eq. (3.48), where we now include a subleading term,

$$\begin{aligned} & \phi_{f|a}(w_1)\phi_{a|f}(w_4) && \text{(Fig. 3.8(b))} \\ \sim & w_{14}^{-2h_{f|a}} \left(\mathbf{1}_{f|f} + C_{f|a|f}^{(1)} w_{14}^{h_{f|f}^{(1)}} \phi_{f|f}^{(1)}(w_1) + \dots \right) \end{aligned} \quad (3.58)$$

$$\begin{aligned} & \phi_{f|b}(w_1)\phi_{b|f}(w_4) \\ \sim & w_{14}^{-2h_{f|a}} \left(\mathbf{1}_{f|f} + C_{f|b|f}^{(1)} w_{14}^{h_{f|f}^{(1)}} \phi_{f|f}^{(1)}(w_1) + \dots \right) \end{aligned} \quad (3.59)$$

where $\phi_{f|f}^{(1)}(w_1)$ denotes the most relevant subleading operator that does not change this boundary condition (i.e. “which appears in the $f|f$ -channel”). Here, $C_{f|a|f}^{(1)}$ and $C_{f|b|f}^{(1)}$ denote OPE

coefficients of the corresponding BCC operators, where¹⁴ in general $C_{f|a|f}^{(1)} \neq C_{f|b|f}^{(1)}$. The same OPE in Eq. (3.58) holds for $\phi_{f|a}(z_3)\phi_{a|f}(z_2)$, that also appears in Eq. (3.45).

By using these OPEs, one can express the leading behavior of the 4-point function in Eq. (3.45) in the limit $\eta \rightarrow 1$, in terms of the limiting behavior of the following two functions

$$\begin{aligned} F_{fafa}(\eta) &= \frac{\langle \phi_{f|a}(w_3)\phi_{a|f}(w_2)\phi_{f|b}(w_1)\phi_{b|f}(w_4) \rangle}{\langle \phi_{a|f}(w_2)\phi_{f|a}(w_3) \rangle \langle \phi_{f|b}(w_1)\phi_{b|f}(w_4) \rangle} \\ &= 1 + C_{fafa}(1 - \eta)^{h_{f|f}^{(1)}}, \quad \eta \rightarrow 1. \end{aligned} \quad (3.60)$$

where $C_{fafa} = C_{f|a|f}^{(1)}C_{f|b|f}^{(1)}$, and

$$\begin{aligned} F_{fafa}(\eta) &= \frac{\langle \phi_{f|a}(w_3)\phi_{a|f}(w_2)\phi_{f|a}(w_1)\phi_{a|f}(w_4) \rangle}{\langle \phi_{a|f}(w_2)\phi_{f|a}(w_3) \rangle \langle \phi_{f|a}(w_1)\phi_{a|f}(w_4) \rangle} \\ &= 1 + C_{fafa}(1 - \eta)^{h_{f|f}^{(1)}}, \quad \eta \rightarrow 1. \end{aligned} \quad (3.61)$$

¹⁴To phrase this in a more general language, consider the case where labels A, B, \dots take values in a set specifying M different boundary conditions of type a, b, \dots , i.e. $A, B \in \{a, b, \dots\}$. Permutation symmetry of these M boundary conditions implies, under the condition listed below, the following generalized form of the OPE considered in Eq. (3.58): $\psi_{f|A}(w_1)\psi_{A|f}(w_4) \sim w_{14}^{-2h_{f|A}}\mathbf{1}_{f|f} + C_{f|f}^{(1)}w_{14}^{-2h_{f|A}+h_{f|f}^{(1)}}\psi_{f|f}^{(1);A}(w_4)$. Under permutations of the M boundary conditions, the left hand side forms a representation of the permutation group S_M of M objects which is known to decompose into a sum of the totally symmetric one-dimensional and the $(M-1)$ -dimensional irreducible representation. This decomposition is reflected on the right hand side: The set of operators on the right hand side satisfy $\sum_{A=1}^M \psi_{f|f}^{(1);A} = 0$ and transform in the $(M-1)$ -dimensional representation. In writing this OPE we have assumed that the first subleading operator beyond the identity operator is the operator $\psi_{f|f}^{(1);A}$ transforming in the $(M-1)$ irreducible representation as opposed to another (singlet) operator, besides the identity operator, which transforms in the one-dimensional (totally symmetric) representation. We note that the linear dependency condition immediately implies the following condition for the two point function $\langle \psi_{f|f}^{(1);a}\psi_{f|f}^{(1);a} \rangle + (M-1)\langle \psi_{f|f}^{(1);a}\psi_{f|f}^{(1);b} \rangle = 0$ where permutation symmetry was used. This implies that the generalizations of Eq. (3.60) and Eq. (3.61) below to M permutation symmetric boundary conditions are not equal, which is a necessary condition for obtaining a non-trivial result in the subsequent equation Eq. (3.63), which is confirmed by our numerics. At the same time, had the first subleading operator in the above OPE been the totally symmetric one-dimensional representation, the first subleading terms in Eq. (3.60) and Eq. (3.61) would be equal, in contrast to our numerical results. [Our assumption is thus confirmed by the numerics.] - We can now immediately recover the formulation presented in Eq. (3.58) upon specializing to the case of $M=2$ boundary conditions of this type, i.e. $A, B \in \{a, b\}$: In this case the linear dependency condition reads $\psi_{f|f}^{(1);a} + \psi_{f|f}^{(1);b} = 0$. Upon making the identifications $C_{f|f}^{(1)}\psi_{f|f}^{(1);a} \equiv C_{f|a|f}^{(1)}\phi_{f|f}^{(1)}$ as well as $C_{f|f}^{(1)}\psi_{f|f}^{(1);b} = (-1)C_{f|f}^{(1)}\psi_{f|f}^{(1);a} \equiv C_{f|b|f}^{(1)}\phi_{f|f}^{(1)}$, we recover Eq. (3.58) with $C_{f|b|f}^{(1)} = (-1)C_{f|a|f}^{(1)}$.

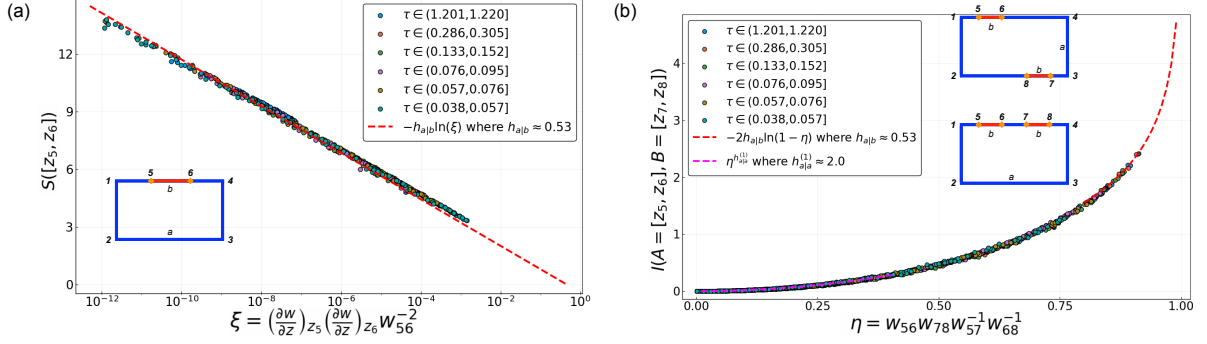


Figure 3.9: Numerical results for the *aaaa* circuit. (a) Entanglement entropy fitted to 2-point functions according to Eq. (3.65). Here we take $z_5, z_6 \in [z_1, z_4]$ for simplicity. (b) Mutual information fitted to 4-point functions according to Eq. (3.66). The two intervals are either both on the same side $[z_1, z_4]$, or on opposite sides $[z_1, z_4]$ and $[z_2, z_3]$. The limiting behaviors are given in Eqs. (3.69), (3.71).

where $C_{fafa} = C_{f|a|f}^{(1)} C_{f|a|f}^{(1)}$. Inserting the above results into Eq. (3.45), we obtain

$$\begin{aligned} \exp[-S([z_1, z_4])] &= \frac{F_{fafb}(\eta)}{F_{fafa}(\eta)} \\ &\approx 1 - (C_{fafa} - C_{fafb})(1 - \eta)^{h_{f|f}^{(1)}}, \quad 1 - \eta \rightarrow 0. \end{aligned} \quad (3.62)$$

Since $\eta = 1 - 16 \exp(-\pi\tau)$ in the limit $\tau \rightarrow \infty$ (Eq. (3.20)), we can show that

$$S([z_1, z_4]) \propto (1 - \eta)^{h_{f|f}^{(1)}} \propto \exp\left(-h_{f|f}^{(1)} \pi\tau\right). \quad (3.63)$$

From our fit in Fig. 3.8(b)(inset), we have the conformal dimension $h_{f|f}^{(1)} \approx 0.41$. We note that the exponential decay in Eq. (3.63) is understood as a consequence of crossover to a quasi-one-dimensional system as $Y \gg L$, where every correlation function falls off exponentially, with the correlation length set by L .

3.2.4 Circuit with boundary conditions *aaaa* - Fig. 3.2(d)

Entanglement entropies as 2-point functions

As mentioned in Sec. 3.1, the *aaaa* circuit has physical qubits on all four edges of the rectangle, therefore the background partition function of the circuit is defined without any

boundary condition changing operators; see Fig. 3.2(d). This is convenient since now the entanglement entropy of a contiguous subregion is given by a 2-point function, which has a simple form. (Recall that in contrast, for boundary conditions of the rectangle of type *ffa* and *fafa*, the entanglement entropies map to (more complicated) 3- or higher-point functions.) In terms of the conformal mapping, the entanglement entropy of an interval $[z_5, z_6]$ reads for the present boundary conditions

$$\begin{aligned}
 & \exp[-S([z_5, z_6])] && \text{(Fig. 3.9(a))} \\
 = & \left(\frac{\partial w}{\partial z}\right)_{z_5}^{h_{a|b}} \left(\frac{\partial w}{\partial z}\right)_{z_6}^{h_{a|b}} \langle \phi_{a|b}(w_5) \phi_{b|a}(w_6) \rangle \\
 \propto & \left[\frac{\left(\frac{\partial w}{\partial z}\right)_{z_5} \left(\frac{\partial w}{\partial z}\right)_{z_6}}{(w_{56})^2} \right]^{h_{a|b}}, && (3.64)
 \end{aligned}$$

hence

$$S([z_5, z_6]) = -h_{a|b} \ln \left[\frac{\left(\frac{\partial w}{\partial y}\right)_{z_5} \left(\frac{\partial w}{\partial y}\right)_{z_6}}{(w_{12})^2} \right] + \text{const.} \quad (3.65)$$

The computed entanglement entropy and fit to the 2-point function is shown in Fig. 3.9, where we took $h_{a|b} = 0.53$.

Mutual information as 4-point functions

We compute the mutual information of two subregions to further confirm the conformal symmetry. We take the two subregions to be the intervals $A = [z_5, z_6]$ and $B = [z_7, z_8]$ which sit at various positions, either both on the upper edge, or with one on the upper edge and the other on the lower edge of the rectangle, as shown in the insets of Fig. 3.9(b). The mutual information is expressed in terms of the 4-point correlation function of the same bcc operators

as

$$\begin{aligned}
 & \exp[-I([z_5, z_6], [z_7, z_8])] && \text{(Fig. 3.9(b))} \\
 = & \frac{\langle \phi_{a|b}(z_5) \phi_{b|a}(z_6) \rangle \langle \phi_{a|b}(z_7) \phi_{b|a}(z_8) \rangle}{\langle \phi_{a|b}(z_5) \phi_{b|a}(z_6) \phi_{a|b}(z_7) \phi_{b|a}(z_8) \rangle} \\
 = & \frac{\langle \phi_{a|b}(w_5) \phi_{b|a}(w_6) \rangle \langle \phi_{a|b}(w_7) \phi_{b|a}(w_8) \rangle}{\langle \phi_{a|b}(w_5) \phi_{b|a}(w_6) \phi_{a|b}(w_7) \phi_{b|a}(w_8) \rangle} \\
 \equiv & \frac{1}{F_{abab}(\eta)} && (3.66)
 \end{aligned}$$

where we used the crossratio

$$\eta \equiv \frac{w_{56} w_{78}}{w_{57} w_{68}}. \quad (3.67)$$

The numerical results are shown in Fig. 3.9(b), where we find $I([z_5, z_6], [z_7, z_8])$ collapses well to a function only of η .

The limiting behaviors in $\eta \rightarrow 0$ and $\eta \rightarrow 1$ can be similarly obtained by considering the appropriate OPE, namely Eq. (3.36), in a fashion parallel to Sec. 3.2.1.

- Limit $z_5 \rightarrow z_6$, $z_7 \rightarrow z_8$, in which $\eta \rightarrow 0$. Using twice the OPE in Eq. (3.36) (once for $z_5 \rightarrow z_6$ and once for $z_7 \rightarrow z_8$), leads to the following form

$$F_{abab}(\eta \rightarrow 0) = 1 + \# \eta^{h_{a|a}^{(1)}}, \quad (3.68)$$

and therefore we obtain, upon making use of Eq. (3.66),

$$I([z_5, z_6], [z_7, z_8]) \propto \eta^{h_{a|a}^{(1)}}, \eta \rightarrow 0, \quad (3.69)$$

where we extract¹⁵ $h_{a|a}^{(1)} \approx 2.0$ from the plot in Fig. 3.9(b), consistent with Ref. [59].¹⁶

¹⁵Comments regarding features of logarithmic CFTs [Log-CFT], analogous to those made in footnote 11 of Sec. 3.2.1, could be made here. Again, because of the inability to determine the presence of absence of corresponding logarithms multiplying powerlaws we do not elaborate here on these possible features.

¹⁶The same numerical value for this exponent was found in the mutual information for the Hartley entropy

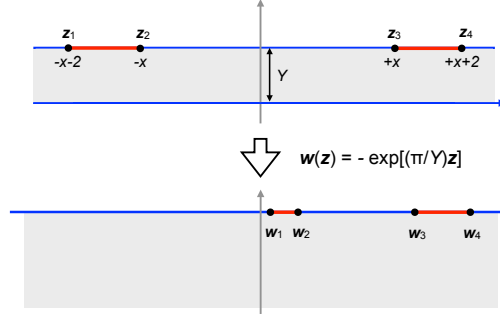


Figure 3.10: The conformal mapping from the infinite strip with finite width Y to the LHP, allowing calculation of entanglement entropies and mutual information for finite segments. The infinite strip is obtained by taking the thermodynamic limit ($L \rightarrow \infty$) of the $aaaa$ circuit.

- Limit $z_6 \rightarrow z_7$, $z_5 \rightarrow z_8$, in which $\eta \rightarrow 1$. Using again the relevant OPE Eq. (3.36), we obtain

$$\begin{aligned} & \exp[-I([z_5, z_6], [z_7, z_8])] \\ & \propto \frac{\left(\frac{1-\eta}{\eta}\right)^{2h_{a|b}}}{1 + \# \left(\frac{1-\eta}{\eta}\right)^{h_{a|a}^{(1)}}}, \end{aligned} \quad (3.70)$$

thus

$$\begin{aligned} & I([z_5, z_6], [z_7, z_8]) \\ & \approx -2h_{a|b} \ln(1-\eta) + \# (1-\eta)^{h_{a|a}^{(1)}}, \quad \eta \rightarrow 1 \end{aligned} \quad (3.71)$$

which has the same form as that in Eq. (3.40) and the leading behavior $\ln(1-\eta)$ dependence is verified in Fig. 3.9(b).

Entanglement dynamics and the absence of entanglement lightcone

As in Sec. 3.2.1, based on the consistency between the numerics and CFT calculations, we try to obtain an analytic understanding of the entanglement dynamics for $aaaa$ using the

for circuits with Haar unitaries obtained in Ref. [16]. The same comments concerning logarithms multiplying powerlaws, as in the previous footnote, can be made here.

conformal mapping. The simplicity of this boundary condition allows us to compute the entanglement entropy in an infinitely large system by first taking $L \rightarrow \infty$, where the corners are now unimportant. (Note that, in contrast, for rectangles with boundary conditions $fffa$ the corners are always important because of the bcc operators present.)

In Fig. 3.10 we show a infinite-length system ($L = \infty$) with finite $Y \propto T$, i.e. an infinite strip. The conformal mapping from the infinite strip to the LHP takes the form

$$w(z) = -\exp\left[\frac{\pi}{Y}z\right], \quad (3.72)$$

where the upper and lower edge of the strip map to the positive and negative real axis, respectively. Using this map, the entanglement entropy of a finite interval $A = [z_1, z_2]$ now can be easily computed,

$$\begin{aligned} S([z_1, z_2]) &= -h_{a|b} \ln \left[\frac{\left(\frac{\pi}{Y}\right)^2}{\cosh\left(\frac{\pi}{Y}z_{12}\right) - 1} \right] + \text{const.} \\ &\approx \begin{cases} 2h_{a|b} \ln Y + \frac{h_{a|b}\pi}{Y}z_{12}, & Y \propto T \ll z_{12} \\ 2h_{a|b} \ln z_{12}, & Y \propto T \gg z_{12} \end{cases} \end{aligned} \quad (3.73)$$

Interestingly, at early times we see a $\ln Y$ growth in addition to the volume law of the entropy (due to the maximal entanglement in the initial state) which “purifies” as $\frac{z_{12}}{Y}$ in a similar fashion as Eq. (3.50), while at late times the entanglement entropy crosses over to the familiar logarithmic form. Notice that $2h_{a|b}$ has the meaning of the “coefficient of the log”, found to be approximately $2h_{a|b} \approx 1.6 \ln 2$ in Refs. [59, 21]. It is immediate from the computation that for two intervals $[z_1, z_2]$ and $[z_3, z_4]$ which sit next to each, i.e. where $z_2 = z_3$, their mutual

information dynamics becomes

$$\begin{aligned}
 & I([z_1, z_2], [z_2, z_3]) \\
 & \approx \begin{cases} 2h_{a|b} \ln Y, & Y \propto T \ll z_{12}, z_{23} \\ 2h_{a|b} \ln \left(\frac{z_{12}z_{23}}{z_{13}} \right), & Y \propto T \gg z_{12}, z_{23} \end{cases} \quad (3.74)
 \end{aligned}$$

where the early time dynamics is reminiscent of the $\ln Y$ growth of bipartite mutual information in Ref. [21].

The dynamics of mutual information of two distant regions is more interesting in that the two regions can share non-zero mutual information with infinite speed. Consider again the setup in Fig. 3.10, where we take two finite intervals (both of size 2 in this case), separated by a distance $r = 2x$, in an *infinite* system after a circuit evolution of finitely many layers, where the qubits are at the $y = Y$ boundary. The mutual information between these two intervals follows Eq. (3.69) in the limit $\eta \rightarrow 0$, that is

$$I(\eta) \sim \eta^{h_{a|a}^{(1)}}, \text{ where } \eta = \frac{w_{12}w_{34}}{w_{13}w_{24}} = \frac{\sinh^2(\frac{\pi}{Y})}{\sinh^2[\frac{\pi}{Y}(1+x)]}. \quad (3.75)$$

It is obvious that $I(\eta)$ is nonzero for arbitrarily small but finite values of Y/x , indicating an infinite entangling speed, in contrast to a finite light speed in a local unitary circuit model, i.e. one in which random projective measurements are *absent*. More generally, it can be shown that there do not exist finite constants B, C, v such that [111]

$$I(\eta) \leq B \exp[-C(x - vT)], \text{ for all } x \text{ and } T. \quad (3.76)$$

In particular, this inequality is violated by Eq. (3.75) in the regime $x \gg vT \gg 1$.

The infinite entanglement speed is a direct consequence of conformal invariance, where time is identified as the vertical spatial dimension. Intuitively, the long-range correlations at

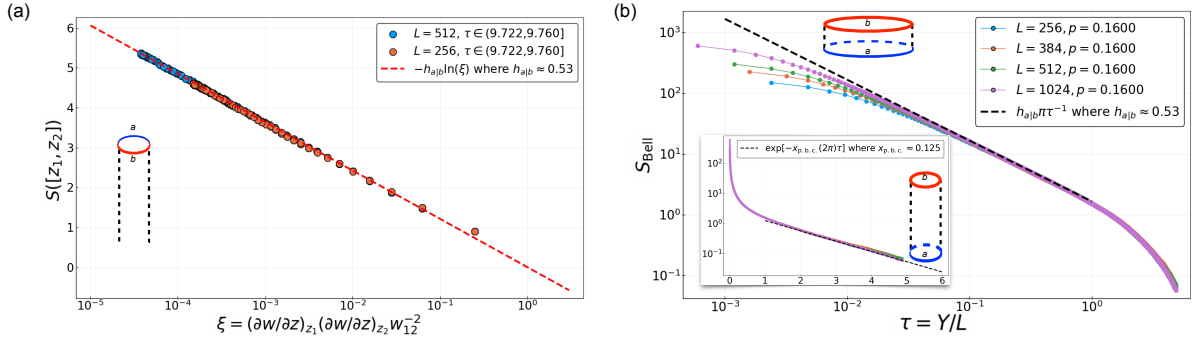


Figure 3.11: (a) Starting from a product initial state with periodic spatial b.c., the entanglement entropy in the steady state $\tau \rightarrow \infty$ is mapped to a 2-point function. (b) Starting from a Bell-pair initial state with periodic spatial b.c., the entanglement entropy of either the upper and lower edge is predicted to also have the form $S_{\text{Bell}} = h_{a|b} \pi \tau^{-1}$ in the $\tau \rightarrow 0$ limit, as in Eq. (3.81). In the limit $\tau \rightarrow \infty$, we fit to $S_{\text{Bell}} = \exp(-x_{\text{p.b.c.}}(2\pi)\tau)$ with $x_{\text{p.b.c.}} \approx 0.125$, as in Eq. (3.84).

the critical point are present for an arbitrarily narrow strip $Y \ll L$, or equivalently, for an arbitrarily shallow circuit. Physically, this is possible since we have introduced local, unitarity-breaking measurements, leading to an “entanglement swapping” mechanism (see Fig. 3.1) that survives in a random many-body system.¹⁷

3.3 Periodic boundary condition

3.3.1 Numerical results

In this section we consider circuits with periodic spatial b.c., which therefore have cylindrical geometry. This is not quite as simple as a rectangle, since a finite cylinder is topologically distinct from the LHP, and a conformal mapping to the latter is not available. Therefore, the dynamics of entanglement and mutual information is in general more difficult to discuss as compared to a circuit of rectangular geometry. However, several simplifications occur in suitable limits to be discussed below.

¹⁷We note in passing that in Clifford circuits, the growth of the stabilizers is necessarily non-local and there must be no lightcone at the critical point, in any gauge, as required by the long-range mutual information; therefore, a hydrodynamic description with local rules of stabilizer growth cannot be accurate. Natural extension can be made away from critical point: with a finite correlation length ξ , there will be a maximal velocity as ξ/λ_t , where λ_t is the temporal lattice spacing; this velocity diverges as we approach the critical point (compare discussion in Sec. 3.4.4).

One simplification occurs in the “late time limit”, where the depth of the circuit is much larger than the number of qubits, $Y \propto T \gg L$, which is when the qubit chain is already in its steady state. This limit can be described by a semi-infinite cylindrical circuit, which in turn can then be mapped to the LHP via the following conformal map,

$$z \mapsto w(z) = \tan(\pi z/L). \quad (3.77)$$

This leads to the following form of the entanglement entropy in the steady state,

$$\begin{aligned} S([z_1, z_2]) & \quad (\text{Fig. 3.11(a)}) \\ = -h_{a|b} \ln \left[\frac{\left(\frac{\partial w}{\partial z}\right)_{z_1} \left(\frac{\partial w}{\partial z}\right)_{z_2}}{(w_{12})^2} \right] + \text{const.}, \end{aligned} \quad (3.78)$$

and the collapse of $S([z_1, z_2])$ against $\xi = \frac{\left(\frac{\partial w}{\partial z}\right)_{z_1} \left(\frac{\partial w}{\partial z}\right)_{z_2}}{(w_{12})^2}$ is shown in Fig. 3.11(a), where we again find $h_{a|b} = 0.53$.

In the steady state it is also possible to compute the mutual information of two non-overlapping intervals, where the OPE in Eq. (3.36) is now relevant, and the limiting behavior of $I(\eta)$ end up being the same as that in Eqs. (3.69) and (3.71). We again find the same values of the critical exponents $h_{a|a}^{(1)} = 2.0$ and $h_{a|b} = 0.53$ (data not shown) that were found in Sec. 3.2.4. The value for both exponents are consistent with that found in Ref. [59].

Another simplification occurs in the limits $Y \ll L$ and $Y \gg L$ for the Bell entanglement entropy for the L Bell pair initial state. This is analogous to corresponding limit of the rectangular circuit with *fafa* b.c.’s, discussed in Sec. 3.2.3 above, except that the qubit chains now have periodic b.c.’s:

1. We first consider $Y \ll L$, in parallel to Sec. 3.2.3. Using the transfer matrix formalism by treating the spatial direction as the “direction of propagation” of the transfer matrix, the partition function for this setup is given by

$$Z_{ab} = \text{Tr} \exp(-H_{ab} \times L), \quad (3.79)$$

where the trace accounts for the periodic b.c., and H_{ab} is the same Hamiltonian as that in Eq. (3.52) (compare the two insets of Fig. 3.11(b)). As $L \gg Y$, Z_{ab} is again given by the ground state energy of H_{ab} . A similar reasoning applies to Z_{aa} . Combining these results, we obtain

$$\exp[-S_{\text{Bell}}] = \frac{Z_{ab}}{Z_{aa}} \sim \exp(-h_{a|b}\pi L/Y), \quad (3.80)$$

thus (recall from Eq. (3.6) that $\tau = Y/L$)

$$S_{\text{Bell}} \sim h_{a|b}\pi\tau^{-1}, \quad (3.81)$$

which is the same result as that in Eq. (3.50).

2. As $Y \gg L$, we take the temporal direction as the “direction of propagation” of the transfer matrix, with initial and final states now denoted by $|a\rangle$ and $|b\rangle$. We have

$$\begin{aligned} Z_{ab} &= \langle a | \exp(-H_{\text{p.b.c.}} \times Y) | b \rangle \\ &= e^{-\epsilon_0 Y} \left[\langle a|0\rangle \langle 0|b\rangle + \langle a|1\rangle \langle 1|b\rangle e^{-(\epsilon_1 - \epsilon_0)Y} + \dots \right] \end{aligned} \quad (3.82)$$

and similarly

$$\begin{aligned} Z_{aa} &= \langle a | \exp(-H_{\text{p.b.c.}} \times Y) | a \rangle \\ &= e^{-\epsilon_0 Y} \left[\langle a|0\rangle \langle 0|a\rangle + \langle a|1\rangle \langle 1|a\rangle e^{-(\epsilon_1 - \epsilon_0)Y} + \dots \right] \end{aligned} \quad (3.83)$$

where $H_{\text{p.b.c.}}$ is the Hamiltonian of the underlying CFT with *periodic* b.c.'s., whose excita-

tions energies are known to be related to scaling dimensions of the *bulk* CFT. Specifically, we have denote by ϵ_0 and ϵ_1 the energies of the lowest and first excited states $|0\rangle$ and $|1\rangle$ of $H_{\text{p.b.c.}}$ which have non-vanishing overlap with both, the final and initial states. Due to conformal symmetry, the so-defined excitation energy has the form $\epsilon_1 - \epsilon_0 \equiv 2\pi x_{\text{p.b.c.}}/L$, where $x_{\text{p.b.c.}}$ is a critical exponent of the bulk CFT.¹⁸ Therefore we have

$$S_{\text{Bell}} = \exp(-x_{\text{p.b.c.}} (2\pi) \tau), \quad (3.84)$$

where $x_{\text{p.b.c.}}$ is a scaling dimension in the *bulk* Clifford CFT (i.e. a universal quantity), and which in general will not coincide with *boundary* scaling dimension $h_{f|f}^{(1)}$ (discussed, e.g., in Fig. 3.8(b)).

The results of the numerical computation of S_{Bell} are shown in Fig. 3.11(b), where we find $h_{a|b} \approx 0.53$ and $x_{\text{p.b.c.}} \approx 0.125$.

3.3.2 Determination of p_c and Y/T

Due to the simplicity of the periodic b.c. at late times, namely the absence of corner operators and therefore the simple form of Eq. (3.78), we use this setup for determining p_c . Specifically, we choose p_c such that the plot in Fig. 3.11(a) fits best to a straight line; this gives us $p_c = 0.1600 \pm 0.0003$, as well as $h_{a|b} \approx 0.53$. We further define Y/T (where $\tau = Y/L = (Y/T)(T/L)$) such that Fig. 3.11(b) fits best to $S_{\text{Bell}} \approx h_{a|b}\pi\tau^{-1}$ at small τ . This gives us $Y/T \approx 0.61$.

p_c and Y/T are the only tuning parameters in our fitting scheme. Once they are obtained from Fig. 3.11, they are fixed for all random Clifford circuits in this Chapter, for which we have found good data collapse. This confirms our anticipation that Y/T and p_c are b.c.-independent properties of the bulk.

¹⁸Here $x_{\text{p.b.c.}} = h + \bar{h} = 2h$ where $h = \bar{h}$ due to translational invariance of the initial and final states. h is the scaling dimension (conformal weight) of a primary field in the *bulk* CFT.

3.4 Discussion and outlook

3.4.1 Summary

In this Chapter we presented extensive numerical evidence supporting the presence of conformal symmetry at the measurement-driven entanglement transition in the random Clifford quantum circuit, via identifying entanglement entropies of the circuit with boundary free energies of the conformal field theory in the bulk of the circuit in response to changes of boundary condition. With this identification, the critical dynamics of entanglement and mutual information can be understood from analytic computations of correlations of boundary condition changing (bcc) operators whose functional form is highly constrained by conformal symmetry, and we verify explicitly the specific constraint forms of these correlations in our numerics. Moreover, by fitting numerical results for such correlation function to their functional form predicted by conformal symmetry, we are able to extract numerical values for scaling dimensions of several bcc operators for the circuit with *several* sets of *different* boundary conditions, and find a remarkable agreement. These results constitute a consistent characterization of the Clifford CFT underlying the circuit at criticality.

Crucial to our analysis is the interpretation of the temporal direction of the circuit as the vertical spatial dimension of the CFT, which then allows a conformal mapping among circuits of different aspect ratios of the (space-time) rectangle, relating dynamics at different time scales. This interpretation of “time” was implicit, or has been anticipated in previous works on the entanglement transition [16, 17, 59, 21, 31, 30].

Conformal symmetry combined with the standard Schwarz-Christoffel conformal map gives analytical control over various finite-size scaling behaviors in the rectangular geometry of the critical circuit. The circuit depth T corresponds to the size of the “Euclidean time” coordinate and thus T or the spatial size L sets the correlation length in the quasi-one-dimensional geometry of a narrow strip when $\tau \ll 1$, or $\tau \gg 1$, respectively, with $\tau \propto T/L$. This naturally explains the logarithmic growth of the entanglement entropy from an initial product state, as well as the

purification dynamics of mixed state [21] ($h_{a|b}\pi\tau^{-1}$ at small τ , and $e^{-h_{\text{eff}}^{(1)}\pi\tau}$ at large τ). Other interesting scaling behaviors discussed in this Chapter can be understood in a similar fashion: they follow directly from conformal invariance.

An immediate consequence of the “imaginary time” and criticality is the absence of a light-cone in the dynamics of the entanglement structure of the circuit, as highlighted by the infinite speed at which two distant finite regions develop nonzero mutual information (whereas the entire system is in the thermodynamic limit). This is only possible in the presence of measurements that break unitarity of the time evolution, via a mechanism similar to entanglement swapping. It is interesting to notice that while measurements reduce entanglement entropy on average, they sometimes “trade” short-range entanglement for long-range entanglement, which then helps stabilizing the volume-law phase. This provides a view of the volume-law phase complementary to the quantum error correction argument in Ref. [20].

Although we have established our results exclusively for the Clifford circuit, our approach builds upon general principles such as conformal invariance and reasonable assumptions about the boundary conditions, without assuming detailed knowledge of the universality class. Therefore, most of these conclusions will thus clearly immediately generalize to entanglement dynamics in other hybrid unitary-measurement circuits for all the Rényi entropies, including the $n \geq 1$ Rényi entropies of Haar circuits [30], as well the $n = 0$ (Hartley) Rényi entropy in the same circuits [16] (see also Appendix C.4).

3.4.2 Restatement of the central assumptions

In this subsection we restate the central assumptions underlying our work and the underlying logic, which are as follows:

- (i) We assume there is an emergent CFT describing the two-dimensional space-time in the bulk of the circuit at the entanglement transition. We provide extensive numerical verification of this assumption in this Chapter.
- (ii) Furthermore, we assume that various boundary conditions on the circuit described at

microscopic scales in terms of specific configurations of qubits at the boundary, are described at the transition by conformally invariant boundary conditions (as long as the former does not possess non-local entanglement). This is a general feature of CFT, and emerges ultimately from thinking of such boundary conditions in a Renormalization Group picture.

- (iii) Subsequently, we assume that entanglement properties (such as Rényi entropies) of the critical circuit are described by imposition of different boundary conditions which, by item (ii) above, can be viewed as conformal boundary conditions. Note that the connection between entanglement entropies and imposition of different boundary conditions (for bipartite entanglement properties, different in boundary region A , as opposed to at its complement) originates from Ref. [85] and its sequel [30], and does not really require an assumption. Indeed, by repeating the steps presented in Ref. [30], but now for the reduced density matrix for the *Clifford* circuit, one directly obtains the central relation Eq. (3.2) between entanglement entropies and the ratio of two partition functions of the circuit, one where different (numerator) and one where the same (denominator) boundary conditions are imposed on the circuit in region A and its complement. Physically, as first stressed in this context in Ref. [85], the (negative) logarithm of such a ratio of partition functions corresponds to a difference of boundary free energies. In other words, entanglement entropies of the circuit are described by (differences of) boundary free energies.
- (iv) Then, at each point on the boundary where *different* conformal boundary conditions meet (for the bipartite situation the endpoints of region A), a conformal boundary condition changing (bcc) operator appears. The leading (lowest scaling dimension) operator appearing at a boundary change is primary in standard CFT, and we make the (probably weak) assumption that this is also the case in the (complicated) CFT describing the circuit. (This assumption is verified numerically in the work presented here.)
- (v) Finally, we make important assumptions central to our work about the nature of boundary

conditions which we denote by f, a, b , and which are defined (in Sec. 3.1.1) at the microscopic (lattice) scale in terms of specific properties of qubits and their physical properties. The central objects of our work are then bcc operators changing between different such qubit-based boundary conditions, such as e.g. $\phi_{f|a}$ or $\phi_{a|b}$, and the entanglement properties described by correlation functions of several such bcc operators, as detailed in the main text for many different situations of physical interest. Assumptions about the nature of these microscopically defined boundary conditions, whose validity we confirm through numerics, are necessary for the *Clifford* circuits since, in contrast to *random Haar* circuits, there is no explicit Statistical Mechanics model available for the former in terms of which an explicit microscopic formulation of these boundary conditions can be formulated.

3.4.3 Universality class of the transition and relationship with critical 2D percolation

The universality class of the transition is an interesting question. For the measurement-induced transition in Haar random circuits with (finite) on-site Hilbert space dimension q , all n th Rényi entropies with $n \geq 1$ are described by a known statistical mechanics model [31, 30] in the bulk of the circuit (the Rényi entropies with different $n \geq 1$ being described by different boundary observables on the same bulk which therefore become critical at the same value of the tuning parameter, the space-time density of measurements p). On the other hand, the 0th Rényi (Hartley) entropy is described by a different statistical mechanics model which becomes critical at a different (higher) value of the density of measurements.

This statistical mechanics model describing all n th Rényi entropies with $n \geq 1$ turns out [31, 30] to be exactly solvable in the limit of infinite onsite Hilbert space dimension $q \rightarrow \infty$, possessing a critical point in the universality class of two-dimensional percolation. This limit provides a starting point for a systematic access to the so-far not analytically understood generic transition at finite q , which is the infrared limit of a renormalization group flow out of percolation by a single relevant perturbation which emerges because [85, 30] a finite onsite Hilbert

Operator scaling dimension	A) Clifford CFT	B) S_0 in Haar (percolation)	C) $S_{n \geq 1}$ in Haar as $q \rightarrow \infty$ (percolation)
$h_{a b}$ ^a	$0.76 \ln(2) \approx 0.53$	$\frac{\sqrt{3}}{2\pi} \ln(2) \approx 0.191$ [121, 16]	$\frac{1}{6} \approx 0.167$ [30]
$h_{f a}^{(1)} - h_{f a}$	0.9	0.8	-
$h_{ff}^{(1)}$ ^b	0.41	$\frac{1}{3} \approx 0.333$	$\frac{1}{3} \approx 0.333$
$h_{a a}^{(1)}$	2.0^c	2 ^c [16]	-
$x_{\text{p.b.c.}}$ ^d	0.125	$\frac{5}{48} \approx 0.104$ [122]	$\frac{5}{48} \approx 0.104$

Table 3.2: A comparison of operator scaling dimensions between the Clifford CFT and critical percolation. Results of A) was already summarized in Table 3.1, and reproduced here for comparison. B) refers to the first-passage percolation description of Hartley entropy (S_0) in random Haar circuits [16] (where the numerical results are obtained in Appendix C.4), and C) refers to the percolation description of $S_{n \geq 1}$ derived in the limit of infinite on-site Hilbert space dimension (q) in random Haar circuits [30].

^aWe adopt the same convention for all three cases, namely always taking the natural logarithm (\ln) in defining the entropy, as specified in Eq. (3.21). The $\ln(2)$ factors for A) and B) come from the fact that “qubits” (with local Hilbert space dimension $q = 2$) are used for constructing the circuits, both in this Chapter and in Ref. [16].

^bIn general, this quantity is the lowest dimension boundary operator at the f boundary condition (see Eq. (3.53) in Sec. 3.2.3), also denoted by $\eta_{||}/2$ in Ref. [113]. In 2D percolation the f boundary condition is the *free* boundary condition of the spins of the Q -state Potts model whose $Q \rightarrow 1$ limit describes percolation. Here, the lowest dimension boundary operator at that *free* boundary condition is the boundary spin operator, known to have scaling dimension $\frac{1}{3}$.

^cThe appearance of the scaling dimension 2 here might possibly be related to logarithmic features of the underlying CFT [119].

^dThe scaling dimension $x_{\text{p.b.c.}}$ of the *bulk* operator was defined in Eq. (3.83) of Sec. 3.3.1. In 2D critical percolation, it corresponds to the known scaling dimension $\frac{5}{48}$ of the *bulk* spin operator.

space dimension q turns out to (explicitly) break a symmetry that is present when $q = \infty$. On the other hand, the 0th Rényi (Hartley) entropy for any onsite Hilbert space dimension q is described [16] by “minimal cut paths” in two-dimensional percolation (argued to be described by “first passage percolation”).

Clifford circuits have only been accessible numerically, but can be studied for very large system sizes. Recently in Ref. [113], several operator dimensions in Clifford CFT were found to have numerical values close to their counterparts in percolation, while recognizing some do not. In a particular setup, one scaling dimension was extracted by looking at the early-time purification dynamics of a single “reference qubit”, and further identified with the lowest scaling dimension of the boundary spin operator at a *free* boundary in critical percolation, $\frac{\eta_{\parallel}}{2} = \frac{1}{3}$. We revisit this setup in Appendix C.2, where we denote this scaling dimension by $h_{f|f}^{(1)}$ (defined in Table 3.1 and in Sec. 3.2.3) whose value appears to be distinct from $\frac{\eta_{\parallel}}{2} = \frac{1}{3}$. A more thorough comparison between Clifford CFT and critical percolation is summarized in Table 3.2, which further highlights their differences. It might perhaps be conceivable that the appearance of scaling dimensions observed in Refs. [113, 123] with values close to percolation, could be due to a possible proximity of a percolation fixed point in a generalized phase diagram.

3.4.4 Outlook

Extensions within the current framework

Besides going to even larger systems as mentioned above, it would be interesting to also extend the current fitting algorithm off the critical point, and to extract critical exponents such as ν and β [113, 123].

It is satisfying that the trivial product state and the L -Bell pair state map to conformal boundary conditions in the CFT formalism. Exploring other quantum states (such as a maximally entangled Page state [124], which has non-local entanglement) and attempting to fit them into the current framework would be an interesting direction.

Implications of non-unitary dynamics

The emergence of conformal symmetry in hybrid circuits is perhaps in itself not surprising given previous numerical work on Clifford circuits [17, 59] as well as analytical results on Haar circuits [16, 31, 30]. What is surprising is the way the time dimension fits in the CFT picture, and the consequences that emerge from the fact that the real time coordinate ends up acting as imaginary time. Therefore, this type of hybrid dynamics is in a class distinct from ordinary unitary dynamics.

Although we have established the imaginary time using conformal invariance that is only present at the critical point, one can generate a finite (bulk) correlation length by detuning from the critical point (by letting $p \neq p_c$). Certainly, as long as one remains within the scaling limit where the correlation length is much larger than the microscopic lattice scale, the physics is expected to be the standard deformation to a theory with exponentially decaying correlations. Therefore, one also expects that real time to still act as imaginary time. This can be seen explicitly in the 2D statistical mechanics lattice model describing Haar unitary circuits with measurements [30].¹⁹ However, since all correlations fall off exponentially away from the critical point [16, 59], it is only on length scales short compared the correlation length that the measurement-induced quantum non-locality and violations of the Lieb-Robinson bound will be manifest.

Going beyond the current model, it is possible that imaginary time is a general consequence of non-unitarity, and might not be restricted to this family of unitary-measurement circuits (see e.g. Ref. [125]). It will be interesting if concrete examples of criticality in unitarity-breaking dynamics can be found to confirm this expectation, possibly identifying other universality classes.

¹⁹Detuning from criticality only affects the local Boltzmann weights, and thus does not change the fact that physical (real) time acts as one of two spatial coordinates of the lattice on which the 2D statistical mechanics model is defined.

Experimental relevance

As addressed in Refs. [59, 31, 113], the experimental cost of directly accessing the entanglement transition grows exponentially in the product of system size and circuit depth, since one has to post-select on all the measurement outcomes (which are intrinsically probabilistic, following Born’s rule) to produce multiple copies of any wavefunction in order to measure the entanglement entropy (see also footnote 1), or to estimate variances of correlation functions [59]. Our findings in this Chapter suggest that the critical behavior is already present at early stages of the circuit evolution, and one does not have to evolve the circuit all the way to saturation to measure the entanglement entropy; an early time measurement would suffice. In principle, it can slightly alleviate the experimental challenge. Yet we have not been able to identify a general experimental protocol that allows efficient access to the transition.

In the special case of Clifford circuits, the quantum state is a “stabilizer error-correcting code” at all times [67], for which the two possible post-measurement states resulting from a Pauli measurement are related to one another via a single Pauli string operator, that can be efficiently computed given the knowledge of the stabilizer representation of the state [68]. Thus, one can fix a choice of all the unitary gates \mathcal{U} and measurement placements \mathcal{X} in the circuit, as well as all the measurement outcomes \mathcal{M} , and replicate the stabilizer code state resulting from the hybrid circuit evolution $(\mathcal{U}, \mathcal{X}, \mathcal{M})$, by simulating the $(\mathcal{U}, \mathcal{X})$ circuit while “correcting” the “errors” – measurement outcomes that differ from their counterparts in \mathcal{M} – with the application of one “error correcting” Pauli string operator (mentioned above) immediately after each error occurs. This replication algorithm runs in polynomial time; therefore, entanglement entropies can be efficiently measured, at the cost of keeping track of the time evolution of all the stabilizers (a polynomial-time and polynomial-space overhead).

On the other hand, purity of “reference qubits” [113], as well as the quantum Fisher information [20], might enable indirect access to the transition in polynomial time on near-term quantum computing platforms [12, 13, 14].

Chapter 4

Capillary wave theory of dynamically generated quantum error correcting codes in the volume law phase

Quantum error correcting codes (QECC) [126, 127] are important constructions of quantum states that can be used for protecting information from decoherence and other types of errors. A QECC encodes quantum information nonlocally, so that sufficiently local errors are detectable and reversible, allowing for explicit protocols to counter the errors [128, 129]. Besides concrete constructions of QECCs with an intended use for quantum computation [130, 131, 128, 44, 132, 45], they can also occur naturally in physical contexts, e.g. in many-body quantum systems as a consequence of topological orders [133, 102], or in quantum gravity as a consequence of the holographic principle [134].

Recently, in (1+1)-dimensional “hybrid” quantum circuits [16, 18, 17] that exhibit a “measurement-driven transition” [59, 20, 21, 31, 30, 113, 123, 22, 60] between a highly-entangled phase and a disentangled one (see Sec. 4.1.1), the notion of QECC also appears, and provides an interesting

perspective [20, 21, 31, 22]. The idea is to view the quantum states generated by the circuit dynamics as QECCs. Indeed, in Clifford hybrid circuits, where numerical characterizations are most accessible, the states are “stabilizer quantum error correcting codes” in a strict sense, for which the “code space” changes at each time step of the circuit evolution. Local measurements in the circuit can be correspondingly interpreted as “local errors”, which tend to decrease the code rate, and when frequent enough, can drive the QECC through a transition from a phase where the QECC is resilient to local errors and thus retains a finite code rate, to a phase where the “error rate” is so high that a finite code rate cannot be sustained.

A complementary approach, as firmly established in hybrid random Haar circuits [30, 31],¹ translates the measurement-driven transition into a “conventional” finite-temperature ordering transition by mapping to an underlying statistical mechanical (stat. mech.) model of spins in $(2 + 0)$ -dimensions with short-range interactions, with the temporal dimension of the circuit viewed as the second spatial dimension.² Within this mapping, the disorder-averaged entanglement entropy of a subregion corresponds to the free energy cost upon a change of boundary condition in that subregion. In the low-temperature ordered phase, this change of boundary condition requires the presence of sharp domain walls. This geometrical picture raises the possibility of a stat. mech. description of the entanglement structure, and, in turn, of QECCs in hybrid circuits in terms of these “entanglement domain walls”. The aim of this work is to demonstrate such a description.

We focus on error correcting properties of stabilizer codes, as generated dynamically after running a random Clifford circuit into the steady state, where the circuit depth scales at most polynomially in the system size. We will mostly focus on the case with a maximally-mixed initial state, and with the measurement rate below the transition threshold, $p < p_c$ (i.e. the mixed phase [21]; see Sec. 4.1.1), which was shown to have a finite code rate on relevant time scales.

¹We note that Refs. [30, 31] extended a mapping first obtained in Refs. [116, 72, 28, 29] for random Haar unitary circuits *without* measurements, where it was first pointed out that the entanglement entropy can be viewed as free energies of “entanglement domain walls”. This mapping has been extended in various contexts of unitary quantum dynamics [135, 136, 137], and this development is independent of hybrid circuits.

²See also Refs. [116, 85], where a similar mapping was derived for random tensor networks.

We start in Sec. 4.1 by introducing the model using the stabilizer code formalism, and translate the circuit dynamics into their actions on the code space. We then state a theorem in Sec. 4.1.4 that applies to all stabilizer codes, which equates the number of independent, undetectable (hence uncorrectable) errors supported on a subregion, with the mutual information between the subregion and the environment.

In Sec. 4.2, we review the domain wall picture of free energies as established analytically in Refs. [30, 31], and numerically for Clifford circuits in Refs. [113, 60]. Since the Clifford stat. mech. model is not known at this stage, we choose to model the “entanglement domain walls” as the simplest type, i.e. that of the liquid-gas interface (or Ising domain walls) in the low-temperature phase, as described by what is called “capillary-wave theory” [86, 87, 138]. This simplification allows analytic calculations, and, as we shall see, quite generally captures qualitative features of entanglement domain walls. Using the theorem, we translate certain *algebraic* properties of the QECC to *geometric* properties of the domain walls. In particular, the code rate is interpreted as the surface tension, and the code distance as the length scale below which the transverse, entropic fluctuations of the domain wall dominates over the surface energy. The “correctability” of a subregion, as quantified by the “decoupling principle”, translates into a geometric decoupling condition of domain walls.

In Sec. 4.3, we perform entanglement entropy calculations for a random Clifford circuit model, and demonstrate that capillary-wave theory gives a qualitatively accurate description of the results. However, quantitative deviations from capillary-wave theory are present in our numerics, which presumably reflects the specific nature of the entanglement domain walls within a stat. mech. description for such Clifford circuit dynamics.

In Sec. 4.4, we discuss implications of our result, and mention several possible future directions.

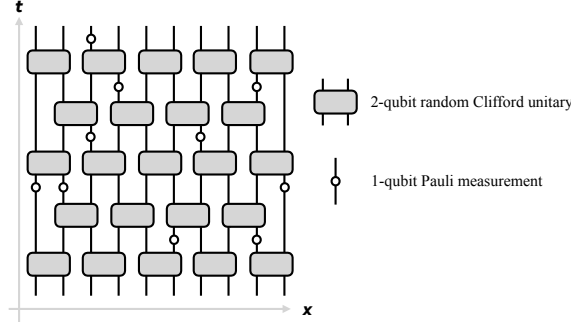


Figure 4.1: The hybrid circuit composed of local unitaries and local measurements. The rectangles represent random Clifford unitary gates, arranged alternatively in a “brickwork” fashion. Projective measurements of single-site Pauli operators are made between unitary layers, and at each site independently with probability $p < p_c$, represented by hollowed dots.

4.1 Model and setting

4.1.1 The random Clifford circuit

We consider “hybrid” circuit models [16, 18, 17] as shown in Fig. 4.1, acting on a set of qubits $Q = \{1, \dots, L\}$, arranged in a one-dimensional array. The circuit is composed of nearest-neighbor unitary gates, which we restrict to the two-qubit Clifford group;³ and sporadic single-qubit projective measurements, which we restrict to be of the Pauli operators. We focus on the quantum trajectories of the state density matrix under circuit evolution, namely,

$$\rho_Q \rightarrow U \rho_Q U^\dagger, \quad \text{under a Clifford unitary gate,} \quad (4.1)$$

$$\rho_Q \rightarrow \frac{P \rho_Q P}{\text{Tr}[P \rho_Q P]}, \quad \text{under a Pauli measurement.} \quad (4.2)$$

Here, the projection operator P is given by $P = \frac{1 \pm g}{2}$, where g is the Pauli operator being measured, and the plus-minus signs are the (possibly random) outcomes of the measurement. In the case when this outcome is indeed random, we choose either outcome randomly with the corresponding probability given by Born’s rule.

For concreteness, we choose to sample the unitaries uniformly from the two-qubit Clifford group, and perform single-qubit measurements of probability p at each time step, independently

³Recall that the Clifford group contains all unitaries that maps every Pauli string operator to another under conjugation.

on each qubit (the “random Clifford circuit” [59]).

We will focus on the maximally-mixed initial state with maximal entropy, $S(\rho_Q) = |Q| \ln 2 = L \ln 2$.⁴ This entropy can be equivalently thought of as the entanglement entropy between Q and a “reference system”, R , where Q and R together holds a pure state $|\Psi_{QR}\rangle$, and ρ_Q is the reduced density matrix after tracing out R ,

$$\rho_Q = \text{Tr}_R |\Psi_{QR}\rangle \langle \Psi_{QR}| = \frac{1}{2^{|Q|}} \mathbb{1}_Q. \quad (4.3)$$

With these specifications, the circuit model is unambiguously defined. Within this model, the entropy of ρ_Q is a monotonically decreasing function of time, T , the circuit depth. The decrease of entropy is due to measurements (Eq. (4.2)) that try to read out some information about the state, while the unitaries (Eq. (4.1)) “scramble/delocalize” the information, protecting it from being read-out by local measurements. This competition leads to a “purification transition” at $p = p_c \approx 0.16$ [21, 60], where

- When $p < p_c$, the state ρ_Q retains a finite density of entropy at times T at most polynomial in $|Q|$ (or formally $T = O(\text{poly}(|Q|))$), therefore in the “mixed phase”.⁵ An arbitrary subset of Q also has a finite density of entanglement entropy, or equivalently, the entanglement entropy has a volume law scaling.
- When $p > p_c$, the entropy density drops to zero on those time scales, therefore in the “pure phase”. A subset of Q thus has zero density of entanglement entropy, or equivalently, the entanglement entropy has an area-law scaling.

We will primarily restrict our attention to “intermediate” time scales, with $T = O(\text{poly}(|Q|))$,

⁴In this Chapter we compute the (von Neumann) entropy by taking the natural logarithm,

$$S(\rho) := -\text{Tr} \rho \ln \rho.$$

This is the convention adopted in Refs. [31, 30, 116, 85], for which the equality between (average) entanglement entropies and free energies can be made (see Eq. (4.18)). This choice of convention accounts for the extra factor of $\ln 2$ here, as well as those appearing in Eqs. (4.7, 4.13, 4.23) and Appendix A.3.

⁵In the case of a pure initial state [16, 17] where this transition was first found, $p < p_c$ corresponds to a “volume law entangled phase”, where one should be thinking in terms of the reduced (mixed) density matrix of a subsystem which holds a finite entropy density as $T \rightarrow \infty$.

since for T exponentially large in $|Q|$, the circuit dynamics should fully purify the state, even when $p < p_c$.

As discussed below, the state ρ_Q at any point of the circuit evolution can be thought of as a “stabilizer code”, that can in principle be used for quantum error correcting purposes. When the state is viewed as a QECC, the purification transition acquires a new interpretation: it is a transition from “good” to “bad” QECCs, where the QECC has a nonzero/zero code rate (which is equal to the entropy density, see below) at relevant time scales, respectively, in the two phases.

4.1.2 The stabilizer formalism

Here we summarize several basic notions of stabilizer QECC that are necessary for stating and using the theorem appearing towards the end of this section. We refer the reader to Refs. [45, 69] and Appendix A.3 for details.

A “stabilizer group” \mathcal{S} is an abelian subgroup of the Pauli group on Q (denoted $\mathcal{P}(Q)$) generated by $m \leq |Q|$ independent and mutually commuting Pauli string operators,

$$\begin{aligned}
 \mathcal{S} &= \left\{ \prod_{j=1}^m (g_j)^{b_j} \mid b_j \in \{0, 1\}, g_j \in \mathcal{P}(Q), [g_j, g_{j'}] = 0 \right\} \\
 &= \langle g_1, \dots, g_m \rangle \\
 &\equiv \langle \mathcal{G} \rangle,
 \end{aligned} \tag{4.4}$$

where $\mathcal{G} = \{g_1, \dots, g_m\}$ is called a “generating set” of \mathcal{S} . The group \mathcal{S} is abelian, where each element has order 2, and can therefore be viewed as an m -dimensional vector space on \mathbb{F}_2 , the isomorphism being given explicitly above in terms of the b -vector.

We list a few more properties that follow from the notion of a stabilizer group [45]:

1. A stabilizer group defines a “code space”, that is, the subspace $\mathcal{H}_Q(\mathcal{S})$ of the Hilbert space

\mathcal{H}_Q on which all elements of \mathcal{S} acts trivially. We have

$$\dim \mathcal{H}_Q(\mathcal{S}) = 2^k \equiv 2^{|Q|-|\mathcal{G}|}, \quad (4.5)$$

where $k := |Q| - |\mathcal{G}| = L - m$ is known as the number of “logical qubits” encoded.

2. The stabilizer group also defines its “code state”, namely the maximally-mixed state on the code space. Its density matrix is proportional to the projection operator onto the code space, and is explicitly given by [81],

$$\rho_Q(\mathcal{S}) = \frac{1}{2^{|\mathcal{Q}|}} \sum_{g \in \mathcal{S}} g. \quad (4.6)$$

As an example, the maximally-mixed state (i.e. the initial state of the circuit model in Fig. 4.1) is such a code state, for which the stabilizer group is empty. Consequently, as we will show below, the state at any point of the random Clifford circuit evolution remains a code state, and therefore is a “stabilizer QECC” in a strict sense.

Since we will mostly be concerned with codes states as in Eq. (4.6), we will usually write ρ_Q as a shorthand notation for $\rho_Q(\mathcal{S})$, where its dependence on \mathcal{S} is implicit.

3. A code state ρ_Q as in Eq. (4.6) has a flat spectrum, and all its Rényi entropies are equal to [81]

$$(\ln 2)^{-1} S(\rho_Q) = |Q| - |\mathcal{G}| = k = \log_2 \dim \mathcal{H}_Q(\mathcal{S}). \quad (4.7)$$

That is, the entropy of the code state is equal to $(\ln 2)$ times the number of logical qubits. It follows that the “code rate”, defined to be the ratio between the number of logical and physical qubits, $\frac{k}{|Q|}$, is equal to the entropy density of ρ_Q up to a factor of $\ln 2$.

4. We recall that a “logical operator” is an element in $\mathcal{P}(Q)$ that commutes with all elements

in \mathcal{S} , that is, an element of the centralizer $\mathcal{C}(\mathcal{S})$.⁶ A logical operator operator is “trivial” if it is itself an element of \mathcal{S} , and “nontrivial” otherwise. Consequently, a nontrivial logical operator acts *within* the code space, but *nontrivially*, and therefore is a so-called “undetectable and uncorrectable error” of the code.

With this trivial/nontrivial distinction, it is clear that a logical operator is defined up to gauge freedom, that is, up to arbitrary multiplications of elements in \mathcal{S} (which do not change its action on the code space). Thus logical operators are most easily thought of as “equivalence classes”, or formally, cosets of \mathcal{S} in $\mathcal{C}(\mathcal{S})$. We define the “logical group” \mathcal{L} as the following quotient group, $\mathcal{L} := \mathcal{C}(\mathcal{S})/\mathcal{S}$, with $|\mathcal{L}| = 2^{2k}$. We note that \mathcal{L} can be generated by representative “logical Pauli X - and Z -operators”, conventionally denoted as $\{\overline{X}_{1\dots k}, \overline{Z}_{1\dots k}\}$.

4.1.3 The circuit evolution in the stabilizer formalism

We briefly describe the circuit dynamics in the stabilizer formalism, with the help of notions introduced above. We show that the state at any point of the circuit evolution, as governed by Eqs. (4.1, 4.2), remains a code state as in Eq. (4.6).

1. Firstly, we notice that the initial maximally-mixed state is a code state with $\mathcal{S} = \emptyset$.
2. Under a Clifford unitary gate U as in Eq. (4.1)

$$\rho_Q(\mathcal{S}) \rightarrow U \rho_Q(\mathcal{S}) U^\dagger = \rho_Q(USU^\dagger), \quad (4.8)$$

⁶Throughout the paper, by $\mathcal{C}(\mathcal{S})$ we really mean the abelianized centralizer,

$$\mathcal{C}(\mathcal{S}) = \frac{\{g \in \mathcal{P}(Q) \mid [g, \mathcal{S}] = 0\}}{\{\pm 1, \pm i\}}.$$

That is, we “forget about” the (uninteresting) coefficients / commutation relations of the logical operators, and focus on their operator contents. This way, $\mathcal{C}(\mathcal{S})$ can be viewed as vector spaces on \mathbb{F}_2 , and group homomorphisms (e.g. those in Appendix A.3) can be viewed as linear maps between vector spaces. On the other hand, we *do* care about commutation relations of stabilizers (elements of \mathcal{S}). We always require \mathcal{S} to be abelian and hence identical to its abelianization. Thus, \mathcal{S} is a subgroup of the abelianized centralizer $\mathcal{C}(\mathcal{S})$, and the logical group \mathcal{L} is defined by their quotient.

where $\mathcal{S}' = USU^\dagger$ is obtained from \mathcal{S} by conjugating each element of \mathcal{S} by U . Thus \mathcal{S}' is also an abelian subgroup of $\mathcal{P}(Q)$. Moreover, we have $S(\rho_Q(\mathcal{S})) = S(\rho_Q(\mathcal{S}'))$.

3. Under a Pauli measurement of $g \in \mathcal{P}(Q)$ as in Eq. (4.2)⁷, one can easily verify that [68]
- (i) When g anticommutes with some elements of \mathcal{S} (hence a detectable error), it is always possible to choose \mathcal{G} such that it has *exactly one* element that anticommutes with g . The updated stabilizer group \mathcal{S}' is generated by \mathcal{G}' , where

$$\mathcal{G}' = \{g_j | g_j \in \mathcal{G}, [g_j, g] = 0\} \cup \{g\}. \quad (4.9)$$

- (ii) When g commutes with all elements in \mathcal{S} and is itself within \mathcal{S} (a trivial logical operator/trivial error),

$$\mathcal{G}' = \mathcal{G}. \quad (4.10)$$

- (iii) When g commutes with all elements in \mathcal{S} and is itself *not* within \mathcal{S} (a nontrivial logical operator/undetectable error),

$$\mathcal{G}' = \mathcal{G} \cup \{g\}. \quad (4.11)$$

Thus, if the initial state of the circuit is a “code state” as in Eq. (4.6), then at any point of the circuit evolution the state is a code state, which admits an efficient representation in terms of \mathcal{G} , and consequently efficient simulation of the circuit dynamics, a result known as the Gottesman-Knill theorem [67, 68].

Moreover, one sees from above that the entropy of the state decreases by $\ln 2$ (i.e. the state gets “purified” by one unit) if a nontrivial logical operator (or equivalently an “undetectable error”) g is measured (compare Eq. (4.7)), but remains unchanged otherwise [22, 37]. This

⁷The results here holds generally for all Pauli operators g , although we are mostly interested in single site Pauli operators that are relevant in the context of the circuit model in Fig. 4.1 and in Eq. (4.2).

observation provides a first clue to a possible connection between the error correcting properties of the state (when viewed as a QECC) and the purification dynamics.

4.1.4 Code distance and the theorem

An important metric of a QECC is its “code distance”, d , defined to be the minimal weight of all nontrivial logical operators.⁸ In our circuit model that has locality, it is natural to define a similar quantity, the “contiguous code distance” [21, 37], d_{cont} , as the minimal length of a contiguous segment of qubits that supports a nontrivial logical operator. By definition, $d \leq d_{\text{cont}}$.

We say that a logical operator $g \in \mathcal{C}(\mathcal{S})$ is “localizable” on a set A of qubits, if there exists $g' \in \mathcal{S}$ such that gg' acts trivially on \bar{A} , where $\bar{A} := Q - A$ is the complement of A in Q . It can be verified that all logical operators localizable on a given set A form a subgroup of $\mathcal{C}(\mathcal{S})$. It can also be verified that this subgroup of operators localizable on A contains \mathcal{S} as a subgroup, upon taking $g' = g \in \mathcal{S}$ above. We take the quotient between these two, and denote the corresponding quotient group as \mathcal{L}_A , which is a subgroup of \mathcal{L} (see Appendix A.3 for a detailed characterization of \mathcal{L}_A). We have $|\mathcal{L}_A| = 2^{\ell_A}$, where ℓ_A is an integer, and has the meaning of “the maximal number of independent and inequivalent logical operators (undetectable errors)” on A . The quantity ℓ_A thus measures how susceptible the QECC is to undetectable errors on A .

By definition, any subset (resp. segment) A of qubits with weight (resp. length) smaller than d (resp. d_{cont}) supports no logical operators (therefore $\ell_A = 0$), or equivalently, no “undetectable errors”. An error occurring on A must therefore be either “detectable” (that brings states outside the code space) or “trivial” (that leaves states within the code space unchanged). When a detectable error located on A occurs, an error correcting unitary supported on A that reverses the effect of the error can be found, given its error syndrome [45, 69].

Following the standard nomenclature, we may say that the circuit defines a $[[Q, k, d_{\text{cont}}]$ -

⁸Recall that the weight of a Pauli string operator is the number of qubits on which its content is not the identity operator.

code over the course of its time evolution, where both k and d_{cont} are functions of time. A central purpose of this Chapter is to characterize the code dynamics, and develop an intuitive picture of its error correcting capabilities as quantified by k and d_{cont} . This is partly achieved by the following relation between ℓ_A and the entanglement structure of the state:

Theorem 1. Let ρ_Q be a code state (defined in Eq. (4.6) to be the maximally-mixed state on the code space), and $|\Psi_{QR}\rangle$ be an arbitrary purification of ρ_Q ,

$$\rho_Q = \text{Tr}_R |\Psi_{QR}\rangle \langle \Psi_{QR}|. \quad (4.12)$$

Then for any subset A of Q , $A \subseteq Q$, we have

$$\ell_A = (\ln 2)^{-1} I_{A,R}, \quad (4.13)$$

where the RHS is the mutual information between A and R ,

$$\begin{aligned} I_{A,R} &= S(\rho_A) + S(\rho_R) - S(\rho_{AR}) \\ &= S(\rho_A) + S(\rho_Q) - S(\rho_{\bar{A}}). \end{aligned} \quad (4.14)$$

Here again, $\bar{A} := Q - A$ is the complement of A on Q . □

The proof of the theorem is given in Appendix A.3.

Several comments are in order:

- The quantity ℓ_A was introduced and explored in Refs. [139, 140] (see also Ref. [141]), although not explicitly cast in the form of a mutual information. From the theorem it follows directly that $\ell_A + \ell_{\bar{A}} = 2k$, the “cleaning lemma” [141, 142].
- Clearly, from its definition, $\ell_A \leq \ell_{AB}$ since $A \subseteq AB$, which implies $I_{A,R} \leq I_{AB,R}$ or,

equivalently,

$$S(\rho_A) + S(\rho_{ABR}) \leq S(\rho_{AB}) + S(\rho_{AR}), \quad (4.15)$$

the strong subadditivity inequality.

- We have not specified the pure state $|\Psi_{QR}\rangle$. However, since both sides of Eq. (4.13) can be defined from ρ_Q alone (see the last line of Eq. (4.14)), any purification of ρ_Q would work equally well.
- For concreteness, let us choose $|R| = k$, the minimal number of qubits required, and consider the following “encoded state” as a purification of ρ_Q ,

$$|\Psi_{QR}\rangle = \frac{1}{\sqrt{2^k}} \sum_x |\bar{x}_Q\rangle |x_R\rangle, \quad (4.16)$$

where $\{|\bar{x}_Q\rangle\}$ is an orthonormal basis of the code space, and $\{|x_R\rangle\}$ is an orthonormal basis of R . This pure state can be obtained by starting from k Bell pairs, collecting one qubit from each pair, and encoding this collection of k qubits in the QECC (on Q) while labelling the other k qubits as R .

The implication of the theorem when A is a contiguous segment and $|A| < d_{\text{cont}}$ is important, and perhaps familiar from general considerations of QECCs. The LHS of Eq. (4.13) is zero, following the definition of d_{cont} . The RHS is therefore also zero, as it must be [143]: Since all errors on A can be detected (and hence corrected), no observables on A can reveal any information about the encoded state, and there should be no correlations between A and R .⁹ Therefore, they must “decouple” on the level of density

⁹In particular, no measurements on A should be able to change the entropy of $\rho_Q(\mathcal{S})$. The “decoupling condition” in Eq. (4.17) was argued to hold for typical states when $p < p_c$, thus responsible for the very existence of a “mixed” phase [20]. We will come back to these points in Sec. 4.4.

matrices [144, 145, 19, 146],

$$|A| < d_{\text{cont}} \quad \Rightarrow \quad \rho_{AR} = \rho_A \otimes \rho_R, \quad (4.17)$$

leading to a vanishing mutual information between A and R .

On a practical level, the theorem provides a concrete relationship between error correcting capabilities of the QECC and its entanglement structure. For example, one can readily “read off” the code distance of the QECC, assuming a complete knowledge of the entanglement structure.

4.2 Domain wall picture of entanglement entropies

In this section we review the mapping of the circuit dynamics to effective stat. mech. models, as first developed for unitary Haar circuits in Refs. [116, 72, 28, 29, 137], and later extended to hybrid Haar circuits in Refs. [31, 30]. In either case, the entanglement entropy can be related to a domain wall free energy in the stat. mech. model, which can receive both “energetic” and “entropic” contributions. We will however focus on the case of hybrid circuits with a nonzero measurement strength p , where results in Refs. [30, 31] can be directly applied.

4.2.1 Mapping to a spin model

The upshot of the mapping introduced in Refs. [31, 30] for the hybrid random Haar circuit can be very roughly summarized as follows (compare Fig. 4.2(a)), where we omit technical details. Recall that the hybrid random Haar circuit [31, 30] is structurally identical to the circuit in Fig. 4.1, except with each unitary gate sampled from the Haar measure on $U(4)$, and the sporadic projective measurements replaced by generalized weak measurements of the same strength on each qubit at each time step. This strength plays a role similar to the frequency of sporadic projective measurements in Fig. 4.1.

1. In the bulk of the circuit, there is one Potts-like spin degree-of-freedom associated with

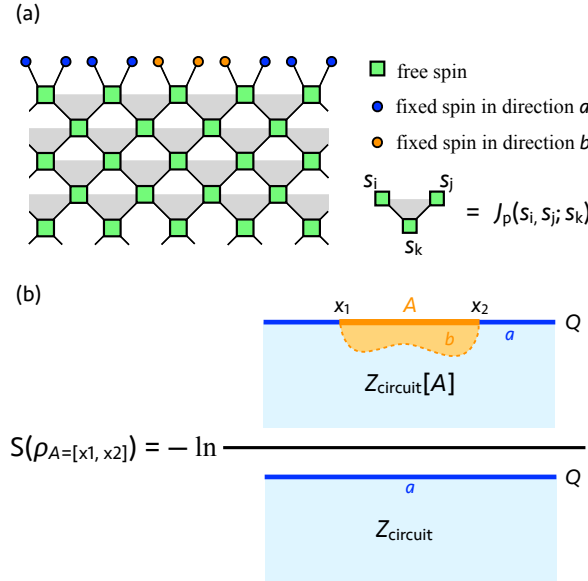


Figure 4.2: (a) Illustration of the underlying spin model in Refs. [31, 30] for the hybrid random Haar circuit. This figure is adapted from Ref. [30]. Each bulk unitary maps to a bulk spin (green square), that is “free”. Qubits at the final time $t = T$ (solid dots) correspond to “fixed” spins all pointing in either the a or b direction. A Boltzmann weight is associated with each downward-pointing triangle (shaded), and is a function of spins on its vertices. (b) Representation of the entanglement entropy of the segment A as the difference of two free energies (see main text). In this figure, we have chosen to “zoom in” on a small part near the upper edge of the circuit; the upper edge corresponds to physical qubits Q at the final time $t = T$ of the circuit evolution. The other boundaries are far away, and need not be specified. The illustrations on the RHS represent typical configurations in the low-temperature “ferromagnetic” phase, possibly after a sufficient number of coarse-graining steps. In the denominator (Z_{circuit}), the upper edge is colored blue, corresponding to the fixed boundary condition a ; thus, the bulk spins tend to also order along a . In the numerator ($Z_{\text{circuit}}[A]$) the segment A is colored yellow, and the spins are aligned to have a different value b . This will induce the alignment of proximate bulk spins along the same direction b . A domain wall is then present where the two domains meet.

each unitary gate, taking values in $\{a, b, c, \dots\}$. The bulk spins form a square lattice (see Fig. 4.2(a), and compare with Fig. 4.1). A Boltzmann weight is defined on each downward-pointing triangle of the lattice (see Fig. 4.2(a)). The “circuit partition function”, Z_{circuit} , is obtained by contracting all free spin indices of the Boltzmann weights.

2. At the $t = T$ (final time) boundary of the circuit, there is a spin associated with each physical qubit in Q . All spins in Q are fixed to have the same value (say a), and therefore corresponds to a “fixed” boundary condition (b.c.) of the spin model.
3. At the $t = 0$ (initial time) boundary of the circuit, there is also a spin associated with each physical qubit in Q , and certain short-range entangled initial states on Q corresponds to simple b.c. of the spin model. In particular, a pure product initial state corresponds to a “free” b.c., where each spin can independently take all allowed values. On the other hand, the maximally-mixed initial state corresponds to the same “fixed” b.c. (a) as at the $t = T$ boundary.
4. When the spatial b.c. is periodic, the circuit geometry is cylindrical, and there are no other boundaries of the circuit. When the spatial b.c. is open, the circuit geometry is rectangular, and the boundary conditions on the left and right sides of the rectangle are also “free”.
5. To compute the entanglement entropy of a segment $A = [x_1, x_2]$ in the final state (at $t = T$), one needs to compute another partition function. This partition function is defined by the same boundary condition as Z_{circuit} , except with all spins in the segment A at the upper edge of the circuit “aligned” to another different value, say b . We call this new partition function $Z_{\text{circuit}}[A]$.

As shown in [30, 31, 85], the (ensemble averaged) entanglement entropy follows,

$$S(\rho_A) = -\ln \frac{Z_{\text{circuit}}[A]}{Z_{\text{circuit}}}, \quad (4.18)$$

taking the form of a “free energy cost” due to the change of b.c. (see Fig. 4.2(b)).

6. The purification/entanglement transition corresponds to an ordering transition of the spin model, where the measurement strength p plays a role similar to temperature. Within the low-temperature ordered phase of the spin model, a well-defined domain wall with finite surface tension must be present to account for the b.c. change (see Fig. 4.2(b)).¹⁰ The free energy cost, mostly coming from the domain wall, will be extensive, leading to volume law entanglement entropies. We will, for brevity, call it “the entanglement domain wall”. The surface tension decreases with increasing p , and eventually vanishes at the critical point.

As demonstrated for random Haar circuits [31, 30], this mapping requires a replica limit of the spin model (the limit where the number of available values of the Potts spins goes to 1), and enables certain predictions for critical properties of the model [30] for $n \geq 1$ Rényi entropies. However, the more general viewpoint of entanglement entropies (namely as free energies of domain walls) [72, 28, 29, 137, 135, 136] has proven useful in understanding the phase transition in other contexts: for the zeroth Rényi entropy [16] (where the entanglement entropy is equal to a “geometrical minimal cut” of the underlying lattice); and for critical properties of the random Clifford circuit [113, 60].

We will henceforth assume this general domain wall picture holds for the random Clifford circuit in the mixed phase. Since a derivation of the underlying stat. mech. model (if it exists) is unavailable at present, the precise nature of the domain walls is unknown. Nevertheless, as we shall see, the domain wall picture alone, with the additional assumption that the domain walls are of the simplest type (“Ising like”; see Fig. 4.2), captures much of the qualitative aspects of the entanglement entropies in the Clifford circuit. We will devote the rest of this section to capillary-wave theory of Ising domain walls and its implications, and the next section to

¹⁰Notice that in Fig. 4.2(b), we have chosen to present the domain wall in the simplest form, where a and b can meet directly (so that there can be as few as only one domain wall) and are the only spin values that need to be considered. The spins are therefore Ising like. In general, it might be energetically favorable to have yet other different domains inserted between the a - and b -domains in typical configurations subject to this b.c., resulting in multiple mutually-avoiding domain walls [30].

numerical checks of capillary-wave theory for the Clifford circuit.

4.2.2 Capillary-wave theory of Ising domain walls

Capillary-wave theory [86, 87, 138] was originally proposed for describing domain walls in the low-temperature ordered phase of the Ising model. For the example in Fig. 4.2, a sharp domain wall must be present to be consistent with the assigned boundary conditions. For this geometry, one can further argue that it is sufficient to consider configurations with a single domain wall, which also admits the following parametrization as a “height function”,

$$\begin{aligned}
 y &: [x_1, x_2] \rightarrow [-T, 0], \\
 x &\mapsto y(x),
 \end{aligned}
 \tag{4.19}$$

where $y(x_1) = y(x_2) = 0$. With this parameterization, we are neglecting all “overhangs” and “bubbles” that might be present in the relevant configurations; these have a finite typical size in the low-temperature phase, and will eventually disappear under coarse-graining. This reasoning leads to the following approximation for the entanglement entropy,

$$\begin{aligned}
 &S(\rho_{A=[x_1, x_2]}) \\
 &= -\ln \frac{Z_{\text{circuit}}[A]}{Z_{\text{circuit}}} \\
 &\approx -\ln \int \mathcal{D}[y(x)] \exp \left[-\beta\sigma \int_{x_1}^{x_2} dx \sqrt{1 + (\partial_x y)^2} \right],
 \end{aligned}
 \tag{4.20}$$

where β is the “inverse temperature”, and σ the “surface tension”. This resulting “capillary-wave theory” partition function is the canonical ensemble of all domain walls (i.e. height functions $y(x)$ defined in Eq. (4.19)), where the energy of each domain wall is the product of the surface tension and its surface area.

After expanding the square root and dropping higher-order irrelevant terms, Eq. (4.20) becomes a Gaussian theory, and can be readily evaluated. With details in Appendix D, we

find,

$$\begin{aligned}
 S(\rho_A) & \\
 &\approx F_{\text{CW}}(A) \\
 &= \beta\sigma|A| + \frac{3}{2} \ln |A|, \text{ when } T \gg \sqrt{L} \gg \sqrt{|A|},
 \end{aligned} \tag{4.21}$$

for $|A| \gg 1$. Here the first term is the surface energy, and the second term is “entropic”, coming from transverse, thermal fluctuations of $y(x)$, with a universal coefficient $3/2$, as found in Ref. [22] within a quantized regularization of the Ising model. Notice that we have reserved the notation $S(\rho_A)$ for the entanglement entropy of A , and $F_{\text{CW}}(A)$ for the free energy of the domain wall due to a change of b.c. in A .

In Fig. 4.2 we have not specified boundary conditions on the lower-, left-, and right-sides of the circuit, as it is a “zoomed-in” view. In this way, we are assuming implicitly that $|A| \ll L$, and also that the circuit depth is large compared to the vertical extent of the domain wall, $T \gg \sqrt{|A|}$. It is within this regime that the approximation of $S(\rho_A)$ with $F_{\text{CW}}(A)$ in Eq. (4.21) is established, and is valid regardless of the other boundary conditions (as the domain wall is sufficiently far away from the other boundaries).

The subleading “entropic” correction of $S(\rho_A)$ was found to be characteristic of the mixed phase $0 < p < p_c$ of hybrid circuits [59, 21], and is now shown to be present generically whenever the fluctuating domain wall picture is valid, though its analytic form ($\frac{3}{2} \ln |A|$) here is special to capillary-wave theory. Its importance will be made clear in the next subsection.

We conclude this subsection by mentioning the limit $p = 0$, which corresponds to a random unitary circuit *without* measurements. In this case, the entanglement domain walls are directed in the temporal direction of the circuit (as opposed to the case here with $p > 0$, in Fig. 4.2, where the domain wall is directed in the spatial direction of the circuit). This domain wall can now fluctuate in the transverse (spatial) direction, and these fluctuations leads to a similar entropic term $\frac{1}{2} \ln t$ when $t \ll L$ [29], where the coefficient $\frac{1}{2}$ is universal, and also comes from

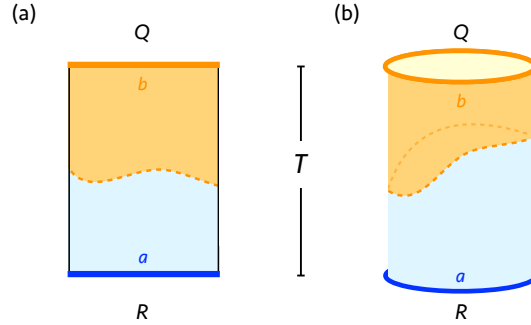


Figure 4.3: Illustrations of boundary conditions for $F_{\text{CW}}(Q)$ with open b.c. (left) and periodic b.c. (right). It is understood that both $F_{\text{CW}}(Q)$ are obtained by subtracting the background free energy with both Q and R fixed to have b.c. a (not plotted), from the free energy of the configuration plotted (with Q in b and R in a).

the diffusion equation (see Appendix D). However, this term will disappear as $t = \text{poly}(L) \gg L$, the regime we focus on in this Chapter.¹¹

4.2.3 The maximally-mixed initial state

We have seen in Sec. 4.1.3 that the hybrid circuit dynamics with the maximally-mixed initial state can be formulated as the dynamics of the corresponding QECC. The entropy of the entire system Q , $S(\rho_Q)$, is monotonically decreasing, corresponding to a monotonically decreasing “code rate”. On the other hand, according to the prescriptions summarized at the beginning of this section (for mapping to a spin model), the corresponding circuit partition function Z_{circuit} is defined by the fixed b.c. a on both the upper and lower edges of the circuit [31, 60]; whereas the entropy $S(\rho_Q)$ is the change in free energy upon changing the b.c. of the upper edge (i.e. qubits in Q) to a different, fixed one, b . The b.c. relevant to this calculation is illustrated in Fig. 4.3. Since the maximally-mixed initial state admits a natural purification in terms of $|Q| = L$ Bell pairs where Q consists of one qubit from each pair, the upper and lower edges can be naturally viewed as Q (the system, that is acted upon by the circuit), and R (the “reference”, consisting of the other half of the Bell pairs, that is left un-evolved by the circuit), respectively [60]. We will henceforth adopt this labelling, for we find it intuitive to have a concrete reference R at

¹¹We thank Tianci Zhou and Adam Nahum for explaining to us Ref. [29] on these points.

the far end of the circuit that Q is trying to disentangle itself from, even if this choice of R is not unique.

The dominant contribution to $S(\rho_Q)$ comes from a single domain wall separating the upper and lower edges, going around the “waist” of the circuit (again compare Fig. 4.3):

- With open spatial b.c., the domain wall endpoints are “free”, and can independently take any vertical coordinate $y(x = 0) \in [-T, 0]$ and $y(x = L) \in [-T, 0]$.
- With periodic spatial b.c., the domain wall is periodic, but otherwise “free” to take any position along the vertical direction, leading to $y(x = 0) = y(x = L) \in [-T, 0]$.

The free energies can then be calculated within capillary-wave theory (Appendix D),

$$\begin{aligned}
 & S(\rho_Q) \\
 &= -\ln \frac{Z_{\text{circuit}}[Q]}{Z_{\text{circuit}}} \\
 &\approx F_{\text{CW}}(Q) \\
 &= \begin{cases} \beta\sigma L - \ln T, & \text{open b.c.} \\ \beta\sigma L - \ln \frac{T}{\sqrt{L}}, & \text{periodic b.c.} \end{cases} \quad \text{when } T \gg \sqrt{L}. \tag{4.22}
 \end{aligned}$$

The $-\ln T$ term comes from the “center of mass entropy” of the “waist domain wall”, whose form is consistent with an exponentially long purification time within the mixed phase [21] (see Sec. 4.2.5). The $\ln \sqrt{L}$ difference between open and periodic b.c. is attributed to the additional endpoint entropy with open b.c., as mentioned above.

We see also that the quantity $\beta\sigma$ can be identified as ($\ln 2$ times) the code rate,

$$\lim_{|Q| \rightarrow \infty} \frac{k \ln 2}{|Q|} = \lim_{L \rightarrow \infty} \frac{S(\rho_Q)}{L} = \beta\sigma, \tag{4.23}$$

for $T = \text{poly}(L)$.

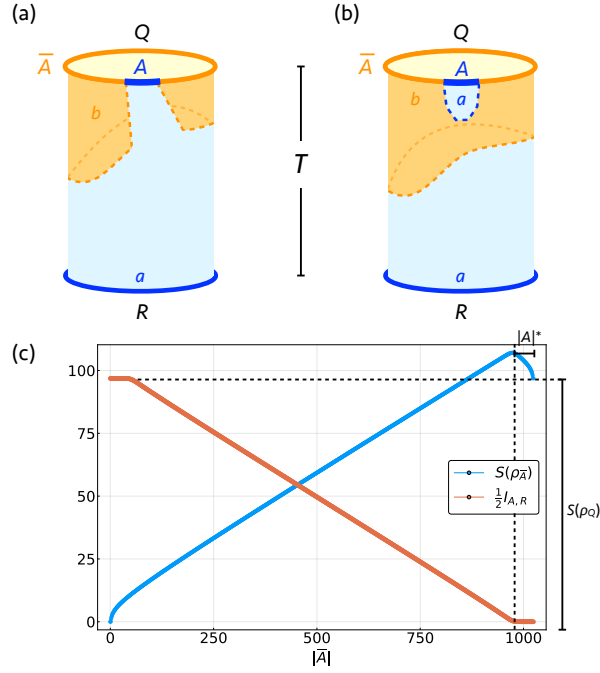


Figure 4.4: (a,b) Illustrations of boundary conditions for $F_{CW}(\bar{A})$ with periodic spatial boundary conditions. The partition function $Z_{\text{circuit}}[\bar{A}]$ is the sum of the two contributions, $Z_{\text{circuit}}[\bar{A}] = Z_{\text{circuit}}^{(1)}[\bar{A}] + Z_{\text{circuit}}^{(2)}[\bar{A}]$. (c) The resulting entanglement entropy $S(\rho_{\bar{A}})$ and (half) the mutual information $I_{A,R}$, as computed from capillary-wave theory (specifically Eqs. (4.21, 4.22, 4.26)). We have taken $|Q| = L = 1024$, $T = 8L$, and $\beta\sigma = 0.1$ in this plot. We emphasize the non-monotonicity in $S(\rho_{\bar{A}})$ as $|A| \rightarrow L$. Moreover, there is a linearly decreasing segment of the $\frac{1}{2}I_{A,R}$ versus $|\bar{A}|$ plot, with horizontal extent $L - 2|A|^*$ and vertical extent $S(\rho_Q)$. Since its slope must be bounded between $[-\ln 2, \ln 2]$, we have $(\ln 2)^{-1}S(\rho_Q) \leq L - 2|A|^*$.

4.2.4 Decoupling of domain walls

We are now ready to investigate the entropy of a *contiguous* subregion A of Q with arbitrary length. Notice that the previous result in Eq. (4.21) was obtained for $|A| \ll |Q| = L$, and that Eq. (4.22) accounts for the limiting case $|A| = |Q| = L$. These two regimes must then be interpolated by some intermediate behavior. For convenience, below, we will instead study the entropy $S(\rho_{\bar{A}})$, defined on the complement of A .

Consider first the limit with small A , $|A| \ll |Q|$. In this regime, the partition function $Z_{\text{circuit}}[\bar{A}]$ (defined by a on AR and b on \bar{A}) receives two possibly comparable contributions (see Fig. 4.4 with periodic b.c.):

1. A single domain wall separating \bar{A} from AR as before. There are then two domains, with

spins aligned along a and b , respectively (see Fig. 4.4(a)). The corresponding partition function is approximated within capillary wave theory as

$$Z_{\text{circuit}}^{(1)}[\bar{A}] \approx Z_{\text{circuit}} e^{-F_{\text{CW}}(\bar{A})}. \quad (4.24)$$

2. Two “decoupled” domain walls, one separating A from \bar{A} , and the other, a “waist domain wall”, separating $Q = A\bar{A}$ from R . There are now three domains, as shown in Fig. 4.4(b), and to go from A to R *two domain walls must be crossed*. The corresponding partition function is approximated within capillary wave theory as

$$Z_{\text{circuit}}^{(2)}[\bar{A}] \approx Z_{\text{circuit}} e^{-F_{\text{CW}}(A) - F_{\text{CW}}(Q)}. \quad (4.25)$$

After summing these contributions, we have, according to Eq. (4.18),

$$S(\rho_{\bar{A}}) \approx -\ln \left[e^{-F_{\text{CW}}(\bar{A})} + e^{-F_{\text{CW}}(A) - F_{\text{CW}}(Q)} \right]. \quad (4.26)$$

The first contribution $F_{\text{CW}}^{(1)} = F_{\text{CW}}(\bar{A})$ is always *energetically* more favorable than $F_{\text{CW}}^{(2)} = F_{\text{CW}}(A) + F_{\text{CW}}(Q)$, but is not necessarily *entropically* so. The competition is only present due to fluctuations of the domain walls.¹²

To illustrate this, we evaluate Eq. (4.26) with periodic b.c. (using Eqs. (4.21, 4.22)), where F_{CW} is simply a function of the size of the region, and plot the result in Fig. 4.4(c). Notice the striking non-monotonic behavior in $S(\rho_{\bar{A}})$, which has a width labelled as $|A|^*$. The non-monotonicity comes from a competition between the two contributions, which we can readily

¹²A similar competition between domain wall topologies is also present in the limit $p = 0$ [29], which leads to an $O(1)$ “Page correction” to the entanglement entropy.

understand for large $|Q| = L$,

$$\begin{aligned}
 & S(\rho_{\bar{A}}) \\
 & \approx -\ln \left[e^{-F_{\text{CW}}(\bar{A})} + e^{-F_{\text{CW}}(A) - F_{\text{CW}}(Q)} \right] \\
 & \approx \min \{ F_{\text{CW}}(\bar{A}), F_{\text{CW}}(A) + F_{\text{CW}}(Q) \} \\
 & \approx \begin{cases} F_{\text{CW}}(\bar{A}), & 0 \leq |\bar{A}| < L - |A|^* \\ F_{\text{CW}}(A) + F_{\text{CW}}(Q), & L - |A|^* < |\bar{A}| \leq L. \end{cases} \tag{4.27}
 \end{aligned}$$

Here $|A|^*$ is the length scale when the entropic and energetic terms are comparable, and may be defined as follows,

$$\begin{aligned}
 & F_{\text{CW}}(L - |A|^*) = F_{\text{CW}}(|A|^*) + F_{\text{CW}}(L) \\
 \Rightarrow & |A|^* \approx \frac{1}{2\beta\sigma} \left(\frac{3}{2} \ln L + \ln \frac{T}{\sqrt{L}} \right), \tag{4.28}
 \end{aligned}$$

to leading order for large T and L . The length scale $|A|^*$ is thus inversely proportional to the code rate $\beta\sigma$, and grows with both L and T logarithmically. For any circuit depth $T = O(\text{poly}(L))$, $|A|^*$ is proportional to $\ln L$.

In the regime with $L - |A|^* < |\bar{A}| \leq L$ (i.e. $0 \leq |A| < |A|^*$), we recognize that the free energies $F_{\text{CW}}(A)$ and $F_{\text{CW}}(Q)$ in Eq. (4.27) represent the corresponding entanglement entropies $S(\rho_A)$ and $S(\rho_Q)$ according to Eqs. (4.21, 4.22). The last line in Eq. (4.27) can then be rewritten as,

$$\begin{aligned}
 0 \leq \frac{|A|}{|A|^*} < 1 & \Rightarrow S(\rho_{\bar{A}}) \approx S(\rho_A) + S(\rho_Q) \\
 & \Leftrightarrow S(\rho_{AR}) \approx S(\rho_A) + S(\rho_R) \\
 & \Leftrightarrow I_{A,R} \approx 0. \tag{4.29}
 \end{aligned}$$

We thereby conclude that if $\frac{|A|}{|A|^*} < 1$, the subsystems A and R decouple. This decoupling

corresponds to the regime where the configuration in Fig. 4.4(b) dominates, i.e. when the domain wall decouples, with two domain walls separating A and R .

In Fig. 4.4(c) we have also plotted (half) the mutual information between A and R , $I_{A,R}$, as computed from capillary-wave theory using Eqs. (4.14, 4.21, 4.26). Notice the (near) vanishing of $I_{A,R}$ for $0 \leq |A| < |A|^*$, consistent with Eq. (4.29).

A more detailed calculation shows that,

$$\begin{aligned}
 I_{A,R} & \\
 &\approx \ln \left[1 + e^{F_{\text{CW}}(A) + F_{\text{CW}}(Q) - F_{\text{CW}}(\bar{A})} \right] \\
 &\approx \ln \left[1 + e^{-2\beta\sigma(|A|^* - |A|)} \right] \\
 &\approx \begin{cases} e^{-2\beta\sigma(|A|^* - |A|)}, & 0 \leq |A| < |A|^*; \\ 2\beta\sigma(|A| - |A|^*), & |A| > |A|^*. \end{cases} \quad (4.30)
 \end{aligned}$$

Here we have used Eq. (4.28), and only kept the leading linear terms in F_{CW} . Since $|A|^*$ diverges in the thermodynamic limit (see Eq. (4.28)), for $\frac{|A|}{|A|^*} \in [0, 1)$ the mutual information $I_{A,R}$ vanishes *exactly*. On the other hand, $I_{A,R}$ is *strictly* positive if $\frac{|A|}{|A|^*} > 1$.

Upon combining with Theorem 1 in Sec. 4.1.4, we conclude that $\ell_A = 0$ *if and only if* $|A| < |A|^*$. We can then make the important identification between the code distance d_{cont} and $|A|^*$,

$$d_{\text{cont}} = |A|^*. \quad (4.31)$$

With this equality, we may deduce from Fig. 4.4(c) (see the figure caption) that

$$k = (\ln 2)^{-1} S(\rho_Q) \leq L - 2|A|^* = |Q| - 2d_{\text{cont}}. \quad (4.32)$$

This is essentially the quantum Singleton bound [129], with $d \rightarrow d_{\text{cont}} \gg 1$.

To summarize, capillary-wave theory predicts that the dynamically generated QECC has

code distance that diverges with system size on relevant time scales, while also keeping a finite code rate. Qubit segments with length smaller than $|A|^* = d_{\text{cont}}$ are protected from undetectable errors by thermodynamic fluctuations of the entanglement domain walls.

4.2.5 Crossover to late times

In this subsection, we deviate from our main focus on polynomial time scales $T = O(\text{poly}(L))$, and briefly discuss how the domain wall picture can account for the late time crossover behavior when T is exponential in L . On these time scales, the entropy of the code state $S(\rho_Q)$ is expected to decay to zero [21], i.e. the state is completely purified.

Previously, when computing $S(\rho_Q)$ from Fig. 4.3 obtaining the result in Eq. (4.22), we only took into account configurations with a single waist domain wall – valid since the energy term $\beta\sigma L$ is always dominant over the entropy term $-\ln T$ when $T = O(\text{poly}(L))$, and single-domain wall configurations have the lowest energy. This simplification eventually breaks down when $T \gg \exp[\beta\sigma L]$, and we have to consider the possibility of multiple waist domain walls. In particular, Z_{circuit} will now receive contributions from all configuration with an *even* number of waist domain walls, and $Z_{\text{circuit}}[Q]$ from those with an *odd* number. Here we are again assuming the Ising nature of these domain walls. Moreover, the vertical (i.e. time direction) extent of each domain wall scales as \sqrt{L} (see Appendix D), much smaller than either L or T . These domain walls are therefore effectively “local” along the time direction, and the only interaction between the domain walls is onsite repulsion (i.e. the domain walls cannot overlap/cross, but otherwise non-interacting). We thus have a picture of a “(waist) domain wall gas”, and can

readily compute the corresponding partition functions using Eq. (4.22),

$$\begin{aligned}
 & S(\rho_Q) \\
 &= -\ln \frac{Z_{\text{circuit}}[Q]}{Z_{\text{circuit}}} \\
 &\approx -\ln \frac{\sum_{n \text{ odd}} (1/n!) \exp[-nF_{\text{CW}}(Q)]}{\sum_{n \text{ even}} (1/n!) \exp[-nF_{\text{CW}}(Q)]} \\
 &\approx -\ln \tanh \left(e^{-F_{\text{CW}}(Q)} \right) \\
 &\approx \begin{cases} -\ln \tanh (T e^{-\beta\sigma L}) & \text{open b.c.} \\ -\ln \tanh \left(\frac{T}{\sqrt{L}} e^{-\beta\sigma L} \right) & \text{periodic b.c.} \end{cases}. \tag{4.33}
 \end{aligned}$$

Notice that

$$\lim_{T \rightarrow \infty} S(\rho_Q) = 0, \tag{4.34}$$

as expected for a pure state.

The same reasoning leads to a similar modification of $S(\rho_{\bar{A}})$ in Eq. (4.26),

$$S(\rho_{\bar{A}}) \approx -\ln \left[e^{-F_{\text{CW}}(\bar{A})} + e^{-F_{\text{CW}}(A)} \tanh \left(e^{-F_{\text{CW}}(Q)} \right) \right], \tag{4.35}$$

which implies,

$$\begin{aligned}
 & \lim_{T \rightarrow \infty} S(\rho_{\bar{A}}) \\
 &\approx -\ln \left[e^{-F_{\text{CW}}(\bar{A})} + e^{-F_{\text{CW}}(A)} \right] \\
 &\approx \min \{ F_{\text{CW}}(\bar{A}), F_{\text{CW}}(A) \}, \tag{4.36}
 \end{aligned}$$

again as expected for the pure state ρ_Q that is dynamically generated on exponentially long times.

Inclusion of multiple domain walls also introduces some crossover time dependence in d_{cont} ,

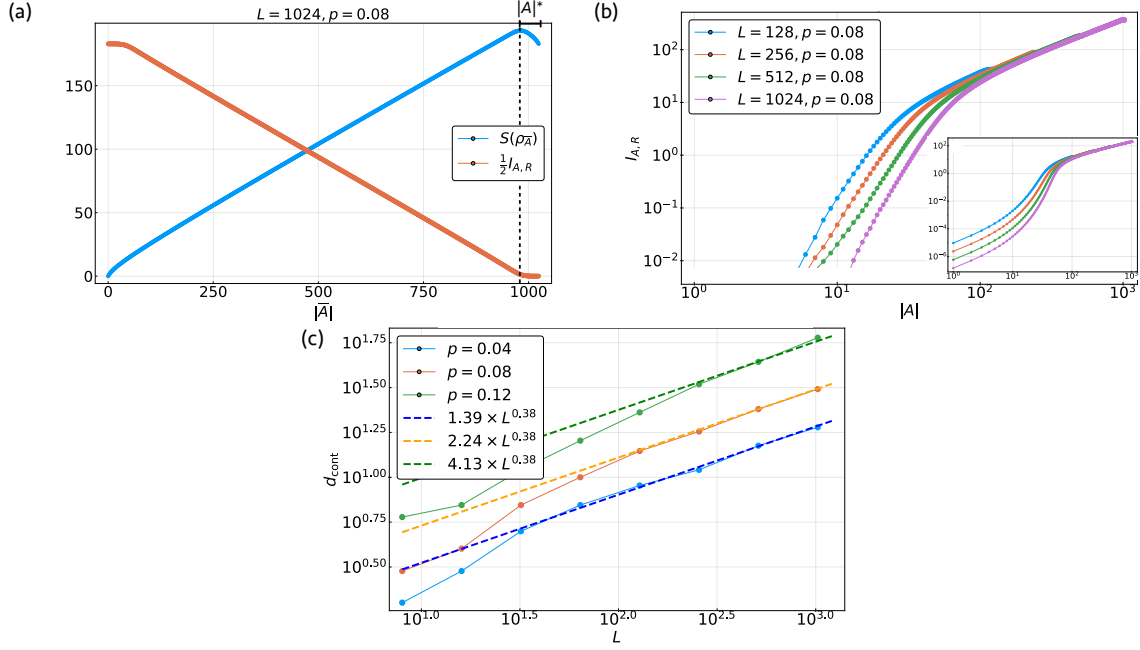


Figure 4.5: (a) $S(\rho_A)$ and $\frac{1}{2}I_{A,R}$ from random Clifford circuit numerics, where we observe qualitative agreements with capillary-wave theory (Fig. 4.4(c)). (b) A closer look at $I_{A,R}$ on a log-log scale, where we find qualitative agreement, within accessible numerical resolutions, with the capillary-wave theory result (inset), computed from Eqs. (4.21, 4.22, 4.30) at $\beta\sigma = 0.1$. (c) The scaling of the code distance (obtained from (a,b) upon setting $\epsilon = \ln 2$) with the system size for $p = 0.04, 0.08, 0.12$, where we find $d_{\text{cont}} \propto L^{\gamma_1}$ with $\gamma_1 \approx 0.38$.

accounting for its eventual linear scaling in L when $T \gg \exp[\beta\sigma L]$. Indeed, the decoupling conditions Eqs. (4.29, 4.30) retain their forms in this limit, and d_{cont} can still be identified with $|A|^*$, which approaches $L/2$ in the long time limit.

4.3 Numerical results

In this section, we compare our capillary-wave theory results with numerical computations in the random Clifford circuit (Fig. 4.1) for the observables explored in the previous section. Overall, we find qualitative agreement between the two, but as we shall see, a complete quantitative agreement is lacking. We interpret the former as support for the general entanglement domain wall picture, and the latter as an indication of a more complex nature of these domain walls for the random Clifford circuit.

4.3.1 Code distance for Clifford QECCs

The most striking qualitative prediction of the domain wall picture from Sec. 4.2 is the phenomenon of decoupled domain walls as illustrated in Fig. 4.4. To explore this for random Clifford circuits, we compute $S(\rho_{\bar{A}})$ and $I_{A,R}$ with varying $|A|$, taking a maximally-mixed initial state and averaging over the random ensemble of circuits, as well as over a time window $6L < T < 8L$. Within this time window, we have $T \gg L^{1/2}$, so that Eqs. (4.21, 4.22) should apply.

Our numerical results are shown in Fig. 4.5(a) for $L = 1024$ and $p = 0.08 \approx 0.5p_c$. Strikingly, we observe the same non-monotonicity in $S(\rho_{\bar{A}})$, decreasing with \bar{A} in the range $L - |A|^* < |\bar{A}| \leq L$, in accordance with the capillary-wave theory results in Fig. 4.4. Moreover, within this range, $I_{A,R}$ is very small, showing a plateau with height ≈ 0 . The Clifford numerical results for both $S(\rho_{\bar{A}})$ and $I_{A,R}$ are thus fully consistent with the domain wall decoupling results in Fig. 4.4. Evidently, the domain wall picture holds for random Clifford circuits, being qualitatively consistent with capillary-wave theory.

Our particular choice of $p = 0.08$ was unimportant. Indeed, for the Clifford circuit we find consistency with Fig. 4.4 for a wide range of p with $0 < p < p_c$ (not shown). This is as expected, since the domain wall picture should be valid at any “temperature” p below the “critical temperature” p_c of the spin model, i.e. throughout the “ordered phase”.

We also explore finite size effects on $I_{A,R}$ (see Fig. 4.5(b)). For a fixed $|A| < |A|^*$, we find that $I_{A,R}$ decreases with increasing system size L , consistent with Eq. (4.30). We therefore expect that in the thermodynamic limit, $I_{A,R} = 0$ if and only if $|A| < |A|^*$; the identification between $|A|^*$ and d_{cont} can then be made. In a finite system, we define $|A|^*$ as the size of A for which $I_{A,R} \approx \epsilon$, where ϵ is a small number independent of L .

With this identification, we may now examine how $d_{\text{cont}} = |A|^*$ depends on the system size (as obtained from Fig. 4.5(a,b)). As shown in Fig. 4.5(c), we find that the code distance d_{cont} increases with increasing p , qualitatively consistent with capillary-wave theory. The code distance also grows with L , but as a power-law function, $d_{\text{cont}} \propto L^{\gamma_1}$. The exponent is estimated

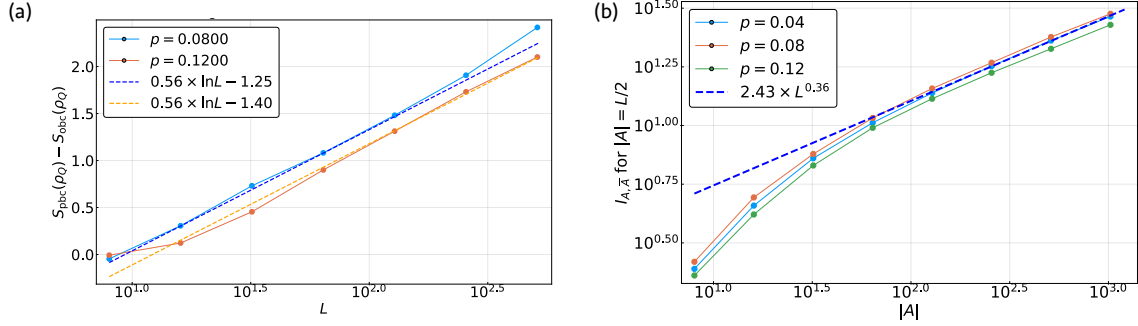


Figure 4.6: (a) The difference between entropies of the entire system as computed for the random Clifford circuit with periodic and open boundary conditions. We observe a logarithmic dependence on the system size, $S_{\text{pbc}}(\rho_Q) - S_{\text{obc}}(\rho_Q) = \zeta \ln L$, with $\zeta \approx 0.56$. This difference has a weak time dependence, but not displayed here. (b) The halfcut mutual information $I_{A, \bar{A}}$ for $|A| = |\bar{A}| = L/2$ as a function of L , with periodic b.c., where we find $I_{A, \bar{A}} \propto L^{\gamma_2}$ with $\gamma_2 \approx 0.36$.

to be $\gamma_1 \approx 0.38$, in agreement with a direct computation (from the algebraic definition of d_{cont}) in Ref. [21]. The power-law scaling of d_{cont} quantitatively differs from capillary-wave theory in Eq. (4.28), where a logarithmic scaling was found.

4.3.2 Clifford dynamics versus (generalized) capillary-wave theory

We next numerically compute a few more quantities that we can compare with capillary-wave theory, as shown in Fig. 4.6. Once again, these results were obtained for the random Clifford circuit with a maximally-mixed initial state, upon averaging over both circuit realizations and the time window $6L < T < 8L$.

In Fig. 4.6(a), we plot the difference between $S(\rho_Q)$ with periodic and open boundary conditions, $\Delta S(\rho_Q) := S_{\text{pbc}}(\rho_Q) - S_{\text{obc}}(\rho_Q)$. Capillary-wave theory (Eqs. (4.21, 4.22)) predicts cancellations of the time dependence as well as of the “surface energy” term, leaving only the extra endpoint entropy term, $(1/2) \ln L$. This logarithmic scaling is indeed observed numerically, with the coefficient of $\ln L$ given by ≈ 0.56 , close in value to that of capillary-wave theory. We have also confirmed a very weak T -dependence of $\Delta S(\rho_Q)$ on intermediate time scales, but the data is not displayed here.

In Fig. 4.6(b), we plot the “halfcut mutual information” [21], $I_{A, \bar{A}}$ with $|A| = |\bar{A}| = L/2$

versus L with periodic b.c.. Upon varying L , we find $I_{A,\bar{A}} \propto L^{\gamma_2}$ with $\gamma_2 \approx 0.36$, and the overall amplitude having a weak dependence on p . As for the code distance in Fig. 4.5(c) which grows with a similar power $\gamma_1 \approx \gamma_2$, this power-law scaling is quantitatively different from capillary-wave theory. The latter predicts a logarithmic scaling, $I_{A,\bar{A}} = (7/2) \ln L$ for $T \propto L$.

To account for the power-laws in Fig. 4.5(c) and Fig. 4.6(b), we introduce a phenomenological description, which we call “generalized capillary-wave” (GCW), with the following (minimal) modifications of the free energies for “pinned” and “waist” domain walls (Eqs. (4.21, 4.22)), respectively

$$\begin{aligned}
 & F_{\text{GCW}}(A) \\
 &= \beta\sigma|A| + \chi|A|^\gamma, \quad \text{when } T \gg L^\zeta \gg |A|^\zeta,
 \end{aligned} \tag{4.37}$$

$$\begin{aligned}
 & F_{\text{GCW}}(Q) \\
 &= \begin{cases} \beta\sigma L - \ln T, & \text{open b.c.} \\ \beta\sigma L - \ln \frac{T}{L^\zeta}, & \text{periodic b.c.} \end{cases} \quad \text{when } T \gg L^\zeta.
 \end{aligned} \tag{4.38}$$

Here $0 \leq \gamma < 1$ is the exponent characterizing domain wall free energies in GCW, and $0 < \zeta < 1$ is the exponent of vertical extent of the domain walls.¹³ The constant χ is expected to be independent of $|A|, L, T, \beta\sigma$. Capillary-wave theory thus has $\gamma_{\text{CW}} = 0$ and $\zeta_{\text{CW}} = \frac{1}{2}$; compare Eqs. (4.21, 4.22). This generalization of capillary-wave theory remains qualitatively consistent with Fig. 4.5(a,b) and Fig. 4.6(a), where we found $\zeta \approx 0.56$.

Eqs. (4.37, 4.38), together with the definition of $|A|^*$ in Eq. (4.28),¹⁴ lead to the following

¹³Notice that with $0 < \zeta < 1$, we still have $T \gg L^\zeta$ for $6L < T < 8L$, the time window we took in the numerics. As we saw in Fig. 4.6(a), the exponent $\zeta \approx 0.56$ falls within this range, and seems to be close in value to $\zeta_{\text{CW}} = 1/2$.

¹⁴We note that the form of Eq. (4.30) is identical for capillary-wave theory and its generalization in Eqs. (4.37, 4.38), since in its derivation we only kept the leading linear term, which is common for both cases. Thus the identification between $|A|^*$ and d_{cont} can still be made for GCW.

scaling behaviors for the code distance and half-cut mutual information,

$$d_{\text{cont}} = |A|^* \approx \frac{\chi}{2\beta\sigma} L^\gamma, \quad (4.39)$$

$$I_{A,\bar{A}} \propto L^\gamma. \quad (4.40)$$

These are both consistent with our Clifford numerics in Fig. 4.5(c) and Fig. 4.6(b), provided we take $\gamma = \gamma_1 = \gamma_2$.

We emphasize that Eqs. (4.37, 4.38) are phenomenological, motivated by both capillary-wave theory and our Clifford numerics (specifically Fig. 4.5(c) and Fig. 4.6(b)). At this moment we do not have a theory from which these free energies can be derived.

We note that direct numerical computations of $S(\rho_A)$ (for $|A| \ll L$) and $S(\rho_Q)$ are qualitatively consistent with both capillary wave theory (Eqs. (4.21, 4.22)) and its generalization in Eqs. (4.37, 4.38), as established in Refs. [59, 21]. In particular,

- For the approximation $S(\rho_A) \approx F_{\text{CW}}(A)$ when $|A| \ll L$, the “linear plus log” form of $F_{\text{CW}}(A)$ is consistent with the stabilizer length distribution [59];
- For the approximation $S(\rho_Q) \approx F_{\text{CW}}(Q)$, the $-\ln T$ dependence on circuit depth is consistent with an exponentially long purification time [21].

On the other hand, a quantitative comparison between capillary-wave theory and GCW is tricky, due to the difficulty in distinguishing a logarithmic function from a small power-law in the presence of a background linear term. Thus, we will not here attempt to compare capillary-wave theory and GCW for the quantities $S(\rho_A)$ (with $|A| \ll L$) and $S(\rho_Q)$.

4.4 Discussion

4.4.1 Summary

In this Chapter we established a correspondence between QECCs generated by random hybrid Clifford circuit dynamics, and the statistical mechanics of fluctuating “entanglement

domain walls”. The number of encoded logical qubits k of the QECC maps to the “surface energy” that is extensive in the number of physical qubits $|Q|$, and the code distance maps to a crossover length scale proportional to the “entropy” of transverse fluctuations, that is subextensive in $|Q|$. Fluctuations of entanglement domain walls are entirely responsible for the diverging code distance, which protects the state against local (undetectable/uncorrectable) errors, a characteristic property of QECCs.

Our results rest upon two well-motivated assumptions, namely the validity of the entanglement domain wall picture, and the “linear plus sublinear” form of their free energies. The former has been analytically established in the context of hybrid random Haar circuits [30, 31], and the latter follows from the former within capillary-wave theory. We expect that both assumptions are also valid for Clifford circuits, as supported by the Clifford numerics in Refs. [59, 21], as well as those in Sec. 4.3.

We emphasize that the qualitative properties of the QECC do not depend crucially on the specific form of the entropic term, which diverges logarithmically with $|Q|$ in capillary-wave theory, and as a small power-law in our Clifford numerics. The latter is possibly described by a certain generalization of capillary-wave theory. In some sense, one can view capillary-wave theory as a “mean-field theory” of the entanglement domain walls.

4.4.2 The diverging code distance as a self-consistency condition

The error correcting nature of the dynamically generated state, as exemplified by the diverging code distance, is consistent with the resilience of this finite entropy-density (and code rate) state to repeated local measurements. Indeed, a measurement decreases the entropy only if the measured operator is a nontrivial logical operator (see Sec. 4.1.3), and with a diverging code distance the probability of each local measurement in the circuit (Fig. 4.1) being a logical operator (denoted p_{logical}) vanishes in the thermodynamic limit (equivalently, each qubit in Q decouples from the reference state R with probability one). We can estimate p_{logical} by setting $|A| = 1$ in Eq. (4.30), giving $p_{\text{logical}} \propto \ell_A = I_{A,R} \approx \exp[-2\beta\sigma d_{\text{cont}}]$, leading to $p_{\text{logical}} \propto L^{-2}$

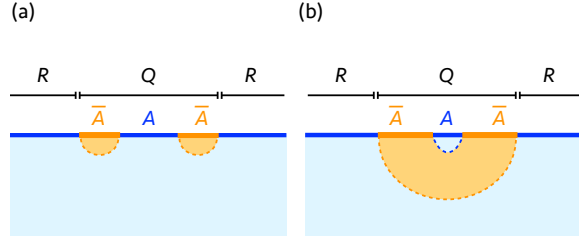


Figure 4.7: The circuit, when dynamically evolving an initial pure state, can also be incorporated in the QECC framework by taking an extensive subsystem Q as the QECC, and the complement of Q as the reference R , with $|Q| < |R|$. When $A > d_{\text{cont}}$, the dominant domain wall configuration is shown in (a), and in this regime, A and R have nonvanishing correlation. On the other hand, when $A < d_{\text{cont}}$ the dominant domain wall configuration is the “rainbow diagram” shown in (b), implying that A and R should fully decouple (for $|Q|$ large), with vanishing mutual information. In this regime, an error on A will have no effect on $S(\rho_Q)$.

within capillary-wave theory for $T \propto L$, and $p_{\text{logical}} \propto \exp[-\chi L^\gamma]$ within a generalized capillary-wave description. In either case, this leads to a vanishing rate of purification in the mixed phase when $O(L)$ measurements are made in each time step [21], and subsequently to the stability of the finite code rate.¹⁵

Our discussion above is not an explanation of the stability of the mixed phase, but a requirement of self-consistency, since the diverging code distance is itself computed from the steady state within the mixed phase. The domain wall picture itself also requires the assumption of an ordered phase.

Moreover, a quantum Hamming bound [147, 44] on p_c , as in Ref. [22], cannot be inferred from our discussion. Besides the code distance being subextensive rather than extensive, here we are viewing the one-qubit measurements within one circuit time step as a sequence of one-qubit errors, rather than a single $p|Q|$ -qubit error. With respect to these single qubit errors, the code is highly degenerate, and the Hamming bound does not apply.

Finally, we mention that QECCs can also be dynamically generated for circuits with a pure initial state in the volume law entangled phase when $p < p_c$ [20, 22], if we take the “system”

¹⁵When T is allowed to be independent of and longer than L , capillary-wave theory gives,

$$p_{\text{logical}} \propto (LT)^{-1} \Rightarrow \frac{dS(\rho_Q)}{dT} \approx -(pL)p_{\text{logical}} \propto T^{-1},$$

consistent with Eq. (4.22) and an exponentially long purification time (see Sec. 4.2.5).

Q to be an extensive subsystem, R to be the complement of Q with $|R| > |Q|$, and consider the decoupling of $A \subseteq Q$ from R (see Fig. 4.7). Indeed, in this case our Clifford numerics (not shown) demonstrate the presence of these decoupling conditions (e.g. a vanishing $I_{A,R}$ for $|A| < |A|^* = d_{\text{cont}}$), qualitatively consistent with capillary-wave theory. Other results within this setup should be similar to those obtained in Refs. [59, 20, 22].

4.4.3 The role of disorder

As for random Haar circuits [30, 31] and random tensor networks [85], the identification in Eq. (4.18) is between free energies in the stat. mech. model and entanglement entropies *averaged* over an ensemble of circuits. Thus we have been studying the averaged entropies, and comparing them with (generalized) capillary-wave theory. Capillary-wave theory assumes translational symmetry by construction, with no reference to sample-to-sample fluctuations or the role of disorder.

In Fig. 4.8, we present the statistical sample-to-sample fluctuation of $S(\rho_A)$ over an ensemble of random Clifford circuits, versus the subregion size $|A|$, for $0 \leq |A| \leq L/2$. Previously in Ref. [59], the distribution of $S(\rho_A)$ was found to be Gaussian-like. Here, we find the following power-law scaling for the standard deviation (square root of the variance) of the entropy, $\sqrt{\text{var}[S(\rho_A)]} \propto |A|^{0.33}$, with an amplitude that depends weakly on p . This power-law behavior is interesting, yet beyond *any* generalization of capillary-wave theory, as the latter always describes a clean system, for which the notion of an ensemble of disorder realizations is irrelevant. This result suggests that disorder could dramatically modify the structure of the domain walls, possibly accounting for the power-law dependences in d_{cont} and $I_{A,\bar{A}}$ in Sec. 4.3.

We remark that the exponent for the standard deviation 0.33, as well as the exponent $\gamma \approx 0.36$, are both close to the exponent $1/3$ for subextensive corrections to free energies of a directed polymer in random media (DPRM) [148, 149, 150, 151] that falls within the Kardar–Parisi–Zhang (KPZ) universality class [152]. Such corrections are due to quenched disorder. We note that similar scaling behaviors have been found in random unitary circuits *without*

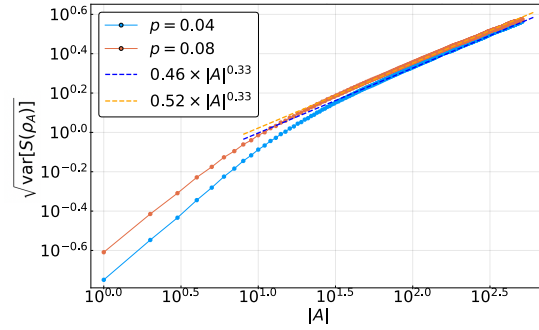


Figure 4.8: The sample-to-sample fluctuation of $S(\rho_A)$ as a function of $|A|$, obtained from an ensemble of random Clifford circuits. We take $L = 1024$ and $0 \leq |A| \leq L/2$.

measurements [72, 28, 29, 137]. This picture was recently confirmed in Ref. [35], that the entanglement domain walls are indeed DPRM-like. In this context, it could be interesting to find “clean” circuit models, for which effects of quenched disorder are absent, so that the subleading “entropic” term only receives contribution from thermal fluctuations, just like simple Ising domain walls. These open issues are left for future work.

Chapter 5

Linear cross entropy benchmark for experimental observation of the phase transition

Open quantum dynamics host a rich phenomenology, including a family of measurement-induced phase transitions (MIPT) in the scaling of entanglement along quantum trajectories in monitored systems [16, 18, 17, 20, 21, 30, 31]. While the MIPT occurs generically in a number of different models (see for example [63, 59, 153, 154, 36, 155, 38, 39, 37, 156, 157, 41, 158, 159, 160, 161, 162, 51, 52], among others), its verification can be challenging even on an error-corrected quantum computer, due to the so-called “postselection problem”. Quantum trajectories are labeled by the measurement history \mathbf{m} , whose length is extensive in the space-time volume V of the circuit; thus, the number of possible trajectories \mathbf{m} is exponential in V , but they each occur with roughly the same probability. On the other hand, one needs multiple copies of the same \mathbf{m} in order to verify any quantum entanglement; and then many different \mathbf{m} to perform a proper statistical average. On a quantum simulator there is no general recipe for producing such copies other than running the quantum circuit many times and waiting until the measurement results coincide (“postselection”). In other words, the preparation of the

output state is not readily “repeatable”, and $O(e^V)$ runs of the circuit are required to generate multiple copies, thus severely restricting the scalability of such experiments. Nevertheless, in an impressive recent experiment that carries out postselection [163], the MIPT is observed for small system sizes.

More generally, the postselection problem can be avoided in two cases. First, when only Clifford circuits are considered, the entanglement can be verified by “decoding” the circuit, either through a full classical simulation within the stabilizer formalism [164] or via machine learning [165]. With machine learning the authors claim that “decoding” is possible also beyond Clifford circuits, although they did not explore this in detail. Second, when the non-unitary (monitored) dynamics is a spacetime dual of a unitary one [166, 167, 168], postselection is partially ameliorated, the output state preparation becomes repeatable, and correspondences between unitary dynamics and monitored dynamics can be made.

Here we propose another experimental protocol for verifying the MIPT in random circuits, by estimating the “linear cross-entropy” (denoted χ) between the probability distribution of (bulk-circuit) measurement outcomes \mathbf{m} in two samples with the same bulk but different initial states, ρ and σ . This quantity was previously discussed by Bao *et. al.* [31], and is closely related to the order parameter proposed by Gullans and Huse [21, 113]. In terms of the spin model description of the MIPT [31, 30], χ can be interpreted as a boundary correlation function. Moreover, as we establish both numerically and analytically, in the thermodynamic limit $\chi = 1$ in the volume law phase. However, even though all samples of \mathbf{m} would contribute to χ — since no postselection is involved — measuring the difference between the probability distributions of the two initial states to estimate χ in a generic circuit to a constant precision ε still requires $O(e^V)$ samples of \mathbf{m} , and is thus unfeasible (see Eq. (5.6) below). In Sec. 5.1, we show that this issue can be resolved (again) in Clifford circuits, where χ can be efficiently sampled by running the ρ -circuit on a quantum simulator, aided by a classical simulation of the σ -circuit. In particular, for a fixed circuit we estimate the number of samples of \mathbf{m} scales as $\text{poly}(1/\varepsilon)$. We provide numerical evidence that χ is an order parameter for the MIPT (i.e. $\chi = 1$ in the

volume law phase and $\chi < 1$ in the area law phase), and simulate the effect of depolarizing noise.

We note that a comparison between two circuits is necessary, and it is likely very difficult to locate the transition by looking at the distribution over measurement outcomes in a single circuit. The Shannon entropy of the distribution can be mapped to the free energy of an underlying spin model [169], whose leading term is extensive in the spacetime volume of the circuit. An exponential number of runs of the circuit seems necessary in order to learn anything from the measurements.

By choosing the circuit bulk to be composed of Clifford operations and σ to be a stabilizer state, the protocol is scalable on both the quantum and the classical sides. Nevertheless, unless ρ is also a stabilizer state, the circuit output state is still highly nontrivial and hard to represent classically. In Appendix F, we consider one nontrivial aspect of the output state in the volume law phase, and show that with a generic (non-stabilizer) choice of ρ the probability distribution over the output bitstrings obeys a nontrivial distribution with a long tail, similar to, but different in detail than, the Porter-Thomas distribution from purely unitary random circuits. We discuss possible implications of this result.

5.1 Linear cross-entropy and an order parameter

We consider the “hybrid” circuit shown in Fig. 5.1, composed of both unitary gates on nearest-neighbor qubits and single-site measurements in the bulk, performed with probability p at each qubit within each time step. By convention, each time step contains $L/2$ unitary gates. Different from the usual setup [59], we have an additional “encoding” stage before the hybrid evolution for time $t_{\text{encoding}} = 2L$, following Ref. [21]. The reason for this somewhat unusual choice is practical, to get a clearer experimental signal of the MIPT; see Sec. 5.1.3. We call the evolution after the encoding stage the “circuit bulk”, which lasts for another $t_{\text{bulk}} = 2L$. The total circuit time is $T = t_{\text{encoding}} + t_{\text{bulk}} = 4L$.

For concreteness, we take all the measurements to be of the Pauli Z operator. Given a

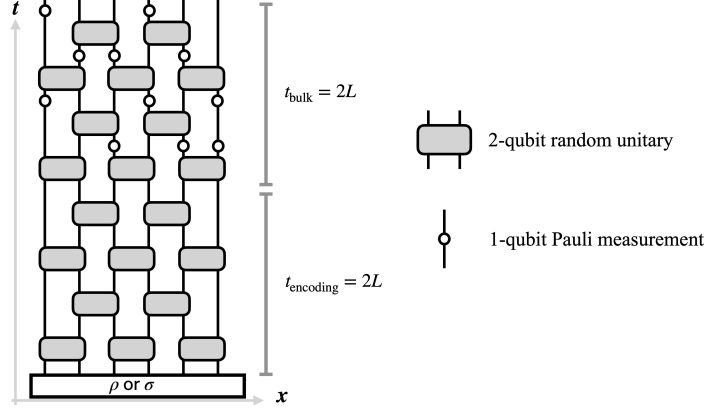


Figure 5.1: The layout of the hybrid circuit considered in this Chapter. Different from the usual setup [59], we have an additional “encoding” stage before the hybrid evolution for time $t_{\text{encoding}} = 2L$, following Ref. [21]. We call the evolution after the encoding stage the “circuit bulk”, which last for another $t_{\text{bulk}} = 2L$. The total circuit time is $T = t_{\text{encoding}} + t_{\text{bulk}} = 4L$. We will compare two different initial states ρ and σ (left unspecified for the moment) undergoing the same circuit evolution.

circuit layout (i.e. the locations of unitary gates and measurements) and the unitary gates in the bulk – which we denote collectively as C – the *unnormalized* output state is defined by C and the measurement record $\mathbf{m} = \{m_1, m_2, \dots, m_N\}$ as

$$\rho_{\mathbf{m}} = C_{\mathbf{m}} \rho C_{\mathbf{m}}^{\dagger}, \quad (5.1)$$

where $C_{\mathbf{m}}$ is the time-ordered product of all the unitaries and projectors in the circuit, written schematically as

$$\begin{aligned} C_{\mathbf{m}} = & P_{m_N} P_{m_{N-1}} \cdots P_{m_{N-N_T+1}} \cdot U_T \\ & \cdot P_{m_{N-N_T}} \cdots P_{m_{N-N_T-N_{T-1}+1}} \cdot U_{T-1} \\ & \cdot P_{m_{N-N_T-N_{T-1}}} \cdots P_{m_{N-N_T-N_{T-1}-N_{T-2}+1}} \cdot U_{T-2} \\ & \cdots \end{aligned} \quad (5.2)$$

Here each line contains all quantum operations in one circuit time step, and N is the total number of measurements, which is proportional to the spacetime volume of the circuit, $N \propto$

$pV = pLT$. The corresponding probability of obtaining \mathbf{m} is given by

$$p_{\mathbf{m}}^{\rho} = \text{tr } \rho_{\mathbf{m}}. \quad (5.3)$$

We define similar quantities for a different initial state σ ,

$$\sigma_{\mathbf{m}} = C_{\mathbf{m}} \sigma C_{\mathbf{m}}^{\dagger}, \quad (5.4)$$

$$p_{\mathbf{m}}^{\sigma} = \text{tr } \sigma_{\mathbf{m}}. \quad (5.5)$$

With these, we define the (normalized) linear cross-entropy of the circuit between the two initial states as

$$\chi_C = \frac{\sum_{\mathbf{m}} p_{\mathbf{m}}^{\rho} p_{\mathbf{m}}^{\sigma}}{\sum_{\mathbf{m}} (p_{\mathbf{m}}^{\sigma})^2}. \quad (5.6)$$

Here, after averaging over \mathbf{m} , χ_C only depends on the circuit C , and we have explicitly included this dependence in our notation. Finally, we take its average over C ,

$$\chi := \mathbb{E}_C \chi_C = \mathbb{E}_C \frac{\sum_{\mathbf{m}} p_{\mathbf{m}}^{\rho} p_{\mathbf{m}}^{\sigma}}{\sum_{\mathbf{m}} (p_{\mathbf{m}}^{\sigma})^2}. \quad (5.7)$$

It was previously pointed out [31] that χ corresponds to the free energy cost after fixing a boundary condition in a (replicated) spin model [28, 29, 30, 31]; in Appendix E we provide a similar calculation for our circuit with the “encoding” stage. From this derivation we expect $1 - \chi = e^{-L}$ for large L in the volume law phase ($p < p_c$), and $1 - \chi > 0$ in the area law phase ($p > p_c$), even as $L \rightarrow \infty$.

The physical meaning of χ should be clear: it quantifies the difference between the probability distributions over measurement histories for the two initial states. In the volume law phase, $\chi = 1$ implies the impossibility of distinguishing different initial states from bulk measurements, due to the “coding” properties of this phase (i.e. the dynamics in the volume law phase generates a “dynamical quantum memory” [21, 20, 22, 61, 23, 24]). The code breaks down when p is

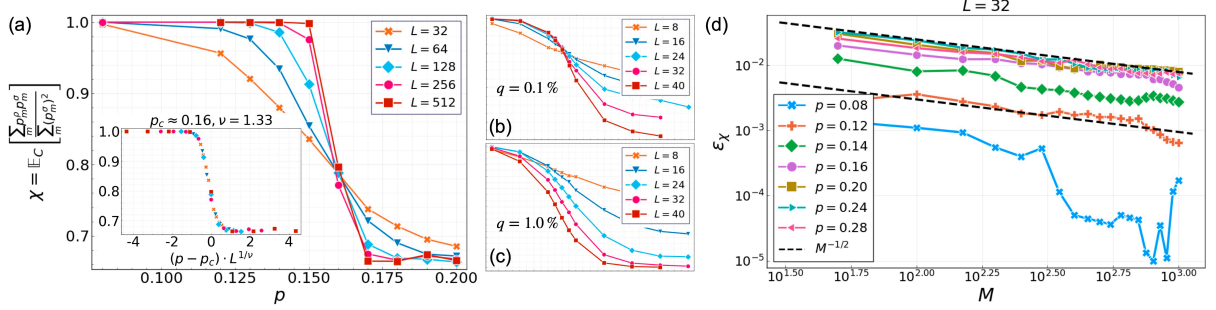


Figure 5.2: (a) Numerical results for χ_C when averaged over Clifford circuits in the bulk (denoted by \mathbb{E}_C), with the initial states $\rho = \frac{1}{2^L}\mathbb{1}$ and $\sigma = (|0\rangle\langle 0|)^{\otimes L}$. Here, for each C , the calculation is exact, and M can be thought of as infinity in Eq. (5.11). (Inset) Collapsing the data to a scaling form, with parameters p_c and ν close to those found near the MIPT in entanglement entropy [17, 59]. (b,c) The behavior of χ when depolarizing noise is present in the ρ -circuit. As we see, at noise rate $q = 0.1\%$ (b), there is still evidence for a phase transition, although the location of the transition has shifted from $p_c \approx 0.16$ to $p_c \approx 0.14$. At noise rate 1% (c), there is no crossing, and any signature of the phase transition is completely washed out. (d) The fluctuation in χ from a finite number M of samples, as defined in Eq. (5.12).

increased past the transition, and χ saturates to a finite, nonuniversal constant strictly smaller than 1. In this phase, information about the initial state leaks into the measurement outcomes.

5.1.1 Typical-case hardness of estimating χ

We first briefly outline a protocol for estimating χ , in close analogy with the linear cross-entropy benchmark (“linear XEB”) for random unitary circuits; then we discuss its limitations when applied to the MIPT.

Consider running the circuit with initial state ρ (“the ρ -circuit”) on a quantum simulator. From the simulation we obtain a measurement record \mathbf{m} , an event that occurs with probability $p_{\mathbf{m}}^{\rho}$. Given \mathbf{m} we can perform a classical simulation with the initial state σ , and calculate the corresponding probability $p_{\mathbf{m}}^{\sigma}$. Repeating this M times, we obtain a sequence of probabilities $\{p_{\mathbf{m}_1}^{\sigma}, p_{\mathbf{m}_2}^{\sigma}, \dots, p_{\mathbf{m}_M}^{\sigma}\}$. Their mean converges to the numerator of Eq. (5.6),

$$\lim_{M \rightarrow \infty} \left\langle p_{\mathbf{m}_{j=1}^M}^{\sigma} \right\rangle_{\rho} := \lim_{M \rightarrow \infty} \frac{1}{M} \sum_{j=1}^M p_{\mathbf{m}_j}^{\sigma} = \sum_{\mathbf{m}} p_{\mathbf{m}}^{\rho} p_{\mathbf{m}}^{\sigma}. \quad (5.8)$$

The denominator of Eq. (5.6) can be estimated similarly with a separate classical simulation,

by running the σ -circuit M' times, and computing the mean of probabilities $\{p_{\mathbf{m}_j}^\sigma\}$. This way we get

$$\lim_{M' \rightarrow \infty} \left\langle p_{\mathbf{m}_{j=1}^{M'}}^\sigma \right\rangle_\sigma := \lim_{M' \rightarrow \infty} \frac{1}{M'} \sum_{j=1}^{M'} p_{\mathbf{m}_j}^\sigma = \sum_{\mathbf{m}} (p_{\mathbf{m}}^\sigma)^2. \quad (5.9)$$

Although both equations above are well-defined, and in this protocol each run of the circuit is used (i.e. no postselection is required), obtaining these estimates is not practical. Each of Eq. (5.8) and Eq. (5.9) are of the order $O(e^{-N})$, and an accurate estimate of them would require $M, M' = O(e^N)$, to avoid numerical uncertainty in the ratio. As such, one still needs $O(e^N)$ runs of both the quantum and the classical simulation — a complexity similar to the postselection problem. This might be one reason why this quantity has not been considered much in the context of MIPT after Ref. [31].

5.1.2 Numerical methods and results

Here we focus on the case where σ is a stabilizer state, and the circuit bulk $C_{\mathbf{m}}$ is composed of stabilizer operations (Clifford gates and Pauli measurements) [45, 67, 68]. In this special case, the denominator of Eq. (5.6) can be computed exactly in polynomial time, without doing any sampling as in Eq. (5.9) (see Appendix E.3 for details). Thus, we may rewrite Eq. (5.6) as

$$\chi_C = \sum_{\mathbf{m}} p_{\mathbf{m}}^\rho \frac{p_{\mathbf{m}}^\sigma}{\sum_{\mathbf{m}} (p_{\mathbf{m}}^\sigma)^2}, \quad (5.10)$$

and in analogy with Eq. (5.8),

$$\chi_C = \lim_{M \rightarrow \infty} \left\langle \frac{p_{\mathbf{m}_{j=1}^M}^\sigma}{\sum_{\mathbf{m}} (p_{\mathbf{m}}^\sigma)^2} \right\rangle_\rho. \quad (5.11)$$

For each run of the ρ -circuit, we can compute $\frac{p_{\mathbf{m}_j}^\sigma}{\sum_{\mathbf{m}} (p_{\mathbf{m}}^\sigma)^2}$ in polynomial time, and take its mean over runs. The new “observable” $\frac{p_{\mathbf{m}_j}^\sigma}{\sum_{\mathbf{m}} (p_{\mathbf{m}}^\sigma)^2}$ should be typically of $O(1)$, and this average converges much more quickly with increasing M (than in the generic case, by taking the ratio of

Eq. (5.8) and Eq. (5.9) for large but finite M and M' .

Now we provide numerical results for χ across the transition. We consider two types of choices for the state ρ , but take σ to be a stabilizer state in both cases.

Stabilizer state ρ versus stabilizer state σ

We first take ρ to be a stabilizer state, while keeping σ another stabilizer state. As we explain in Appendix E.3, now χ_C in Eq. (5.10) admits a closed form expression that does not involve any summation over \mathbf{m} , see Eq. (E.18). This allows an exact calculation of χ_C without the need of performing any sampling, at the cost of introducing N extra qubits that records the measurement history. These qubits are usually called “registers”.

A further simplification occurs when ρ is obtainable from σ via erasure or dephasing channels, so that the N register qubits can also be dispensed with; see Eq. (E.22). We will focus on this case below, where the numerical simulation is most scalable so that we can confidently extrapolate the results to more general choices of ρ .

In Fig. 5.2(a), we plot $\chi = \mathbb{E}_C \chi_C$ for $\rho = \frac{1}{2^L} \mathbb{1}$ and $\sigma = (|0\rangle\langle 0|)^{\otimes L}$, which satisfies the condition above. The data shows a clear “crossing” of χ near the transition, confirming our expectation that χ can be used to determine the location and the nature of the MIPT. Indeed, in the large L limit and for $p < p_c$, χ approaches unity, demonstrating that the measurement distribution functions become equal, independent of the initial state. Moreover, data collapse in Fig. 5.2(d) shows good agreement to a standard scaling form, with numerical values of the location of the transition p_c and of the critical exponent ν close to previous characterizations of the MIPT [59].

Although in the exact method for Fig. 5.2(a) no sampling of the measurement results is needed in the numerics (and we have essentially taken the limit $M \rightarrow \infty$ in Eq. (5.11)), we nevertheless simulate the sampling process for a finite M and compute the mean in Eq. (5.11). By

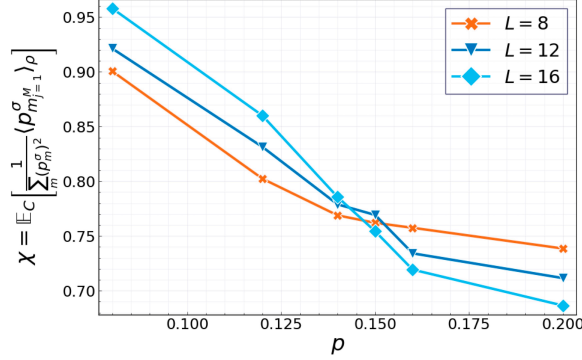


Figure 5.3: Numerical results of χ for initial states $\rho = (|0\rangle\langle 0|)^{\otimes L/2} \otimes (|T\rangle\langle T|)^{\otimes L/2}$ (see Eq. (5.13)) and $\sigma = (|0\rangle\langle 0|)^{\otimes L}$, following the procedure in Eq. (E.24). Despite a different choice of initial state and smaller system sizes, the results are qualitatively similar to Fig. 5.2(a).

comparing this to the exact result, we calculate the following measure of statistical fluctuations,

$$\varepsilon_\chi := \mathbb{E}_C \left[\left| \left\langle \frac{p_{\mathbf{m}_{j=1}}^\sigma}{\sum_{\mathbf{m}} (p_{\mathbf{m}}^\sigma)^2} \right\rangle_\rho - \chi_C \right| \right]. \quad (5.12)$$

As we increase M we find $\varepsilon_\chi \propto M^{-1/2}$, as shown in Fig. 5.2(d). This is consistent with the samples $\left\{ \frac{p_{\mathbf{m}_{j=1}}^\sigma}{\sum_{\mathbf{m}} (p_{\mathbf{m}}^\sigma)^2} \right\}$ being bounded and having weak correlations.

We also consider the effect of depolarizing noise, occurring randomly in the ρ -circuit with probability q per qubit per time step; whereas the σ -circuit is still taken to be noiseless. The setup is to mimic an experimental sampling procedure, where we run the ρ -circuit on a quantum processor subject to noise, whereas our supplementary classical simulation of the σ -circuit is noiseless. The depolarizing noise acts as a symmetry-breaking field in the effective spin model [30, 31, 60, 35, 170, 166, 167],¹ and in its presence the MIPT is no longer sharply defined. Nevertheless, evidence of the MIPT may still be observable if the error rate is small compared to the inverse spacetime volume of the circuit, as we see in Fig. 5.2(b,c).

Magic state ρ versus stabilizer state σ

We take ρ to be a non-stabilizer state, and σ to be a stabilizer state. In particular, we choose a state with $|0\rangle$ and $|T\rangle$ on alternating sites,

$$\rho = \bigotimes_{i=1}^{L/2} (|0\rangle\langle 0|_{2i-1} \otimes |T\rangle\langle T|_{2i}), \quad (5.13)$$

where $|T\rangle = \frac{1}{\sqrt{2}} (|0\rangle + e^{i\pi/4} |1\rangle)$ is a magic state. We still take the other initial state to be $\sigma = (|0\rangle\langle 0|)^{\otimes L}$.

Based on our calculation in Appendix E, we expect χ_C to exhibit similar behavior as in Sec. 5.1.2. This is confirmed in Fig. 5.3, where we follow the sampling procedure in Eq. (5.11). In particular, for a given C , we take $L \in \{8, 12, 16\}$, and sample $M = 100$ measurement trajectories, and compute $\left\langle \frac{p_{\mathbf{m}}^{\sigma M}}{\sum_{\mathbf{m}} (p_{\mathbf{m}}^{\sigma})^2} \right\rangle_{\rho} \approx \chi_C$. We then take the average over many different choices of C , namely $\mathbb{E}_C \left\langle \frac{p_{\mathbf{m}}^{\sigma M}}{\sum_{\mathbf{m}} (p_{\mathbf{m}}^{\sigma})^2} \right\rangle_{\rho} \approx \mathbb{E}_C \chi_C$. We observe a crossing of χ near $p \approx p_c \approx 0.16$.

It is interesting to notice that though the classical side of the computation (the σ -circuit) can be carried out efficiently, the quantum side (the ρ -circuit) is still classically hard [174]. This limits the system sizes that we can access classically in Fig. 5.3, but we hope larger system sizes can be achieved on near-term quantum processors.

5.1.3 Necessity of the encoding stage

Here we briefly discuss the choice of the circuit architecture in Fig. 5.1, in particular the inclusion of an encoding stage. In the usual setup [59] without the encoding stage, and when the two initial states differ on an extensive number of qubits, χ should vanish as $L \rightarrow \infty$ for all values of p , and thus cannot be used to probe the transition (see Appendix E.2). When ρ and σ differ only on a constant number of qubits [21, 31], χ would be instead related to a local

¹See also Refs. [171, 172, 173] for related discussion in random unitary circuits.

spontaneous magnetization [113], having the following scaling form near the transition,

$$\bar{\chi} \approx \begin{cases} |p - p_c|^\beta + \chi_0, & p < p_c \\ \chi_0, & p > p_c \end{cases},$$

see Appendix E.2 for a detailed discussion. In this case, we do not expect a crossing as in Fig. 5.2, but instead a collapse of the curves for different system sizes L . In experiments, a collapse is likely harder to detect than a crossing. Moreover, the collapse will be more susceptible to noise for a given system size; compare Fig. 5.2(b,c). For this reason, we have chosen to focus on the circuit with an encoding stage throughout the Chapter.

Moreover, for the purpose of observing MIPT, including the encoding stage should only introduce minor experimental overhead. For example, noise in the encoding stage $t \in [0, t_{\text{encoding}}]$ would not affect the signal for MIPT in any important way as its effect can be accounted for by a different choice of ρ , which is not essential (see discussions in Appendix E); only noise in the circuit bulk $t \in [t_{\text{encoding}}, t_{\text{encoding}} + t_{\text{bulk}}]$ is important (see Fig. 5.2(b,c)).

5.2 Discussions

Our protocol requires a simulation of many instances of the random hybrid circuit with mid-circuit measurements, and for each instance $O(1/\varepsilon^2)$ trajectories to estimate the cross-entropy to accuracy ε . This should be a task of similar complexity to Google’s simulation of random unitary circuits [14], except that here we do not make measurements on the output state but in the bulk. However, different from that experiment, for observing the MIPT it suffices to focus on Clifford circuits, for which the classical simulation is not hard. This protocol is thus scalable as the quantum processors. Our protocol does not require extra quantum operations, and is flexible in the choice of the initial state. The signal for the phase transition persists at $L = 40$ for sufficiently weak ($\approx 0.1\%$) depolarizing noise. Thus, we hope this protocol might be achievable on existing or near-term devices.

We emphasize that if the circuit is not composed of Clifford gates, our protocol is expected to require exponential classical resources. It is presently unclear whether it is in fact possible to probe the MIPT beyond Clifford circuits with polynomial resources [165].

Although the classical simulation is chosen to be easy for practical purposes, in our protocol the quantum simulation is classically hard for a generic choice of the initial state, which would result in a highly nontrivial output state. Our numerical results in Appendix F suggest that sampling measurement outcomes on the output state of the quantum simulation is classically hard in the volume law phase. Whether this can be used in practice for demonstrating quantum advantage is not known, due to apparent need of postselection of sampling from this distribution.

Another interesting question is the (classical) sampling complexity of the bulk measurement outcomes in a hybrid Clifford circuit with magic initial states. We have shown that the bulk measurement history in the volume law phase does not depend on the initial state, and thus may be reproduced in polynomial time for a Clifford circuit with a stabilizer initial state. Similarly, in the area law phase and at the critical point, a classical simulation using matrix product states can (also) serve as a polynomial-time sampler, due to low entanglement entropy. Thus, in one spatial dimension, sampling classically from the bulk measurement outcome distribution should, in principle, always be easy. The situation is much less clear in the area law phase of two dimensional hybrid circuits [160, 175].

Appendix A

Brief review of the stabilizer formalism and gauge fixing

A.1 Basics

In this subsection we review the stabilizer formalism and Clifford circuits. The references for this subsection are Refs. [44, 67, 69, 68, 72].

A.1.1 Codewords, stabilizers, and gauge freedom

The defining property of the Clifford circuit is that the pure state wavefunction $|\psi\rangle$ at any time is a *codeword*, the simultaneous $+1$ eigenstate of L mutually commuting and linear independent (under multiplication) Pauli string operators

$$\mathcal{G} = \{g_1, \dots, g_L\} \subset \mathcal{P}_+(L), \quad \mathcal{P}_+(L) = \{g \in \mathcal{P}(L) : g^2 = 1\}, \quad (\text{A.1})$$

among which none of the g_i 's is proportional to the identity. These Pauli string operators generate the *stabilizer group* [44, 132] of the codeword, denoted $\mathcal{S}(|\psi\rangle) = \langle \mathcal{G} \rangle$, or simply \mathcal{S} . The codeword is uniquely determined given the stabilizer group, and the stabilizer group is uniquely

determined given the codeword $|\psi\rangle$,

$$\mathcal{S} = \{g \in \mathcal{P}_+(L) : g|\psi\rangle = |\psi\rangle\}. \quad (\text{A.2})$$

One can explicitly write down all elements of \mathcal{S} given \mathcal{G} ,

$$\mathcal{S} = \{g_1^{p_1} g_2^{p_2} \dots g_L^{p_L} : (p_1, \dots, p_L) \in \{0, 1\}^L\}. \quad (\text{A.3})$$

In this case, we also write $\mathcal{G} = \mathcal{G}(\mathcal{S})$, which means the same thing as $\mathcal{S} = \langle \mathcal{G}(\mathcal{S}) \rangle$. Because of the linear independence of \mathcal{G} , each element of \mathcal{S} has a unique representation in this form, hence there is a one-to-one mapping between $\{0, 1\}^L$ and \mathcal{S} . It follows that \mathcal{S} is a finite abelian group of order $|\mathcal{S}| = 2^L$.

Being a finite abelian group, and with each element of order 2, \mathcal{S} can be viewed as an L -dimensional vector space on \mathbb{Z}_2 , and group multiplication can be viewed as addition in this vector space (ignoring phase factors). Thus, an independent generating set $\mathcal{G}(\mathcal{S})$ corresponds to a choice of basis for this vector space. Such a choice is not unique, and the freedom in choosing $\mathcal{G}(\mathcal{S})$ is referred to as the *gauge freedom* in this paper.

For the rest of this appendix, we will always take $\mathcal{G}(\mathcal{S})$ to be an independent generating basis (thus has L elements), and use the word *stabilizer* for elements of $\mathcal{G}(\mathcal{S})$. When we talk about a codeword state, we mostly work with its stabilizers, $\mathcal{G}(\mathcal{S})$.

A.1.2 Simulating Clifford circuits

We briefly review our simulation of the Clifford circuits with Pauli measurements. The main result we use is the Gottesman-Knill theorem.

First consider the action of a unitary operator, U . For a state $|\psi\rangle$ whose stabilizer group is $\mathcal{S} = \{g_1, \dots, g_{|\mathcal{S}|}\}$, the state evolves as $|\psi\rangle \mapsto U|\psi\rangle$, while the stabilizer group evolves as

$$\mathcal{S} \mapsto \mathcal{S}^U = \{g_1^U, \dots, g_{|\mathcal{S}|}^U\} = \{Ug_1U^\dagger, \dots, Ug_{|\mathcal{S}|}U^\dagger\}. \quad (\text{A.4})$$

For the state to remain a codeword under unitary time evolution, the unitaries must be taken from the *Clifford group*, which transforms a Pauli string operator g into $g^U = UgU^\dagger$ that is still a Pauli string operator. Thus, \mathcal{S}^U remains a group of Pauli string operators, hence the wavefunction remains a codeword. To simulate a circuit under Clifford unitary evolution, one only needs to keep track of \mathcal{S} , or equivalently (and more conveniently) its generating set $\mathcal{G}(\mathcal{S})$. Such a simulation only takes polynomial time in L .

It is common knowledge that the Clifford group on two-qubits is generated by {CNOT, SWAP, H, P}, where in the standard bases

$$\text{CNOT} = \begin{pmatrix} 1 & 0 & 0 & 0 \\ 0 & 1 & 0 & 0 \\ 0 & 0 & 0 & 1 \\ 0 & 0 & 1 & 0 \end{pmatrix}, \quad \text{SWAP} = \begin{pmatrix} 1 & 0 & 0 & 0 \\ 0 & 0 & 1 & 0 \\ 0 & 1 & 0 & 0 \\ 0 & 0 & 0 & 1 \end{pmatrix}, \quad (\text{A.5})$$

$$\text{H} = \frac{1}{\sqrt{2}} \begin{pmatrix} 1 & 1 \\ 1 & -1 \end{pmatrix}, \quad \text{P} = \begin{pmatrix} 1 & 0 \\ 0 & i \end{pmatrix}. \quad (\text{A.6})$$

The CNOT gate defined here is also known as CNOT_L , whereas $\text{CNOT}_R = \text{SWAP} \cdot \text{CNOT}_L \cdot \text{SWAP}$.

Next we consider Pauli measurements, that is, measuring a Pauli string operator g . Let $\mathcal{G} = \{g_1, \dots, g_k, g_{k+1}, \dots, g_L\}$ be the stabilizers of $|\psi\rangle$ and suppose that $[g_j, g] = 0$ for $j \leq k$, and $\{g_j, g\} = 0$ for $j > k$. After the measurement, there are two possible outcomes (1 or -1), hence two possibilities of the measured wavefunction,

$$|\psi\rangle_{\pm} \propto \frac{1 \pm g}{2} |\psi\rangle. \quad (\text{A.7})$$

Their corresponding probabilities can be computed, as detailed in [68]. Remarkably, the measured state is still a codeword, and its corresponding stabilizer group is generated by the fol-

lowing stabilizers [69]

$$\mathcal{G}_{\pm} = \{g_1, \dots, g_k, g_{k+1}g_{k+2}, \dots, g_{L-1}g_L, \pm g\}. \quad (\text{A.8})$$

Such a simulation can also be performed in polynomial time.

We use the particular algorithm in [68] for our simulation of the Clifford circuits, where we take the unitary and measurement gates to be local.

A.1.3 Generating random Clifford unitaries

In the random Clifford circuit, the local unitaries are taken from the uniform distribution on the two-qubit Clifford group. Here we explain the sampling process from the L -qubit Clifford group $\mathcal{C}(L)$ [176]. It applies to $L = 2$ as a special case.

First we notice that the Clifford group acts on the Pauli group transitively, and that a Clifford unitary U is determined (up to a sign) by images of the generators of $\mathcal{P}_+(L)$, conveniently taken to be $\{X_1, Z_1, \dots, X_L, Z_L\}$. Thus, sampling a random Clifford unitary is equivalent to sampling random images of the generators. We proceed by induction, and start with assuming that one is able to sample from the uniform distribution on $\mathcal{C}(k)$. Now consider the action of a random Clifford unitary on $\{X_{k+1}, Z_{k+1}\}$. Since the random unitary is taken from the uniform distribution, it maps X_{k+1} to all the non-identity elements of $\mathcal{P}_+(k+1)$ with equal probability. X_{k+1}^U is essentially a random non-trivial Pauli string operator of length $k+1$; there are $2(4^{k+1} - 1)$ choices, where the factor of 2 comes from the sign. Z_{k+1}^U is also almost random, except that it must also square to 1, and anticommute with X_{k+1}^U ; there are $2(2 \times 4^k)$ choices.

Having randomly chosen X_{k+1}^U and Z_{k+1}^U , we can find *one* unitary U' (again represented by its action on the generators of $\mathcal{P}_+(k+1)$) such that $X_{k+1}^{U'} = X_{k+1}^U$ and $Z_{k+1}^{U'} = Z_{k+1}^U$ satisfying the following relations,

$$(U')^\dagger X_{k+1}^U U' = X_{k+1}, \quad (\text{A.9})$$

$$(U')^\dagger Z_{k+1}^U U' = Z_{k+1}. \quad (\text{A.10})$$

To preserve the commutation relations, we must have for $i \leq k$,

$$(U')^\dagger X_i^U U' = (\dots) \otimes I_{k+1}, \quad (\text{A.11})$$

$$(U')^\dagger Z_i^U U' = (\dots) \otimes I_{k+1}, \quad (\text{A.12})$$

which is equivalent to

$$X_i^V = (\dots) \otimes I_{k+1}, \quad (\text{A.13})$$

$$Z_i^V = (\dots) \otimes I_{k+1}, \quad (\text{A.14})$$

where $V = (U')^\dagger U$ is now shown to be in the Clifford group of the first k qubits. Thus to sample U from $\mathcal{C}(k+1)$, we just need to sample V from $\mathcal{C}(k)$, and multiply it by U' (which is determined by X_{k+1}^U and Z_{k+1}^U , which are also random), to get a random U from $\mathcal{C}(k+1)$. Since it is easy to generate elements in $\mathcal{C}(1)$, we know how to generate elements in $\mathcal{C}(k+1)$, by induction.

From the above, we get the following recurrence relation

$$|\mathcal{C}(L+1)| = 2(4^{L+1} - 1) \times (4^{L+1}) \times |\mathcal{C}(L)|, \quad (\text{A.15})$$

where the first factor corresponds to the number of choices of the image of X_{L+1} , and the second factor corresponds to that of Z_{L+1} .

A.1.4 Entanglement entropy for pure stabilizer states

Given a pure state wavefunction $|\psi\rangle$, the n -th Rényi entanglement entropy with respect to a given bipartition (A, \bar{A}) is defined to be (c.f. Eq. (2.5))

$$S_A^n = \frac{1}{1-n} \log_2 \text{Tr}(\rho_A)^n, \quad \text{where } \rho_A = \text{Tr}_{\bar{A}} |\psi\rangle \langle \psi|.$$

When $|\psi\rangle$ is a codeword, the Rényi entropies are independent of the Rényi index n , and is related to its stabilizers through the following relation [82, 83, 72]

$$S_A = |A| - \log_2 |\mathcal{S}_A|, \quad (\text{A.16})$$

where \mathcal{S}_A is the subgroup of \mathcal{S} of all elements that have trivial content (I) on \bar{A} . Equivalently,

$$S_A = |A| - |\mathcal{G}(\mathcal{S}_A)|, \quad (\text{A.17})$$

where $\mathcal{G}(\mathcal{S}_A)$ is an arbitrary generating set of \mathcal{S}_A .

We recall an alternative formula as derived in Ref. [72]. Define the linear operator proj_A such that $\text{proj}_A(\mathcal{S})$ contains all elements from \mathcal{S} with their contents on \bar{A} set to identity (“projected out”). In this notation we have $|\mathcal{G}(\mathcal{S}_A)| = \dim \text{Ker}(\text{proj}_{\bar{A}})$. By a theorem in linear algebra we have $\dim \text{Ker}(\text{proj}_{\bar{A}}) + \dim \text{Im}(\text{proj}_{\bar{A}}) = \dim \mathcal{S} = L$, so that

$$\begin{aligned} S_A &= |A| - \dim \text{Ker}(\text{proj}_{\bar{A}}) \\ &= |A| - (L - \dim \text{Im}(\text{proj}_{\bar{A}})) \\ &= \dim \text{Im}(\text{proj}_{\bar{A}}) - |\bar{A}|, \end{aligned} \quad (\text{A.18})$$

or, interchanging the roles of A and \bar{A} ,

$$\begin{aligned} S_A &= S_{\bar{A}} = \dim \text{Im}(\text{proj}_A) - |A| \\ &= \text{rank}(\text{proj}_A(\mathcal{S})) - |A|. \end{aligned} \quad (\text{A.19})$$

Given the entanglement entropy, the computation of the bipartite mutual information is immediate.

A.1.5 Entanglement entropies of mixed stabilizer states

Let the stabilizer group \mathcal{S} be an abelian subgroup of $\mathcal{P}(Q)$ as defined in Eq. (4.4). Let $\rho_Q(\mathcal{S})$ be the corresponding stabilizer code state as in Eq. (4.6) [81],

$$\rho_Q(\mathcal{S}) = 2^{-|Q|} \sum_{g \in \mathcal{S}} g. \quad (\text{A.20})$$

We can directly compute its Rényi entropies [81],

$$\begin{aligned} & (\ln 2)^{-1} S^{(n)}(\rho_Q(\mathcal{S})) \\ &= \frac{1}{1-n} \log_2 \text{Tr} [(\rho_Q(\mathcal{S}))^n] \\ &= \frac{1}{1-n} \log_2 \text{Tr} \left[\left(2^{-|Q|} |\mathcal{S}| \right)^{n-1} \rho_Q(\mathcal{S}) \right] \\ &= |Q| - \log_2 |\mathcal{S}|. \end{aligned} \quad (\text{A.21})$$

Since this result is independent of the Rényi index n , we will suppress it henceforth. As in Sec. 4.1, we take

$$|\mathcal{S}| = 2^m \quad (\text{A.22})$$

and define

$$k := |Q| - m = (\ln 2)^{-1} S(\rho_Q(\mathcal{S})). \quad (\text{A.23})$$

Given a bipartition of the system, $A \subseteq Q$, $\bar{A} = Q - A$, we define the following group homomorphism

$$\begin{aligned} \text{proj}_{\bar{A}} : \quad & \mathcal{P}(Q) \rightarrow \mathcal{P}(\bar{A}) \\ & g_A \otimes g_{\bar{A}} \mapsto g_{\bar{A}} \end{aligned} \quad (\text{A.24})$$

We take the following reduced density matrix on A ,

$$\begin{aligned}
& \rho_A(\mathcal{S}) \\
&= \text{Tr}_{\bar{A}}[\rho_Q(\mathcal{S})] \\
&= 2^{-|Q|} \sum_{g \in \mathcal{S}} \text{Tr}_{\bar{A}}(g) \\
&= 2^{-|A|} \sum_{g \in \mathcal{S} \cap \text{Ker proj}_{\bar{A}}} g \\
&= 2^{-|A|} \sum_{g \in \mathcal{S}_A} g, \tag{A.25}
\end{aligned}$$

where we noticed that $\text{Tr}_{\bar{A}}(g)$ is nonzero only if $\text{proj}_{\bar{A}}(g) = \mathbb{1}_{\bar{A}}$, and defined \mathcal{S}_A to be the following subgroup of \mathcal{S} ,

$$\mathcal{S}_A := \mathcal{S} \cap \text{Ker proj}_{\bar{A}}. \tag{A.26}$$

Thus, we have

$$\begin{aligned}
& \text{proj}_{\bar{A}}(\mathcal{S}) \cong \mathcal{S}/\mathcal{S}_A, \\
& |\text{proj}_{\bar{A}}(\mathcal{S})| = |\mathcal{S}|/|\mathcal{S}_A|, \tag{A.27}
\end{aligned}$$

and from Eqs. (A.21, A.25),

$$\begin{aligned}
& (\ln 2)^{-1} S(\rho_A(\mathcal{S})) \\
&= |A| - \log_2 |\mathcal{S}_A| \\
&= |A| - \log_2 |\mathcal{S}| + \log_2 |\text{proj}_{\bar{A}}(\mathcal{S})|. \tag{A.28}
\end{aligned}$$

A.1.6 Computing Pauli correlation function

Consider the following ZZ correlator for the state ψ ,

$$c_{xy} = \langle \psi | Z_x Z_y | \psi \rangle, \quad (\text{A.29})$$

which can be written as a difference,

$$c_{xy} = \langle \psi | \frac{1 + Z_x Z_y}{2} | \psi \rangle - \langle \psi | \frac{1 - Z_x Z_y}{2} | \psi \rangle \quad (\text{A.30})$$

$$= p_+ - p_-, \quad (\text{A.31})$$

where the first term is the probability of measuring the Pauli operator $g = Z_x Z_y$ and getting $+$, and the second of getting $-$. Since the probabilities can be computed [68], the computation of correlation functions of Pauli string operators is straightforward.

A.2 The clipped gauge

In this subsection we review the clipped gauge and the clipping algorithm introduced in Ref. [72], and slightly extend the computation of entanglement entropy within this gauge.

Consider an L -qubit codeword $|\psi\rangle$ with stabilizer group \mathcal{S} , where $\mathcal{S} = \langle \mathcal{G}(\mathcal{S}) \rangle$. For a stabilizer $g \in \mathcal{G}(\mathcal{S})$, we define $\mathbf{l}(g)$ to be the position of the left endpoint, and $\mathbf{r}(g)$ to be the position of the right endpoint, as in Eqs. (2.7, 2.8),

$$\mathbf{l}(g) = \min\{x : g \text{ acts non-trivially on site } x\}, \quad (\text{A.32})$$

$$\mathbf{r}(g) = \max\{x : g \text{ acts non-trivially on site } x\}, \quad (\text{A.33})$$

where x is the coordinate of the site, which takes values in $\{1, 2, \dots, L\}$. For systems with open spatial boundary conditions, there is a natural coordinate system: we label the sites sequentially, from the left boundary to the right one. For systems with periodic spatial boundary conditions,

there is an arbitrariness in choosing the origin of the coordinate system, and there is no absolute distinction between left and right. To resolve this arbitrariness we will assume that the origin is chosen and fixed (by hand), so that the functions $\mathbf{l}(g)$ and $\mathbf{r}(g)$ are well-defined.

We further define $\rho_{\mathbf{l}}$ and $\rho_{\mathbf{r}}$, the *densities of left and right endpoints*, to be

$$\rho_{\mathbf{l}}(x) = \sum_{x=1}^L \delta_{\mathbf{l}(g_i), x}, \quad (\text{A.34})$$

$$\rho_{\mathbf{r}}(x) = \sum_{x=1}^L \delta_{\mathbf{r}(g_i), x}. \quad (\text{A.35})$$

The total number of left and right endpoints are conserved, and $\sum_x \rho_{\mathbf{l}}(x) = \sum_x \rho_{\mathbf{r}}(x) = L$. It was shown in Ref. [72] that it is always possible to “gauge fix” a stabilizer basis \mathcal{G} in an arbitrary gauge into the *clipped gauge*, where

- $\rho_{\mathbf{l}}(x) + \rho_{\mathbf{r}}(x) = 2$, for all sites x .
- For each site with $\rho_{\mathbf{l}}(x) = 2$ or $\rho_{\mathbf{r}}(x) = 2$, the two stabilizers that end at x must have different content on x .

A.2.1 Clipping algorithm

We here give an explicit algorithm for gauge fixing an arbitrary stabilizer basis \mathcal{G} into the clipped gauge \mathcal{G}^c , such that $\langle \mathcal{G} \rangle = \langle \mathcal{G}^c \rangle$. We use the word “clipping” for this process. Such a process was given in Ref. [72].

Clipping algorithm part 1. Given a stabilizer group \mathcal{S} , there exists an generating set \mathcal{G} of \mathcal{S} such that

- $\forall x, \rho_{\mathbf{l}}(x) \leq 2$;
- If $\rho_{\mathbf{l}}(x) = 2$, the two Pauli operators at the left endpoints must be different.

We call this the *pre-gauge* condition. It is different from the gauge condition in that it does not refer to the right endpoints of the stabilizers.

[*Sketch:* Recall that elements of \mathcal{G} can be viewed as basis vectors of the L -dimensional vector space, \mathcal{S} . For concreteness, we construct an $L \times 2L$ matrix M on \mathbb{Z}_2 , for which the i -th row corresponds to g_i , where each Pauli matrix is represented by two bits,

$$I \mapsto 00, X \mapsto 10, Y \mapsto 11, Z \mapsto 01. \quad (\text{A.36})$$

Then we perform Gaussian elimination (row reduction) on M to reduce it into the row echelon form. The resultant matrix, with each row viewed as a stabilizer, satisfy the pre-gauge condition.]

Clipping algorithm part 2. A generating set \mathcal{G} that satisfies the pre-gauge constraint in part 1 can be transformed into the clipped gauge while preserving ρ_1 .

[*Sketch:* This is achieved by performing another Gaussian elimination based on the resulting matrix of the previous algorithm, focusing the right endpoints, from the right to the left. In doing so, one has to always eliminate the longer stabilizer by the shorter one. One can check that ρ_1 is not changed under this process. That the stabilizers commute with each other guarantees that after the algorithm terminates, each site has no more than 2 endpoints, and both left and right endpoints satisfy the pre-gauge constraint in part 1. It follows that the resultant \mathcal{G} is in the clipped gauge.]

A.2.2 From clipped gauge to $\mathcal{B}(\mathcal{G})$

Consider the following quantity (which we call **bigrams**) defined for the generating set \mathcal{G} in the clipped gauge,

$$\mathcal{B}(\mathcal{G}) \equiv \{(1(g_1), \mathbf{r}(g_1)), \dots, (1(g_L), \mathbf{r}(g_L))\}. \quad (\text{A.37})$$

$\mathcal{B}(\mathcal{G})$ is a set of L ordered pairs.

Proposition 1. If $\langle \mathcal{G} \rangle = \langle \mathcal{G}' \rangle$, where \mathcal{G} and \mathcal{G}' are both independent and in the clipped gauge, then $\mathcal{B}(\mathcal{G}) = \mathcal{B}(\mathcal{G}')$.

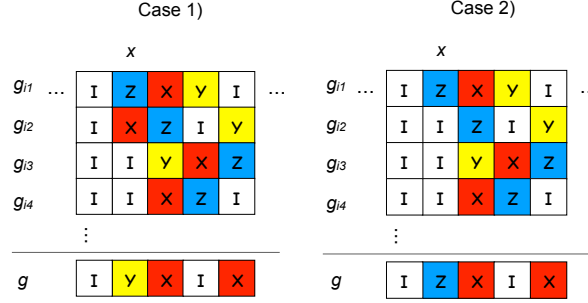


Figure A.1: Illustration of the two cases in the proof of the Lemma.

But before we prove Proposition 1, it is helpful to state the following

Lemma. Let \mathcal{G} be in the clipped gauge. For an arbitrary product of the stabilizers,

$$g = g_{i_1} \dots g_{i_k}, \quad (\text{A.38})$$

where $g_{i_j} \in \mathcal{G}$, and $\{i_1, \dots, i_k\}$ are mutually distinct, we have

$$\mathbf{l}(g) = \min \{\mathbf{l}(g_{i_1}), \dots, \mathbf{l}(g_{i_k})\}, \quad (\text{A.39})$$

$$\mathbf{r}(g) = \max \{\mathbf{r}(g_{i_1}), \dots, \mathbf{r}(g_{i_k})\}. \quad (\text{A.40})$$

Intuitively, this is saying that the “span” of the product would be the outer envelope of its factors.

Proof of the Lemma: Without loss of generality, let $\mathbf{l}(g_{i_1}) \leq \mathbf{l}(g_{i_2}) \leq \dots \leq \mathbf{l}(g_{i_k})$. According to the clipped gauge condition we have two possibilities (see Fig. A.1),

1. $x = \mathbf{l}(g_{i_1}) = \mathbf{l}(g_{i_2}) < \mathbf{l}(g_{i_3}) \leq \mathbf{l}(g_{i_4}) \leq \dots \leq \mathbf{l}(g_{i_k})$. In this case, the clipped gauge condition guarantees that the g_{i_1} and g_{i_2} have different but nontrivial (X , Y , or Z) contents on x , and g_{i_j} has trivial content (I) on site x , for $j \geq 3$. The product g would then have nontrivial content on x , but trivial content for $y < x$.
2. $x = \mathbf{l}(g_{i_1}) < \mathbf{l}(g_{i_2}) \leq \mathbf{l}(g_{i_3}) \leq \mathbf{l}(g_{i_4}) \leq \dots \leq \mathbf{l}(g_{i_k})$. In this case, only g_{i_1} has nontrivial (X , Y , or Z) content on x , and g_{i_j} has trivial content (I) on site x , for $j \geq 2$. The product

g would then have nontrivial content on x , but trivial content for $y < x$.

Thus $\mathbf{l}(g) = \mathbf{l}(g_{i_1})$ as claimed. A similar reasoning gives $\mathbf{r}(g)$. \square

Proof of Proposition 1: First recall that $\rho_{\mathbf{l}/\mathbf{r}}$ in the clipped gauge are completely fixed by the entanglement entropy (which is a gauge invariant quantity) through the following relation [72],

$$S_A(x) = \sum_{y \leq x} (\rho_{\mathbf{l}}(y) - 1) = \sum_{y > x} (\rho_{\mathbf{r}}(y) - 1). \quad (\text{A.41})$$

To reach our conclusion, we are going to show that, for two arbitrary generating sets \mathcal{G} and \mathcal{G}' (both in the clipped gauge), the lengths of the $\rho_{\mathbf{l}}(x)$ stabilizers that start at site x are the same for \mathcal{G} and \mathcal{G}' , for all sites x .

1. First, the case $\rho_{\mathbf{l}}(x) = 0$ is trivial.
2. Second, consider the case where $\rho_{\mathbf{l}}(x) = 1$. Let $g_i \in \mathcal{G}$ and $g'_i \in \mathcal{G}'$, where $\mathbf{l}(g_i) = \mathbf{l}(g'_i) = x$. Since both \mathcal{G} and \mathcal{G}' are independent generating sets, g_i has a unique representation as products of elements from \mathcal{G}' , and conversely, g'_i has a unique representation as products of elements from \mathcal{G} . That is,

$$g_i = \prod_{j=1}^L (g'_j)^{p'_j}, \quad g'_i = \prod_{j=1}^L (g_j)^{p_j}, \quad (\text{A.42})$$

where p_j, p'_j take values in $\{0, 1\}$. Since $\mathbf{l}(g_i) = \mathbf{l}(g'_i)$, we know $p_i = p'_i = 1$ from the Lemma. Then, again from the Lemma,

$$\mathbf{r}(g_i) \geq \mathbf{r}(g'_i), \quad (\text{A.43})$$

$$\mathbf{r}(g'_i) \geq \mathbf{r}(g_i). \quad (\text{A.44})$$

Hence $\mathbf{r}(g_i) = \mathbf{r}(g'_i)$, and g_i and g'_i have the same lengths.

3. Finally, consider the case where $\rho_{\mathbf{l}}(x) = 2$, and let $g_i, g_j \in \mathcal{G}$, $g'_i, g'_j \in \mathcal{G}'$, where $\mathbf{l}(g_i) =$

$1(g_j) = 1(g'_i) = 1(g'_j) = x$. We again have

$$g_i = \prod_{k=1}^L (g'_k)^{p'_k}, \quad g_j = \prod_{k=1}^L (g'_k)^{q'_k}, \quad (\text{A.45})$$

$$g'_i = \prod_{k=1}^L (g_k)^{p_k}, \quad g'_j = \prod_{k=1}^L (g_k)^{q_k}. \quad (\text{A.46})$$

Without loss of generality, assume $\mathbf{r}(g_i) \leq \mathbf{r}(g_j)$ and $\mathbf{r}(g'_i) \leq \mathbf{r}(g'_j)$. From the Lemma, we know that

$$p'_i + p'_j \geq 1, \quad p_i + p_j \geq 1, \quad (\text{A.47})$$

$$q'_i + q'_j \geq 1, \quad q_i + q_j \geq 1. \quad (\text{A.48})$$

That is, g_i must have at least one factor of either g'_i or g'_j , to have its left endpoint at x . So from the Lemma we have

$$\mathbf{r}(g_i) \geq \min\{\mathbf{r}(g'_i), \mathbf{r}(g'_j)\} = \mathbf{r}(g'_i). \quad (\text{A.49})$$

Similarly,

$$\mathbf{r}(g'_i) \geq \min\{\mathbf{r}(g_i), \mathbf{r}(g_j)\} = \mathbf{r}(g_i). \quad (\text{A.50})$$

Hence $\mathbf{r}(g_i) = \mathbf{r}(g'_i)$.

Again, without loss of generality, assume $\mathbf{r}(g_j) \leq \mathbf{r}(g'_j)$, thus $\mathbf{r}(g_i) \leq \mathbf{r}(g_j) \leq \mathbf{r}(g'_j)$.

We observe that $p'_j + q'_j \geq 1$; otherwise $p'_j = q'_j = 0$, and we must have $p'_i = q'_i = 1$, which implies that g_i and g_j have the same content on x , in contradiction with the clipping condition. Thus, from the Lemma, we must have at least one of the following,

(a) $\mathbf{r}(g_i) \geq \mathbf{r}(g'_j)$, in which case

$$\mathbf{r}(g_i) = \mathbf{r}(g'_i) = \mathbf{r}(g_j) = \mathbf{r}(g'_j). \quad (\text{A.51})$$

(b) $\mathbf{r}(g_j) \geq \mathbf{r}(g'_j)$, in which case

$$\mathbf{r}(g_i) = \mathbf{r}(g'_i), \quad \mathbf{r}(g_j) = \mathbf{r}(g'_j). \quad (\text{A.52})$$

Therefore, the stabilizers starting at x have the same length in \mathcal{G} and in \mathcal{G}' .

The above arguments work for every site x . We have thus proven the Proposition. \square

We immediately have the

Corollary. Let $\mathbf{len}(g) \equiv \mathbf{r}(g) - \mathbf{l}(g)$, and

$$\mathfrak{D}_{\mathcal{G}}(\ell) = \frac{1}{L} \sum_{i=1}^L \delta_{\mathbf{len}(g_i), \ell}, \quad (\text{A.53})$$

where $\mathcal{G} = \{g_1, \dots, g_L\}$. For \mathcal{G} and \mathcal{G}' satisfying the conditions in the Proposition, we have

$$\mathfrak{D}_{\mathcal{G}} = \mathfrak{D}_{\mathcal{G}'}. \quad (\text{A.54})$$

Thus, the length distribution of stabilizers in the clipping gauge is well defined.

A.2.3 From $\mathcal{B}(\mathcal{G})$ to entanglement entropy

Define the following subset of \mathcal{G} :

$$\mathcal{G}_A = \{g \in \mathcal{G} : g \text{ is supported only on } A\}. \quad (\text{A.55})$$

Proposition 2. Let \mathcal{G} be a generating set of \mathcal{S} in the clipped gauge, and A be a *contiguous* subregion of the system. Then \mathcal{S}_A , defined in Eq. (A.16) as the subgroup of \mathcal{S} of all the stabilizers that are only supported on A , is generated by \mathcal{G}_A .

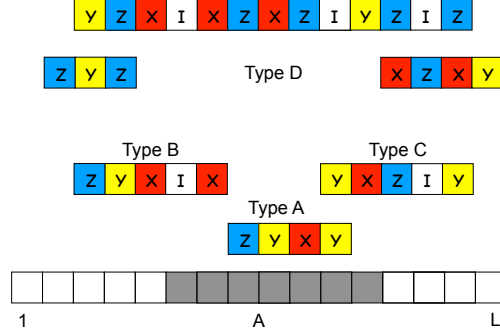


Figure A.2: The 4 types of stabilizers.

Proof: Let g_A be an arbitrary element of \mathcal{S}_A . It has the following representation,

$$g_A = \prod_{i=1}^L (g_i)^{p_i}, \quad (\text{A.56})$$

where we recall that $\mathcal{G} = \{g_1, \dots, g_L\}$, and $p_i = 0, 1$. Suppose g_i is supported on both A and \bar{A} . Either $l(g_i) \in \bar{A}$ or $r(g_i) \in \bar{A}$. From the Lemma, we see that $p_i = 0$, otherwise g_A will have support on \bar{A} , in contradiction with the assumption that $g_A \in \mathcal{S}_A$. Thus, $p_i = 1$ implies that g_i is supported only on A .

We have shown that $\mathcal{S}_A = \langle \mathcal{G}_A \rangle$. □

Noticing that \mathcal{G}_A is also independent, from Eq. (A.17) we have the following

Corollary. The entanglement of a contiguous subregion A is given by $S_A = |A| - |\mathcal{G}_A|$.

From now on, we will assume that A is contiguous, unless otherwise specified ¹.

All the stabilizers in \mathcal{G} can be divided into 4 types (see Fig. A.2),

(A) Those that are contained in A . These constitute \mathcal{G}_A . Let there be $a = |\mathcal{G}_A|$ of them.

¹In stating these results, the requirement that A is contiguous is important. Consider the following example of $L = 3$,

$$\mathcal{G} = \{XXI, IXZ, YZY\}. \quad (\text{A.57})$$

This set is in the clipped gauge. Let $A = \{1, 3\}$. S_A can be shown to be 1, while $|\mathcal{G}_A| = 0 \neq |A| - S_A = 1$. Thus, this simple formula *cannot* be readily used for computation of the mutual information,

$$I_{A,B} = S_A + S_B - S_{A \cup B}, \quad (\text{A.58})$$

where A and B are qubits that could be far away.

(B) Those that have their right endpoint in A , but left endpoint outside A . Let there be b of them.

(C) Those that have their left endpoint in A , but right endpoint outside A . Let there be c of them.

(D) Those that have their left and endpoints outside A . Let there be d of them.

Counting the number of endpoints in subregion A , we have

$$2|A| = 2a + b + c. \quad (\text{A.59})$$

Thus

$$S_A = |A| - |\mathcal{G}_A| = |A| - a = \frac{1}{2}(b + c). \quad (\text{A.60})$$

When A contains the first site, $b = 0$, it reduces to the familiar formula Eq. (A.41). Surprisingly, the entanglement entropy of A depends only on the endpoints of the stabilizers, but not the contents of the stabilizers, as in the more general formulae Eqs. (A.16, A.17, A.19). This simplicity is only present in the clipped gauge.

Several comments are in order.

1. This formula works for any \mathcal{G} that is in the clipped gauge. It provides another proof that $\mathcal{B}(\mathcal{G})$, hence $\mathfrak{D}_{\mathcal{G}}$, are well-defined in the clipped gauge.

Here is an algorithm for getting $\mathcal{B}(\mathcal{G})$ from S_A for all contiguous subregions (segments) A . At the beginning of the algorithm, we define the variables $a_{[l,r]} = |\mathcal{G}_{[l,r]}|$ for all segments $[l,r]$, and let $\mathcal{B} = \{\}$. In the w -th stage of the algorithm, we look at *all* segments $[x,y]$ of length w ($w = y - x + 1$). $a_{[x,y]} > 0$ means that there are $a_{[x,y]}$ stabilizers that start at x and end at y , and we add $a_{[x,y]}$ copies of (x,y) to \mathcal{B} . Then we subtract $a_{[x',y']}$ by the amount of $a_{[x,y]}$, for all $[x',y'] \supset [x,y]$. This marks the end of the w -th stage.

The algorithm terminates after L stages. The resultant \mathcal{B} gives the correct $\mathcal{B}(\mathcal{G})$. Hence, it is a quantity that is uniquely determined by entanglement entropy (assuming clipped gauge).

2. It has the intuitive interpretation that the entanglement is half the number of stabilizers that span the boundaries of the subregion. In certain limits the formula reduces to simply counting the number of entangled Bell pairs across the boundary, which is an example we know and like. However, the Bell pair picture fails to characterize multipartite entanglement because of the trivial internal structure of the stabilizers.

A.3 Proof of Theorem 1 in Sec. 4.1.4

Recall that $\mathcal{C}(\mathcal{S}) \subseteq \mathcal{P}(Q)$ is the abelianized centralizer of \mathcal{S} in $\mathcal{P}(Q)$. Recall also that the group of logical operators is defined as the quotient group $\mathcal{L} = \mathcal{C}(\mathcal{S})/\mathcal{S}$ (see Sec. 4.1.2). The homomorphism $\text{proj}_{\bar{A}}$ naturally induces the following homomorphism between quotient groups,

$$\begin{aligned} \widetilde{\text{proj}}_{\bar{A}} : \quad \mathcal{L} &\rightarrow \frac{\text{proj}_{\bar{A}}(\mathcal{C}(\mathcal{S}))}{\text{proj}_{\bar{A}}(\mathcal{S})} \\ g \cdot \mathcal{S} &\mapsto \text{proj}_{\bar{A}}(g) \cdot \text{proj}_{\bar{A}}(\mathcal{S}) \end{aligned} \quad (\text{A.61})$$

It can be straightforwardly verified that this homomorphism is well defined, and is in fact surjective,

$$\widetilde{\text{proj}}_{\bar{A}}(\mathcal{L}) = \frac{\text{proj}_{\bar{A}}(\mathcal{C}(\mathcal{S}))}{\text{proj}_{\bar{A}}(\mathcal{S})}. \quad (\text{A.62})$$

Recall that the group \mathcal{L}_A is defined in Sec. 4.1.2 as follows

$$\mathcal{L}_A := \frac{\{g \in \mathcal{C}(\mathcal{S}) \mid \text{proj}_{\bar{A}}(g) \in \text{proj}_{\bar{A}}(\mathcal{S})\}}{\mathcal{S}}, \quad (\text{A.63})$$

where $\text{proj}_{\bar{A}}$ is understood as from $\mathcal{P}(Q)$ to $\mathcal{P}(\bar{A})$, as in Eq. (A.24). It follows from the definitions

that

$$\mathcal{L}_A = \text{Ker } \widetilde{\text{proj}}_{\overline{A}} \subseteq \mathcal{L}, \quad (\text{A.64})$$

thus

$$\begin{aligned} & |\mathcal{L}_A| \\ &= |\text{Ker } \widetilde{\text{proj}}_{\overline{A}}| \\ &= \frac{|\mathcal{L}|}{|\widetilde{\text{proj}}_{\overline{A}}(\mathcal{L})|} \\ &= \frac{|\mathcal{C}(\mathcal{S})| \cdot |\text{proj}_{\overline{A}}(\mathcal{S})|}{|\mathcal{S}| \cdot |\text{proj}_{\overline{A}}(\mathcal{C}(\mathcal{S}))|}. \end{aligned} \quad (\text{A.65})$$

In the following, we associate these factors with entanglement entropies, using Eq. (A.28).

We state without proof that an arbitrary generating set of \mathcal{S} can be extended into one of $\mathcal{C}(\mathcal{S})$ [132, 68]:

$$\mathcal{G}_{\mathcal{S}} = \{g_1, \dots, g_m\}, \quad (\text{A.66})$$

$$\mathcal{G}_{\mathcal{C}(\mathcal{S})} = \{g_1, \dots, g_m, h_1^X, \dots, h_k^X, h_1^Z, \dots, h_k^Z\}. \quad (\text{A.67})$$

Each of $\mathcal{G}_{\mathcal{S}}$ and $\mathcal{G}_{\mathcal{C}(\mathcal{S})}$ is a set of independent operators in $\mathcal{P}(Q)$; thus

$$|\mathcal{S}| = 2^{|\mathcal{G}_{\mathcal{S}}|} = 2^m, \quad (\text{A.68})$$

$$|\mathcal{C}(\mathcal{S})| = 2^{|\mathcal{G}_{\mathcal{C}(\mathcal{S})}|} = 2^{m+2k} = 2^{|Q|+k}. \quad (\text{A.69})$$

Each of $\{g_{1\dots m}\}$, $\{h_{1\dots k}^X\}$, $\{h_{1\dots k}^Z\}$ is a set of mutually commuting operators in $\mathcal{P}(Q)$. In addition, the g 's commute with the h^X 's as well as with the h^Z 's; and $h_i^X h_j^Z = (-1)^{\delta_{ij}} h_j^Z h_i^X$. The h operators can be thought of the so-called ‘‘representative logical X - and Z -operators’’.

Next, we construct a purification of the state $\rho_Q(\mathcal{S})$. Let R be a system of k qubits, and let $\tilde{\mathcal{S}} \subseteq \mathcal{P}(QR)$ be generated by the following set $\tilde{\mathcal{G}}$, obtained from $\mathcal{G}_{\mathcal{C}(\mathcal{S})}$ by ‘‘extending’’ its

elements to QR ,

$$\tilde{\mathcal{G}} = \left\{ (g_j)_Q \otimes \mathbb{1}_R \mid j = 1 \dots m \right\} \cup \left\{ (h_j^X)_Q \otimes (X_j)_R \mid j = 1 \dots k \right\} \cup \left\{ (h_j^Z)_Q \otimes (Z_j)_R \mid j = 1 \dots k \right\}, \quad (\text{A.70})$$

where $(X_j)_R$ is the Pauli X -operator on the j -th qubit of R ; and similarly for $(Z_j)_R$. It is clear that $\tilde{\mathcal{G}}$ is a set of independent, mutually commuting elements of $\mathcal{P}(QR)$, and thus defines a physical state on QR ,

$$\rho_{QR}(\tilde{\mathcal{S}}) = 2^{-|QR|} \sum_{g \in \tilde{\mathcal{S}}} g. \quad (\text{A.71})$$

Since $|\tilde{\mathcal{G}}| = |\mathcal{G}_{\mathcal{C}(\mathcal{S})}| = |Q| + k = |QR|$, we have $|\tilde{\mathcal{S}}| = 2^{|QR|}$, and from Eq. (A.21)

$$(\ln 2)^{-1} S(\rho_{QR}(\tilde{\mathcal{S}})) = 0. \quad (\text{A.72})$$

Moreover, by construction,

$$\begin{aligned} \rho_Q(\tilde{\mathcal{S}}) &:= \text{Tr}_R \left[\rho_{QR}(\tilde{\mathcal{S}}) \right] \\ &= 2^{-|QR|} \sum_{g \in \tilde{\mathcal{S}}} \text{Tr}_R(g) \\ &= 2^{-|Q|} \sum_{g \in \mathcal{S}} g \\ &= \rho_Q(\mathcal{S}). \end{aligned} \quad (\text{A.73})$$

Therefore, $\rho_{QR}(\tilde{\mathcal{S}})$ is a purification of $\rho_Q(\mathcal{S})$ on QR , as claimed.

On the other hand, let us compute the reduced density matrix on R ,

$$\begin{aligned}
& \rho_R(\tilde{\mathcal{S}}) \\
&= \text{Tr}_Q \left[\rho_{QR}(\tilde{\mathcal{S}}) \right] \\
&= 2^{-|QR|} \sum_{g \in \tilde{\mathcal{S}}} \text{Tr}_Q(g) \\
&= 2^{-|R|} \mathbb{1}_R,
\end{aligned} \tag{A.74}$$

i.e. the maximally-mixed state on R , as expected. Thus we have

$$(\ln 2)^{-1} S(\rho_R(\tilde{\mathcal{S}})) = |R| = k. \tag{A.75}$$

It is easy to verify that for $A \subseteq Q$ and $\bar{A} := Q - A$,

$$\text{proj}_{\bar{A}}(\mathcal{C}(\mathcal{S})) = \text{proj}_{\bar{A}}(\tilde{\mathcal{S}}), \tag{A.76}$$

where $\text{proj}_{\bar{A}}$ on the LHS is understood as from $\mathcal{P}(Q)$ to $\mathcal{P}(\bar{A})$, and that on the RHS from $\mathcal{P}(QR)$ to $\mathcal{P}(\bar{A})$. Thus, using Eq. (A.28), but now for $AR \subseteq QR$, $\bar{A} = Q - A = QR - AR$, and $\tilde{\mathcal{S}}$, we have

$$\begin{aligned}
& (\ln 2)^{-1} S(\rho_{AR}(\tilde{\mathcal{S}})) \\
&= |AR| - \log_2 |\tilde{\mathcal{S}}| + \log_2 |\text{proj}_{\bar{A}}(\tilde{\mathcal{S}})| \\
&= |AR| - \log_2 |\tilde{\mathcal{S}}| + \log_2 |\text{proj}_{\bar{A}}(\mathcal{C}(\mathcal{S}))|.
\end{aligned} \tag{A.77}$$

Combining this equation with Eqs. (A.28, A.65), we have (compare Eq. (4.13))

$$\begin{aligned}
& \ell_A \\
&= \log_2 |\mathcal{L}_A| \\
&= \log_2 |\mathcal{C}(\mathcal{S})| - \log_2 |\mathcal{S}| + \log_2 |\text{proj}_{\bar{A}}(\mathcal{S})| - \log_2 |\text{proj}_{\bar{A}}(\mathcal{C}(\mathcal{S}))| \\
&= \log_2 |\mathcal{C}(\mathcal{S})| - \log_2 |\mathcal{S}| + \left[(\ln 2)^{-1} S(\rho_A(\mathcal{S})) - |A| + \log_2 |\mathcal{S}| \right] - \left[(\ln 2)^{-1} S(\rho_{AR}(\tilde{\mathcal{S}})) - |AR| + \log_2 |\tilde{\mathcal{S}}| \right] \\
&= \left[\log_2 |\mathcal{C}(\mathcal{S})| - \log_2 |\tilde{\mathcal{S}}| \right] + \left[\log_2 |\mathcal{S}| - \log_2 |\mathcal{S}| \right] + \left[(\ln 2)^{-1} S(\rho_A(\mathcal{S})) - |A| - (\ln 2)^{-1} S(\rho_{AR}(\tilde{\mathcal{S}})) + |AR| \right] \\
&= (\ln 2)^{-1} S(\rho_A(\mathcal{S})) - (\ln 2)^{-1} S(\rho_{AR}(\tilde{\mathcal{S}})) + |R| \\
&= (\ln 2)^{-1} \left[S(\rho_A(\tilde{\mathcal{S}})) - S(\rho_{AR}(\tilde{\mathcal{S}})) + S(\rho_R(\tilde{\mathcal{S}})) \right] \\
&= (\ln 2)^{-1} I_{A,R}. \tag{A.78}
\end{aligned}$$

Thus, we have proven the result stated in Sec. 4.1.4, by constructing a particular purification of $\rho_Q(\mathcal{S})$ using a particular generating set of $\mathcal{C}(\mathcal{S})$. But this choice is really arbitrary, and there is no surprise that it should work. In fact, any purification of $\rho_Q(\mathcal{S})$ on QR with $|R| = k$ has a generating set of the form in Eq. (A.70), and thus gives a generating set of $\mathcal{C}(\mathcal{S})$.

Appendix B

Entanglement dynamics under Clifford unitary-projective evolution

In this section, we try to give a simple picture for the entanglement entropy for contiguous subregions starting from the 1st site, which we define as the height function,

$$h(x) := S_{A=\{1,\dots,x\}}. \tag{B.1}$$

This is the same function considered in Ref. [72] and shown in Fig. 2.22.

Alternatively, based on Eq. (A.41), we can also consider dynamics of ρ_1 within the clipped gauge, which encodes the same information as the height function. We will use the pictorial representation in Fig. B.1, where each blue dot represents a left endpoint, and each white dot represents a right endpoint. We will view the left endpoints as “particles” and the right ones as “holes”. Recall that the clipped gauge requires that the total number of dots on each site is 2.

For the convenience of discussion, we consider systems with open boundary condition in this appendix.

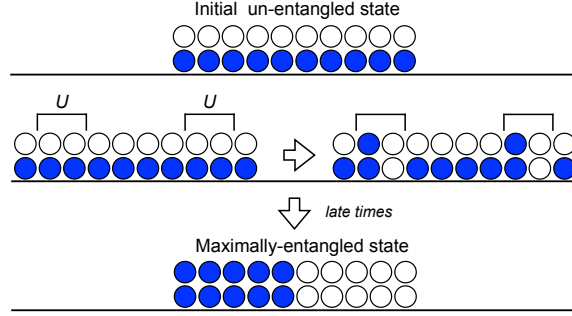


Figure B.1: Schematic illustration of the particle movement under purely unitary evolution, from a trivial product state to a maximally entangled state.

B.1 Unitary dynamics

Consider a local unitary on qubits x and $x + 1$, as in Fig. B.1. According to Eq. (A.41),

$$\rho_1(x) + \rho_1(x + 1) - 2 = h(x + 1) - h(x - 1). \quad (\text{B.2})$$

The local unitary on the bond $(x, x + 1)$ does not change $h(x + 1)$ or $h(x - 1)$, thus, restricting to the clipped gauge before and after the gate, the quantity $\rho_1(x) + \rho_1(x + 1)$ remains the same as before the unitary gate. Moreover, $\rho_1(y)$ is left invariant by $U_{x,x+1}$ for $y \neq x, x + 1$ for a similar reason. Hence the following

Observation: a local unitary gate on qubits $(x, x + 1)$ can only redistribute particles on sites x and $x + 1$, while leaving particles on other sites untouched, as illustrated in Fig. B.1.

If the unitary is taken from the Haar measure, and we take the local Hilbert space dimension q to infinity, the entanglement growth is governed by the following equation [72]

$$h(x, t + 1) = \min\{h(x - 1, t), h(x + 1, t)\} + 1. \quad (\text{B.3})$$

This is the crystal growth model. Since ρ_1 is the derivative of $h(x)$, under the action of a random Haar unitary, the particles within the range of action will drift to the left as much as they can with the filling constraint $\rho_1(x) \leq 2$, while particles outside the range of action stay where they are.

The difference between Clifford unitaries and random Haar unitaries is that instead of ballistic movement, the particles experience the biased diffusion with filling constraint. This is captured by the KPZ equation derived in Ref. [72]. Without further justification, we assume that this is the correct picture for entanglement growth under Clifford dynamics.

At long times $t \rightarrow \infty$, all the particles will clump to the left half of the system, corresponding to a maximally entangled state (see Fig. B.1). The fluctuation of $h(x)$ around the maximal value is expected to be small [72].

B.2 Measurement dynamics

Here we consider one-qubit Pauli- Z measurements and their effects on ρ_1 .

First recall the transformation of \mathcal{G} under the effect of a measurement of Z_x in Eq. (A.8). Let $\mathcal{G} = \{g_1, \dots, g_k, g_{k+1}, \dots, g_L\}$ be in the clipped gauge and suppose that $[g_j, Z_x] = 0$ for $j \leq k$, and $\{g_j, Z_x\} = 0$ for $j > k$. The stabilizer group of the measured wavefunction is generated by

$$\mathcal{G}' = \{g_1, \dots, g_k, g_{k+1}g_{k+2}, \dots, g_{L-1}g_L, Z_x\}. \quad (\text{B.4})$$

This set does not necessarily respects the clipped gauge; some clipping is necessary. In Appendix A we see that ρ_1 is determined by just the pre-gauge condition, and is left invariant by the second Gaussian elimination. Since we are focusing on the ρ_1 dynamics, it suffices to check only the pre-gauge condition.

Observe that since x is disentangled from the rest of the system after the measurement, Z_x will remain in \mathcal{G}' after clipping.

In Eq. (B.4), the ordering of the stabilizers is not essential; different orderings correspond to the same wavefunction. For convenience, we assume that $g_{k+1}, g_{k+2}, \dots, g_L$ are ordered in

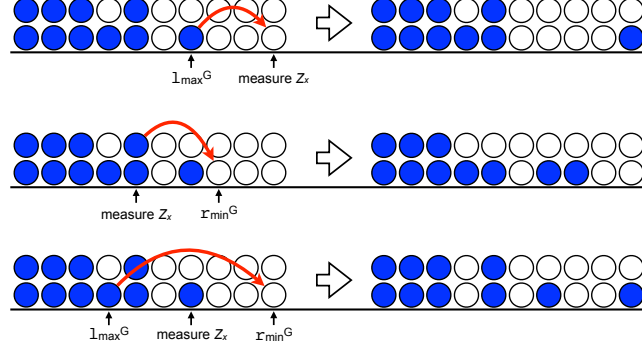


Figure B.2: Illustration of the hopping processes of the particles under a local measurement at site x .

such a way that their left endpoints are non-decreasing,

$$l(g_{k+1}) \leq l(g_{k+2}) \leq \dots \leq l(g_L). \quad (\text{B.5})$$

The clipped gauge guarantees that $g_j g_{j+1}$ has the same left endpoint as g_j , for $j > k$. Thus, comparing ρ_1 for \mathcal{G} and \mathcal{G}' , the net effect of a measurement Z_x is the following,

$$\rho_1(l(g_L)) \rightarrow \rho_1(l(g_L)) - 1, \quad \rho_1(x) \rightarrow \rho_1(x) + 1. \quad (\text{B.6})$$

If we now run the clipping algorithm and check for the pre-gauge (i.e. the first Gaussian elimination), it will find that the pre-gauge constraints are satisfied for all $y < x$. The first site that might violate this constraint is x . The clipping algorithm would then check the constraint and move the left-endpoints to the right of x (the row elimination process), if necessary.

The coordinate $l(g_L)$ where a particle gets removed is the right-most left-endpoint among stabilizers that anticommute with Z_x , which we define to be

$$l_{\max}^{\mathcal{G}} := \max\{l(g) : g \in \mathcal{G}, \mathcal{G} \text{ clipped, and } \{g, Z_x\} = 0.\} \quad (\text{B.7})$$

We define a similar quantity which will prove to be useful,

$$\mathbf{r}_{\min}^{\mathcal{G}} := \min\{\mathbf{r}(g) : g \in \mathcal{G}, \mathcal{G} \text{ clipped, and } \{g, Z_x\} = 0.\} \quad (\text{B.8})$$

Using this notation, we can further deduce the change of ρ_1 under a local measurement. There are three cases (see Fig. B.2),

1. $\rho_1(x) = 0$ before measurement. It follows that $\mathbf{l}_{\max}^{\mathcal{G}} < x$, and $\rho_1(\mathbf{l}_{\max}^{\mathcal{G}}) \geq 1$. After the operation in Eq. (B.6), the pre-gauge constraint is satisfied everywhere, and the algorithm terminates. The height $h(w)$ is reduced by 1 for $w \in [\mathbf{l}_{\max}^{\mathcal{G}}, x)$.
2. $\rho_1(x) = 2$ before measurement. It follows that $\mathbf{l}_{\max}^{\mathcal{G}} = x$. After clipping, $\rho_1(x)$ is reduced by 1, and that reduction is compensated by the increase of $\rho_1(y)$ for some $y > x$, for which $\rho_1(y) \leq 1$ before the measurement.

If we view this processes from the perspective of $\rho_{\mathbf{r}}$, it would have the particle-hole symmetric dynamics, where the symmetry operation is

$$x \rightarrow L - x, \quad \rho \rightarrow 2 - \rho. \quad (\text{B.9})$$

Consequently, the position y is equal to $\mathbf{r}_{\min}^{\mathcal{G}}$, and the height $h(w)$ is reduced by 1 for $w \in [x, \mathbf{r}_{\min}^{\mathcal{G}})$.

3. $\rho_1(x) = 1$ before measurement. If this stabilizer has X or Y on site x , the measurement has no effect on $\rho_1(x)$. If this stabilizer has Z on site x , the measurement will first hop a particle from site $\mathbf{l}_{\max}^{\mathcal{G}} < x$ to x , then hop a particle from x to $\mathbf{r}_{\min}^{\mathcal{G}} > x$, as described in the previous two cases. The height $h(w)$ is reduced by 1 for $w \in [\mathbf{l}_{\max}^{\mathcal{G}}, \mathbf{r}_{\min}^{\mathcal{G}})$.

Given these observations, we see that the effect of a local measurement at x , in the particle picture, is to hop exactly one particle across x via clipping. Thus we have an apparently simple picture for the entanglement dynamics in the unitary-measurement Clifford circuit in terms of

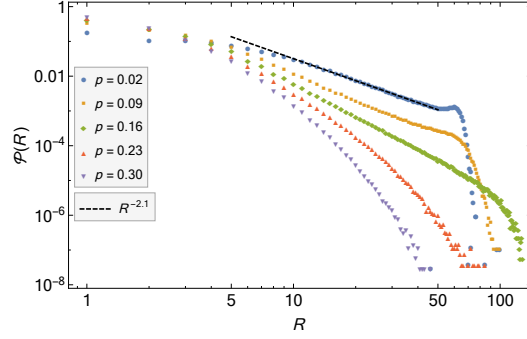


Figure B.3: The normalized distribution function of R , on a log-log scale.

the particles, which are drifted to the left in a local fashion under unitary gates, and “hopped” to the right under measurements in a non-local fashion.

What remains unspecified is the hopping distance, R , that is, the distance between the initial and final positions of the moving particle. This quantity takes the values $x - \mathbf{1}_{\max}^{\mathcal{G}}$, $\mathbf{r}_{\min}^{\mathcal{G}} - x$, and $\mathbf{r}_{\min}^{\mathcal{G}} - \mathbf{1}_{\max}^{\mathcal{G}}$ in the three cases above, respectively. For concreteness, consider the following function,

$$H := \sum_w h(w). \quad (\text{B.10})$$

From the discussion above, it is easy to see that the change in H after a time cycle is

$$\Delta H = O(L) + \sum_{k=1}^{pL} (-R_k), \quad (\text{B.11})$$

where R_k is the distance of the hopping in the k -th measurement, and the $O(L)$ terms comes from the unitary gates. We replace the second term by its mean value,

$$\Delta H = O(L) - pL \langle R \rangle. \quad (\text{B.12})$$

Within the steady state, the two terms must cancel out, so that $\langle R \rangle = O(1)$.

In Fig. B.3, we plot the normalized distribution function of R , denoted $\mathcal{P}(R)$, for several different values of p within a system of size $L = 128$, within the random Clifford circuit. Within

the volume law phase $p < p_c$, the distribution function takes the form of a power law decaying function whose magnitude does not depend on the system size (as we verify but not shown), $\mathcal{P}(R) \sim R^{-\gamma}$ up to $R \sim L/2$. Within the area law phase the distribution is short ranged. Schematically,

$$\mathcal{P}(R) \sim \begin{cases} \frac{1}{R^\gamma}, p < p_c, \\ \frac{e^{-R/R_0}}{R^\gamma}, p > p_c, \end{cases} \quad (\text{B.13})$$

where γ , which varies throughout the volume phase, always satisfies $\gamma > 2$, and R_0 is a finite length scale. As of now, we have not understood this power law distribution, and leave it for future work. Nevertheless, the expectation values of the hopping distance can be readily computed, $\langle R \rangle = \int^{L/2} dR R \mathcal{P}(R)$. In the volume law phase, the mean value of R is finite (as $L \rightarrow \infty$) since $\gamma > 2$, while in the area law phase this value is finite regardless.

Notice that the quantity $\delta_M \bar{h}$, defined in Sec. 2.6, is proportional to the hopping distance R within the Clifford context, $\delta_M \bar{h} = -R/L$, so that $\langle \delta_M \bar{h} \rangle = O(1/L)$.

B.3 Toy particle traffic-flow model

The apparent simplicity of the dynamical rules governing the particles motion in the Clifford circuit studied in the previous subsection is somewhat misleading; to faithfully simulate the particle dynamics, the knowledge of particle densities are not enough, and one has to specify the internal contents of the stabilizers (so as to obtain $\mathbf{l}_{\max}^{\mathcal{G}}$ and $\mathbf{r}_{\min}^{\mathcal{G}}$). In this subsection, we design an effective toy model which we term the ‘‘traffic-flow model’’, that aims to capture the essence of the Clifford particle dynamics without resorting to a full stabilizer simulation. As we shall see, the particles motion is designed to mimic the motion of the stabilizers left-endpoints under both unitaries and measurements, as described in detail in the previous subsection.

Specifically, we start with a one dimensional system of L sites with open boundary condition, and initially put in L particles (mimicking the left endpoints of the stabilizers), one on each site,

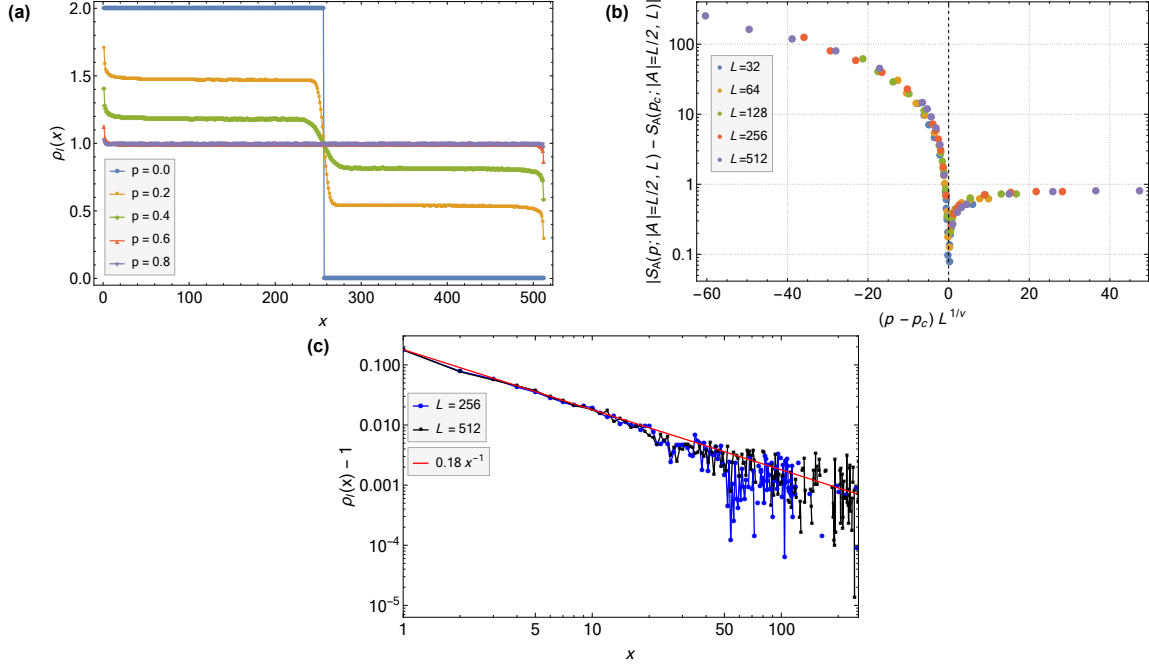


Figure B.4: (a) The average steady state particle density for different values of p with fixed $L = 512$. As seen in Eq. (A.41), the volume law phase corresponds to a plateau in $\rho_1(x)$ with height greater than 1, while the transition is signified by a continuous decrease of this height to 1. There is clearly a particle hole symmetry in $\rho_1(x)$ (see Eq. (B.9)) at all values of p . (b) Collapse of the entanglement entropy using the scaling form in Eq. (2.20), where we choose $\nu = 1.33$ and $p_c = 0.56$. (c) The particle density at the critical point. The data can be fit to a slope -1 on a log-log scale, suggesting logarithmic scaling of entanglement entropy (see Eq. (A.41)), reproducing the result of the full Clifford dynamics.

as in a product state; the total number of particles is conserved. At all times, we impose the constraint that on any site there are at most two particles, equivalent to the clipping condition.

To imitate the random Clifford circuit, we choose the particle motion under unitary gates to be ballistic and uni-directional (to the left), instead of diffusive. The particle motion under “measurements” is chosen to satisfy the following simple rules:

1. When $\rho_1(x) = 0$, choose the closest particle to the left of x at $y < x$, and hop it from y to x .
2. When $\rho_1(x) = 2$, choose the closest hole to the right of x at $z > x$, and hop one particle from x to z .
3. When $\rho_1(x) = 1$, leave the particle density untouched.

4. After each measurement, the measured qubit is taken out of the system, until the layer (with pL measurements) terminates. This is because the measurements within the same layer commute with each other, so that a site that is already measured cannot serve as $\mathbf{l}_{\max}^{\mathcal{G}}$ or $\mathbf{r}_{\min}^{\mathcal{G}}$ for subsequent measurements. Moreover, the temporal ordering of the measurements is inessential given this rule, as expected.

In effect, we are replacing $\mathbf{l}_{\max}^{\mathcal{G}}$ and $\mathbf{r}_{\min}^{\mathcal{G}}$ above with possibilities that are closest to x . This choice is of course an over-simplification, and is not faithful to real Clifford dynamics. In particular, the hopping distance distribution is strictly short-ranged (data not shown), and does not have the power law form. However, as we will see below, this toy model captures some universal features of the random Clifford circuit.

We numerically simulate this classical model and present the results in Fig. B.4. The function ρ_1 shows a volume law to area law transition, with similar critical exponents and logarithmic scaling of entanglement at the critical point (although the coefficient of the logarithmic function is significantly smaller than $\alpha(p_c)$ we found in earlier sections). Thus the rules of our toy model are partially justified.

The traffic-flow model provides a different perspective for studying entanglement dynamics. While our “traffic rules” are over-simplified, one might still hope to design a set of rules that faithfully represents the particle dynamics under the full Clifford evolution. In fact, this framework could be more versatile than what is already envisioned, and tweaking with the rules might result in a whole class of different entanglement dynamics, not necessarily within the same universality class as the Clifford ones. We leave these studies to future works.

Appendix C

Conformal invariance

C.1 Review of some elementary results in CFT

In this Appendix we summarize very briefly a number of very basic properties pertaining to correlation functions and the operator product expansion (OPE) of *primary fields* in CFT [177]. Notice that in a boundary CFT, only the (say) holomorphic part of an operator appears, and all correlation functions below are holomorphic.

- Two-point function:

$$\langle \phi_1(w_1)\phi_2(w_2) \rangle = \begin{cases} c_{12}w_{12}^{-2h}, & \text{if } h_1 = h_2 = h. \\ 0, & \text{if } h_1 \neq h_2. \end{cases} \quad (\text{C.1})$$

- Three-point function:

$$\begin{aligned} & \langle \phi_1(w_1)\phi_2(w_2)\phi_3(w_3) \rangle \\ = & c_{123}w_{12}^{-(h_1+h_2-h_3)}w_{23}^{-(h_2+h_3-h_1)}w_{13}^{-(h_3+h_1-h_2)}. \end{aligned} \quad (\text{C.2})$$

- Four-point function:

$$\begin{aligned} & \langle \phi_1(w_1)\phi_2(w_2)\phi_3(w_3)\phi_4(w_4) \rangle \\ &= F(\eta) \prod_{i<j} w_{ij}^{h/3-h_i-h_j}, \end{aligned} \quad (\text{C.3})$$

where $h = \sum_i h_i$, and $\eta = \frac{w_{12}w_{34}}{w_{13}w_{24}}$ is the cross ratio. In the case when $h_1 = h_4, h_2 = h_3$, it simplifies to

$$\begin{aligned} & \langle \phi_1(w_1)\phi_2(w_2)\phi_3(w_3)\phi_4(w_4) \rangle \\ &= \tilde{F}(\eta) w_{14}^{-2h_1} w_{23}^{-2h_2}. \end{aligned} \quad (\text{C.4})$$

- Correlation functions are covariant under conformal mappings (in this case $w(z)$),

$$\begin{aligned} & \langle \phi_1(z_1) \dots \phi_n(z_n) \rangle \\ &= \left[\prod_{j=1}^n \left(\frac{\partial w}{\partial z} \right)_{z_j} \right]^{h_j} \langle \phi_1(w_1) \dots \phi_n(w_n) \rangle. \end{aligned} \quad (\text{C.5})$$

- The operator product expansion accounts for the short-distance behavior of two operators. It usually takes the following form,

$$\begin{aligned} & \lim_{w_2 \rightarrow w_1} \phi_i(w_1)\phi_j(w_2) \\ & \propto (w_{12})^{-h_i-h_j} \sum_k (w_{12})^{h_k} C_{ijk} \phi_k(w_1), \end{aligned} \quad (\text{C.6})$$

where both sides have the same dimension under global scale transformations (dilations). The numbers C_{ijk} are “boundary OPE coefficients”. The operators ϕ_k are usually organized in increasing order of their scaling dimensions h_k . Throughout the paper we have

being using the following shorthand notation

$$\phi_i(w_1)\phi_j(w_2) \sim (w_{12})^{-h_i-h_j} \sum_k (w_{12})^{h_k} \phi_k(w_1). \quad (\text{C.7})$$

C.2 Purification dynamics of reference qubits in the Clifford Circuit

In this Appendix we consider yet another boundary condition on the Clifford circuit discussed in the main part this paper, which is similar to the circuit introduced in Ref. [113]. The setup is as follows.

- One starts with a chain of L qubits in a product state.
- One picks a contiguous segment A containing a number of $|A|$ qubits from this chain, and entangles each of them with an extra, additional “reference qubit” with which it forms a maximally entangled Bell pair. There are therefore $|A|$ Bell pairs, each containing one “reference qubit” and one “system qubit”, in addition to the remaining $L - |A|$ “system qubit” of the original chain of L qubits. In Ref. [113], $|A|$ is always taken to be unity, $|A| = 1$.

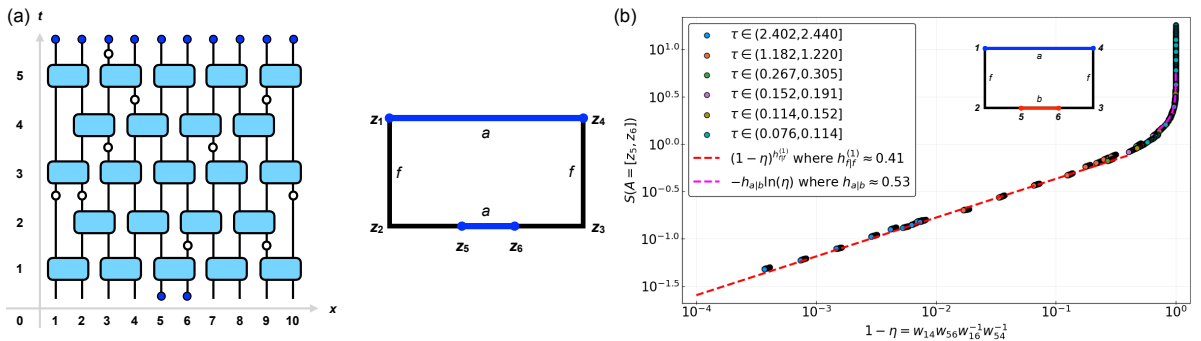


Figure C.1: (a) The circuit considered in Appendix C.2, where the description is given in the text. This is an generalization of one setup introduced in Ref. [113]. (b) Collapsing $S([z_5, z_6])$ to the cross ratio, following Eqs. (C.8, C.10). The data is obtained for various z_{56} and various circuit depths.

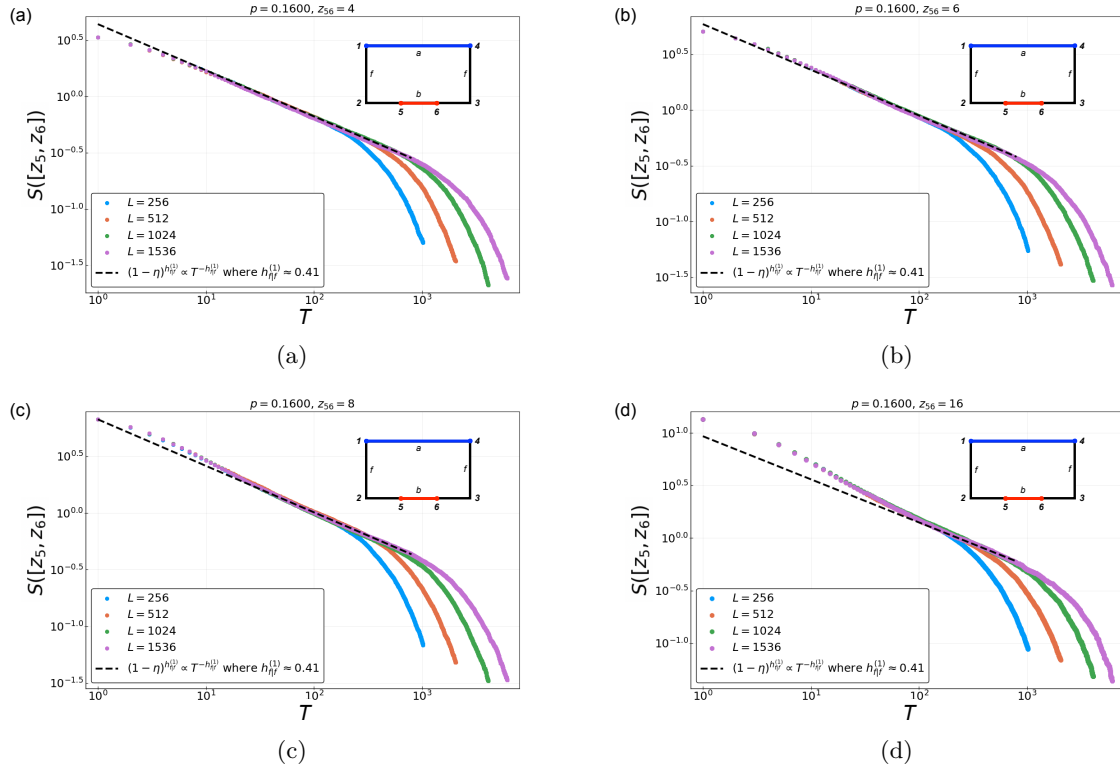


Figure C.2: Early time data of $S(A = [z_5, z_6])$, with $|A| = z_{56}$ in $\{4, 6, 8, 16\}$. The data matches well with Eq. (C.17) at intermediate times $z_{56} \ll T \ll L$, which we fit for $h_{ff}^{(1)} = 0.41$. As $|A|$ increases, the allowed time window for fitting to the powerlaw shrinks.

- One then evolves the “system”, by which we mean the original chain of L qubits (i.e. the $|A|$ “system qubits” as well as the remaining $L - |A|$ qubits of the original chain, but *not* the “reference qubits”) with the critical hybrid circuit.¹
- The quantity of interest is the entanglement entropy between “the reference qubits” and “the system”, a quantity denoted by S_Q in Ref. [113].

This circuit is illustrated Fig. C.1(a). Following our conventions in Fig. 3.2(c), we postulate that there are now $|A|$ physical qubits living on the lower edge of the rectangle (on $A = [z_5, z_6] \subset [z_2, z_3]$), indicated by solid blue dots, and L qubits living on the top (on $[z_1, z_4]$), also indicated

¹Note that the case where $|A| = L$, i.e. where the “system qubits” are all the L qubits of the original chain, was the *fafa* circuit previously discussed in Fig. 3.2(c) and Sec. 3.2.3. In that previous discussion the “system qubits” were referred to as “the system”, whereas the “reference qubits” were referred to as “the environment”. The current situation is thus a generalization of this previously considered setup, and everything said in this Appendix is a natural extension of the discussion of that previous discussion in the main text.

by solid blue dots, implying the b.c. shown in the same figure. Note that this is again the b.c. of type *fafa* (as in Fig. 3.2(c)), whereas the entanglement between “the system” and “the reference qubits” is again given by the difference in free energy between boundary conditions of types *fafb* and *fafa*, completely analogous to the discussion in Sec. 3.2.3. In fact, when $|A| = L$, this is exactly the circuit discussed in in Sec. 3.2.3 (as already mentioned in the previous footnote).

Explicitly, $S(A = [z_5, z_6])$ is given by

$$\begin{aligned} & \exp[-S(A = [z_5, z_6])] \\ &= \frac{\langle \phi_{f|a}(z_1) \phi_{a|f}(z_4) \phi_{f|b}(z_6) \phi_{b|f}(z_5) \rangle}{\langle \phi_{f|a}(z_1) \phi_{a|f}(z_4) \phi_{f|a}(z_6) \phi_{a|f}(z_5) \rangle} \\ &= \frac{F_{fafb}(\eta)}{F_{fafa}(\eta)}, \end{aligned} \tag{C.8}$$

where the F functions are those defined in Eq. (3.62), and

$$\eta = \frac{w_{15}w_{64}}{w_{16}w_{54}} \tag{C.9}$$

is the relevant cross ratio. The data collapse of $S(A = [z_5, z_6])$ against η , computed by varying z_{56} and the circuit depth, is shown in Fig. C.1(b). The quality of the collapse supports our assumption about the b.c., and the behavior of the collapsed function in the two limits ($\eta \rightarrow 0$ and $\eta \rightarrow 1$) are consistent with Eqs. (3.50, 3.63), namely,

$$S([z_5, z_6]) = \begin{cases} -h_{a|b} \ln \eta, & \eta \rightarrow 0, \\ (1 - \eta)^{h_{f|f}^{(1)}}, & \eta \rightarrow 1. \end{cases} \tag{C.10}$$

In particular, the numerical estimates for the exponents $h_{a|b}$ and $h_{f|f}^{(1)}$, extracted from this analysis, are fully consistent with those obtained previously for the same exponents in the main text.

We can now use this result to obtain an analytic understanding of the behavior of $S(A = [z_5, z_6])$. We focus on the regime, $|A| = z_{56} \ll Y \ll L$. In order to simplify the calculation of

η , we adopt a different convention for the conformal mapping, where

$$w_1 = w(z_1) = -m^{-1/2}, \quad (\text{C.11})$$

$$w_2 = w(z_2) = -1, \quad (\text{C.12})$$

$$w_3 = w(z_3) = +1, \quad (\text{C.13})$$

$$w_4 = w(z_4) = +m^{-1/2}. \quad (\text{C.14})$$

This is related to the previous convention defined in Fig. 3.4 by a global (“fractional linear”) conformal transformation, under which η is invariant. We further focus on the case when z_5 sits at the center of the system, where

$$\begin{aligned} w_5 &= w(z_5) = 0, \\ w_6 &= w(z_6) \approx \left(\frac{\partial w}{\partial z} \right)_{z_5} z_{56} = \frac{K(1-m)}{Y} z_{56}. \end{aligned} \quad (\text{C.15})$$

Given $z_{56} \ll Y \ll L$, the cross ratio can be shown to be (using Eq. (3.20))

$$1 - \eta \propto \frac{\pi z_{15}}{Y}, \quad \frac{z_{56}}{L} \ll \tau \ll 1. \quad (\text{C.16})$$

Therefore, at early times,

$$S([z_5, z_6]) \propto (1 - \eta)^{h_{f|f}^{(1)}} \propto Y^{-h_{f|f}^{(1)}} \propto T^{-h_{f|f}^{(1)}}. \quad (\text{C.17})$$

This behavior is directly observed in Fig. C.2, where $|A| = z_{56}$ takes values in $\{4, 6, 8, 16\}$, where we find $h_{f|f}^{(1)} = 0.41$. In this particular case, it is preferable to keep z_{56} small, while going to rather large system sizes, because of the constraint $z_{56} \ll Y \ll L$. When Y is comparable to L , the decay is exponential, as the circuit starts to crossover to a quasi-one-dimensional system (similar to Sec. 3.2.3).²

²Notice that the powerlaw form $T^{-h_{f|f}^{(1)}}$ in Eq. (C.17) does not depend on Y/T , and therefore should be regarded as an estimation of $h_{f|f}^{(1)}$ independent of that in Fig. C.1. Off the critical point, there should still be a

Extending Eq. (C.17) into the volume law phase $p < p_c$ in the late time limit when $T \gg \xi$ (the correlation length), the time T should be replaced by ξ . Therefore, Eq. (C.17) gives steady state value of $S([z_5, z_6])$,

$$\lim_{T \rightarrow \infty} S([z_5, z_6]) \propto \xi^{-h_{f|f}^{(1)}} \propto |p - p_c|^{\nu \times h_{f|f}^{(1)}}. \quad (\text{C.18})$$

This means that the reference qubit can only purify to a finite nonzero value when measurements are below the critical rate, i.e. $p < p_c$. In Ref. [113], $h_{f|f}^{(1)}$ is identified with $\frac{\eta_{\parallel}}{2}$, therefore $\nu \times h_{f|f}^{(1)}$ can be identified with β_{\parallel} , following a standard hyperscaling relation $\beta_{\parallel} = \frac{1}{2} (d - 2 + \eta_{\parallel}) \nu$ in $d = 2$. Therefore, $S([z_5, z_6])$ acquires the meaning of an order parameter.

In Ref. [113], a different value of $h_{f|f}^{(1)} \approx 0.33$ is extracted from $S([z_5, z_6])$ with $z_{56} = 1$, for a slightly different location of the transition ($p_c \approx 0.1590$) and with periodic spatial b.c.. Within our setup, we also find $h_{f|f}^{(1)} \approx 0.33$ to be a reasonable fit for $z_{56} = 1$, but not so for $z_{56} > 1$. This is possibly due to the following subtleties with the one-qubit-purification data:

- Statistical error. In a Clifford circuit, all the entanglement entropies (when measured in units of $\ln 2$) are integers, and when $z_{56} = 1$, the entropy $S([z_5, z_6])$ jumps discretely between 1 and 0 in a single realization of disorder of the circuit. Therefore, one must sample a large number of disorder realizations in order to arrive at a good resolution for the expectation value of the entropy. The smallness of this quantity at small values of z_{56} also makes it more susceptible to statistical fluctuations.
- Effects arising from finite subsystem size. $S([z_5, z_6])$ always starts for small circuit depth with the value $\ln 2$, as given by the number of reference qubits. Numerically, this initial value is below the predicted form in Eq. (C.17), therefore one must wait for a while (T^*) before $S([z_5, z_6])$ matches on to Eq. (C.17). Before T^* , the purification will be slower than predicted, thereby giving a smaller estimation of $h_{f|f}^{(1)}$. T^* presumably depends on

time window $z_{56} \ll T \ll \xi$ for which Eq. (C.17) applies, and therefore this estimation of $h_{f|f}^{(1)}$ is also expected to be insensitive to the choice of p_c . This expectation is numerically confirmed but the results are not displayed here.

the details of the model, as well as on z_{56} .

Due to these subtleties, we are hesitant to extract $h_{f|f}^{(1)}$ from $S([z_5, z_6])$ with $z_{56} = 1$, and are instead more comfortable using values when $z_{56} \geq 4$. These issues, however, should be resolved with a larger disorder ensemble and even larger system sizes, but this is beyond the scope of the current work. Despite these issues, $S([z_5, z_6])$ (or S_Q) should still be viewed as an order parameter, which will represent a possible experimental probe of the transition.

Ref. [113] also presents results of growth of mutual information between two disjoint reference qubits. In the current framework, these would correspond to 6- or higher-point functions, for which the calculations require detailed knowledge of the CFT (although in certain limits they reduce to simpler, 4-point functions). We have not attempted to analyze these.

C.3 The scaling dimension $h_{f|f}^{(1)}$ from “localizable entanglement”

In this Appendix, we present another method for extracting the scaling dimension $h_{f|f}^{(1)}$, using a quantity similar to the so-called “localizable entanglement” [178]. In this set up, the circuit initial state is taken to be a product state, corresponding to the boundary condition f (see e.g. Fig. 3.2(a)). In the final state of the circuit, we choose two disjoint subregions $A = [z_1, z_2]$ and $B = [z_3, z_4]$, and perform a projective measurement on every qubit outside $A \cup B$. The projective measurements create a product state in $A \cup B$, thus also correspond to the boundary condition f , as we posit.³ The boundary conditions are shown in the insets of Fig. C.3(a,b).

For the circuit with periodic boundary condition, we focus on the steady state ($\tau = Y/L \gg 1$) and collapse the mutual information $I(A = [z_1, z_2], B = [z_3, z_4])$ against the cross ratio η , following the conformal mapping in Eq. (3.77) from the semi-infinite cylinder to the LHP. The results are shown in Fig. C.3(a). In particular, in the limit of small η , the OPE channel of two

³In the random Haar circuit, it can be shown that projective measurements do indeed create the free boundary condition, following the mapping developed in Refs. [30, 31].

$\phi_{f|a}$ fields is relevant (see Eq. (3.58)), and we expect

$$I([z_1, z_2], [z_3, z_4]) \propto \eta^{h_{f|f}^{(1)}}, \quad \eta \rightarrow 0. \quad (\text{C.19})$$

From Fig. C.3(a), we fit for $h_{f|f}^{(1)} \approx 0.41$, in excellent agreement with Figs. (3.8, C.1, C.2). Recall that in Figs. (3.8, C.1) the estimate of $h_{f|f}^{(1)}$ relies on the fitting parameter Y/T , and in Fig. C.2 the estimate is restricted to an intermediate time scale. The method here avoids both issues, and gives us an independent, consistent estimate of $h_{f|f}^{(1)}$, lending strong support that the Clifford CFT is distinct from percolation (see Table 3.2).

For the circuit with open boundary condition, the mutual information $I(A = [z_1, z_2], B = [z_3, z_4])$ is again given by the difference in free energy between boundary conditions of types *fafb* and *fafa*, completely analogous to the discussion in Sec. 3.2.3. In particular, we find, using the OPE in Eq. (3.58), that

$$I([z_1, z_2], [z_3, z_4]) \propto \eta^{h_{f|f}^{(1)}}, \quad \eta \rightarrow 0. \quad (\text{C.20})$$

Fitting for $h_{f|f}^{(1)}$ in Fig. C.3(b), we again find $h_{f|f}^{(1)} \approx 0.41$, consistent with all previous results.

C.4 Parallel results for the Hartley entropy in Haar circuits from minimal cuts in critical first-passage percolation

In this Appendix we apply the same CFT formalism introduced in the main text to the analysis of the Hartley (0th Rényi) entropy in Haar random unitary circuits with measurements, following Ref. [16].

The goal of this Appendix is to further justify our conjectures presented in the main part of this paper for the Clifford hybrid quantum circuits, by analyzing corresponding setups for the Hartley entropy in Haar random hybrid quantum circuits. While the ability to describe the latter in terms of “minimal cuts” in the theory of critical percolation has been established [16],

here we aim at showing that various boundary condition setups discussed in the main text for Clifford circuits can be analyzed in a completely analogous way for the Hartley entropy in the Haar circuits, and we obtain corresponding critical exponents for this case.

We consider two different possibilities for performing the required “minimal cuts” on the underlying “brickwall” lattice as illustrated in Fig. C.4. In both cases, the lattice geometry is that of a rectangular hybrid circuit as in Fig. 3.2: the horizontal links are arranged in an even-odd fashion and represent two-qubit unitary gates, and the vertical links represent qubit propagation in time, which are interrupted by hollow circles that break the link, representing the single-qubit measurements. To make connections with the bond percolation problem on a square lattice, one can view the lattices in Fig. C.4 as obtained from a perfect square lattice, by breaking the vertical bonds at random (with probability p) and by erasing every other horizontal bond (i.e. in an alternating but regular fashion), which could be thought of as eliminating (or “breaking”) with probability $= 1/2$ exactly a fraction $1/2$ of all the horizontal bond (a regular version of the process that is implemented on the vertical bonds in a random fashion at criticality with the same probability $p = 1/2$).⁴ The “minimal cut” is defined to be the path that begins at the point on the boundary where the two differently colored (red and blue) boundary segments join (possibly at infinity), and which crosses a minimal number of unbroken links in the bulk. In other words, the “minimal cut” path is one which minimizes the “cost” defined to be number of unbroken links crosses by the path. The “cost” of the “minimal cut” path is proportional to the Hartley (0-th Rényi) entropy [16]. It is evident from this setup that the coloring pattern is a crucial input in defining the minimal cut.

- In the first case (Fig. C.4(a)), we label a segment (left) of the upper edge with red color, and the rest (right) of the upper edge blue, while the other three edges are uncolored (denoting “free” b.c.s ‘ f ’). In the figure, the minimal cut starts from the interface between red and blue segments, and can terminate anywhere on the three uncolored “free” edges.

⁴Notice that the microscopic details of this construction differs slightly from that in Ref. [16], but can be exactly mapped to the latter by “shrinking” the two endpoints of each horizontal link (representing the unitary gate) to a single lattice site, thereby obtaining a square lattice rotated by 45° . Details of this construction should not affect the universal critical properties, as we have verified numerically, but chose not to display here.

When the lattice has zero depth, the minimal cut has zero “cost”, and its “cost” grows as the lattice grows in depth.

- In the second case (Fig. C.4(b)), we label the lower edge blue and the upper edge red, where a cut separating them must start from the left edge and terminate at the right edge, which are both “free”. Initially, the minimal cut must go through all vertical links, so is infinite in the thermodynamic limit; however, as the circuit grows deeper, the minimal cut path can make use of broken links in the bulk (of which there will be more as the depth increases) to lower its “cost”. Therefore the “cost” of the minimal cut path will decrease monotonically as the depth *increases*, and so will the Hartley entropy which this “cost” represents.

Recall that the “cost” of the minimal cut path in Fig. C.4(a) exactly describes the Hartley (zeroth Renyi) entropy in a random Haar circuit (Ref. [16]), where the initial state is a trivial product state (the situation is exactly like *fffa* in Fig. 3.3(c)); while for Fig. C.4(b), the minimal cut is exactly S_{Bell} for the *fafa* boundary condition (see Fig. 3.7(b)). The boundary conditions are also entirely similar: we follow the same coloring scheme, identifying “blue” with *a*, “red” with *b*, and “uncolored” with *f*.

From Fig. C.4(b), the symmetry between the upper and the lower edge is evident. As emphasized in Sec. 3.2.3, the symmetry is only possible due to unitarity-breaking measurements that induce entanglement swapping (see a similar discussion in Ref. [36]).

Recognizing that minimal cuts have the meaning of (Hartley) entanglement entropy, we numerically compute “entanglement entropies” and “mutual information” at the critical point $p_c = 0.5$ as in Ref. [16], making use of well-known algorithms for minimal cuts in graph theory [179, 180]. The results are shown in Fig. C.5. We also consider similar setups with periodic boundary condition, where the results are shown in Fig. C.6. In fitting the data, we have taken $Y = T$ for both open and periodic b.c. (see Sec. 3.1 for definitions), due to the rotational symmetry of the percolation problem.

The extracted scaling dimensions are summarized in Table 3.2, and they match well with

those from the existing literature, where available. This further supports our strategy of extracting scaling dimensions from the Clifford CFT. Comparing Clifford and percolation, we notice that the difference between the corresponding scaling dimensions are small but discernable under the present framework. We also observe that the scaling dimensions in the Clifford CFT are consistently larger than or equal to their percolation counterparts.

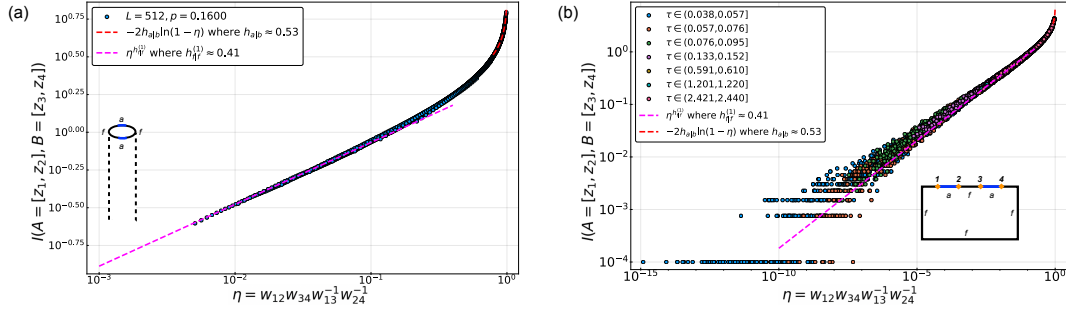


Figure C.3: The mutual information between $A = [z_1, z_2]$ and $B = [z_3, z_4]$, after all qubits outside $A \cup B$ are projected out in the final state of the circuit. For both (a) periodic and (b) open boundary conditions, we find $I([z_1, z_2], [z_3, z_4]) \propto \eta^{h_{f|f}^{(1)}}$ as $\eta \rightarrow 0$, where the value of $h_{f|f}^{(1)} \approx 0.41$ is in excellent agreement with previous results (see Figs. (3.8, C.1, C.2)) and is markedly different from percolation (see Table 3.2).

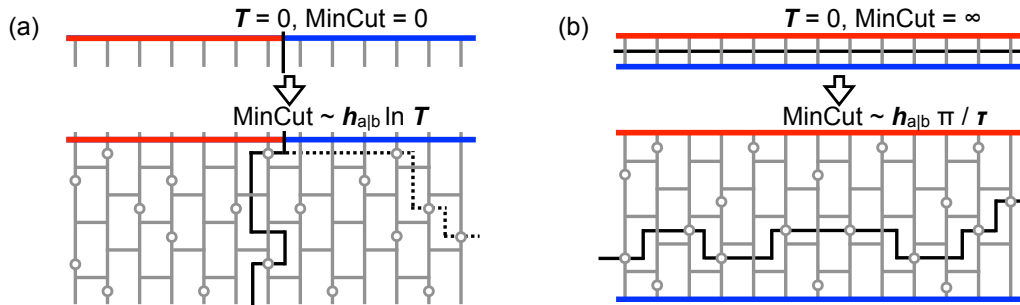


Figure C.4: Minimal cuts for two sets of different boundary conditions. (a) should be compared with the *ffa* circuit in Fig. 3.3, and (b) with the *fafa* circuit in Fig. 3.7. The finite time behavior follows from data collapse in Fig. C.5 and calculations in the main text.

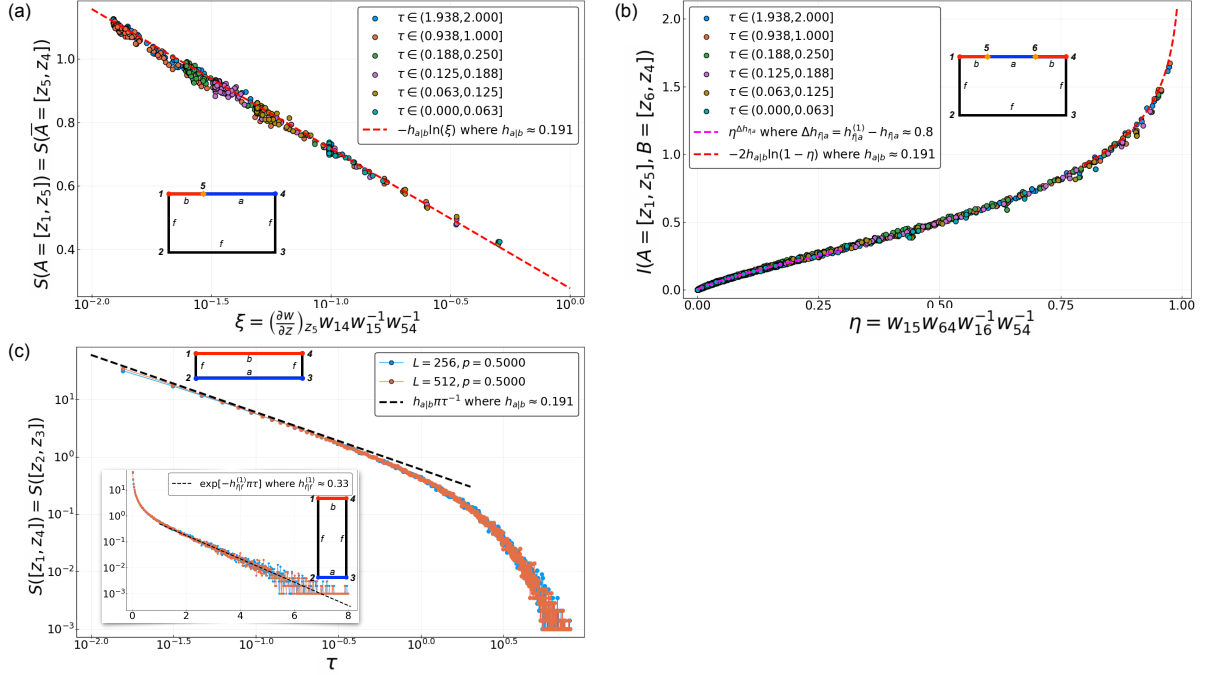


Figure C.5: (a,b) Numerical results of minimal cuts as in the setup of Fig. C.4(a), and should be compared with Fig. 3.5. (c) Numerical results as in the setup of Fig. C.4(b), and should be compared with Fig. 3.8. The extracted scaling dimensions are summarized in Table 3.2.

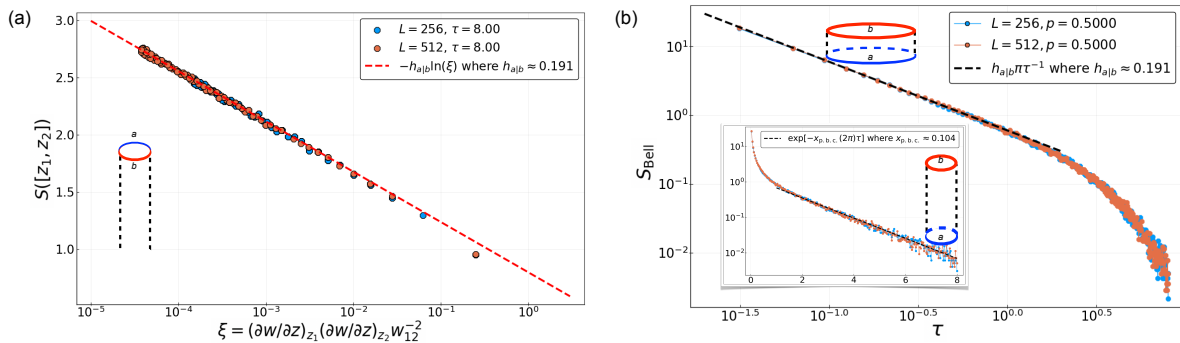


Figure C.6: Numerical results for the Hartley (0-th Rényi) entropy in Haar random circuits with measurements, in a geometry of the type of Fig. C.4(b), but with periodic spatial b.c. This figure should be compared with Fig. 3.11 in the main text.

Appendix D

Capillary-wave theory calculations

We compute within capillary-wave theory the free energies of two types of domain walls: those with pinned endpoints, as in Fig. 4.2(b); and those with free endpoints that wrap around the “waist” of the circuit, as in Fig. 4.3.

D.1 Domain walls with pinned endpoints

For the case in Fig. 4.2(b), we have (compare Eq. (4.20))

$$F_{\text{CW}}(A) \tag{D.1}$$

$$= -\ln \int \mathcal{D}[y(x)] \exp \left[-\beta\sigma \int_{x_1}^{x_2} dx \sqrt{1 + (\partial_x y)^2} \right], \tag{D.2}$$

where the functional integral over $y(x)$ is over the following class of “height functions”,

$$\begin{aligned} y : [x_1, x_2] &\rightarrow [-T, 0], \\ x &\mapsto y(x), \end{aligned} \tag{D.3}$$

with the additional constraint that the endpoints are “pinned”, $y(x_1) = y(x_2) = 0$. To regularize the path integral, we will however take $y(x_1) = y(x_2) = \epsilon$ to be a small constant, which can be

understood as the lattice spacing.

We first expand the square root,

$$\sqrt{1 + (\partial_x y)^2} = 1 + \frac{1}{2} (\partial_x y)^2 + O\left((\partial_x y)^4\right), \quad (\text{D.4})$$

and neglect quartic and higher order terms in $(\partial_x y)$; these are irrelevant under a renormalization group transformation. Thus we have a Gaussian theory,

$$\begin{aligned} F_{\text{CW}}(A) &= -\ln \int \mathcal{D}[y(x)] \exp \left[-\beta\sigma \int_{x_1}^{x_2} dx \left(1 + \frac{1}{2} (\partial_x y)^2 \right) \right] \\ &= \beta\sigma |A| - \ln \int \mathcal{D}[y(x)] \exp \left[-\frac{\beta\sigma}{2} \int_{x_1}^{x_2} dx (\partial_x y)^2 \right]. \end{aligned} \quad (\text{D.5})$$

The second term in this equation is the summation over all admissible configurations of paths/height functions $y(x)$, and can be viewed as a “random walk” with “diffusion constant” $(\beta\sigma)^{-1}$. It is thus regarded as the “thermal entropy” of transverse fluctuations of the domain walls. The magnitude of the fluctuation scales with x_{12} identically to that of a random walker, and can, for example, be quantified by the following quantity,

$$\sqrt{\langle [y(\bar{x}) - y(x_1)]^2 \rangle} \propto \sqrt{\frac{|A|}{\beta\sigma}}, \quad (\text{D.6})$$

where $\bar{x} := (x_1 + x_2)/2$.

In the following we will, for convenience, treat the path integral in Eq. (D.5) as a quantum mechanical transition amplitude, from which Eq. (D.6) can also be deduced. However, we note that there are other ways to evaluate this integral, e.g. by solving the diffusion equation subject to the constraint $y(x) \in [-T, 0]$.

We now “quantize” the path integral, with the spatial direction x viewed as “imaginary time”. We then have an imaginary time path integral of a free quantum particle with mass $\beta\sigma$,

confined within a potential well $y \in [-T, 0]$,

$$\begin{aligned}
& \exp[-F_{\text{CW}}(A) + \beta\sigma|A|] \\
&= \int_{y(x) \in [-T, 0], y(x_1)=y(x_2)=\epsilon} \mathcal{D}[y(x)] \exp\left[-\frac{\beta\sigma}{2} \int_{x_1}^{x_2} dx (\partial_x y)^2\right] \\
&= \langle y(x_2) | \exp[-\hat{H}x_{12}] | y(x_1) \rangle,
\end{aligned} \tag{D.7}$$

where the Hamiltonian is that of a “particle in box” problem,

$$\hat{H} = \frac{\hat{p}_y^2}{2M} + V(\hat{y}), \text{ where } V(y) = \begin{cases} 0, & -T \leq y \leq 0; \\ \infty, & \text{otherwise.} \end{cases} \tag{D.8}$$

The eigenstates and their corresponding energies are

$$\begin{aligned}
\phi_n(y) &= \langle y|n \rangle = \sqrt{\frac{2}{T}} \sin\left(\frac{n\pi y}{T}\right), \quad y \in [-T, 0], \\
E_n &= \frac{1}{2\beta\sigma} \left(\frac{n\pi}{T}\right)^2, \quad n = 1, 2, 3, \dots
\end{aligned} \tag{D.9}$$

We expand Eq. (D.7) in the eigenbasis,

$$\begin{aligned}
& \exp[-F_{\text{CW}}(A) + \beta\sigma|A|] \\
&= \sum_{n=1}^{\infty} \langle y(x_2)|n \rangle \langle n|y(x_1) \rangle \exp[-E_n x_{12}] \\
&= \frac{2}{T} \sum_{n=1}^{\infty} \sin^2\left(\frac{n\pi\epsilon}{T}\right) \exp\left[-\frac{1}{2\beta\sigma} \left(\frac{n\pi\sqrt{x_{12}}}{T}\right)^2\right].
\end{aligned} \tag{D.10}$$

When $\pi\sqrt{x_{12}}/T \ll 1$, we may approximate the summation with the following integral over

$$u = \frac{n\pi\sqrt{x_{12}}}{T},$$

$$\begin{aligned}
& \exp[-F_{\text{CW}}(A) + \beta\sigma|A|] \\
& \approx \frac{2}{T} \int_{\pi\sqrt{x_{12}}/T}^{\infty} \frac{T du}{\pi\sqrt{x_{12}}} \sin^2\left(\frac{u\epsilon}{\sqrt{x_{12}}}\right) \exp\left(-\frac{u^2}{2\beta\sigma}\right) \\
& \approx \frac{2}{\pi\sqrt{x_{12}}} \int_0^{\infty} du \sin^2\left(\frac{u\epsilon}{\sqrt{x_{12}}}\right) \exp\left(-\frac{u^2}{2\beta\sigma}\right) \\
& \approx \frac{2\epsilon^2}{\pi(x_{12})^{3/2}} \int_0^{\infty} du u^2 \exp\left(-\frac{u^2}{2\beta\sigma}\right) \\
& = \frac{2\epsilon^2}{\pi|A|^{3/2}} \int_0^{\infty} du u^2 \exp\left(-\frac{u^2}{2\beta\sigma}\right) \\
& = \sqrt{\frac{2}{\pi}} \epsilon^2 (\beta\sigma)^{3/2} |A|^{-3/2}, \tag{D.11}
\end{aligned}$$

and thus (compare Eq. (4.21))

$$\begin{aligned}
& F_{\text{CW}}(A) \\
& = \beta\sigma|A| + \frac{3}{2} \ln|A| + \text{const.}, \text{ when } \sqrt{|A|} \ll T. \tag{D.12}
\end{aligned}$$

In arriving at this result, we made the following replacement in the integrand

$$\sin^2\left(\frac{u\epsilon}{\sqrt{x_{12}}}\right) \exp\left(-\frac{u^2}{2\beta\sigma}\right) \rightarrow \left(\frac{u\epsilon}{\sqrt{x_{12}}}\right)^2 \exp\left(-\frac{u^2}{2\beta\sigma}\right); \tag{D.13}$$

this is valid when

$$\frac{\epsilon\sqrt{\beta\sigma}}{\sqrt{x_{12}}} \ll 1 \Leftrightarrow \epsilon \ll \sqrt{\frac{|A|}{\beta\sigma}}. \tag{D.14}$$

Physically, it means that the temperature cannot be too low, so that the transverse fluctuation of the domain wall is large compared to the ‘‘lattice spacing’’, ϵ . This is consistent with the $p = 0$ limit of the circuit (now without measurements), corresponding to the zero-temperature limit of capillary-wave theory, where the subleading logarithmic term is absent in the entanglement entropy (see discussions near footnote 11).

D.2 “Waist” domain walls

As shown in Fig. 4.3, the “waist” domain wall for open b.c. has two independent free endpoints; whereas for periodic b.c. the two endpoints must coincide, but otherwise free.

In the case of open b.c., let $y_1 = y(x_1 = 0)$, and $y_2 = y(x_2 = L)$. The analog to Eq. (D.7) reads

$$\begin{aligned}
& \exp[-F_{\text{CW}}(Q) + \beta\sigma|Q|] \\
&= \int_{y(x) \in [-T, 0]} \mathcal{D}[y(x)] \exp\left[-\frac{\beta\sigma}{2} \int_0^L dx (\partial_x y)^2\right] \\
&= \int_{-T}^0 dy_1 \int_{-T}^0 dy_2 \langle y_2 | \exp[-\hat{H}L] | y_1 \rangle \\
&= \int_{-T}^0 dy_1 \int_{-T}^0 dy_2 \sum_{n=1}^{\infty} \langle y_2 | n \rangle \langle n | y_1 \rangle \exp[-E_n L] \\
&= \frac{2}{T} \int_{-T}^0 dy_1 \int_{-T}^0 dy_2 \sum_{n=1}^{\infty} \sin\left(\frac{n\pi y_1}{T}\right) \sin\left(\frac{n\pi y_2}{T}\right) \exp\left[-\frac{1}{2\beta\sigma} \left(\frac{n\pi\sqrt{L}}{T}\right)^2\right] \\
&= \sum_{n \text{ odd}} \frac{8T}{n^2\pi^2} \exp\left[-\frac{1}{2\beta\sigma} \left(\frac{n\pi\sqrt{L}}{T}\right)^2\right] \\
&\approx \frac{1}{2} \int_{\pi\sqrt{L}/T}^{\infty} \frac{T du}{\pi\sqrt{L}} \frac{8L}{T u^2} \exp\left[-\frac{u^2}{2\beta\sigma}\right] \\
&= \frac{4\sqrt{L}}{\pi} \int_{\pi\sqrt{L}/T}^{\infty} du u^{-2} \exp\left[-\frac{u^2}{2\beta\sigma}\right] \\
&= \frac{4\sqrt{L}}{\pi} \left\{ \left[-u^{-1} \exp\left[-\frac{u^2}{2\beta\sigma}\right] \right] \Big|_{\pi\sqrt{L}/T}^{\infty} - \int_{\pi\sqrt{L}/T}^{\infty} du (-u^{-1}) \left(-\frac{u}{\beta\sigma}\right) \exp\left[-\frac{u^2}{2\beta\sigma}\right] \right\} \\
&\approx \frac{4}{\pi^2} T, \tag{D.15}
\end{aligned}$$

where we assumed $T \gg \sqrt{L}$ throughout.

For periodic b.c., letting $y = y(x_1 = 0) = y(x_2 = L)$, we have

$$\begin{aligned}
& \exp[-F_{\text{CW}}(Q) + \beta\sigma|Q|] \\
&= \int_{y(x) \in [-T, 0], y(0)=y(L)} \mathcal{D}[y(x)] \exp\left[-\frac{\beta\sigma}{2} \int_0^L dx (\partial_x y)^2\right] \\
&= \int_{-T}^0 dy \langle y | \exp[-\hat{H}L] | y \rangle \\
&= \int_{-T}^0 dy \sum_{n=1}^{\infty} \langle y | n \rangle \langle n | y \rangle \exp[-E_n L] \\
&= \sum_{n=1}^{\infty} \exp\left[-\frac{1}{2\beta\sigma} \left(\frac{n\pi\sqrt{L}}{T}\right)^2\right] \\
&\approx \int_{\pi\sqrt{L}/T}^{\infty} \frac{T du}{\pi\sqrt{L}} \exp\left[-\frac{u^2}{2\beta\sigma}\right] \\
&\approx \frac{T}{\pi\sqrt{L}} \int_0^{\infty} du \exp\left[-\frac{u^2}{2\beta\sigma}\right] \\
&= \sqrt{\frac{\beta\sigma}{2\pi}} \frac{T}{\sqrt{L}}, \tag{D.16}
\end{aligned}$$

where we again assumed $T \gg \sqrt{L}$ throughout.

Summarizing, we have (compare Eq. (4.22))

$$F_{\text{CW}}(Q) = \begin{cases} \beta\sigma L - \ln T + \text{const.}, & \text{open b.c.} \\ \beta\sigma L - \ln \frac{T}{\sqrt{L}} + \text{const.}, & \text{periodic b.c.} \end{cases} \quad \text{when } T \gg \sqrt{L}. \tag{D.17}$$

Similarly to domain walls with pinned endpoints, the subleading logarithmic term can again be understood as coming from thermal entropies of transverse fluctuations. The $\ln \sqrt{L}$ difference is the extra endpoint entropy in open b.c..

D.3 Point-to-line (pl) domain walls

We consider domain walls in the upper half plane, with one endpoint pinned. That is, $y(x_1) = \epsilon$, but $y(x_2) \in [-T, 0]$ unconstrained (a free endpoint). We have

$$\begin{aligned}
& \exp \left[-F_{\text{CW}}^{\text{pl}}(Q) + \beta\sigma|Q| \right] \\
&= \int_{y(x) \in [-T, 0], y(x_1) = \epsilon} \mathcal{D}[y(x)] \exp \left[-\frac{\beta\sigma}{2} \int_{x_1}^{x_2} dx (\partial_x y)^2 \right] \\
&= \int_{-T}^0 dy \langle y | \exp \left[-\hat{H}x_{12} \right] | \epsilon \rangle \\
&= \int_{-T}^0 dy \sum_{n=1}^{\infty} \langle y | n \rangle \langle n | \epsilon \rangle \exp \left[-E_n x_{12} \right] \\
&= \int_{-T}^0 dy \sum_{n=1}^{\infty} \left(\frac{2}{T} \right) \sin \left(\frac{n\pi y}{T} \right) \sin \left(\frac{n\pi \epsilon}{T} \right) \exp \left[-\frac{1}{2\beta\sigma} \left(\frac{n\pi\sqrt{x_{12}}}{T} \right)^2 \right] \\
&= \sum_{n=1}^{\infty} \left(\frac{2}{T} \right) \left[\int_{-T}^0 dy \sin \left(\frac{n\pi y}{T} \right) \right] \sin \left(\frac{n\pi \epsilon}{T} \right) \exp \left[-\frac{1}{2\beta\sigma} \left(\frac{n\pi\sqrt{x_{12}}}{T} \right)^2 \right] \\
&= \sum_{n=1}^{\infty} \left(\frac{2}{T} \right) \left[\frac{2T}{n\pi} \delta_{n \text{ odd}} \right] \sin \left(\frac{n\pi \epsilon}{T} \right) \exp \left[-\frac{1}{2\beta\sigma} \left(\frac{n\pi\sqrt{x_{12}}}{T} \right)^2 \right] \\
&\approx \left(\frac{4\epsilon}{T} \right) \sum_{n \geq 1, n \text{ odd}} \exp \left[-\frac{1}{2\beta\sigma} \left(\frac{n\pi\sqrt{x_{12}}}{T} \right)^2 \right] \\
&\approx \left(\frac{4\epsilon}{T} \right) \frac{1}{2} \int_{\pi\sqrt{x_{12}}/T}^{\infty} \frac{T du}{\pi\sqrt{x_{12}}} \exp \left[-\frac{u^2}{2\beta\sigma} \right] \\
&\approx \left(\frac{2\epsilon}{\pi\sqrt{x_{12}}} \right) \int_0^{\infty} du \exp \left[-\frac{u^2}{2\beta\sigma} \right] \\
&\approx \left(\frac{2\epsilon}{\pi\sqrt{x_{12}}} \right) \sqrt{\frac{\pi\beta\sigma}{2}} \\
&\approx \sqrt{\frac{2\beta\sigma}{\pi}} \epsilon \cdot (x_{12})^{-1/2}. \tag{D.18}
\end{aligned}$$

where we again assumed $T \gg \sqrt{L}$ throughout.

Appendix E

Cross entropy as boundary correlation function

E.1 Bulk cross entropy

We unpack the circuit averaged linear cross-entropy χ defined in Eq. (5.7),

$$\begin{aligned}\chi &:= \mathbb{E}_C \chi_C \\ &= \mathbb{E}_C \frac{\sum_{\mathbf{m}} p_{\mathbf{m}}^{\rho} p_{\mathbf{m}}^{\sigma}}{\sum_{\mathbf{m}} (p_{\mathbf{m}}^{\sigma})^2} \\ &= \mathbb{E}_C \frac{\sum_{\mathbf{m}} \left(\text{tr } C_{\mathbf{m}} \rho C_{\mathbf{m}}^{\dagger} \right) \left(\text{tr } C_{\mathbf{m}} \sigma C_{\mathbf{m}}^{\dagger} \right)}{\sum_{\mathbf{m}} \left(\text{tr } C_{\mathbf{m}} \sigma C_{\mathbf{m}}^{\dagger} \right)^2} \\ &= \mathbb{E}_C \frac{\sum_{\mathbf{m}} \text{tr } C_{\mathbf{m}}^{\otimes 2} \cdot (\rho \otimes \sigma) \cdot C_{\mathbf{m}}^{\dagger \otimes 2}}{\sum_{\mathbf{m}} \text{tr } C_{\mathbf{m}}^{\otimes 2} \cdot (\sigma \otimes \sigma) \cdot C_{\mathbf{m}}^{\dagger \otimes 2}}.\end{aligned}\tag{E.1}$$

Recall that the letter C encodes the circuit layout (i.e. the locations of unitary gates and measurements) and the unitary gates, but not the measurement outcomes. The summation over \mathbf{m} is taken inside the average, in both the numerator and denominator, independently. Thus, χ is different from the trajectory-averaged entanglement entropies that are used previously for identifying the MIPT. Nevertheless, in Fig. 5.2 we see that the location of the transition and

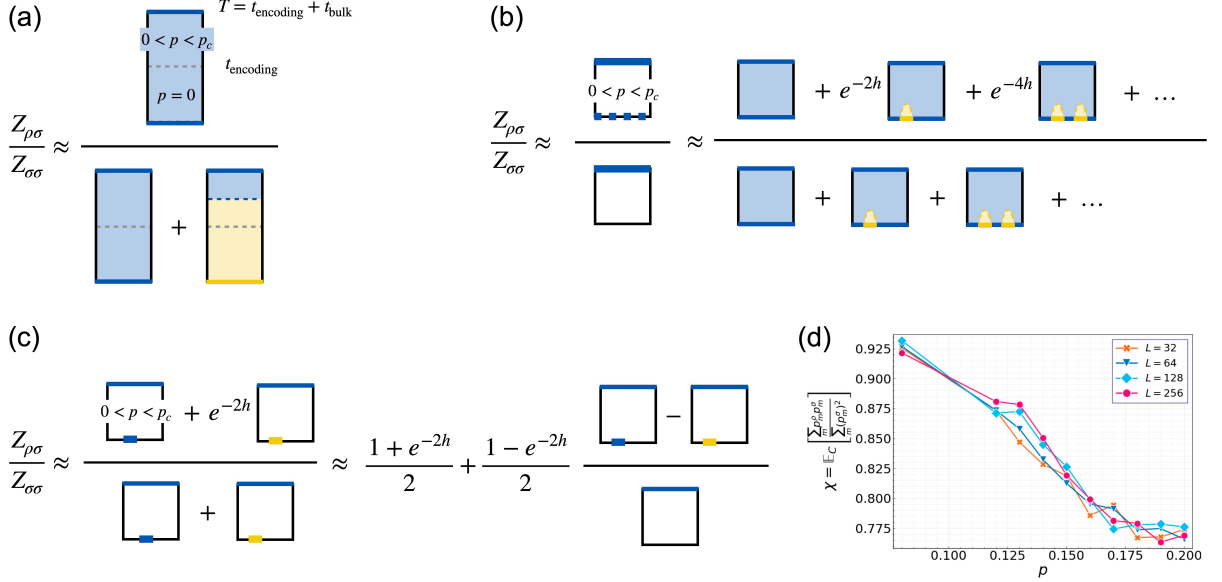


Figure E.1: (a) Pictorial representation of the partition function ratio $Z_{\rho\sigma}/Z_{\sigma\sigma}$ in Eq. (E.8), for $p = 0$ in the encoding stage and $p < p_c$ in the circuit bulk. (b) Pictorial representation of the partition function ratio in Eq. (E.10). Here we do not have an encoding stage, and there is a *uniform*, finite magnetic field of strength h (represented with a dashed line) applied at the $t = 0$ boundary. (c) Pictorial representation of the partition function ratio in Eq. (E.11), Here we do not have an encoding stage, and there is a *local*, finite magnetic field of strength h applied at the $t = 0$ boundary. In all figures the blue color represents spins pointing in the “+” direction, the yellow color represents spins pointing in the “−” direction, and the black color represents a “free” boundary condition, where the spins can point in either direction.

the critical exponent ν do not change much when we use χ as an order parameter.

A proper treatment of the quenched average leads to a replicated spin model.¹ For our purposes here, we can instead consider the annealed average [22, 61], while keeping in mind that this is only an illustrative tool. In particular, consider

$$\bar{\chi} = \frac{\mathbb{E}_C \sum_{\mathbf{m}} \text{tr} C_{\mathbf{m}}^{\otimes 2} \cdot (\rho \otimes \sigma) \cdot C_{\mathbf{m}}^{\dagger \otimes 2}}{\mathbb{E}_C \sum_{\mathbf{m}} \text{tr} C_{\mathbf{m}}^{\otimes 2} \cdot (\sigma \otimes \sigma) \cdot C_{\mathbf{m}}^{\dagger \otimes 2}}. \quad (\text{E.2})$$

After the average over C , the numerator and the denominator each becomes an Ising partition function on a triangular lattice. They have bulk weights $J_p(s_i, s_j; s_k)$ for each downward-pointing triangle [30, 31] (see also Refs. [28, 29, 137]), and only differ in their boundary condi-

¹Due to the difference we stressed above, this leads to a stat mech model that differs from those obtained in Refs. [30, 31]. In particular, the spins here take values in the permutation group $S_{Q=2n}$ with the replica limit $n \rightarrow 0$, and which has a different symmetry.

tions. We denote them $Z_{\rho\sigma}$ and $Z_{\sigma\sigma}$, respectively.

We take ρ and σ to be products of local density matrices, i.e.

$$\rho = \prod_{x=1}^L \rho_x, \quad \sigma = \prod_{x=1}^L \sigma_x, \quad \text{where } \text{tr } \rho_x = \text{tr } \sigma_x = 1 \quad \forall x. \quad (\text{E.3})$$

Moreover, we also have $\text{tr } \sigma_x^2 = 1$ since σ is a pure product state. Thus,

$$\begin{aligned} Z_{\sigma\sigma} &= \sum_{\{s_i=\pm 1\}} \prod_{\langle i,j,k \rangle \in \nabla} J_p(s_i, s_j; s_k) \cdot \prod_{x \in \partial \mathcal{M}_T} \delta_{s_x=+1} \cdot \prod_{x \in \partial \mathcal{M}_0} (\delta_{s_x=+1} (\text{tr } \sigma_x)^2 + \delta_{s_x=-1} \text{tr}(\sigma_x^2)) \\ &= \sum_{\{s_i=\pm 1\}} \prod_{\langle i,j,k \rangle \in \nabla} J_p(s_i, s_j; s_k) \cdot \prod_{x \in \partial \mathcal{M}_T} \delta_{s_x=+1}, \end{aligned} \quad (\text{E.4})$$

and

$$\begin{aligned} Z_{\rho\sigma} &= \sum_{\{s_i=\pm 1\}} \prod_{\langle i,j,k \rangle \in \nabla} J_p(s_i, s_j; s_k) \cdot \prod_{x \in \partial \mathcal{M}_T} \delta_{s_x=+1} \cdot \prod_{x \in \partial \mathcal{M}_0} (\delta_{s_x=+1} (\text{tr } \rho_x)(\text{tr } \sigma_x) + \delta_{s_x=-1} \text{tr}(\rho_x \cdot \sigma_x)) \\ &= \sum_{\{s_i=\pm 1\}} \prod_{\langle i,j,k \rangle \in \nabla} J_p(s_i, s_j; s_k) \cdot \prod_{x \in \partial \mathcal{M}_T} \delta_{s_x=+1} \cdot \prod_{x \in \partial \mathcal{M}_0} (\delta_{s_x=+1} + \delta_{s_x=-1} \text{tr}(\rho_x \cdot \sigma_x)) \\ &= \sum_{\{s_i=\pm 1\}} \prod_{\langle i,j,k \rangle \in \nabla} J_p(s_i, s_j; s_k) \cdot \prod_{x \in \partial \mathcal{M}_T} \delta_{s_x=+1} \cdot \prod_{x \in \partial \mathcal{M}_0} e^{h_x(s_x-1)}. \end{aligned} \quad (\text{E.5})$$

Here, we use $\partial \mathcal{M}_0$ to denote the $t = 0$ boundary of the circuit, and $\partial \mathcal{M}_T$ to denote the final time ($t = T$) boundary. We see that at $t = 0$, $Z_{\sigma\sigma}$ has a “free” boundary condition, and $Z_{\rho\sigma}$ has a magnetic field with strength $h_x = -\frac{1}{2} \ln [\text{tr}(\rho_x \cdot \sigma_x)]$. At $t = T$, in both partition functions spins are fixed to be $s_x = +1$.

Our circuit in Fig. 5.1 has an “encoding” stage without measurements ($p = 0$) up until $t_{\text{encoding}} = 2L$. This makes the lower half of the circuit a pure unitary one, where domain walls with both endpoints on the $t = 0$ boundary are disallowed by the microscopics of the stat mech model [28, 29]. In this case, the finite-strength field at the $t = 0$ boundary of $Z_{\rho\sigma}$ becomes

essentially infinite, putting a hard boundary condition at $t = 0$:

$$\begin{aligned}
Z_{\rho\sigma} &\approx \sum_{\{s_i=\pm 1\}} \prod_{\langle i,j,k \rangle \in \nabla} J_p(s_i, s_j; s_k) \\
&\quad \cdot \prod_{x \in \partial\mathcal{M}_T} \delta_{s_x=+1} \cdot \prod_{x \in \partial\mathcal{M}_0} \delta_{s_x=+1} \\
&:= Z_{++},
\end{aligned} \tag{E.6}$$

where Z_{++} denotes the partition function with $+$ boundary condition at $t = 0$ and $+$ boundary condition at $t = T$. By the same reasoning and the same notation, we can rewrite

$$Z_{\sigma\sigma} \approx Z_{++} + Z_{-+}. \tag{E.7}$$

We represent these partition functions diagrammatically in Fig. E.1, where the boundary conditions are highlighted with color: blue for $+$ and orange for $-$. (In the figure, we only illustrated the case where $p < p_c$ after the initial encoding stage; these two stages are separated by a gray, dashed line.) We have

$$\bar{\chi} = \frac{Z_{\rho\sigma}}{Z_{\sigma\sigma}} = \frac{1}{1 + Z_{-+}/Z_{++}}. \tag{E.8}$$

In the volume law phase, we expect $Z_{-+}/Z_{++} \propto \exp(-L + o(L))$, because a domain wall with finite line tension of length L must be inserted between $t \in [t_{\text{encoding}}, T]$, to accommodate the boundary conditions change from $-$ to $+$ in time; see Fig. E.1. On the other hand, in the area law phase, the domain wall line tension vanishes, and we have $Z_{-+}/Z_{++} = O(1)$. Thus,

$$\bar{\chi} = \begin{cases} 1 + \exp(-L), & p < p_c \\ O(1), & p > p_c \end{cases}. \tag{E.9}$$

Despite the fact that we are adopting an annealed average in $\bar{\chi}$, it captures the qualitative behavior of the quenched average χ in Sec. 5.1 in the two phases (but presumably not the

critical properties).

E.2 Bulk cross entropy without encoding

Here we extend our discussion in Sec. 5.1.3 on χ in the absence of the encoding stage, so that the entire two-dimensional magnet is now at finite temperature; see Fig. E.1(b). Here, the partition functions $Z_{\rho\rho}$ and $Z_{\sigma\sigma}$ have boundary conditions that are identical to those in Eqs. (E.4, E.5). However, the spins at the $t = 0$ boundary now need not be completely aligned, and small domain walls can be created at the cost of a finite free energy per unit length.

Using the same graphical notation as in Fig. E.1(a), with an additional color, black, representing the “free” boundary condition f , and dashed blue line representing the finite strength boundary magnetic field h_x in the “+” direction at $t = 0$, we represent $\bar{\chi} = \frac{Z_{\rho\sigma}}{Z_{\sigma\sigma}}$ again with partition functions of appropriate boundary conditions in Fig. E.1(b). First consider a case where the boundary magnetic field $h_x = -\frac{1}{2} \ln [\text{tr}(\rho_x \cdot \sigma_x)]$ is uniform and independent of x . This would be the case when, say, $\rho = \frac{1}{2L} \mathbb{1}$ and $\sigma = (|0\rangle\langle 0|)^{\otimes L}$. Let the free energy cost of a domain wall with unit length be δF and define the fugacity to be $y = e^{-\delta F}$, we have (compare Fig. E.1(b))

$$\begin{aligned} \bar{\chi} &= \frac{Z_{\rho\sigma}}{Z_{\sigma\sigma}} \\ &= \frac{1 + \binom{L}{1} e^{-2h} y + \binom{L}{2} e^{-4h} y^2 + \dots}{1 + \binom{L}{1} y + \binom{L}{2} y^2 + \dots} \\ &\approx \frac{(1 + e^{-2h} y)^L}{(1 + y)^L}. \end{aligned} \tag{E.10}$$

Both $Z_{\rho\sigma}$ and $Z_{\sigma\sigma}$ numerator are now a series of terms, with the i -th leading term having i domain walls each of unit length (neglecting their interactions). Thus, $\bar{\chi}$ is exponentially suppressed by L for any $h > 0$, thus negligible throughout the phase diagram.

We can also generalize Eq. (E.10) to the case where ρ and σ only differ on one site, as

discussed in Sec. 5.1.3. The partition functions are shown in Fig. E.1(c), where we obtain

$$\bar{\chi} \approx \frac{1 + e^{-2h}}{2} + \frac{1 - e^{-2h}}{2} \langle s_{x \in \partial \mathcal{M}_0} \rangle_{s_{x \in \partial \mathcal{M}_T} = +1}. \quad (\text{E.11})$$

Here $\langle s_{x \in \partial \mathcal{M}_0} \rangle_{s_{x \in \partial \mathcal{M}_T} = +1}$ is the expectation value of a boundary spin. Thus, we expect the following behavior of χ near the critical point:

$$\bar{\chi} \approx \begin{cases} |p - p_c|^\beta + \chi_0, & p < p_c \\ \chi_0, & p > p_c \end{cases}. \quad (\text{E.12})$$

Here, $\chi_0 \approx \frac{1+e^{-2h}}{2}$ is a nonuniversal constant between 0 and 1.

E.3 Numerical algorithm for cross entropy in Clifford circuits

We first recall a ‘‘purified’’ representation of the hybrid circuit. As pointed out in Refs. [21, 31], the dynamics of the hybrid circuit can be purified by introducing one ‘‘register’’ qubit for each single site measurement. In particular, each measurement can be replaced by a controlled-NOT (CNOT) gate from the measured qubit to the register, followed by a dephasing channel on the register.² With these, at the end of the time evolution we have the following joint state

²To see this, it is sufficient to consider the case of one qubit and one register. Initially, let the qubit be in the state $|\psi\rangle = \alpha|0\rangle + \beta|1\rangle$, and the register be in the state $|0\rangle$, so the joint state is

$$\rho_{QR} = |\psi\rangle \langle \psi|_Q \otimes |0\rangle \langle 0|_R. \quad (\text{E.13})$$

After the CNOT gate, we have

$$\begin{aligned} \rho'_{QR} &= \text{CNOT}_{Q \rightarrow R} \cdot \rho_{QR} \cdot \text{CNOT}_{Q \rightarrow R} \\ &= (\alpha|00\rangle + \beta|11\rangle)(\alpha^* \langle 00| + \beta^* \langle 11|)_{QR}. \end{aligned} \quad (\text{E.14})$$

Under the dephasing channel on R ,

$$\begin{aligned} \rho''_{QR} &= \frac{1}{2} (\rho'_{QR} + Z_R \rho'_{QR} Z_R) \\ &= |\alpha|^2 |0\rangle \langle 0|_Q \otimes |0\rangle \langle 0|_R + |\beta|^2 |1\rangle \langle 1|_Q \otimes |1\rangle \langle 1|_R \\ &= (P_0 |\psi\rangle \langle \psi| P_0)_Q \otimes |0\rangle \langle 0|_R + (P_1 |\psi\rangle \langle \psi| P_1)_Q \otimes |1\rangle \langle 1|_R. \end{aligned} \quad (\text{E.15})$$

The result ρ''_{QR} is a mixture of different trajectories, with the measurement outcome stored in R . Generalization to many qubits and many registers can be carried out in a similar fashion.

on physical qubits Q and register qubits R ,

$$\rho_{QR} = \sum_{\mathbf{m}} C_{\mathbf{m}} \rho C_{\mathbf{m}}^{\dagger} \otimes |\mathbf{m}\rangle \langle \mathbf{m}|_R. \quad (\text{E.16})$$

And similarly for the initial state σ ,

$$\sigma_{QR} = \sum_{\mathbf{m}} C_{\mathbf{m}} \sigma C_{\mathbf{m}}^{\dagger} \otimes |\mathbf{m}\rangle \langle \mathbf{m}|_R. \quad (\text{E.17})$$

The cross-entropy will then have the following representation

$$\chi_C = \frac{\sum_{\mathbf{m}} p_{\mathbf{m}}^{\rho} p_{\mathbf{m}}^{\sigma}}{\sum_{\mathbf{m}} (p_{\mathbf{m}}^{\sigma})^2} = \frac{\text{tr } \rho_R \sigma_R}{\text{tr } \sigma_R^2}, \quad (\text{E.18})$$

where ρ_R is the reduced state of ρ_{QR} on R , and similarly for σ_R .

We now focus on the case where ρ and σ are both stabilizer states and the circuit is a Clifford circuit, so that $\rho_{QR}, \sigma_{QR}, \rho_R, \sigma_R$ are all stabilizer states. Moreover, we will choose the state ρ to be obtainable from σ via erasure and dephasing channels. Equivalently, we choose states ρ and σ such that the stabilizer group \mathcal{S}_{ρ} is a subgroup of \mathcal{S}_{σ} . Whenever this condition is satisfied for the initial state, it follows that $\mathcal{S}_{\rho_{QR}} \subseteq \mathcal{S}_{\sigma_{QR}}$ and $\mathcal{S}_{\rho_R} \subseteq \mathcal{S}_{\sigma_R}$ at any point of the purified circuit evolution. With this property, Eq. (E.18) can be greatly simplified. We have

$$\rho_R = \frac{1}{2^{|R|}} \sum_{g \in \mathcal{S}_{\rho_R}} g, \quad \sigma_R = \frac{1}{2^{|R|}} \sum_{h \in \mathcal{S}_{\sigma_R}} h, \quad (\text{E.19})$$

and

$$\begin{aligned} \text{tr } \rho_R \sigma_R &= \frac{1}{2^{2|R|}} \sum_{g \in \mathcal{S}_{\rho_R}} \sum_{h \in \mathcal{S}_{\sigma_R}} \text{tr } gh \\ &= \frac{1}{2^{2|R|}} \sum_{g \in \mathcal{S}_{\rho_R}} \sum_{h \in \mathcal{S}_{\rho_R}} \text{tr } gh \\ &= \text{tr } \rho_R^2. \end{aligned} \quad (\text{E.20})$$

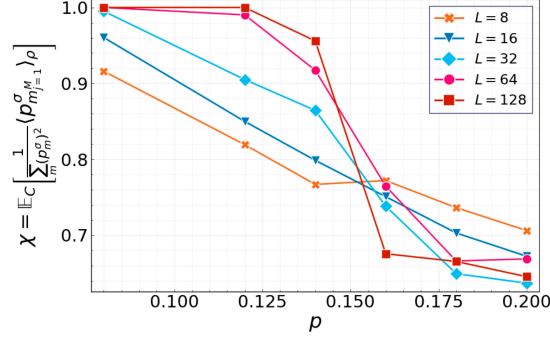


Figure E.2: Numerical results of χ for initial states $\rho = (|0\rangle\langle 0|)^{\otimes L/2} \otimes (|+\rangle\langle +|)^{\otimes L/2}$ and $\sigma = (|0\rangle\langle 0|)^{\otimes L}$, following the procedure in Eq. (E.24). Despite a different choice of initial state, the results are comparable to Fig. 5.2(a) and Fig. 5.3.

Here, we noticed that $\text{tr } gh = 2^{|R|} \delta_{gh}$ for Pauli strings g and h , and used $\mathcal{S}_{\rho_R} \subseteq \mathcal{S}_{\sigma_R}$. Thus, the cross-entropy is simply the ratio between the second Renyi purity of the probability distributions $\{p_{\mathbf{m}}^{\rho}\}$ and $\{p_{\mathbf{m}}^{\sigma}\}$,

$$\chi_C = \frac{\text{tr } \rho_R^2}{\text{tr } \sigma_R^2} = \frac{\sum_{\mathbf{m}} (p_{\mathbf{m}}^{\rho})^2}{\sum_{\mathbf{m}} (p_{\mathbf{m}}^{\sigma})^2}. \quad (\text{E.21})$$

For Clifford circuit evolution, the second Renyi purity equals $2^{-N_{\text{rand}}}$, where N_{rand} is the number of measurements (out of the total N) whose outcome is randomly ± 1 .³ This number N_{rand} can be obtained by running the circuit once for each initial state [68]. We have

$$\chi_C = 2^{-N_{\text{rand}}(C,\rho) + N_{\text{rand}}(C,\sigma)}. \quad (\text{E.22})$$

More generally, for initial states ρ and σ that may not satisfy the condition $\mathcal{S}_{\rho} \subseteq \mathcal{S}_{\sigma}$, Eq. (E.20) takes the form

$$\text{tr } \rho_R \sigma_R = \frac{1}{2^{2|R|}} \sum_{g \in \mathcal{S}_{\rho_R}} \sum_{h \in \mathcal{S}_{\sigma_R}} \text{tr } gh = \frac{|\mathcal{S}_{\rho_R} \cap \mathcal{S}_{\sigma_R}|}{2^{|R|}}. \quad (\text{E.23})$$

Computing $|\mathcal{S}_{\rho_R} \cap \mathcal{S}_{\sigma_R}|$ without further simplifications can take time $O(L^3 \cdot T^3)$. In practice

³Recall that for Clifford circuits a measurement either has a deterministic outcome, or has random outcomes ± 1 with equal probabilities $1/2$ [68]. There are $2^{N_{\text{rand}}}$ possible trajectories in total, and they occur with equal probability $2^{-N_{\text{rand}}}$.

it would be most convenient to carry out the sampling procedure outlined at the beginning of Sec. 5.1.2, which, as we have shown, converges in $\text{poly}(1/\varepsilon)$ time. In particular, we can rewrite Eq. (5.11) as

$$\chi_C = \lim_{M \rightarrow \infty} \left\langle \frac{p_{\mathbf{m}_{j=1}^M}^\sigma}{\sum_{\mathbf{m}} (p_{\mathbf{m}}^\sigma)^2} \right\rangle_\rho = \frac{1}{\text{tr } \sigma_R^2} \lim_{M \rightarrow \infty} \left\langle p_{\mathbf{m}_{j=1}^M}^\sigma \right\rangle_\rho. \quad (\text{E.24})$$

That is, we run the ρ -circuit and obtain an ensemble of measurement histories $\{\mathbf{m}_j\}$, and take the average of their corresponding probabilities $p_{\mathbf{m}_j}^\sigma$ in the σ -circuit, divided by $\text{tr } \sigma_R^2 = \sum_{\mathbf{m}} (p_{\mathbf{m}}^\sigma)^2$. Each $p_{\mathbf{m}_j}^\sigma / \text{tr } \sigma_R^2$ can be computed in polynomial time by running a σ -circuit in parallel.

To verify the validity of this method, we consider initial states $\rho = (|0\rangle\langle 0|)^{\otimes L/2} \otimes (|+\rangle\langle +|)^{\otimes L/2}$ and $\sigma = (|0\rangle\langle 0|)^{\otimes L}$. Both are stabilizer states, but $\mathcal{S}_\rho \not\subseteq \mathcal{S}_\sigma$, and Eq. (E.22) does not apply. We carry out the sampling procedure in Eq. (E.24), and plot the results in Fig. E.2, which we find comparable to Fig. 5.2(a) despite a more involved numerical calculation. Thus, to estimate χ we have the freedom of choosing ρ , as consistent with the picture developed in Appendix E.

Appendix F

Bitstring distribution in the output state

As we discussed in the main text, the linear cross-entropy χ for the MIPT is most conveniently estimated numerically for Clifford circuits with a stabilizer initial state ρ , and can be extended to Clifford circuit with a non-stabilizer ρ (and scaled up) given access to a quantum processor. In either case χ admits the same interpretation in the stat mech language, and should contain the same universal data, e.g. the critical exponent ν . Thus, one natural question is whether considering a non-stabilizer initial state on a quantum processor reveals anything new about the physics surrounding the MIPT.

As we have shown, in the volume law phase, $\chi = 1$ almost identically for sufficiently large L ; and it follows that it is impossible – in an information-theoretic sense – to distinguish two different initial states from infrequent ($p < p_c$) bulk measurements. The information about the initial state must therefore be contained in the output state of the circuit.

The difference between the two initial states may be detected using various measures [181, 182]. Here we consider the probability distribution over bitstrings when each qubit of the output state of the ρ -circuit (namely $\rho_{\mathbf{m}} = C_{\mathbf{m}}\rho C_{\mathbf{m}}^\dagger$ in Eq. (5.1)) is measured in the computational basis, where the input state ρ is taken to be the one from Eq. (5.13). For a fixed bitstring

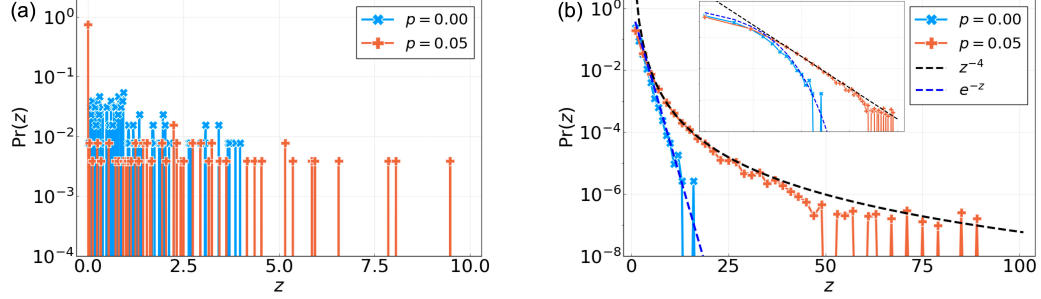


Figure F.1: (a) The bitstring distribution defined in Eq. (F.2), for a typical instance of $C_{\mathbf{m}}$ with a generic (nonstabilizer) initial state ρ in Eq. (5.13). We see a broad distribution, in sharp contrast to the bitstring distribution from a stabilizer initial state in Eq. (F.3). (b) The bitstring distribution defined in Eq. (F.4), when the data in (a) is averaged over $C_{\mathbf{m}}$. The Porter-Thomas distribution $\text{Pr}(z) = e^{-z}$ is reproduced in the unitary limit $p = 0$, and a qualitatively different (powerlaw) distribution is observed for $p > 0$ (see Eq. (F.6)).

$x \in \{0, 1\}^L$, the probability for this outcome to occur in the output state of $C_{\mathbf{m}}$ is

$$\mu(x; C_{\mathbf{m}}, \rho) = \langle x | \bar{\rho}_{\mathbf{m}} | x \rangle, \quad (\text{F.1})$$

where $\bar{\rho}_{\mathbf{m}} = \rho_{\mathbf{m}} / \text{tr } \rho_{\mathbf{m}}$ is the normalized output state. In Fig. F.1(a) we plot the fraction of bistrings with probability $\mu = z/D$ in a typical instance of $C_{\mathbf{m}}$, where z is a random variable and $D = 2^L$ is the dimension of the L -qubit Hilbert space,

$$\text{Pr}(z; C_{\mathbf{m}}, \rho) = \frac{1}{D} \sum_{x \in \{0, 1\}^L} \delta(z - \mu(x; C_{\mathbf{m}}, \rho) \cdot D). \quad (\text{F.2})$$

As we can see, in a typical circuit at $p > 0$ the output distribution is already notably broader than at $p = 0$.

On the other hand, for the output of the σ -circuit, namely $\bar{\sigma}_{\mathbf{m}} = C_{\mathbf{m}} \sigma C_{\mathbf{m}}^\dagger / \text{tr } C_{\mathbf{m}} \sigma C_{\mathbf{m}}^\dagger$ where σ is a stabilizer state, the distribution function $\text{Pr}(z; C_{\mathbf{m}}, \sigma)$ is much simpler:

$$\text{Pr}(z; C_{\mathbf{m}}, \sigma) = \left(1 - \frac{1}{2^{L-n}}\right) \delta(z) + \frac{1}{2^{L-n}} \delta(z - 2^{L-n}). \quad (\text{F.3})$$

Here, n is an integer between 0 and L . The broad distribution in Fig. F.1(a) is markedly different from this, and is due to the fact that ρ is a non-stabilizer state.

We focus on the non-stabilizer state $\bar{\rho}_{\mathbf{m}}$ henceforth. In analogy with random unitary circuits, we consider the circuit average of $\Pr(z; C_{\mathbf{m}})$,

$$\begin{aligned} \Pr(z) &:= \mathbb{E}_{C_{\mathbf{m}}} \Pr(z; C_{\mathbf{m}}) \\ &= \frac{1}{D} \sum_{x \in \{0,1\}^L} \mathbb{E}_{C_{\mathbf{m}}} \delta(z - \mu(x; C_{\mathbf{m}}, \rho) \cdot D) \\ &= \mathbb{E}_{C_{\mathbf{m}}} \delta(z - \mu(x; C_{\mathbf{m}}, \rho) \cdot D). \end{aligned} \tag{F.4}$$

Here, after circuit averaging $\Pr(z)$ does not depend on the bitstring x despite the notation, and we can choose $|x\rangle = |0\rangle^{\otimes L}$, for concreteness.

In the unitary limit $p = 0$, there are no measurements, and $\mathbb{E}_{C_{\mathbf{m}}} = \mathbb{E}_U$. Here $\Pr(z)$ should be the Porter-Thomas distribution since the Clifford group forms a unitary 2-design,

$$\Pr(z) = \mathbb{E}_U \delta(z - \mu(x; U, \rho) \cdot D) = e^{-z}. \tag{F.5}$$

For $p > 0$, we observe numerically that (see Fig. F.1(b))

$$\Pr(z) \propto \alpha \delta(z) + \beta z^{-\gamma}, \quad \gamma \approx 4. \tag{F.6}$$

Since this function $z^{-\gamma}$ diverges as $z \rightarrow 0$, the asymptotics is only valid for z greater than some (possibly L -dependent, see below) cutoff λ . We suspect that the exponent γ is universal (as we have checked for a few values of p), while the constants of proportionality α, β are λ -dependent (to keep $\Pr(z)$ normalized) and nonuniversal.

Since the distributions in Fig. F.1(a,b) have long tails – meaning that in a given $C_{\mathbf{m}}$ the bitstrings occur with rather uneven probabilities – predicting which ones occur more commonly should be hard, and it is tempting to conjecture the classical hardness of sampling x from the probability distribution $\mu(x; C_{\mathbf{m}}, \rho)$, for a generic (non-stabilizer) initial state ρ . Given that on a noiseless quantum computer we can simulate the hybrid circuit and produce the state $\rho_{\mathbf{m}}$, such hybrid circuits may serve the purpose of demonstrating quantum advantage.

However, there is an important caveat here. As evident from the definition of μ , for a fixed C the bitstring distribution as obtained from measuring $\rho_{\mathbf{m}}$ still has an explicit dependence on \mathbf{m} . In each run of the circuit, one gets a new \mathbf{m} , and the bitstring distribution μ changes from run to run. Thus, even the circuit itself cannot efficiently sample $\mu(x; C_{\mathbf{m}}, \rho)$ for any given \mathbf{m} , for we have no control over \mathbf{m} , and cannot repeatedly prepare $\rho_{\mathbf{m}}$. To sample x from $\mu(x; C_{\mathbf{m}}, \rho)$ for a given \mathbf{m} , it seems that we must again resort to postselection.

It might be possible to avoid the need of postselection by focusing on a particular subset of non-stabilizer initial states ρ , for which the bitstring distributions $\mu(x; C_{\mathbf{m}}, \rho)$ for different \mathbf{m} can be related to each other by a change of variable in x . Characterizations of such ρ is beyond the scope of this work, which we will discuss elsewhere.

Bibliography

- [1] A. Einstein, B. Podolsky, and N. Rosen, *Can Quantum-Mechanical Description of Physical Reality Be Considered Complete?*, *Phys. Rev.* **47** (May, 1935) 777–780.
- [2] P. Shor, *Algorithms for quantum computation: discrete logarithms and factoring*, in *Proceedings 35th Annual Symposium on Foundations of Computer Science*, pp. 124–134, 1994.
- [3] J. M. Deutsch, *Quantum statistical mechanics in a closed system*, *Physical Review A* **43** (Feb., 1991) 2046–2049.
- [4] M. Srednicki, *Chaos and quantum thermalization*, *Physical Review E* **50** (Aug., 1994) 888–901, [[cond-mat/9403051](#)].
- [5] P. Calabrese and J. Cardy, *Evolution of entanglement entropy in one-dimensional systems*, *Journal of Statistical Mechanics: Theory and Experiment* **2005** (Apr., 2005) 04010, [[cond-mat/0503393](#)].
- [6] P. Calabrese and J. Cardy, *Quantum quenches in extended systems*, *Journal of Statistical Mechanics: Theory and Experiment* **2007** (June, 2007) 06008, [[arXiv:0704.1880](#)].
- [7] M. Rigol, V. Dunjko, and M. Olshanii, *Thermalization and its mechanism for generic isolated quantum systems*, *Nature* **452** (Apr., 2008) 854–858, [[arXiv:0708.1324](#)].
- [8] H. Kim and D. A. Huse, *Ballistic Spreading of Entanglement in a Diffusive Nonintegrable System*, *Physical Review Letters* **111** (Sept., 2013) 127205, [[arXiv:1306.4306](#)].
- [9] M. Mezei and D. Stanford, *On entanglement spreading in chaotic systems*, *Journal of High Energy Physics* **2017** (May, 2017) 65, [[arXiv:1608.05101](#)].
- [10] R. Nandkishore and D. A. Huse, *Many-Body Localization and Thermalization in Quantum Statistical Mechanics*, *Annual Review of Condensed Matter Physics* **6** (Mar., 2015) 15–38, [[arXiv:1404.0686](#)].
- [11] D. A. Abanin, E. Altman, I. Bloch, and M. Serbyn, *Colloquium: Many-body localization, thermalization, and entanglement*, *Reviews of Modern Physics* **91** (Apr., 2019) 021001, [[arXiv:1804.11065](#)].

- [12] V. Negnevitsky, M. Marinelli, K. K. Mehta, H. Y. Lo, C. Flühmann, and J. P. Home, *Repeated multi-qubit readout and feedback with a mixed-species trapped-ion register*, *Nature* **563** (Nov., 2018) 527–531, [[arXiv:1804.09703](#)].
- [13] Z. K. Mineev, S. O. Mundhada, S. Shankar, P. Reinhold, R. Gutiérrez-Jáuregui, R. J. Schoelkopf, M. Mirrahimi, H. J. Carmichael, and M. H. Devoret, *To catch and reverse a quantum jump mid-flight*, *Nature* **570** (June, 2019) 200–204, [[arXiv:1803.00545](#)].
- [14] F. Arute *et al.*, *Quantum supremacy using a programmable superconducting processor*, *Nature* **574** (Oct., 2019) 505–510, [[arXiv:1910.11333](#)].
- [15] D. Aharonov, *Quantum to classical phase transition in noisy quantum computers*, *Physical Review A* **62** (Dec., 2000) 062311, [[quant-ph/9910081](#)].
- [16] B. Skinner, J. Ruhman, and A. Nahum, *Measurement-Induced Phase Transitions in the Dynamics of Entanglement*, *Physical Review X* **9** (Jul, 2019) 031009, [[arXiv:1808.05953](#)].
- [17] Y. Li, X. Chen, and M. P. A. Fisher, *Quantum Zeno effect and the many-body entanglement transition*, *Physical Review B* **98** (Nov., 2018) 205136, [[arXiv:1808.06134](#)].
- [18] A. Chan, R. M. Nandkishore, M. Pretko, and G. Smith, *Unitary-projective entanglement dynamics*, *Physical Review B* **99** (Jun, 2019) 224307, [[arXiv:1808.05949](#)].
- [19] P. Hayden, M. Horodecki, A. Winter, and J. Yard, *A decoupling approach to the quantum capacity*, *arXiv e-prints* (Feb., 2007) quant-ph/0702005, [[quant-ph/0702005](#)].
- [20] S. Choi, Y. Bao, X.-L. Qi, and E. Altman, *Quantum Error Correction in Scrambling Dynamics and Measurement-Induced Phase Transition*, *Physical Review Letters* **125** (July, 2020) 030505, [[arXiv:1903.05124](#)].
- [21] M. J. Gullans and D. A. Huse, *Dynamical Purification Phase Transition Induced by Quantum Measurements*, *Physical Review X* **10** (Oct., 2020) 041020, [[arXiv:1905.05195](#)].
- [22] R. Fan, S. Vijay, A. Vishwanath, and Y.-Z. You, *Self-organized error correction in random unitary circuits with measurement*, *Physical Review B* **103** (May, 2021) 174309, [[arXiv:2002.12385](#)].
- [23] L. Fidkowski, J. Haah, and M. B. Hastings, *How Dynamical Quantum Memories Forget*, *Quantum* **5** (Jan., 2021) 382, [[arXiv:2008.10611](#)].
- [24] B. Yoshida, *Decoding the Entanglement Structure of Monitored Quantum Circuits*, *arXiv e-prints* (Sept., 2021) arXiv:2109.08691, [[arXiv:2109.08691](#)].
- [25] B. Yoshida, *Projective measurement of black holes*, [arXiv:2203.04968](#).
- [26] A. C. Potter and R. Vasseur, *Entanglement dynamics in hybrid quantum circuits*, [arXiv:2111.08018](#).
- [27] J. Napp, R. L. La Placa, A. M. Dalzell, F. G. S. L. Brandao, and A. W. Harrow, *Efficient classical simulation of random shallow 2D quantum circuits*, *arXiv e-prints* (Dec., 2019) arXiv:2001.00021, [[arXiv:2001.00021](#)].

- [28] A. Nahum, S. Vijay, and J. Haah, *Operator Spreading in Random Unitary Circuits*, *Physical Review X* **8** (Apr., 2018) 021014, [[arXiv:1705.08975](#)].
- [29] T. Zhou and A. Nahum, *Emergent statistical mechanics of entanglement in random unitary circuits*, *Physical Review B* **99** (May, 2019) 174205, [[arXiv:1804.09737](#)].
- [30] C.-M. Jian, Y.-Z. You, R. Vasseur, and A. W. W. Ludwig, *Measurement-induced criticality in random quantum circuits*, *Physical Review B* **101** (Mar., 2020) 104302, [[arXiv:1908.08051](#)].
- [31] Y. Bao, S. Choi, and E. Altman, *Theory of the phase transition in random unitary circuits with measurements*, *Physical Review B* **101** (Mar., 2020) 104301, [[arXiv:1908.04305](#)].
- [32] S. Sang, Y. Li, T. Zhou, X. Chen, T. H. Hsieh, and M. P. A. Fisher, *Entanglement Negativity at Measurement-Induced Criticality*, *PRX Quantum* **2** (Jul, 2021) 030313, [[arXiv:2012.00031](#)].
- [33] Z.-C. Yang, Y. Li, M. P. A. Fisher, and X. Chen, *Entanglement phase transitions in random stabilizer tensor networks*, *Physical Review B* **105** (Mar, 2022).
- [34] Y. Li, R. Vasseur, M. P. A. Fisher, and A. W. W. Ludwig, *Statistical mechanics model for clifford random tensor networks and monitored quantum circuits*, 2021.
- [35] Y. Li, S. Vijay, and M. P. A. Fisher, *Entanglement Domain Walls in Monitored Quantum Circuits and the Directed Polymer in a Random Environment*, *arXiv e-prints* (May, 2021) arXiv:2105.13352, [[arXiv:2105.13352](#)].
- [36] A. Nahum and B. Skinner, *Entanglement and dynamics of diffusion-annihilation processes with Majorana defects*, *Physical Review Research* **2** (June, 2020) 023288, [[arXiv:1911.11169](#)].
- [37] M. Ippoliti, M. J. Gullans, S. Gopalakrishnan, D. A. Huse, and V. Khemani, *Entanglement Phase Transitions in Measurement-Only Dynamics*, *Physical Review X* **11** (Jan., 2021) 011030, [[arXiv:2004.09560](#)].
- [38] A. Lavasani, Y. Alavirad, and M. Barkeshli, *Measurement-induced topological entanglement transitions in symmetric random quantum circuits*, *Nature Physics* **17** (Jan., 2021) 342–347, [[arXiv:2004.07243](#)].
- [39] S. Sang and T. H. Hsieh, *Measurement-protected quantum phases*, *Physical Review Research* **3** (June, 2021) 023200, [[arXiv:2004.09509](#)].
- [40] A. Lavasani, Y. Alavirad, and M. Barkeshli, *Topological order and criticality in (2+1)D monitored random quantum circuits*, *arXiv e-prints* (Nov., 2020) arXiv:2011.06595, [[arXiv:2011.06595](#)].
- [41] O. Alberton, M. Buchhold, and S. Diehl, *Entanglement Transition in a Monitored Free-Fermion Chain: From Extended Criticality to Area Law*, *Physical Review Letters* **126** (Apr., 2021) 170602, [[arXiv:2005.09722](#)].

- [42] N. Lang and H. P. Büchler, *Entanglement transition in the projective transverse field Ising model*, *Physical Review B* **102** (Sept., 2020) 094204, [[arXiv:2006.09748](#)].
- [43] M. Van Regemortel, Z.-P. Cian, A. Seif, H. Dehghani, and M. Hafezi, *Entanglement Entropy Scaling Transition under Competing Monitoring Protocols*, *Physical Review Letters* **126** (Mar., 2021) 123604, [[arXiv:2008.08619](#)].
- [44] D. Gottesman, *Class of quantum error-correcting codes saturating the quantum Hamming bound*, *Physical Review A* **54** (Sept., 1996) 1862–1868, [[quant-ph/9604038](#)].
- [45] D. Gottesman, *Stabilizer codes and quantum error correction*. PhD thesis, California Institute of Technology, Jan., 1997. [quant-ph/9705052](#).
- [46] E. Dennis, A. Kitaev, A. Landahl, and J. Preskill, *Topological quantum memory*, *Journal of Mathematical Physics* **43** (Sept., 2002) 4452–4505, [[quant-ph/0110143](#)].
- [47] A. G. Fowler, M. Mariantoni, J. M. Martinis, and A. N. Cleland, *Surface codes: Towards practical large-scale quantum computation*, *Physical Review A* **86** (Sept., 2012) 032324, [[arXiv:1208.0928](#)].
- [48] Y. Li and M. P. A. Fisher, *Robust decoding in monitored dynamics of open quantum systems with Z_2 symmetry*, *arXiv e-prints* (Aug., 2021) [arXiv:2108.04274](#), [[arXiv:2108.04274](#)].
- [49] E. T. Campbell, *A theory of single-shot error correction for adversarial noise*, *Quantum Science and Technology* **4** (Feb, 2019) 025006.
- [50] H. Bombín, *Single-shot fault-tolerant quantum error correction*, *Physical Review X* **5** (Sep, 2015).
- [51] U. Agrawal, A. Zabalo, K. Chen, J. H. Wilson, A. C. Potter, J. H. Pixley, S. Gopalakrishnan, and R. Vasseur, *Entanglement and charge-sharpening transitions in $U(1)$ symmetric monitored quantum circuits*, *arXiv e-prints* (July, 2021) [arXiv:2107.10279](#), [[arXiv:2107.10279](#)].
- [52] F. Barratt, U. Agrawal, S. Gopalakrishnan, D. A. Huse, R. Vasseur, and A. C. Potter, *Field theory of charge sharpening in symmetric monitored quantum circuits*, *arXiv e-prints* (Nov., 2021) [arXiv:2111.09336](#), [[arXiv:2111.09336](#)].
- [53] F. Barratt, U. Agrawal, A. C. Potter, S. Gopalakrishnan, and R. Vasseur, *Transitions in the learnability of global charges from local measurements*, [arXiv:2206.12429](#).
- [54] B. Eastin and E. Knill, *Restrictions on transversal encoded quantum gate sets*, *Physical Review Letters* **102** (Mar, 2009).
- [55] P. Faist, S. Nezami, V. V. Albert, G. Salton, F. Pastawski, P. Hayden, and J. Preskill, *Continuous symmetries and approximate quantum error correction*, *Physical Review X* **10** (Oct, 2020).
- [56] S. Zhou, Z.-W. Liu, and L. Jiang, *New perspectives on covariant quantum error correction*, *Quantum* **5** (Aug, 2021) 521.

- [57] J. Willsher, S.-W. Liu, R. Moessner, and J. Knolle, *Measurement-induced phase transition in a chaotic classical many-body system*, *Physical Review B* **106** (Jul, 2022).
- [58] A. Pizzi, D. Malz, A. Nunnenkamp, and J. Knolle, *Bridging the gap between classical and quantum many-body information dynamics*, [arXiv:2204.03016](#).
- [59] Y. Li, X. Chen, and M. P. A. Fisher, *Measurement-driven entanglement transition in hybrid quantum circuits*, *Physical Review B* **100** (Oct., 2019) 134306, [[arXiv:1901.08092](#)].
- [60] Y. Li, X. Chen, A. W. W. Ludwig, and M. P. A. Fisher, *Conformal invariance and quantum non-locality in hybrid quantum circuits*, *arXiv e-prints* (Mar., 2020) [arXiv:2003.12721](#), [[arXiv:2003.12721](#)].
- [61] Y. Li and M. P. A. Fisher, *Statistical mechanics of quantum error correcting codes*, *Physical Review B* **103** (Mar., 2021) 104306, [[arXiv:2007.03822](#)].
- [62] Y. Li, Y. Zou, P. Glorioso, E. Altman, and M. P. A. Fisher, *Linear cross entropy benchmark for measurement-induced phase transitions*, 2022.
- [63] X. Cao, A. Tilloy, and A. De Luca, *Entanglement in a fermion chain under continuous monitoring*, *SciPost Physics* **7** (Aug., 2019) 024, [[arXiv:1804.04638](#)].
- [64] B. Misra and E. C. G. Sudarshan, *The Zeno's paradox in quantum theory*, *Journal of Mathematical Physics* **18** (Apr., 1977) 756–763.
- [65] M. L. Mehta, *Random Matrices*. 3rd ed., 2004.
- [66] P. J. Forrester, *Log-Gases and Random Matrices (LMS-34)*. Princeton University Press, 2010.
- [67] D. Gottesman, *The Heisenberg Representation of Quantum Computers*, *arXiv e-prints* (July, 1998) [quant-ph/9807006](#), [[quant-ph/9807006](#)].
- [68] S. Aaronson and D. Gottesman, *Improved simulation of stabilizer circuits*, *Physical Review A* **70** (Nov., 2004) 052328, [[quant-ph/0406196](#)].
- [69] M. A. Nielsen and I. L. Chuang, *Quantum Computation and Quantum Information*. Cambridge University Press, 2010.
- [70] H. M. Wiseman, *Quantum trajectories and quantum measurement theory*, *Quantum and Semiclassical Optics* **8** (Feb., 1996) 205–222, [[quant-ph/0302080](#)].
- [71] H.-P. Breuer and F. Petruccione, *The theory of open quantum systems*. Oxford University Press, 2002.
- [72] A. Nahum, J. Ruhman, S. Vijay, and J. Haah, *Quantum Entanglement Growth under Random Unitary Dynamics*, *Physical Review X* **7** (July, 2017) 031016, [[arXiv:1608.06950](#)].
- [73] J. M. Hammersley and D. J. A. Welsh, *First-Passage Percolation, Subadditive Processes, Stochastic Networks, and Generalized Renewal Theory*, pp. 61–110. Springer Berlin Heidelberg, Berlin, Heidelberg, 1965.

- [74] J. T. Chayes, L. Chayes, and R. Durrett, *Critical behavior of the two-dimensional first passage time*, *Journal of Statistical Physics* **45** (Dec, 1986) 933–951.
- [75] H. Kesten, *Aspects of first passage percolation*, in *École d'été de probabilités de Saint Flour XIV-1984*, pp. 125–264. Springer, 1986.
- [76] H. Kesten, *Percolation theory and first-passage percolation*, *Ann. Probab.* **15** (10, 1987) 1231–1271.
- [77] Y. Li and M. P. A. Fisher [unpublished](#).
- [78] A. Klappenecker and M. Roetteler, *Beyond Stabilizer Codes II: Clifford Codes*, *arXiv e-prints* (Oct., 2000) quant-ph/0010076, [[quant-ph/0010076](#)].
- [79] N. Linden, F. Matúš, M. B. Ruskai, and A. Winter, *The Quantum Entropy Cone of Stabiliser States*, *arXiv e-prints* (Feb., 2013) arXiv:1302.5453, [[arXiv:1302.5453](#)].
- [80] D. P. DiVincenzo, D. W. Leung, and B. M. Terhal, *Quantum Data Hiding*, *arXiv e-prints* (Mar., 2001) quant-ph/0103098, [[quant-ph/0103098](#)].
- [81] D. Fattal, T. S. Cubitt, Y. Yamamoto, S. Bravyi, and I. L. Chuang, *Entanglement in the stabilizer formalism*, *arXiv e-prints* (June, 2004) quant-ph/0406168, [[quant-ph/0406168](#)].
- [82] A. Hamma, R. Ionicioiu, and P. Zanardi, *Bipartite entanglement and entropic boundary law in lattice spin systems*, *Physical Review A* **71** (Feb, 2005) 022315, [[quant-ph/0409073](#)].
- [83] A. Hamma, R. Ionicioiu, and P. Zanardi, *Ground state entanglement and geometric entropy in the Kitaev model*, *Physics Letters A* **337** (Mar, 2005) 22–28, [[quant-ph/0406202](#)].
- [84] A. Chandran and C. R. Laumann, *Semiclassical limit for the many-body localization transition*, *Physical Review B* **92** (July, 2015) 024301, [[arXiv:1501.01971](#)].
- [85] R. Vasseur, A. C. Potter, Y.-Z. You, and A. W. W. Ludwig, *Entanglement transitions from holographic random tensor networks*, *Physical Review B* **100** (Oct, 2019) 134203, [[arXiv:1807.07082](#)].
- [86] F. P. Buff, R. A. Lovett, and F. H. Stillinger, *Interfacial density profile for fluids in the critical region*, *Phys. Rev. Lett.* **15** (Oct, 1965) 621–623.
- [87] J. D. Weeks, *Structure and thermodynamics of the liquid–vapor interface*, *The Journal of Chemical Physics* **67** (1977), no. 7 3106–3121.
- [88] M. M. Wolf, F. Verstraete, M. B. Hastings, and J. I. Cirac, *Area Laws in Quantum Systems: Mutual Information and Correlations*, *Physical Review Letters* **100** (Feb., 2008) 070502, [[arXiv:0704.3906](#)].
- [89] P. Calabrese and J. Cardy, *Entanglement entropy and conformal field theory*, *Journal of Physics A Mathematical General* **42** (Dec, 2009) 504005, [[arXiv:0905.4013](#)].

- [90] P. Di Francesco, P. Mathieu, and D. Senechal, *Conformal Field Theory*. Graduate Texts in Contemporary Physics. Springer-Verlag, New York, 1997.
- [91] A. Chan, A. De Luca, and J. T. Chalker, *Solution of a Minimal Model for Many-Body Quantum Chaos*, *Physical Review X* **8** (Oct., 2018) 041019, [[arXiv:1712.06836](#)].
- [92] A. Chan, A. De Luca, and J. T. Chalker, *Spectral Statistics in Spatially Extended Chaotic Quantum Many-Body Systems*, *Physical Review Letters* **121** (Aug., 2018) 060601, [[arXiv:1803.03841](#)].
- [93] P. Kos, M. Ljubotina, and T. Prosen, *Many-Body Quantum Chaos: Analytic Connection to Random Matrix Theory*, *Physical Review X* **8** (Apr., 2018) 021062, [[arXiv:1712.02665](#)].
- [94] B. Bertini, P. Kos, and T. Prosen, *Exact Spectral Form Factor in a Minimal Model of Many-Body Quantum Chaos*, *ArXiv e-prints* (May, 2018) arXiv:1805.00931, [[arXiv:1805.00931](#)].
- [95] L. Zhang, H. Kim, and D. A. Huse, *Thermalization of entanglement*, *Physical Review E* **91** (June, 2015) 062128, [[arXiv:1501.01315](#)].
- [96] B. Bertini, P. Kos, and T. Prosen, *Entanglement spreading in a minimal model of maximal many-body quantum chaos*, *arXiv e-prints* (Dec., 2018) arXiv:1812.05090, [[arXiv:1812.05090](#)].
- [97] X. Chen, T. Zhou, D. A. Huse, and E. Fradkin, *Out-of-time-order correlations in many-body localized and thermal phases*, *Annalen der Physik* **529** (July, 2017) 1600332, [[arXiv:1610.00220](#)].
- [98] P. Hosur, X.-L. Qi, D. A. Roberts, and B. Yoshida, *Chaos in quantum channels*, *Journal of High Energy Physics* **2016** (Feb., 2016) 4, [[arXiv:1511.04021](#)].
- [99] F. Mezzadri, *How to generate random matrices from the classical compact groups*, *ArXiv Mathematical Physics e-prints* (Sept., 2006) [[math-ph/0609050](#)].
- [100] C. W. von Keyserlingk, T. Rakovszky, F. Pollmann, and S. L. Sondhi, *Operator Hydrodynamics, OTOCs, and Entanglement Growth in Systems without Conservation Laws*, *Physical Review X* **8** (Apr., 2018) 021013, [[arXiv:1705.08910](#)].
- [101] P. Calabrese and J. Cardy, *Entanglement entropy and quantum field theory*, *Journal of Statistical Mechanics: Theory and Experiment* **6** (June, 2004) 06002, [[hep-th/0405152](#)].
- [102] M. Levin and X.-G. Wen, *Detecting Topological Order in a Ground State Wave Function*, *Physical Review Letters* **96** (Mar., 2006) 110405, [[cond-mat/0510613](#)].
- [103] A. Kitaev and J. Preskill, *Topological Entanglement Entropy*, *Physical Review Letters* **96** (Mar., 2006) 110404, [[hep-th/0510092](#)].
- [104] S. Ryu and T. Takayanagi, *Holographic Derivation of Entanglement Entropy from the anti de Sitter Space/Conformal Field Theory Correspondence*, *Physical Review Letters* **96** (May, 2006) 181602, [[hep-th/0603001](#)].

- [105] J. S. Bell, *On the Einstein Podolsky Rosen paradox*, *Physics Physique Fizika* **1** (Nov, 1964) 195–200.
- [106] C. H. Bennett, G. Brassard, C. Crépeau, R. Jozsa, A. Peres, and W. K. Wootters, *Teleporting an unknown quantum state via dual classical and Einstein-Podolsky-Rosen channels*, *Phys. Rev. Lett.* **70** (Mar, 1993) 1895–1899.
- [107] D. Bouwmeester, J.-W. Pan, K. Mattle, M. Eibl, H. Weinfurter, and A. Zeilinger, *Experimental quantum teleportation*, *Nature* **390** (Dec., 1997) 575–579, [[arXiv:1901.11004](#)].
- [108] M. Żukowski, A. Zeilinger, M. A. Horne, and A. K. Ekert, “*Event-ready-detectors*” *Bell experiment via entanglement swapping*, *Phys. Rev. Lett.* **71** (Dec, 1993) 4287–4290.
- [109] J.-W. Pan, D. Bouwmeester, H. Weinfurter, and A. Zeilinger, *Experimental Entanglement Swapping: Entangling Photons That Never Interacted*, *Phys. Rev. Lett.* **80** (May, 1998) 3891–3894.
- [110] T. Jennewein, G. Weihs, J.-W. Pan, and A. Zeilinger, *Experimental Nonlocality Proof of Quantum Teleportation and Entanglement Swapping*, *Phys. Rev. Lett.* **88** (Dec, 2001) 017903.
- [111] E. H. Lieb and D. W. Robinson, *The finite group velocity of quantum spin systems*, *Comm. Math. Phys.* **28** (1972), no. 3 251–257.
- [112] M. B. Hastings, *Locality in Quantum Systems*, *arXiv e-prints* (Aug, 2010) [arXiv:1008.5137](#), [[arXiv:1008.5137](#)].
- [113] M. J. Gullans and D. A. Huse, *Scalable Probes of Measurement-Induced Criticality*, *Physical Review Letters* **125** (Aug., 2020) 070606, [[arXiv:1910.00020](#)].
- [114] A. A. Belavin, A. M. Polyakov, and A. B. Zamolodchikov, *Infinite conformal symmetry in two-dimensional quantum field theory*, *Nuclear Physics B* **241** (Jul, 1984) 333–380.
- [115] J. Cardy, *Boundary Conformal Field Theory*, *arXiv e-prints* (Nov, 2004) [hep-th/0411189](#), [[hep-th/0411189](#)].
- [116] P. Hayden, S. Nezami, X.-L. Qi, N. Thomas, M. Walter, and Z. Yang, *Holographic duality from random tensor networks*, *Journal of High Energy Physics* **2016** (Nov, 2016) 9, [[arXiv:1601.01694](#)].
- [117] T. A. Driscoll and L. N. Trefethen, *Schwarz-Christoffel Mapping*. Cambridge Monographs on Applied and Computational Mathematics. Cambridge University Press, 2002.
- [118] J. L. Cardy, *Critical percolation in finite geometries*, *Journal of Physics A Mathematical General* **25** (Feb, 1992) L201–L206, [[hep-th/9111026](#)].

- [119] V. Gurarie and A. W. W. Ludwig, *Conformal Field Theory at Central charge $c=0$ and Two-Dimensional Critical Systems with Quenched Disorder*, In “*From Fields to Strings: Circumnavigating Theoretical Physics*”, Editors: M. Shifman, A. Vainshtein, J. Wheeler (World Scientific) (2005) 1384–1440, [[0409105](#)].
- [120] J. L. Cardy, *Effect of boundary conditions on the operator content of two-dimensional conformally invariant theories*, *Nuclear Physics B* **275** (Oct, 1986) 200–218.
- [121] J. Jiang and C.-L. Yao, *Critical first-passage percolation starting on the boundary*, *arXiv e-prints* (Dec, 2016) arXiv:1612.01803, [[arXiv:1612.01803](#)].
- [122] D. Stauffer and A. Aharony, *Introduction To Percolation Theory, Second Edition*. Taylor & Francis, 2nd ed., 1992.
- [123] A. Zabalo, M. J. Gullans, J. H. Wilson, S. Gopalakrishnan, D. A. Huse, and J. H. Pixley, *Critical properties of the measurement-induced transition in random quantum circuits*, *Physical Review B* **101** (Feb., 2020) 060301, [[arXiv:1911.00008](#)].
- [124] D. N. Page, *Average entropy of a subsystem*, *Physical Review Letters* **71** (Aug., 1993) 1291–1294, [[gr-qc/9305007](#)].
- [125] Y. Ashida and M. Ueda, *Full-Counting Many-Particle Dynamics: Nonlocal and Chiral Propagation of Correlations*, *arXiv e-prints* (Sept., 2017) arXiv:1709.03704, [[arXiv:1709.03704](#)].
- [126] P. W. Shor, *Scheme for reducing decoherence in quantum computer memory*, *Physical Review A* **52** (Oct., 1995) R2493–R2496.
- [127] A. M. Steane, *Error Correcting Codes in Quantum Theory*, *Physical Review Letters* **77** (July, 1996) 793–797.
- [128] C. H. Bennett, D. P. Divincenzo, J. A. Smolin, and W. K. Wootters, *Mixed-state entanglement and quantum error correction*, *Physical Review A* **54** (Nov., 1996) 3824–3851, [[quant-ph/9604024](#)].
- [129] E. Knill and R. Laflamme, *Theory of quantum error-correcting codes*, *Physical Review A* **55** (Feb., 1997) 900–911.
- [130] A. R. Calderbank and P. W. Shor, *Good quantum error-correcting codes exist*, *Physical Review A* **54** (Aug., 1996) 1098–1105, [[quant-ph/9512032](#)].
- [131] A. Steane, *Multiple-Particle Interference and Quantum Error Correction*, *Proceedings of the Royal Society of London Series A* **452** (Nov., 1996) 2551–2577, [[quant-ph/9601029](#)].
- [132] A. R. Calderbank, E. M. Rains, P. W. Shor, and N. J. A. Sloane, *Quantum Error Correction and Orthogonal Geometry*, *Physical Review Letters* **78** (Jan., 1997) 405–408, [[quant-ph/9605005](#)].
- [133] A. Y. Kitaev, *Fault-tolerant quantum computation by anyons*, *Annals of Physics* **303** (Jan., 2003) 2–30, [[quant-ph/9707021](#)].

- [134] A. Almheiri, X. Dong, and D. Harlow, *Bulk locality and quantum error correction in AdS/CFT*, *Journal of High Energy Physics* **2015** (Apr., 2015) 163, [[arXiv:1411.7041](#)].
- [135] A. Nahum, J. Ruhman, and D. A. Huse, *Dynamics of entanglement and transport in one-dimensional systems with quenched randomness*, *Physical Review B* **98** (July, 2018) 035118, [[arXiv:1705.10364](#)].
- [136] C. Jonay, D. A. Huse, and A. Nahum, *Coarse-grained dynamics of operator and state entanglement*, *arXiv e-prints* (Feb., 2018) arXiv:1803.00089, [[arXiv:1803.00089](#)].
- [137] T. Zhou and A. Nahum, *The entanglement membrane in chaotic many-body systems*, *arXiv e-prints* (Dec., 2019) arXiv:1912.12311, [[arXiv:1912.12311](#)].
- [138] M. P. A. Fisher, D. S. Fisher, and J. D. Weeks, *Agreement of capillary-wave theory with exact results for the interface profile of the two-dimensional ising model*, *Phys. Rev. Lett.* **48** (Feb, 1982) 368–368.
- [139] B. Yoshida and I. L. Chuang, *Framework for classifying logical operators in stabilizer codes*, *Physical Review A* **81** (May, 2010) 052302, [[arXiv:1002.0085](#)].
- [140] J. Haah and J. Preskill, *Logical operator tradeoff for local quantum codes*, *arXiv e-prints* (Nov., 2010) arXiv:1011.3529, [[arXiv:1011.3529](#)].
- [141] J. Haah, *Algebraic Methods for Quantum Codes on Lattices*, *arXiv e-prints* (July, 2016) arXiv:1607.01387, [[arXiv:1607.01387](#)].
- [142] S. Bravyi and B. Terhal, *A no-go theorem for a two-dimensional self-correcting quantum memory based on stabilizer codes*, *New Journal of Physics* **11** (Apr., 2009) 043029, [[arXiv:0810.1983](#)].
- [143] J. Preskill, *Lecture notes for physics 229: Quantum information and computation*. California Institute of Technology, 1998.
- [144] B. Schumacher and M. D. Westmoreland, *Approximate quantum error correction*, *arXiv e-prints* (Dec., 2001) quant-ph/0112106, [[quant-ph/0112106](#)].
- [145] I. Devetak, *The private classical capacity and quantum capacity of a quantum channel*, *arXiv e-prints* (Apr., 2003) quant-ph/0304127, [[quant-ph/0304127](#)].
- [146] A. Abeyesinghe, I. Devetak, P. Hayden, and A. Winter, *The mother of all protocols: restructuring quantum information's family tree*, *Proceedings of the Royal Society of London Series A* **465** (June, 2009) 2537–2563, [[quant-ph/0606225](#)].
- [147] A. Ekert and C. Macchiavello, *Error Correction in Quantum Communication*, *arXiv e-prints* (Feb., 1996) quant-ph/9602022, [[quant-ph/9602022](#)].
- [148] D. A. Huse and C. L. Henley, *Pinning and roughening of domain walls in Ising systems due to random impurities*, *Physical Review Letters* **54** (June, 1985) 2708–2711.
- [149] M. Kardar, *Roughening by impurities at finite temperatures*, *Physical Review Letters* **55** (Dec., 1985) 2923.

- [150] D. A. Huse, C. L. Henley, and D. S. Fisher, *Huse, Henley, and Fisher respond*, *Physical Review Letters* **55** (Dec., 1985) 2924.
- [151] M. Kardar and Y.-C. Zhang, *Scaling of directed polymers in random media*, *Physical Review Letters* **58** (May, 1987) 2087–2090.
- [152] M. Kardar, G. Parisi, and Y.-C. Zhang, *Dynamic scaling of growing interfaces*, *Physical Review Letters* **56** (Mar., 1986) 889–892.
- [153] M. Szyniszewski, A. Romito, and H. Schomerus, *Entanglement transition from variable-strength weak measurements*, *Physical Review B* **100** (Aug, 2019) 064204, [[arXiv:1903.05452](#)].
- [154] Q. Tang and W. Zhu, *Measurement-induced phase transition: A case study in the nonintegrable model by density-matrix renormalization group calculations*, *Physical Review Research* **2** (Jan., 2020) 013022, [[arXiv:1908.11253](#)].
- [155] J. Lopez-Piqueres, B. Ware, and R. Vasseur, *Mean-field theory of entanglement transitions from random tree tensor networks*, *arXiv e-prints* (Mar., 2020) arXiv:2003.01138, [[arXiv:2003.01138](#)].
- [156] X. Chen, Y. Li, M. P. A. Fisher, and A. Lucas, *Emergent conformal symmetry in nonunitary random dynamics of free fermions*, *Physical Review Research* **2** (July, 2020) 033017, [[arXiv:2004.09577](#)].
- [157] Y. Fuji and Y. Ashida, *Measurement-induced quantum criticality under continuous monitoring*, *arXiv e-prints* (Apr., 2020) arXiv:2004.11957, [[arXiv:2004.11957](#)].
- [158] O. Lunt and A. Pal, *Measurement-induced entanglement transitions in many-body localized systems*, *arXiv e-prints* (May, 2020) arXiv:2005.13603, [[arXiv:2005.13603](#)].
- [159] S. Vijay, *Measurement-Driven Phase Transition within a Volume-Law Entangled Phase*, *arXiv e-prints* (May, 2020) arXiv:2005.03052, [[arXiv:2005.03052](#)].
- [160] X. Turkeshi, R. Fazio, and M. Dalmonte, *Measurement-induced criticality in (2+1)-d hybrid quantum circuits*, *arXiv e-prints* (2020) 2007.02970, [[arXiv:2007.02970](#)].
- [161] A. Nahum, S. Roy, B. Skinner, and J. Ruhman, *Measurement and entanglement phase transitions in all-to-all quantum circuits, on quantum trees, and in Landau-Ginsburg theory*, *arXiv e-prints* (Sept., 2020) arXiv:2009.11311, [[arXiv:2009.11311](#)].
- [162] Y. Bao, S. Choi, and E. Altman, *Symmetry enriched phases of quantum circuits*, *arXiv e-prints* (Feb., 2021) arXiv:2102.09164, [[arXiv:2102.09164](#)].
- [163] J. M. Koh, S.-N. Sun, M. Motta, and A. J. Minnich, *Experimental realization of a measurement-induced entanglement phase transition on a superconducting quantum processor*, [arXiv:2203.04338](#).

- [164] C. Noel, P. Niroula, D. Zhu, A. Risinger, L. Egan, D. Biswas, M. Cetina, A. V. Gorshkov, M. J. Gullans, D. A. Huse, and C. Monroe, *Observation of measurement-induced quantum phases in a trapped-ion quantum computer*, *arXiv e-prints* (June, 2021) arXiv:2106.05881, [[arXiv:2106.05881](#)].
- [165] H. Dehghani, A. Lavasani, M. Hafezi, and M. J. Gullans, *Neural-network decoders for measurement induced phase transitions*, [arXiv:2204.10904](#).
- [166] M. Ippoliti and V. Khemani, *Postselection-Free Entanglement Dynamics via Spacetime Duality*, *Physical Review Letters* **126** (Feb., 2021) 060501, [[arXiv:2010.15840](#)].
- [167] M. Ippoliti, T. Rakovszky, and V. Khemani, *Fractal, logarithmic and volume-law entangled non-thermal steady states via spacetime duality*, *arXiv e-prints* (Mar., 2021) arXiv:2103.06873, [[arXiv:2103.06873](#)].
- [168] T.-C. Lu and T. Grover, *Entanglement transitions via space-time rotation of quantum circuits*, *arXiv e-prints* (Mar., 2021) arXiv:2103.06356, [[arXiv:2103.06356](#)].
- [169] A. Zabalo, M. J. Gullans, J. H. Wilson, R. Vasseur, A. W. W. Ludwig, S. Gopalakrishnan, D. A. Huse, and J. H. Pixley, *Operator scaling dimensions and multifractality at measurement-induced transitions*, *arXiv e-prints* (July, 2021) arXiv:2107.03393, [[arXiv:2107.03393](#)].
- [170] S.-K. Jian, C. Liu, X. Chen, B. Swingle, and P. Zhang, *Quantum error as an emergent magnetic field*, *arXiv e-prints* (June, 2021) arXiv:2106.09635, [[arXiv:2106.09635](#)].
- [171] K. Noh, L. Jiang, and B. Fefferman, *Efficient classical simulation of noisy random quantum circuits in one dimension*, *arXiv e-prints* (Mar., 2020) arXiv:2003.13163, [[arXiv:2003.13163](#)].
- [172] A. Deshpande, P. Niroula, O. Shtanko, A. V. Gorshkov, B. Fefferman, and M. J. Gullans, *Tight bounds on the convergence of noisy random circuits to the uniform distribution*, [arXiv:2112.00716](#).
- [173] A. M. Dalzell, N. Hunter-Jones, and F. G. S. L. Brandão, *Random quantum circuits transform local noise into global white noise*, [arXiv:2111.14907](#).
- [174] S. Bravyi and D. Gosset, *Improved Classical Simulation of Quantum Circuits Dominated by Clifford Gates*, *Physical Review Letters* **116** (June, 2016) 250501, [[arXiv:1601.07601](#)].
- [175] Q. Tang, X. Chen, and W. Zhu, *Quantum criticality in the nonunitary dynamics of $(2+1)$ -dimensional free fermions*, *Physical Review B* **103** (May, 2021) 174303, [[arXiv:2101.04320](#)].
- [176] D. Gottesman [private communications](#).
- [177] A. M. Polyakov, *Conformal symmetry of critical fluctuations*, *JETP Lett.* **12** (1970) 381–383. [*Pisma Zh. Eksp. Teor. Fiz.*12,538(1970)].
- [178] M. Popp, F. Verstraete, M. A. Martín-Delgado, and J. I. Cirac, *Localizable entanglement*, *Physical Review A* **71** (Apr, 2005).

- [179] L. R. Ford and D. R. Fulkerson, *Maximal flow through a network*, *Canadian Journal of Mathematics* **8** (1956) 399–404.
- [180] J. Edmonds and R. M. Karp, *Theoretical improvements in algorithmic efficiency for network flow problems*, *J. ACM* **19** (Apr., 1972) 248–264.
- [181] S. Zhou, Z. Yang, A. Hamma, and C. Chamon, *Single T gate in a Clifford circuit drives transition to universal entanglement spectrum statistics*, *SciPost Physics* **9** (Dec., 2020) 087, [[arXiv:1906.01079](https://arxiv.org/abs/1906.01079)].
- [182] J. Iaconis, *Quantum State Complexity in Computationally Tractable Quantum Circuits*, *arXiv e-prints* (Sept., 2020) arXiv:2009.05512, [[arXiv:2009.05512](https://arxiv.org/abs/2009.05512)].